THE UNIVERSITY *of* EDINBURGH

Hydrodynamic Modelling for Structural Analysis of Tidal Stream Turbine Blades

Steven C. Allsop

2018

This thesis is submitted in partial fulfilment of the requirements for the award of an Engineering Doctorate, jointly awarded by the University of Edinburgh, the University of Exeter, and the University of Strathclyde. The work presented has been conducted under the industrial supervision of Électricité de France (EDF R&D) as a project within the Industrial Doctoral Centre for Offshore Renewable Energy (IDCORE).

THE UNIVERSITY *of* EDINBURGH

UNIVERSITY OF EXETER

Declaration

I declare that this thesis has been composed solely by myself and that it has not been submitted, either in whole or in part, in any previous application for a degree. Except where otherwise acknowledged, the work presented is entirely my own.

Steven C. Allsop

11 June 2018

Abstract

The predictable nature of the tides offers a regular, reliable source of renewable energy that can be harnessed using tidal stream turbines (TSTs). The UK's practically extractable tidal stream energy resource has the potential to supply around 7% of the country's annual electricity demand. As of 2016, the world's first commercial scale arrays have been deployed around the UK and France.

The harsh nature of the marine operating environment poses a number of engineering challenges, where the optimal turbine design solution remains under investigation. In this thesis, a numerical model is developed to assess the power production and hydrodynamic behaviour of horizontal axis tidal turbines. The developed model builds upon well established and computationally efficient Blade Element Momentum Theory (BEMT) method for modern three-bladed wind turbines. The main novel contribution of this thesis is extending the application to an alternative design of a ducted, high solidity and open centre TST.

A validation study using measurements from multiple different scale model experimental tank tests has proven the applicability of the model and suitability of the imposed correction factors. The analytical modifications to account for ducted flow were subsequently indirectly verified, where predictions of turbine power and axial thrust forces under optimal operating speeds were within 2% of those using more advanced computational fluid dynamics (CFD) methods.

This thesis presents a commercial application case of two turbines designed

by OpenHydro, examining the BEMT performance with a sophisticated blade resolved CFD study. A comparison of results finds that the model is capable of predicting the average peak power to within 12%, however it under predicts thrust levels by an average of 35%. This study concludes that the model is applicable to ducted turbine configurations, but is limited in capturing the complex flow interactions towards the open centre, which requires further investigation.

The computational efficiency of the newly developed model allowed a structural analysis of the composite blades, thus demonstrating it is suitable to effectively evaluate engineering applications. Stresses are seen to be dominated by flap-wise bending moments, which peak at the mid-length of the blade. This tool will further enable EDF to perform third party assessments of the different turbine designs, to aid decision making for future projects.

Acknowledgements

Throughout the course of this EngD, I have received a huge amount help and support from a number of people who I would like to acknowledge here.

I would firstly like to extend my thanks to my supervisors, whose continual contributions have been invaluable to the completion of this thesis: Christophe Peyrard for direction in all aspects of the research and helpful insights particularly on the hydrodynamic modelling; Dr Philipp Thies for his patient support, guidance and stability; and Pierre Bousseau for the inspired discussions and collaboration on the structural analysis.

Appreciations also go to my internal examiner Professor Nigel Barltrop, and external examiners Professor Tim O'Doherty and Dr Andrew Good for taking the time to read and review my work, and for their constructive discussions during the Viva.

I am extremely grateful to the organisers, lecturers and professors at IDCORE, and to the Laboratoire Saint Venant for hosting me throughout the research phase of this doctorate - it has been a privilege to be a part of this programme. Acknowledgements go to the funding bodies: the Energy Technologies Institute, the Research Councils Energy Programme and EDF R&D, whose financial support made this research possible. Also, recognition should go to OpenHydro who enabled this work to be applied to a commercial case, and to Professor Kueny for supplying results for model comparison.

I'd like to say thanks to all my co-idcorians for all the genuinely great times throughout the course: Ciaran, Claire, Donald, Enrico, George, Leah, Marco, Rob, Scott, Shubba, Simon, Steph and Sunny. Also to my friends and colleagues at the EDF lab for creating an enjoyable and spirited environment to work, especially to: Cecile, Marine, Rafaello and Roberto; members of the elitist ping pong club Adrien, Constantine and Florent; as well as to Agnés, Alex, Ismail, Jeff, Jeremie, Mathieu, Philippe and Sylvain.

I am so grateful to my wonderful friends from home who have (often unknowingly) influenced me (often positively) in some way: firstly to the all the couples who got married throughout the last 4 years, for providing plentiful legitimate excuses for writing distractions: Dave and Lucy, Michelle and Rhi, Tom and Lorna, Aarti, Becky, Fi, and Toby; also thanks to Joey, Sam, Sean, Sid, Tom, Tom and the rest of the Shire folk; and to Bhavin, Erika and Paschal.

A heartfelt thank you to my family: my parents Bernadette and Christopher Allsop for giving me the tools and confidence to head down this path; and to my sisters Jennifer and Alice, my brother David and brother-in-law Shim, who have ever shown me unconditional love and encouragement.

Lastly to Alexandra, who has been my rock in a hard place.

Contents

List of Tables

List of Figures

Nomenclature

α	Angle of attack
β	Blade twist
Δt	Time step
Δx	Length interval
$\dot{m}$	Mass flow rate
ϵ	Blockage ratio
η_{02}	Duct inlet efficiency
η_{34}	Duct diffuser efficiency
μ	Dynamic viscosity
μ_t	Turbulent eddy dynamic viscosity
ν	Kinematic viscosity
Ω	Angular velocity of the turbine
ω	Angular velocity of the wake
ω	Specific rate of dissipation of turbulent kinetic energy
Φ	Azimuthal angle
ϕ	Inflow angle
ϕ_i	Inflow angle at a blade element
ϕ_s	Angle between vortex sheets
ρ	Density
σ_r	Local blade solidity

$\sigma_{br_{0^\circ}}$ Theoretical breaking stress of a uni-directional laminate in transverse direction

$\sigma_{br_{90^\circ}}$ Theoretical breaking stress of a uni-directional laminate in longitudinal direction

σ_{br} Theoretical breaking stress

σ_{maxall} Maximum allowable stress

σ_{vm} Von Mises stress

$\sigma_{xx,x}$ Direct stress from x forces (weight)

$\sigma_{xx,y}$ Bending stress in x direction in x-plane from bending moments around y axis

$\sigma_{xx,z}$ Direct stress in x direction in x-plane from from bending moments around z axis

σ_{xx} Normal stress in the x direction

σ_{yy} Normal stress in the y direction

σ_{zz} Normal stress in the z direction

τ_{xy} Shear stress on: x-plane, y direction = τ_{yx} y-plane, x direction

τ_{xz} Shear stress on: x-plane, z direction = τ_{zx} z-plane, x direction

τ_{yz} Shear stress on: y-plane, z direction = τ_{zy} z-plane, y direction

θ_{in} Diffuser inner surface angle

θ_{out} Diffuser outer surface angle

$\tilde{\beta}$ Normalised blade twist angle

$\tilde{C_P}$ Normalised coefficient of power

$\tilde{C_T}$ Normalised coefficient of thrust

$\tilde{c}$ Normalised chord length

$\tilde{t}$ Normalised hydrofoil thickness

ε Dissipation rate of turbulent kinetic energy

εbr_{0° Theoretical breaking strain of a uni-directional laminate in transverse direction

εbr Theoretical breaking strain

ζ Power law exponent

A Stream tube sectional area

a Axial induction factor

a' Tangential induction factor

a'_0 Tangential induction factor at initial conditions

a'_i Tangential induction factor of blade element

a'_j Old tangential induction factor, at convergence step j

a'_{j+1} New tangential induction factor, at convergence step j+1

a_0 Axial induction factor at initial conditions

A_d Area of the disc

a_i Axial induction factor of blade element

a_j Old axial induction factor, at convergence step j

a_T Transitional axial induction factor to highly loaded regime

A_{in} Duct inlet area

a_{j+1} New axial induction factor, at convergence step j+1

A_{out} Duct exit area

AR Blade aspect ratio

BM Bending moment

BM_{ax} Bending moment around rotor axial direction (in plane)

BM_{tan} Bending moment around rotor tangential direction (out of plane)

c Chord length

C_D Coefficient of drag

c_i Chord length of blade element

C_L Coefficient of lift

C_P Coefficient of power

C_p Coefficient of pressure

C_p02 Duct inlet coefficient of pressure

C_p34 Duct diffuser coefficient of pressure

C_s Coefficient of shear

C_T Coefficient of thrust (axial force)

C_x Coefficient of combined lift and drag vectors in axial direction

C_y Coefficient of combined lift and drag vectors in tangential direction

C_α Unknown coefficient of lift or drag at a particular angle of attack

$C_{D_{2D}}$ 2-D drag coefficient

$C_{D_{3D}}$ 3-D drag coefficient

$C_{L_{2D}}$ 2-D lift coefficient

$C_{L_{3D}}$ 3-D lift coefficient

$C_{P_{error}}$ Error in power coefficient measurement

C_{pb} Base pressure coefficient

$C_{T_{error}}$ Error in thrust coefficient measurement

$C_{T_{loc}}$ Thrust coefficient within an annular ring

CFL Courant number

D Drag force

d Normal distance between vortex sheets

D_i Fatigue damage

d_j Distance to the centroid of individual sub shapes

dA Area of annular ring

E Young's modulus

E_{0° Young's modulus of a uni-directional laminate in transverse direction

E_{90° Young's modulus of a uni-directional laminate in longitudinal direction

F Combined tip / hub loss correction factor

F_w Force due to volumetric weight

F_{ax_1} Axial force from momentum theory

F_{ax_2} Axial force from blade element theory

F_{ax} Axial force (thrust)

F_{hub} Hub loss correction factor

f_{hub} Exponent of the hub loss correction factor

F_{Q_1} Torque from momentum theory

F_{Q_2} Torque from blade element theory

F_{tan} Tangential force

F_{tip} Tip loss correction factor

f_{tip} Exponent of the tip loss correction factor

F_{total} Thrust on turbine and tower combined

F_{tower} Thrust on tower

$F_{y,i}$ Elemental force in edge wise direction (y in local element coordinates)

$F_{z,i}$ Elemental force in flap wise direction (z in local element coordinates)

g Acceleration due to gravity (9.81 ms^{-2})

g Combined BEMT minimisation value in iterative loop

I Moment of inertia

I_j Second moment of area around one sub-shape j

I_{y_i} Second moment of area about y axis

I_{z_i} Second moment of area about z axis

K BEMT implementation factor

k Turbulent kinetic energy

L Angular momentum

L Characteristic length

L Lift force

M Axial momentum

$M_{y,i}$ Elemental moment around edge-wise axis (y in local element coordinates)

$M_{z,i}$ Elemental moment around flap wise axis (z in local element coordinates)

N_b Number of blades

n_i Number of stress cycles

N_{Ri} Number of stress cycles to failure

P Power

p Exponent value in minimisation function

p Fluid pressure

p_d Pressure of fluid at the disc

Q Torque

Q_{error} Error in torque measurement

R Radius of the rotor

r Radius of annular ring (taken at the centre)

R_d Radius of the duct (outer surface)

r_h Radius of the hub / open centre

r_i Elemental radius

R_w Radius to the wake edge

Re Reynolds number

Re_{ch} Chord based Reynolds number

RF_{ax} Resultant force at the blade root in rotor axial direction

RF_{tan} Resultant force at the blade root in rotor tangential direction

SF Safety factor

SF Shear force

t Blade hydrofoil element thickness

t Time

t/c	Blade hydrofoil element thickness to chord ratio
t_i	Blade element hydrofoil thickness
T_{error}	Error in thrust (axial) force measurement
TI	Turbulence Intensity
TSR	Tip Speed Ratio
U	Flow velocity
u_*	Friction velocity at a wall
U_d	Flow velocity at the disc
U_F	Unbounded, free stream flow velocity
U_i	Axial flow velocity at a blade element
U_{hub}	Hub height flow velocity
U_{ref}	Reference flow velocity
W	Resultant fluid velocity
W_s	Resultant wake flow velocity
x_i	Distance from outer radius to centre of blade element (in structural analysis)
x_i	Horizontal distance of blade element from rotor axis
y	Vertical height of the first cell nearest a wall
y^+	Non-dimensional distance to wall in turbulent regime
y_i	Distance from neutral axis to surface of blade in y direction (in structural analysis)
z_i	Distance from neutral axis to surface of blade in z direction (in structural analysis)
z_i	Vertical height of blade element above seabed
z_{ref}	Reference height above seabed (usually at hub axis)

Chapter 1

Introduction and background

1.1 Introduction

Global energy consumption is set to rise, on average, by 1.5% year on year for the next decade (US Energy Information Administration, 2016). The method of satisfying this increasing energy demand is currently going through significant changes, that predominantly stem from three main motivations: i) the finite supply of fossil fuels; ii) concerns regarding energy security; and iii) the increasing rate of climate change (MacKay, 2008). This has driven a shift to renewable sources of energy, which provided an estimated 19.2% of the global final energy demand in 2014 (Renewable Energy Policy Network REN21, 2016).

Within Europe, mounting focus is being directed towards offshore renewable energy resources, which include wind, wave and tidal. The offshore wind industry has shown the largest progression to date, with approximately 4 GigaWatts installed capacity around the United Kingdom (The Crown Estate, 2015), fully operational as of 2015. Devices are becoming larger and deployed further offshore to exploit the higher resource availability, where up to 10 GW of installed capacity in UK waters is expected by 2020 (The Crown Estate, 2014). However, there are drawbacks concerning the unpredictable and intermittent nature of the wind.

Marine renewable energy is lower on the technology maturity level, currently with small levels of deployment resulting in relatively high levelised costs compared with other renewable energy sources. Assuming sufficient cost reductions through technology development, economies of scale and industry experience, the potential practically extractable resource from UK waters is predicted at 50 TWh/year for wave, and 20 TWh/year in tidal (Offshore Renewable Energy Catapult, 2014). This combined resource would provide around 23% of the UK annual electricity demand, based on a final electricity consumption of 304 TWh in 2016 (UK Govenment Statistics, 2017). The Marine Renewables Green Growth paper (The Carbon Trust, 2011) estimates the UK could capture approximately 22% of the accessible global marine energy market, amounting to an estimated worth of £76 billion (cumulative between 2010-2050, undiscounted). This thesis focusses on the tidal energy sector.

1.1.1 Tidal energy

The tidal energy resource, whilst smaller than other sources such as wind or solar, is less intermittent and highly predictable in nature. These are traits which can be exploited to make a regular and reliable contribution to the energy mix.

Tidal barrages and lagoons function through creating a reservoir of water behind a barrier, which captures the rise and fall of the tides. The system uses the change in water level (tidal range) to run a series of turbines connected to electrical generators. These are large civil engineering projects, with a power capacity typically in the order of hundreds of MW. However, the large capital costs and environmental impact concerns have restricted the realisation of present project proposals in the UK.

Another method is to harness the kinetic energy of the natural ebb and flow of the tides, known as streams or currents. Tidal Stream Turbines (TSTs) incorporate rotating hydrofoil blades which capture the movement of fluid from tidal flows to drive an electrical generator. The latest commercial scale individual devices

are typically in the order of 0.5-2.0 MW (Zhou et al., 2017), and connected into an array in a similar fashion to wind farms. There has also been recent growing interest in the feasibility of using a larger number of smaller turbines installed on a multi-rotor platform. Investigations of these slowly rotating structures have recorded minimal associated environmental impact (for example in Savidge et al. (2014)) and require lower capital investments. But the technology has not yet reached a high maturity level, and there remain several engineering and maintenance challenges to be solved.

1.1.2 Tidal stream turbine technologies

TST technology has been in the early stage developmental phase for a number of years. This is partially due to the engineering challenges in designing for harsh operating environments, combined with political and environmental factors has limited the rate of maturity.

One of the earliest landmark projects was SeaGen, shown in Figure 1.1 as developed by Marine Current Turbines (MCT). The device incorporates a 1.2 MW twin rotor, installed in the Strangford Lough, Northern Ireland in 2008. This installation is due to be decommissioned in 2017 after generating 10 GWh of electricity (ReNews, 2016).

Figure 1.1: MCT SeaGen 1.2 MW twin rotor device (with platform raised for maintenance), Strangford Lough, Northern Ireland. Photo by taken by author, 03.2014

The industry has seen the development of many different tidal energy converter concepts, a number of which have proved unable to progress past the point of commercial scale testing. Current state of the art devices incorporate horizontal axis turbines. Recent progression has led to the deployment of the world's first commercial scale arrays around the UK and France.

The MeyGen project phase 1A (MeyGen, 2017) has seen the installation of a four device array in the Pentland Firth, Scotland (shown in Figure 1.2) completed and grid connected earlier this year. The array consists of three turbines developed by Andritz Hydro Hammerfest and one by Atlantis Resource Ltd., each with a rated capacity of 1.5 MW. These are based on 'conventional' turbine designs of unshouded rotors consisting of three blades mounted onto gravity base foundations.

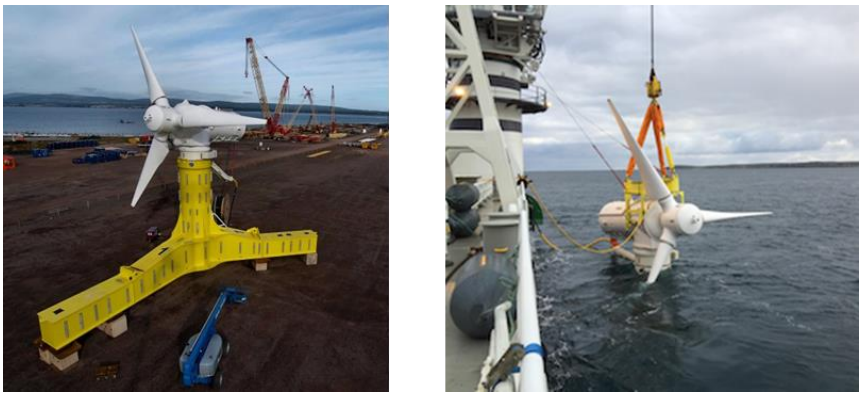

Figure 1.2: Andritz Hydro Hammerfest 1.5 MW rated TST with installation into the Pentland Firth, Scotland as part of the MeyGen Phase 1A (images credit: MeyGen)

An alternative configuration is designed by OpenHydro, part of the Naval Energies group (previously DCNS). Their latest generation 'PS2' device is depicted in Figure 1.3. This turbine consists of a rim generator, housed in a duct structure surrounding a rotor of many blades, which are open at the centre. A previous generation 'OCT16' device connects blade tips via an open centre hub.

Ducts are primarily designed to increase the power extraction through directing a higher mass flow rate through the rotor. Additional benefits include aligning

Figure 1.3: OpenHydro PS2: (left) 2 MW rated turbine for CapeSharp project, Nova Scotia; (right) 500 kW rated turbine undergoing installation at the Paimpol Brhat site, Northern France (images credit: Naval Group)

yawed flow and providing a housing for a rim induction generator. High solidity rotors have a lower optimal rotational velocity, which has benefits including: a reduced risk to marine wildlife; a lower chance of damage from cavitation due to a lower pressure difference across the blades; and enables the use of a direct drive generator which removes the requirement for mechanical systems such as a gearbox.

OpenHydro have installed a pair of 500 kW rated capacity turbines (shown in Figure 1.3), as a demonstration array in Paimpol-Bréhat, Northern France. This project is in collaboration with electricity provider Électricité de France (EDF).

1.1.3 Research motivation

Despite this recent progress, there remain many uncertainties regarding the technology. This presents a risk to investors and utility companies such as EDF. From this perspective, there are two key inputs to determine the economic viability of a project: the potential revenue generated from power production and the losses from life-cycle costs. These values are a function of the turbine performance and hydrodynamic behaviour, which are difficult to predict. This drives the need of robust, efficient and accurate tools to provide reliable information into financial estimations to aid project decision making.

1.1.4 Research challenge

Generating electricity from tidal flows is an enormous technical challenge, where currently no design or approach has yet been considered to be the optimal solution. The current leading designs that have seen the most significant progression to date are horizontal axis turbines, which operate similarly to those used in the wind industry.

Turbine rotors consist of hydrofoil blades with the principle function of harnessing the kinetic energy of the fluid flow to drive an electrical generator. Blades are designed to operate within the extreme marine environment, and therefore must be able to: 1) ensure good power performance to generate sufficient levels of electricity to be profitable; 2) withstand the large and varying load conditions, ensuring functionality throughout the turbine design life (which is typically 20 - 25 years).

Understanding the load conditions is of critical importance in the research and development of TSTs. Predictions can be made through numerical analysis of the hydrodynamic interactions between the blades and the working fluid. A careful choice of hydrodynamic model must be made to enable accurate calculations, yet applicable to performing practical engineering assessments and design iterations.

Computationally efficient hydrodynamic models designed for engineering applications have been developed for conventional, bare TSTs consisting of two or three blades, benefiting from lessons learned in the well established wind industry. However, there is currently a restriction in availability of similar models to analyse turbines of alternative design configurations. This thesis thus focuses on developing tools and methodologies to bridge this gap.

1.1.5 Research aim and objectives

The aim of this thesis is to develop a computationally efficient hydrodynamic model that can be applied to high solidity, ducted and open centre TST designs as proposed by OpenHydro, in order to enable practical engineering assessments.

To achieve this aim, five specific objectives are pursued in this thesis:

1. to develop and verify a classical hydrodynamic model based on blade element momentum theory (BEMT) for 3-bladed bare TSTs;
2. to compile input databases of lift and drag characteristics for various hydrofoil profiles;
3. to devise and implement modifications to model ducted open centre turbine configurations;
4. to verify the new ducted BEMT model with results from higher fidelity computational fluid dynamics (CFD) models;
5. to demonstrate the applicability of the model in engineering assessments through a structural integrity assessment of the composite blades.

1.1.6 Thesis structure

This thesis is structured into the following chapters:

- The remainder of chapter 1 introduces some current numerical models used to analyse the hydrodynamic behaviour of the turbine, with a review of the relevant literature

- Chapter 2 details the principle theories, methodologies and governing equations behind hydrodynamic modelling using classical BEMT. A computational code to analyse conventional horizontal axis turbines is constructed, which is used as a baseline on which modifications are built to account for

the differences in configuration for a ducted, high solidity and open centre turbine.

- Chapter 3 assesses two numerical methods to analyse two-dimensional hydrofoil profiles using a low computational cost panel code 'XFoil', and a higher complexity Reynolds averaged (RANS) CFD code. Lift and drag coefficients generated at various angles of attack are compared with wind tunnel tests in order to assess the accuracy of the models and highlight any limitations. Results are used to build hydrofoil databases that are used as inputs into the BEMT models.

- Chapter 4 seeks to validate the baseline BEMT model built for analysing 'conventional' 3 blade turbine designs. XFoil hydrofoil coefficients are used, and various correction factors to account for limitations in the model are tested. Comparative studies of rotor power and thrust predictions are made with various scale model experimental measurements.

- Chapter 5 focusses on the application of the 'ducted BEMT' model, where a validation study is performed on a generic reference turbine design, comparing results with a coupled RANS study. The code is then used to analyse two commercial cases designed by OpenHydro, which makes use of hydrofoil lift and drag data generated by RANS studies performed in Chapter 3. Comparisons are made with fully blade resolved CFD studies, where the wake characterisation is used to identify any limitations in the BEMT methodology.

- Chapter 6 subsequently demonstrates the capabilities of the ducted BEMT model in performing practical engineering assessments. An analytical tool is developed to determine blade structural response from the element hydrodynamic forces. This was used to perform a structural integrity assessments of composite blades of an OpenHydro PS2 turbine in normal operation, extreme and cyclic loading conditions.

- Chapter 7 lastly presents an overall discussion of thesis outcomes, the conclusions and recommendations for future work.

1.2 Review of related work

This section provides a review of the methods used to analyse the hydrodynamics behaviour of TSTs, and examines the related work on numerical modelling published in the literature. Further in-depth analysis of specific studies from the literature is covered in the relevant chapters.

1.2.1 Hydrodynamic modelling of TSTs

Due to the relatively immature stage of the industry, there are a large number of uncertainties that are of high academic and commercial interest. One aspect concerns the engineering design of the turbine rotor, which is used to extract the energy from tidal flows.

Accurate power predictions are of very high importance for investment decision making, as this is the quantifiable measure of the electricity a device can generate, and therefore how much revenue it can create. Accurate loading predictions are of equally high importance, as these provide information that feed into the engineering design of turbine components, ensuring functionality to desired specifications. These require analyses of the hydrodynamic interactions between the fluid flow and the structure of the blades. This is no simple task, due to the complex physical phenomena observed in the offshore environment coupled with the technical challenges associated to turbine design and operation.

Hydrodynamic analyses are performed in order to gain insight into various aspects of the tidal flow and the turbine. However, there is as yet no universally applied method.

1.2.2 Physical modelling

Field experiments are performed in the marine operational conditions, and therefore offer measurements of real fluid and turbine behaviour in tidal flows. Test campaigns are extremely costly, and usually performed on full or large scale devices. Therefore, these are typically used in the final design validation and proofing stages of a turbine development.

The European Marine Energy Centre (EMEC) in Orkney, Scotland offers a test facility based within the offshore environment. This enables the testing capability of real sea states, with the added benefit of having near site equipment and vessels to enable easy access for observation and maintenance. Site characterisation studies, such as in Sellar and Sutherland (2015), have measured the operating conditions at different locations considered for device deployment. Various developers have tested devices, however results are commercially sensitive and so are not typically published. The Reliable Data Acquisition Platform for Tidal (ReDAPT) programme (Rhymes, 2015) was formed with the aim to "accelerate the development of tidal energy industry". Tests of an Alstom TGL 1MW TST were performed (Alstom Ocean Energy, 2014), to examine the key issues and difficulties associated with operation and maintenance, as well as to assess the impact to marine life. Power and loadings were measured, along with flow velocity fields around the rotor, and published in a series of reports (such as ReDAPT (2014)).

Physical measurements of devices from tank tests can be used to investigate hydrodynamic behaviour under controlled operating conditions, but at high levels of cost. Various scale model tests have been investigated, such as: Bahaj, Molland, Chaplin and Batten (2007), who performed experiments on $1/20^{th}$ scale models in a cavitation tunnel and again in a towing tank; Buvat and Martin (2010) develop a series of flume tests to $1/30^{th}$ scale to investigate the impact of turbulence as part of the PerAWaT (Performance Assessment of Wave and Tidal array systems)

project; and more recent in a wide flume (Stallard, Feng and Stansby, 2015) on $1/60^{th}$ scale rotors to study the effects of interactions within an array.

1.2.3 Numerical modelling

Numerical models offer a lower cost solution, which can also be used to investigate certain aspects that are difficult to measure experimentally. However, present limitations in modelling techniques mean that not all physical effects can be fully replicated.

An extensive range of different numerical models have been developed, each suited to perform different tasks, with a specific set of capabilities, assumptions and limitations. The choice of the numerical model depends on the area of interest or objective of the study. Depending on the level of accuracy sought, the model can either be highly sophisticated and computationally costly, or approximate and computationally efficient.

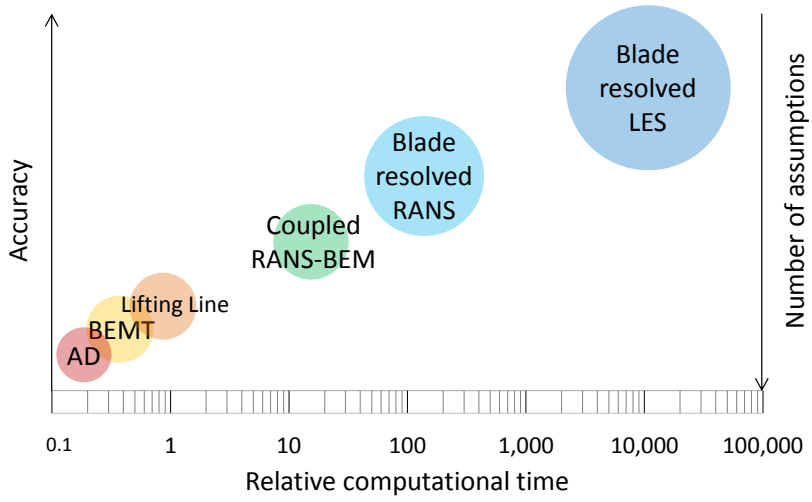

Figure 1.4: Typical hydrodynamic models used to assess TSTs, indicating approximate levels of accuracy, number of assumptions and computational time requirement

Some of the main hydrodynamic modelling methods used to assess TSTs are shown in Figure 1.4. Analytical models including Actuator Disc (AD), BEMT and Lifting Line theory are the simplest and the most computationally efficient,

but suffer from a larger number of modelling assumptions. At the opposite end of the scale are CFD simulations, where Navier Stokes equations can be resolved using Reynolds Average approaches (RANS) or using higher complexity Large Eddy Simulation (LES) methods. These are high fidelity models, which have high associated computational costs.

1.2.3.1 Computational Fluid Dynamics methods

Highly complex, high fidelity models are commonly used in design refinement, or to perform detailed assessments of turbine components under specific operating conditions. Advanced CFD solvers are used to resolve flow conditions using a volume of fluid method, resolving Navier Stokes equations.

A large range of studies on TSTs using CFD methods have been performed and are available in the literature. McSherry et al. (2011) presents validation against scale model experiments, with tests on a number of various blade resolved simulation parameters. McNaughton (2013) presents a blade resolved RANS model using a $k-\omega SST$ turbulence model, and incorporates a sliding mesh routine. This model is validated with scale model experiments, before being applied to a full scale TGL turbine (Stallard, Stansby and Apsley, 2015). This work was extended by Afgan, Apsley and McNaughton (2013) using an LES model, which was reportedly better capable of predicting the high frequency fluctuations due to blade generated turbulence. Computational time requirements are reported to be 4.4 million CPU hours for each LES simulation, over thirty times greater than RANS (Afgan, McNaughton and Rolfo, 2013). Additional capabilities include interactions with foundation types and analysis of the interactions between multiple turbines in an array, such as presented by O'Doherty et al. (2009).

1.2.3.2 Analytical models

Analytical models employ a more simplistic approach which are able to compute the force distributions along the rotor blades, and determine the overall performance of a turbine, aiding early stage decision making on optimal device designs for specific sites. Significantly lower computational requirements have been reported (Cresswell, 2014) and fast processing time can be exploited for engineering applications where many analyses are required. These include performing numerous design iterations, analysing multiple or varying inflow conditions, or assessing fatigue loading.

1.2.3.3 Blade element momentum theory

BEMT was originally developed for aviation and marine propeller applications, and more recently for wind turbine assessments (Hansen, 2008). A number of texts describing the method have been published e.g. (Burton et al., 2011), which form the basis of a number of codes available in the industry, such as industrial standard 'Bladed', developed by a classification society DNV GL Garrad Hassan (2012*a*).

Several industrial (e.g. 'Tidal Bladed', DNV GL Garrad Hassan (2012*b*)) and academic (e.g. Masters et al. (2011)) numerical models have been developed using the BEMT method for conventional tidal turbine applications. These models, whilst relatively simple, are well established and reliable, based on experience from the wind turbine industry.

The blade element model makes use of lift and drag coefficient data. This can be taken from wind tunnel tests such as presented by: Abbott et al. (1945); Abbott and Von Doenhoff (1959); Fuglsang et al. (1999); and Timmer (2008). A number of studies (Batten et al. (2006), Chapman (2008) and Adamski (2013)) use panel code methods such as 'XFoil' (Drela and Youngren, 2001), used to generate curves for standard aerofoil profiles developed for industrial applications. Alternatively,

2-D analyses of foil profiles can be assessed using CFD methods, such as shown by Yao et al. (2012).

Various improvements to the typical baseline method are proposed in the literature, including:

Correction factors: Some assumptions inherent in the theory can be reduced through the application of correction factors to account for tip losses and the larger thrust forces observed under highly loaded conditions (Burton et al., 2011). Combining these reportedly cause a numerical discontinuity, which can be eliminated with the incorporation of an adjustment proposed by (Buhl, 2005), successfully implemented into TST BEMT codes as shown in (Chapman et al., 2013).

BEMT iterative procedure: A modification of the iterative function to incorporate a minimisation equation is proposed to enhance stability, as used by Buckland et al. (2010) and Shives and Crawford (2011). An increase in robustness have been reported by the addition of a Monte Carlo function to gain better initial estimates of the induction factors (Chapman, 2008). Although this increases the computational complexity of the model, overall time reductions are seen within the iterative procedure, as well as increased frequency of convergence on the best solution in multiple root scenarios.

1.2.4 Ducted TST modelling

The availability of BEMT models for ducted, high solidity and open centre turbines is, at present, restricted. Currently, these configurations are analysed using higher complexity CFD simulations.

Fully blade resolved RANS studies such as presented by Fleming et al. (2011) provide highly detailed wake characterisation, and resolve the complex flow interactions between the blades and duct structure. However, a very high

computational requirement restricts the number of operational conditions that can be reasonably simulated.

Less computationally intensive alternatives have been investigated (Fleming et al. (2011); Turnock et al. (2011) and Belloni et al. (2016)) based on a coupled Reynolds Averaged Navier Stokes with blade element momentum (RANS-BEM). Case studies report good comparison between this method and fully blade resolved studies, at a fraction of the processing time (McIntosh et al., 2012). Further savings can be made through combined RANS with actuator disc, where simulations have been performed such as by Fleming and Willden (2016*a*). The cost savings however are insufficient to make such models practical for applications that require many simulations in short time frames.

Analytical approaches for assessing the impact of a duct have been presented in the literature. A one-dimensional momentum method considering flow through a duct was presented by van Bussel (2007) and Jamieson (2008). Modifications to the standard actuator disc model were proposed, where it is shown that increases in mass flux can be achieved through reductions in pressure at the exit. This method was adopted by Lawn (2003) in examining the power production of diffuser augmented turbines. The pressure variations within the duct are modelled using parameters of inlet efficiency, outlet efficiency and base pressure coefficient. An expression was formulated to determine the so called duct 'swallowing capacity', used to assess the axial forces exerted on the disc. The duct parameters are unknowns, which can be solved using input from experimental measurements or through detailed numerical simulations.

Shives and Crawford (2011) developed this method further to formulate an expression for the axial induction factor, which can be incorporated into the BEMT model. RANS CFD simulations of various uni-directional ducts were performed with an actuator disc representation of the turbine. These studies were used to identify trends in pressure variations as a function of duct geometries. Empirical expressions were thus devised, to solve the analytical duct parameters

formulated by Lawn (2003). These expressions are validated within the same study with additional CFD simulations.

Shives and Crawford (2011) formulates axial momentum expressions to be incorporated into BEMT accounting for wake swirl. However, the radial pressure drop balancing the kinetic energy of the rotating wake was found to not cause an additional thrust on the disc, as explained by Burton et al. (2011).

Limitations in this analytical method in accounting for tip losses, turbulence and the wake state were identified by Cresswell (2014). However, there is currently a lack of validation studies to analyse the accuracy and impact of these limitations in the case of ducted and open centre TST applications.

1.2.5 Modelling considerations of the marine environment

Studies such as Turner (2012) have shown that the fundamental components of aerodynamic BEMT models can be largely transferred to hydrodynamic applications. However, there are various parameters specific to the tidal environment which can be considered for TST analyses. These include:

Working fluid properties: The density of seawater is around 800 times greater than that of air and therefore the rotor is subjected to high load concentrations. This results in shorter blade designs with thicker roots than seen in the wind industry, in order to resist the larger bending moments. The kinematic viscosity of sea water is around 1.24E-06 m^2s^{-1} (at 12°C, 3% salinity), an order of magnitude smaller than air which has a value of approximately 1.5E-05 m^2s^{-1} (at 20°C, 1 atm pressure). This means that there is a much greater resistance to deformation through shear stress in water, which affects the boundary layer formation across the blade surfaces and seabed.

Reynolds number: Despite the lower viscosity of water compared with air, the relative flow velocity over the blades is lower, and the chord lengths typically

larger. Therefore chord based Reynolds numbers (describing the ratio of inertial to viscous forces) are of a similar order to those seen in wind turbines.

Compressibility: Water is significantly less compressible than air: comparing the resistance to compression, water has a bulk modulus of 2.2 GPa, four orders of magnitude greater than air at 140 kPa. Therefore compressibility assumptions within models, taking a constant density, are more applicable to the hydrodynamic applications.

Channel flows: TSTs are usually placed within naturally formed channels, for example between headlands and islands, in order to exploit the larger flow velocities in these regions. The effects of solid boundaries on wake expansion is explored by Garrett and Cummins (2007) who propose a new set of axial momentum equations to account for this. This method is also used by Bahaj, Molland, Chaplin and Batten (2007) to provide correction factors to account for the blockage effects in experimental tank tests.

Free surface effects: The presence of a surface between air and water poses a particular boundary condition which is seen to influence the wake flow by a drop in height behind the turbine. Building on flow in a channel, the effects of a free surface have been explored by Whelan et al. (2009).

Turbulence: Turbulence is present in almost all tidal flows, which leads to chaotic, complex and rapid changes in the velocity field. These effects are considered to influence both the overall rotor performance, as well as fatigue loading of the blades (Blackmore et al., 2016). Synthetic turbulence methods offer a convenient solution by imposing a stochastic variation of velocity as described by Togneri and Masters (2012). Programmes such as NREL's TurbSim (Jonkman, 2009) can be used to generate turbulent flow velocity vectors as a time series for input into BEMT models.

Waves: The tidal flow is affected by the particle orbits from waves induced at the water surface. The wave interactions will depend on a number of different

factors such as the height, period and direction. Wave current interactions are of high present interest, explored in many studies such as Tatum et al. (2016), leading to significant oscillatory loads Milne et al. (2011).

Cavitation: Cavitation is a phenomenon whereby localised vaporisation of a liquid followed by its immediate condensation induces extremely high pressure implosions, which can erode away the surface of the blades. This is a risk in the tidal environment, but can be avoided with careful control of rotational velocities and proximity to the free surface (Turner, 2012).

Corrosion and biofouling: The deposit of marine organisms on the turbine rotor can increase the hydrodynamic drag thus reduce the power output. There is also a risk of degradation of components due to corrosion from the sea water (Turner, 2012). Introduction of paints and coatings are currently being investigated to limit this impact, as well as the incorporation of cathodic protection through fixing sacrificial anodes.

1.2.6 Blade structural integrity

Blades are critical components of a TST, failure of which prevents its principle function of generating power. Due to high operational expenditures (OPEX) related to the offshore environment, TSTs are designed to have minimal maintenance requirements and therefore blade structural integrity is a key consideration. Occurrences of blade failures in industry have emphasised the necessity of performing structural integrity analyses in order to ensure survivability under specific operating conditions over the required lifetime. Examples of real life occurrences include: OpenHydro, where a failure case in May 2010 was reported from a deployment in the Bay of Fundy, Nova Scotia (CBC News, 2011) causing all of the blades to break; and Atlantis, who recorded a failure of its experimental composite blades in August 2010 fitted to its twin rotor AK1000 device, installed at the EMEC test facility, Orkney (Atlantis Resources Ltd., 2010).

TST blades are typically constructed from composites due to their high strength to weight properties Bir et al. (2011). There is currently a level of uncertainty concerning the performance of such materials for TST applications, due to the lack of experience with composite rotating machines within the marine environment (Bureau Veritas, 2015). There is a higher level of knowledge of composites used for naval applications, such as in yacht hull construction (e.g. (Bureau Veritas, 2017)), which can be used to estimate behaviour in ocean conditions.

Structural designs of TST blades for 'generic' cases are reported in the literature (Bir et al., 2011), and can be used to calculate the blade bending moments and shear forces from the hydrodynamic loads, as shown by Val and Chernin (2011). These can be subsequently used to assess the stresses under various conditions, to ensure that structural limits are not exceeded. Failure under extreme loading is considered a potential risk (Li et al., 2014), as well as through fatigue, due to stress cycling (Westphal and Nijssen, 2012).

A review of modelling approaches has been previously conducted by EDF R&D in order to determine appropriate methods to perform reliability analyses of horizontal axis wind turbines. This identified the BEMT method as an optimal compromise between accuracy and computational time. The key objective of this thesis is to develop tools to perform engineering assessments of TST composite blades, and thus the BEMT method was selected.

Chapter 2

Numerical modelling of tidal stream turbines

This chapter describes the methodology and governing equations used in the Blade Element Momentum Theory (BEMT), a hydrodynamic model used in this thesis to perform engineering assessments of TST blades. Classical BEMT developed for wind turbine applications has been successfully adopted to 'conventional' 3-bladed TST designs, due to similarities in design and operation.

The main aim of this chapter is to formulate a BEMT model to analyse the hydrodynamic performance and thrust loads on an alternative to conventional TST designs, which consists of a high solidity, open centre and ducted configuration. In order to comprehensively illustrate how and to what extent modifications are made to the classical model to account for ducted flow, derivations are presented in detail from first principles.

2.1 Introduction

A considerable amount of literature is available on the BEMT method, which was originally developed to assess marine and aviation propellers. Here, the majority of underlying procedures follow methodologies described in textbooks for wind turbine applications, including Burton et al. (2011) and Hansen (2008). The more recent applications to TST modelling are also well documented for industrial codes such as: Moriarty and Hansen (2005); and DNV GL Garrad Hassan (2012*b*), as well as university led research in: Masters et al. (2011); and Chapman (2008).

These models mainly concern 'conventional' 3-bladed TST designs, whereas here a Ducted BEMT code is developed, capable of modelling TSTs of ducted and open centre configurations.

2.2 Actuator disc theory

A TST can be modelled as an actuator disc in which the blades and the spaces between are not specifically considered, and instead the rotor is approximated as a semi-permeable disc. This can be used to predict the overall forces exerted on the rotor as a result of being placed in body of fluid flow moving parallel to the rotor axis. This is the most basic form of the turbine representation, which lays the foundation on which subsequent numerical processes can be built.

2.2.1 Axial momentum in unconstrained flow

A disc installed within a moving fluid will cause the flow to slow down, which has an associated force acting on the frontal area in the axial direction. The one-dimensional axial momentum theory can be used to determine the energy absorption of the disc when considering the flow within a control volume of fluid known as the 'stream tube'.

Figure 2.1 shows a representation of the actuator disc in a stream tube for unconstrained flow, with Table 2.1 detailing the notation used in the derivations for this section.

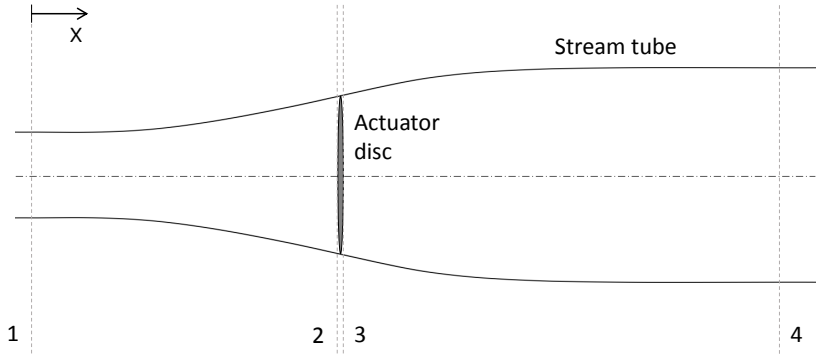

Figure 2.1: Schematic of an actuator disc within a stream tube in unconstrained flow, with numbers representing cross sectional planes relating to: 1 - upstream; 2 - disc upstream; 3 - disc downstream; 4 - downstream

Table 2.1: Table of notation used in one-dimensional actuator disc theory for unconstrained flow, indicating velocities , areas and pressures at four cross sectional locations within the stream tube

Location	1	2	3	4
Velocity	$U_1 = U$	$U_2 = U_d$	$U_3 = U_d$	U_4
Area	A_1	$A_2 = A_d$	$A_3 = A_d$	A_4
Pressure	$p_1 = p$	p_2	p_3	$p_4 = p$

2.2.1.1 Continuity equations

The first assumption is that the stream tube is sufficiently long, such that the far down stream static fluid pressure reaches the same level as the reference pressure upstream, in order for the equilibrium condition to be achieved: $p_1 = p_4 = p$. The disc is also assumed to be infinitely thin, therefore the areas and velocities at the disc are equal such that: $A_2 = A_3 = A_d$; and $U_2 = U_3 = U_d$.

Due to the presence of the turbine, there is a restriction in the flow, hence a decrease in velocity. Assuming that the fluid is incompressible, the flow field

must expand in order to comply with conservation of mass laws. Mass flow rate, $\dot{m} = \rho AU$, must be equal at all points in the stream tube, hence the continuity equations can be written as:

$$\rho A_1 U = \rho A_d U_d = \rho A_4 U_4 \tag{2.1}$$

2.2.1.2 Rate of change in axial momentum

The actuator disc can be considered to extract axial momentum (M) from the fluid flow, which causes the reduction in velocity of the fluid. The rate of change in momentum can be defined as the mass flow rate (constant) multiplied by the overall change in velocity, such that:

$$\frac{\delta M}{\delta t} = \dot{m}\Delta U \tag{2.2}$$

The change in momentum can be equated to the axial force exerted on the disc, assuming that: i) the streamtube is completely surrounded by water at a constant pressure, hence giving a zero net force; and ii) the disc is frictionless and there are no other forms of energy loss. Therefore, it can be stated that:

$$F_{ax} = \rho A_d U_d \left(U - U_4\right) \tag{2.3}$$

2.2.1.3 Bernoulli's formulation

Bernoulli's equation states that in a system where no work is done on the fluid, the total energy in the system is constant, which comprises of kinetic energy, static pressure and gravitational potential energy such that:

$$\frac{1}{2}\rho U^2 + p + \rho g h = constant$$

$$\frac{1}{2}\rho U_1^2 + p_1 = \frac{1}{2}\rho U_2^2 + p_2 \quad \Rightarrow \quad \frac{1}{2}\rho U^2 + p = \frac{1}{2}\rho U_d^2 + p_2 \tag{2.4}$$

$$\frac{1}{2}\rho U_3^2 + p_3 = \frac{1}{2}\rho U_4^2 + p_4 \quad \Rightarrow \quad \frac{1}{2}\rho U_d^2 + p_3 = \frac{1}{2}\rho U_4^2 + p \tag{2.5}$$

These can be rearranged to form an expression for the pressure difference across the disc (Δp_d). Here it is assumed that the flow is inviscid and under steady state conditions, where there is a uniform velocity within each cross section of the stream tube:

$$\Delta p_d = p_2 - p_3 = \frac{1}{2}\rho\left(U^2 - U_4^2\right) \tag{2.6}$$

The reduction in kinetic energy leads to a rise in the static pressure just before the turbine, followed by a drop in static pressure as the flow passes through the rotor disc. The change in momentum is caused by the axial force associated to the pressure difference across the turbine, given by:

$$F_{ax} = \Delta p_d A_d = \frac{1}{2}\rho A_d\left(U^2 - U_4^2\right) \tag{2.7}$$

2.2.1.4 Axial induction factor

There are now two expressions for F_{ax} from rate of change in momentum (Equation 2.3), and Bernoulli (Equation 2.7). These can be equated and rearranged to give an expression for the velocity at the disc:

$$\begin{aligned} \frac{1}{2}\rho A_d\left(U^2 - U_4^2\right) &= \rho A_d U_d\left(U - U_4\right) \\ U_d &= \frac{U + U_4}{2} \end{aligned} \tag{2.8}$$

In order to negate the need to measure this velocity at the disc or far upstream, an axial induction factor (a) can be defined. If Equation 2.8 is rearranged to:

$$1 - \frac{U_d}{U} = \frac{1}{2} - \frac{U_4}{2U}$$

Both sides are known expressions for the axial induction factor. Therefore:

$$a = 1 - \frac{U_d}{U} \qquad \Rightarrow \qquad U_d = U\left(1 - a\right) \tag{2.9}$$

$$a = \frac{1}{2} - \frac{U_4}{2U} \qquad \Rightarrow \qquad U_4 = U\left(1 - 2a\right) \tag{2.10}$$

Which can be used to relate the velocities at the disc and far downstream, to the reference inflow velocity. Inserting these forms either expression of F_{ax} yields:

$$F_{ax} = 2\rho A_d U^2 a\left(1 - a\right) \tag{2.11}$$

2.2.1.5 Rotor disc power

The power can be defined as the axial force multiplied by the velocity at the disc, which (using Equations 2.3 and 2.7), is given by:

$$\begin{aligned} P &= F_{ax} U_d \\ &= \rho A_d U_d^2 \left(U - U_4\right) \quad = \frac{1}{2}\rho A_d U_d \left(U^2 - U_4^2\right) \end{aligned} \tag{2.12}$$

And incorporating a from Equation 2.11 gives:

$$P = 2\rho A_d U^3 a\left(1 - a\right)^2 \tag{2.13}$$

2.2.1.6 Thrust and power coefficients

Non-dimensional coefficients of axial force, or thrust, (C_T) and power (C_P) are useful for making comparisons independent of turbine diameter and inflow velocity.

The coefficient of thrust (using axial force from equation 2.11) can be expressed:

$$C_T = \frac{F_{ax}}{\frac{1}{2}\rho A_d U^2} \tag{2.14}$$

$$= \frac{2\rho A_d U^2 a\,(1-a)}{\frac{1}{2}\rho A_d U^2}$$

$$= 4a(1-a) \tag{2.15}$$

And the coefficient of power as:

$$C_P = \frac{P}{\frac{1}{2}\rho A_d U^3} \tag{2.16}$$

$$= \frac{2\rho A_d U^3 a\,(1-a)^2}{\frac{1}{2}\rho A_d U^3}$$

$$= 4a\,(1-a)^2 \tag{2.17}$$

2.2.1.7 The Betz limit

The maximum thrust $C_{T,max} = 1$ occurs when $\frac{dC_T}{da} = 0$, occurring when $a = 1/2$. Exceeding this value of axial induction factor means that the far upstream velocity becomes negative as per the Equation 2.10. This implies a reversal of the flow in the wake which is physically unrealisable, and is a known flaw in the method. Axial momentum theory is therefore unable to model highly loaded turbines. A typical method to circumvent this limitation is to apply an empirical correction factor when in the 'highly loaded state', as further explained in Section 2.6.4.

It can be seen that the maximum power coefficient occurs at $\frac{dC_P}{da} = 0$, at a=1/3. This gives a peak coefficient known as the 'Betz limit' $C_{P,max} = 16/27 \approx 0.593$. From Equations 2.9 and 2.10 it can be stated that maximum power extraction is achieved when:

$$U_d = \frac{2}{3}U; \qquad U_4 = \frac{1}{3}U$$

Which are combined along with continuity expressions to yield:

$$A_4 = 2A_d \tag{2.18}$$

2.2.2 Axial momentum incorporating a duct

Ducts (also known as augmenters or shrouds) are incorporated into some turbine designs, primarily to improve the hydrodynamic performance. The rationale behind the addition of a convergent/divergent external structure is to direct more flow through the turbine, and hence increase the momentum available for extraction.

This is achieved through a convergent inlet which increases the velocity of the fluid at the disc; and a divergent nozzle which then forces flow expansion, augmenting flow through the throat. The flow is also directed to be aligned more normal to the rotor. These benefits come at the cost of additional material required for the duct structure.

Although the primary focus of this study is not to quantify the cost-benefits of ducted turbines compared to bare turbines, this is a subject of continual discussion in the industry, where a single solution of the optimal turbine configuration is yet to be determined.

2.2.2.1 Ducted flow field

The presence of the duct changes the flow profile through the actuator disc, which alters the conditions of the streamtube (as seen in Figure 2.2), and therefore the basis of the momentum equations. This results in the requirement to formulate a new expression for the rate of change of axial momentum. Table 2.2 details the notation used in the ducted momentum equations, where the far downstream pressure is assumed to return to that at the inlet.

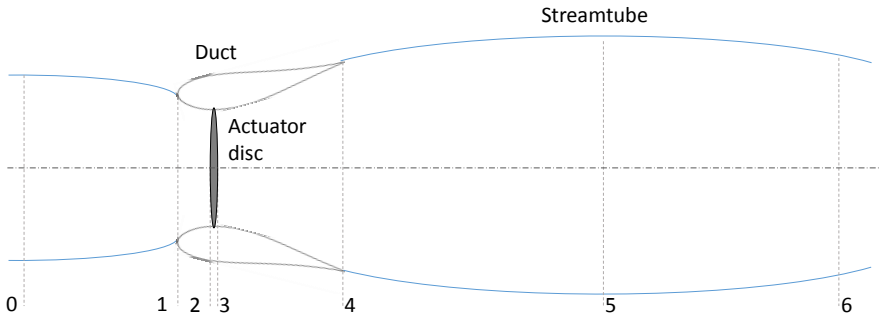

Figure 2.2: Schematic of ducted turbine incorporating the actuator disc bounded by a stream tube, with numbers corresponding to sections in which areas, pressures and velocities are taken, consisting of: 0 inflow upstream; 1 - duct inlet; 2 - actuator disc upstream; 3 - actuator disc downstream; 4 - duct outlet; 5 - wake downstream; 6 - wake far downstream

Table 2.2: Table of notation used in one-dimensional actuator disc theory for unconstrained flow in a duct, indicating velocities, areas and pressures at 7 cross sectional locations within the stream tube

0	1	2	3	4	5	6
$U_0 = U$	U_1	$U_2 = U_d$	$U_3 = U_d$	U_4	U_5	U_6
A_0	A_1	$A_2 = A_d$	$A_3 = A_d$	A_4	A_5	A_6
$p_0 = p$	p_1	p_2	p_3	p_4	p_5	$p_6 = p$

The forcing of an expansion in the diffuser reduces the pressure downstream, which augments the flow at the throat and results in a higher mass flow rate through the turbine.

The hydrodynamic effects of the duct is split into four components: i) the diffuser ratio (ratio of outlet area to throat area); ii) the flow separation within the diffuser; iii) the back pressure reduction at the exit and iv) the associated viscous losses (van Bussel, 2007). A similar 1-D momentum conception through a duct is presented by Jamieson (2008). The four components have been further parametrised analytically by Lawn (2003).

2.2.2.2 Analytical model of ducted flow

The flow contracts up to position 2, at the duct throat where the disc is located, where the change in velocity through Bernoulli's equations can be related to the change in pressure:

$$C_{p02} = \frac{p_2 - p}{\frac{1}{2}\rho U^2} \tag{2.19}$$

Which can be parametrised using an efficiency term such that:

$$C_{p02} = \eta_{02}\left(1 - \frac{U_d^2}{U^2}\right) \tag{2.20}$$

where η_{02} is the efficiency term parametrising the viscous losses in the inlet. The convention used means that efficiency is greater than one for contracting flow.

The coefficient of thrust on the disc as previously defined in Equation 2.14 can be rearranged based on $F_{ax} = \Delta p_d A_d$, so that:

$$C_T = \frac{p_2 - p_3}{\frac{1}{2}\rho U^2} \tag{2.21}$$

Note this uses standard form of BEMT, incorporating upstream velocity (U), whilst Lawn (2003) states a turbine resistance term which uses the velocity at the disc (U_d).

The pressure change in the diffuser can similarly be expressed using an efficiency term as before, as well as incorporating the incompressible continuity expression where $U_d A_d = U_4 A_4$:

$$C_{p34} = \frac{p_4 - p_3}{\frac{1}{2}\rho U_d^2} \tag{2.22}$$

$$= \eta_{34}\left(1 - \frac{U_4^2}{U_d^2}\right) = \eta_{34}\left(1 - \frac{A_d^2}{A_4^2}\right) \tag{2.23}$$

where η_{34} is the diffuser efficiency term. The pressure difference between the diffuser outlet and far downstream can be parametrised by the base pressure coefficient:

$$C_{pb} = \frac{p - p_4}{\frac{1}{2}\rho U^2} \tag{2.24}$$

Note the opposite sign comparing with (Lawn, 2003), in order to be consistent with the following empirical formulation.

Summing the individual pressure differences from the far upstream and far downstream and equating to zero yields:

$$C_T - C_{p02} - C_{p34}\left(\frac{U_d}{U}\right)^2 - C_{pb} = 0 \tag{2.25}$$

Where the velocity ratio (U_d/U) is the measure of mass flow rate through the turbine, known as the 'swallowing capacity'. This can be rearranged to solve for the thrust coefficient, written in terms of the axial induction factor from Equation 2.9:

$$C_T = \eta_{02} + C_{pb} - (\eta_{02} - C_{p34})(1 - a)^2 \tag{2.26}$$

The model is limited to assessments where small numbers of turbines are installed. With larger arrays, the energy extraction is greater and therefore full pressure recovery will not be achieved in the far downstream wake.

This analytical expression for C_T can then be related back to the axial force on the whole disc as:

$$F_{ax} = \frac{1}{2}\rho A_d U^2 \left(\eta_{02} + C_{pb} - (\eta_{02} - C_{p34})(1 - a)^2\right) \tag{2.27}$$

2.2.2.3 Empirical solutions

The efficiencies and base pressure term are unknowns, which can be expressed empirically through experimental observations or through detailed numerical simulations. Once these terms are solved, they can be input back into Equation 2.27, and thus the axial force on the disc can be determined.

RANS CFD simulations from the literature on unidirectional ducts incorporating an actuator disc (Shives and Crawford, 2011) have been performed based on NACA0015 aerofoil shapes (Abbott and Von Doenhoff, 1959). Many different geometries have been investigated within this reference study, which assess various: inlet contraction ratios (A_1/A_d); the diffuser expansion ratios (A_4/A_d); and inner and outer diffuser surface angles (θ_{in} and θ_{out}), as defined in Figure 2.3.

These studies derive empirical approximations of the duct parameters defined in the analytical model which are unknowns, namely the inlet efficiency, diffuser efficiency and base pressure coefficients given by:

$$\eta_{02} \approx 1.0 \tag{2.28}$$

$$\eta_{34} = a_1 + b_1\frac{A_d}{A_4} + c_1\theta_{in} + d_1\frac{A_1}{A_d} \tag{2.29}$$

$$C_{p34} = \eta_{34}\left(1 - \frac{A_d^2}{A_4^2}\right) \tag{2.30}$$

$$C_{p,b} = a_2 + b_2\frac{A_d}{A_4} + c_2\theta_{out} + (d_2 + e_2\theta_{out})C_{Ti} + f_2{C_{Ti}}^2 \tag{2.31}$$

The inlet efficiency was found to be within 5% of unity for all cases tested, therefore assuming a value of 1.0 will have negligible effects on the overall rotor forces. Note that C_{Ti} is the thrust coefficient calculated from blade element theory, as defined later in Section 2.4. All constants are detailed in Table 2.3, which were determined using a least squares optimisation function (Shives and Crawford, 2011).

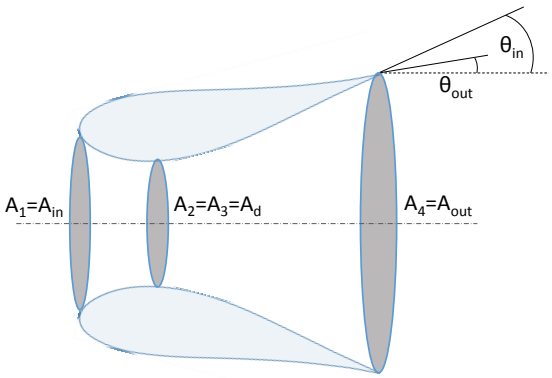

Figure 2.3: Schematic of a uni-directional duct, indicating geometrical parameters used in the empirical formulations

Table 2.3: Constants used in empirical expressions of diffuser efficiency (η_{34}) and base pressure coefficient (C_{pb}), taken from Shives and Crawford (2011)

a1	b1	c1	d1		
0.8867	0.5212	-0.0108	-0.1313		
a2	b2	c2	d2	e2	f2
0.2701	-0.333	0.0269	0.1068	-0.0152	-0.1275

The empirical/ analytical model has been validated against power and thrust curves generated with CFD on three additional validation duct geometries within the reference study (Shives, 2011).

The significance of these parameters is investigated in Chapter 5, Section 5.2.8.2, where comparisons are made with classical BEMT. Note that for symmetrical ducts $A_1 = A_4$, and through the continuity $U_1 = U_4$.

2.2.3 Actuator disc limitations

Taking the representation of an actuator disc, the above methodology can be used to approximate the force exerted on the turbine as if it was a singular body operating in a singular inflow velocity. This enables approximations to be made on the overall turbine performance in terms of thrust and power for uniform inflows. This can be useful in industrial applications, for example regional scale models of

tidal turbine arrays, where a low resolution representation of individual turbines is sufficient.

However, this is a simplistic approach that does not consider any spacial variations in thrust across the turbine frontal area. These can stem from, for example, variations in inflow velocity, which is particularly relevant to tidal flows which are inherently non-uniform in nature. These effects are of higher importance when carrying out detailed assessments of individual turbines.

2.2.3.1 Disc radial discretisation

To calculate any spacial force variations within the momentum theory, a higher resolution of the disc is required, which can be enabled through radial discretisation. The disc is split into a number of annular rings as shown in Figure 2.4a for a 'conventional' 3-bladed bare turbine, and Figure 2.4b for a high solidity, open centre, ducted design. For the latter, the same naming convention is used, with the addition of the duct radius (R_d).

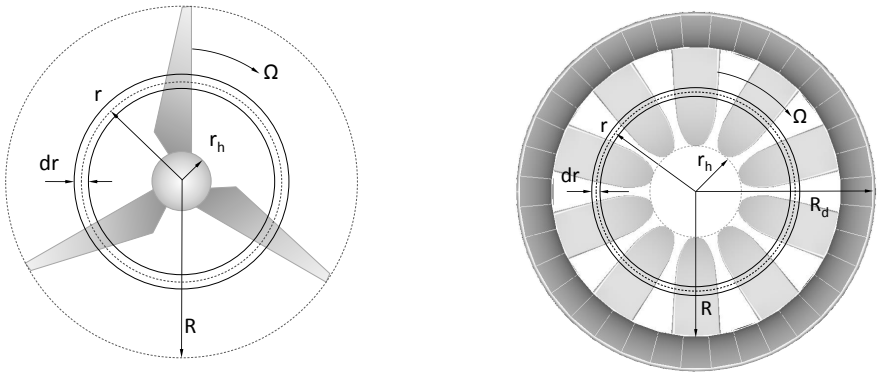

(a) A three-bladed and bare turbine (b) A high solidity, ducted turbine

Figure 2.4: Schematics of two different turbine designs, showing rotors split into discrete annular rings

Each annular section has an area (dA) equivalent to the average circumference ($2\pi r$) multiplied by the element width (dr).

2.2.3.2 Axial momentum theory within the annular rings

Assuming the momentum is extracted only from fluid passing through each individual ring, the pressure / momentum balance can be applied independently such that the axial force at each annular ring (dF_{ax}) can be defined.

For bare turbines using Equation 2.11, this is defines as:

$$dF_{ax} = 4\pi\rho U^2 a(1-a)rdr \tag{2.32}$$

And for ducted turbines using Equation 2.27, the following is written:

$$dF_{ax} = \pi\rho U^2 \left(\eta_{02} + C_{pb} - (\eta_{02} - C_{p34})\,(1-a)^2\right) rdr \tag{2.33}$$

For non-uniform circulation there will be radial interactions and transferral of momentum to adjacent annular rings. However, these are neglected by the theory, which means that any radial interaction in axial flow induction factor is not taken into account. In practice, the error induced from this assumption has been shown to be minimal (Burton et al., 2011).

2.3 Rotor disc theory

Additionally to a change of axial momentum in the fluid as a result of the presence of a semi-permeable disc, there is also a change in angular momentum associated with the turbine rotation. This can be related to the angular forces on the blades, causing a torque which drives the electrical generator.

2.3.1 Angular momentum

The fluid entering the turbine is considered straight, with zero rotational motion. Fluid passing through the rotating disc exerts a torque on the rotor, which requires

an equal and opposite torque imposed on the fluid. This reaction torque causes the fluid to rotate in an opposite direction to turbine rotation. This has an associated gain in angular momentum, as the wake flow now has a velocity component tangential to the rotation. The wake rotates at an angular velocity ω, with the blades rotating in the opposite direction at an angular velocity Ω (see Figure 2.5).

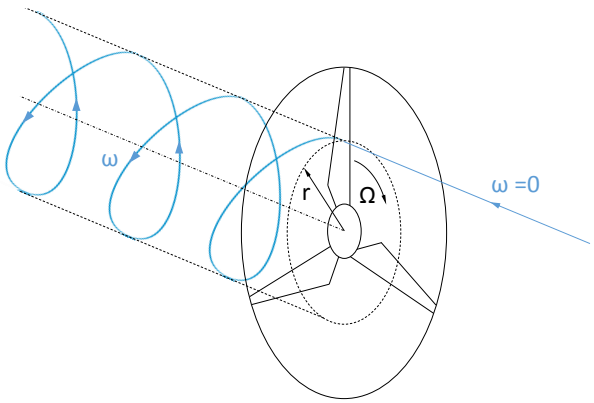

Figure 2.5: Projected trajectory of a fluid particle travelling through a turbine

2.3.2 Disc torque

The torque can be defined as the rate of change of angular momentum:

$$Q = \frac{dL}{dt} \tag{2.34}$$

Where angular momentum $L = I\omega$ and the moment of inertia $I = mr^2$. Therefore it can be stated that:

$$Q = \frac{\delta(mr^2\omega)}{\delta t} \tag{2.35}$$

Where the $\delta m/\delta t = \dot{m}$ is the mass flow rate, and therefore for the entire disc:

$$Q = \rho A_d U_d \omega r^2 \tag{2.36}$$

The axial induction factor from the previous section (Equation 2.9) can then be incorporated so that:

$$Q = \rho A_d U(1-a)\omega r^2 \tag{2.37}$$

2.3.3 Disc radial discretisation

The tangential velocity is not the same for all radial positions, and is also a function of axial induction factor, which may vary radially. Therefore the rotor is split into a number of annular rings, as shown previously in Figure 2.4a. The torque of each annular ring (dQ) can be defined as:

$$\begin{aligned} dQ &= d\dot{m}\omega r^2 \\ &= \rho 2\pi U(1-a)\omega r^3 dr \\ &= \rho 4\pi U(1-a)\Omega a' r^3 dr \end{aligned} \tag{2.38}$$

Which now includes a 'tangential induction factor' a', relating the rotational velocity of the disc to the rotational velocity of the wake, given by:

$$a' = \frac{\omega}{2\Omega} \tag{2.39}$$

The torque on the annular element of fluid is equal and opposite to the driving torque on the transmission to the electrical generator (via a shaft in the case of bare turbines). Therefore, the power can be expressed as:

$$\begin{aligned} dP &= dQ\Omega \\ &= \rho 4\pi U(1-a)\Omega^2 a' r^3 dr \end{aligned} \tag{2.40}$$

2.3.4 Wake structure

There is an increase in kinetic energy as angular momentum is injected into the wake. This was previously believed to reduce the amount of energy available for extraction (Burton et al., 2001), however has been more recently contradicted, as detailed in full by Burton et al. (2011).

As lift forces are in the direction normal to the resultant velocity, no work is done and therefore Bernoulli's equation can be applied to the flow across the disc such that:

$$\frac{1}{2}\rho U_d^2 + \frac{1}{2}\rho(\Omega r)^2 + p_2 = \frac{1}{2}\rho U_d^2 + \frac{1}{2}\rho((\Omega+\omega)r)^2 + p_3 \tag{2.41}$$

Therefore:

$$\begin{aligned}\Delta p_d &= \frac{1}{2}\rho\left(((\Omega+\omega)\,r)^2 - (\Omega r)^2\right) \\ &= 2\rho a'\Omega^2 r^2(1+a')\end{aligned} \tag{2.42}$$

This can be split into two components:

$$\Delta p_{d_1} = 2\rho a'\Omega^2 r^2 \tag{2.43}$$

$$\Delta p_{d_2} = 2\rho a'^2\Omega^2 r^2 \tag{2.44}$$

Equating the power from axial (Equation 2.13) and angular momentum theories (Equation 2.40):

$$\begin{aligned}\rho 4\pi U^3 a(1-a)^2 r dr &= \rho 4\pi U(1-a)\Omega^2 a' r^3 dr \\ a(1-a) &= \left(\frac{\Omega r}{U}\right)^2 a'\end{aligned} \tag{2.45}$$

Inserting this into the pressure change at the disc to calculate the axial force (Equation 2.11) arrives at the same expression for Δp_{d_1}. Therefore this is the pressure drop associated to the change in axial momentum.

The varying rotational velocities across the disc gives rise to a radial pressure gradient, which balances the centrifugal forces on the rotating fluid. This is represented by the secondary pressure drop Δp_{d_2}, which balances the kinetic energy per unit volume of the rotating wake. This results in no loss of energy for extraction.

Some studies include the additional pressure drop in calculating the thrust forces on the disc (e.g. Shives (2011)). This phenomenon was explored by Burton et al. (2011), who concluded that the radial pressure drop does not cause an additional thrust force on the disc. Unlike Δp_{d_1}, which recovers gradually between the disc and the far downstream wake, Δp_{d_2} applies to the entire wake, where no gradient is seen. This causes no further reduction in the axial velocity, which means there can be no corresponding force. This is therefore thought to be an anomaly in the method, stemming from the "physically non-realisable concept of the actuator disc" (Burton et al., 2011).

2.4 Blade element theory

Through the axial and angular momentum theories, the expressions for the thrust, torque and power are derived in terms of axial and tangential induction factors. However, these cannot be solved in their current state without knowledge of the velocities at various positions along the stream tube. These can be determined, for example, through solving the Navier-Stokes equations by coupling the actuator disc to a CFD solver.

As a simpler alternative, the hydrodynamic lift and drag forces on the individual blades can be considered, which are based on predetermined hydrofoil characteristics. These forces can be expressed as a function of the relative flow over the blade, and therefore can be related back to the axial and tangential induction.

This method is known as 'the Blade Element theory', and provides a more physical representation of the turbine than previously taken, as it uses real geometrical properties of the blades.

2.4.1 Blade discretisation

Turbine blades consist of hydrofoil cross sections, which are designed to generate hydrodynamic lift. This has a force component acting in the rotor tangential direction, which is responsible for the production of torque.

The blade can be split into a number of discrete hydrofoil 'elements', where arbitrary numbers of splits on typical blades for a 'conventional' bare turbine (Figure 2.6a), and a bi-directional ducted turbine (Figure 2.6b).

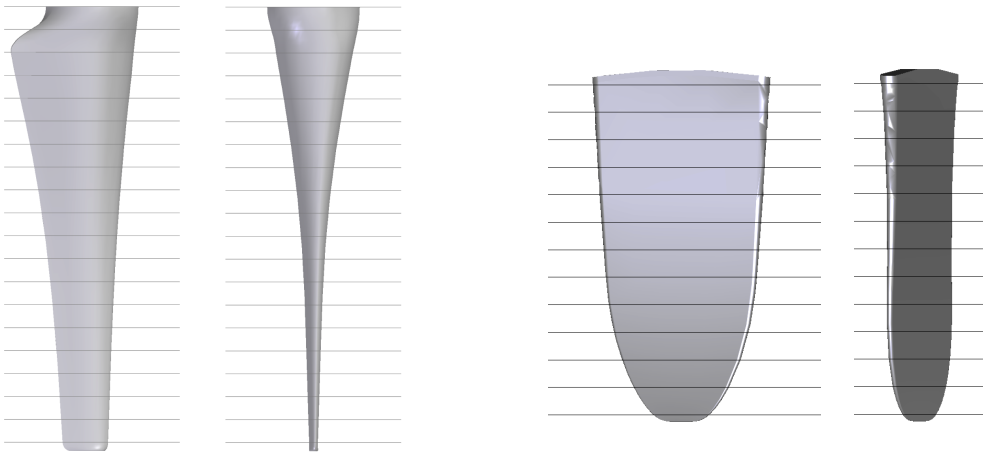

(a) A conventional bare TST blade (b) A ducted, open centre TST blade

Figure 2.6: Elemental sectioning of an arbitrary design of blade from two TST designs, showing front and side views

The result is a number of hydrofoil sections, each with a centre point at a radial distance r to the turbine centre, a length dr and a chord length c, as illustrated in Figure 2.7.

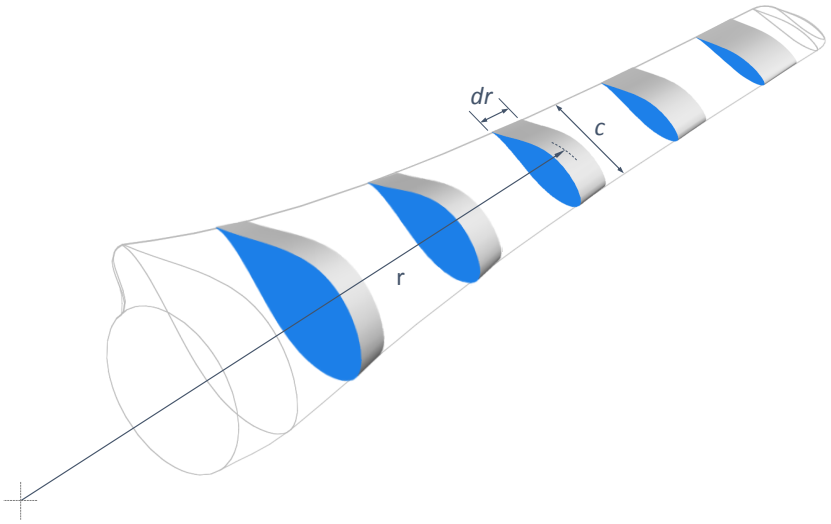

Figure 2.7: TST blade split into discrete elements, showing key element dimensions

2.4.2 Blade element velocities

Each element along the blade is individually considered, as represented in Figure 2.8. The resultant velocity of the flow is given as a function of the axial and in-plane velocities. The latter is a relative velocity taking into account the rotation of the blade in one direction, and the rotation of the fluid in the wake in the other direction (see Figure 2.8).

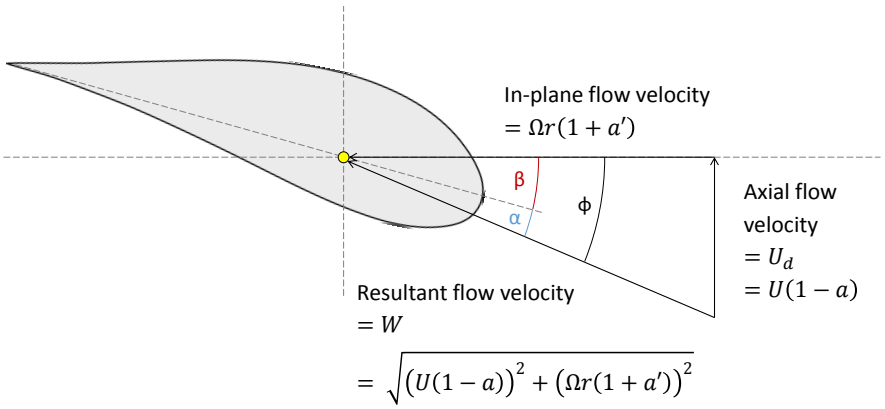

Figure 2.8: Diagram of flow velocities at a TST blade element

The resultant fluid velocity (W) is defined as a function of the in plane and axial

velocities. The inflow angle (ϕ) lies between the flow vectors, and is a function of the blade twist (β) and angle of attack (α). These are expressed in terms of the induction factors defined in the momentum theory section. From this the following trigonometric functions can be stated:

$$\tan(\phi) = \frac{U(1-a)}{\Omega r(1+a')}, \qquad \sin(\phi) = \frac{U(1-a)}{W}, \qquad \cos(\phi) = \frac{\Omega r(1+a')}{W}$$

2.4.3 Blade element hydrodynamic forces

The hydrodynamic lift and drag forces on each blade element act perpendicular and parallel respectively to the resultant velocity. These can be used to determine the axial and tangential forces acting on the element, as a function of the inflow angle, as shown in Figure 2.9.

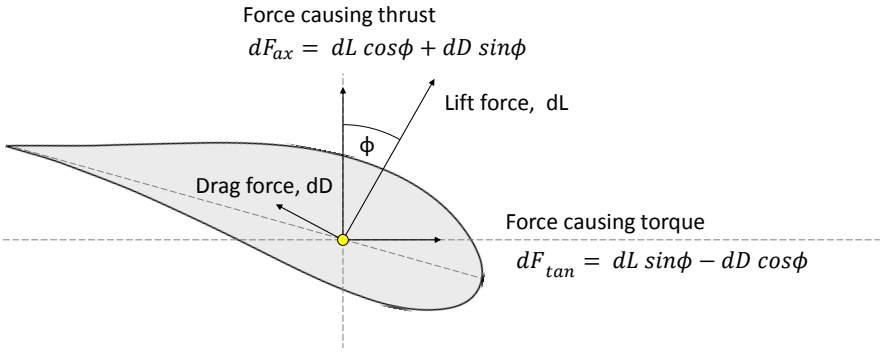

Figure 2.9: Diagram of hydrodynamic forces acting on a TST blade element

The hydrodynamic lift and drag forces are determined using the standard hydrofoil equations (DNV GL Garrad Hassan, 2012*b*):

$$\begin{aligned} dL &= \frac{1}{2} C_L \rho W^2 c dr \\ dD &= \frac{1}{2} C_D \rho W^2 c dr \end{aligned}$$

Where c is the blade chord, and coefficients of lift C_L and drag C_D are inputs from two-dimensional hydrofoil data and are a function of angle of attack. The

forces causing thrust and torque can then be resolved trigonometrically, in order to give:

$$dF_{ax} = \frac{1}{2}\rho W^2 c dr C_x \tag{2.46}$$

$$dF_{tan} = \frac{1}{2}\rho W^2 c dr C_y \tag{2.47}$$

Where: $C_x = C_L \cos(\phi) + C_D \sin(\phi)$

$C_y = C_L \sin(\phi) - C_D \cos(\phi)$

The torque can be calculated by simply multiplying the tangential force by the local element radius:

$$dQ = \frac{1}{2}\rho W^2 c r dr C_y \tag{2.48}$$

2.4.4 Lift and drag coefficient data

Hydrofoil (or aerofoils in air) characteristics of blade elements are properties which describe their hydrodynamic behaviour in specific operating conditions. Coefficients of lift and drag are non dimensional values which can be used to determine the aerodynamic forces. These vary with angle of attack, and can be measured from wind tunnel tests or generated numerically through a number of methods.

Hydrodynamic coefficients of lift and drag are often generated with a maximum resolution of $\Delta\alpha = 1°$, and are read into the model as a series of lookup tables. In order provide information at a higher resolution of α a linear interpolation function is applied, based on:

$$C_\alpha = C_0 + \frac{(\alpha - \alpha_0)(C_1 - C_0)}{(\alpha_1 - \alpha_0)} \tag{2.49}$$

Where C_α is the coefficient at the required exact value of α. C_0 and C_1 are known coefficients of lift and drag at two known angles of attack α_0 and α_1.

The assumption here is that there will be a linear relationship of C between α_0 and α_1. This assumption is not thought to be highly influential for most areas on the curves. However it is of greater importance that the increment size is sufficiently small for conditions where there are sharp changes, such as around stall.

2.5 Blade element and momentum theory

From the momentum equations, the axial force (F_{ax1}) and torque (Q_1) are expressed in relation to the axial and tangential induction factors. From blade element theory, the axial force (F_{ax2}) and torque (Q_2) are expressed as a function of the lift and drag coefficients and inflow angle are (also related to axial and tangential induction factors). The forces can now be resolved by combining the two theories within a BEMT loop, which iteratively seeks induction factors until the forces balance and equilibrium is achieved, as illustrated in Figure 2.10.

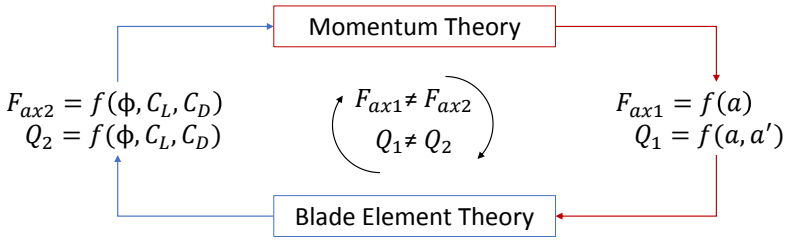

Figure 2.10: Illustration of the BEMT iterative loop, solving for elemental axial force and torque

2.5.1 Combining the theories

In order to combine the two theories, it is assumed that the change of momentum through the annulus swept by the element is solely due to the fluid dynamic forces on that blade element. Therefore each annular ring must have the same radius

(r) and width (dr) as those defining the size of the blade elements. Blade element forces must also multiplied by the number of blades (N_b) on the turbine in order to match the overall force on the corresponding annular ring.

2.5.2 Resolving the axial forces for a bare turbine

The axial force using the axial momentum theory (dF_{ax1}) from Equation 2.32 can be equated to the expression derived in blade element theory (dF_{ax2}) from Equation 2.46 to give:

$$\begin{aligned} dF_{ax1} &= dF_{ax2} \\ 4\pi\rho U^2 a(1-a)rdr &= \frac{1}{2}\rho W^2 N_b c C_x dr \end{aligned} \tag{2.50}$$

Which can be rearranged to solve for the axial induction factor:

$$\frac{a}{(1-a)} = \frac{\sigma_r C_x}{4\sin^2(\phi)} \tag{2.51}$$

Where local blade solidity: $\sigma_r = \dfrac{N_b c}{2\pi r}$

2.5.3 Resolving the axial forces for a ducted turbine

A similar process can be followed for the ducted case, where the axial force (dF_{ax1}) is now taken from Equation 2.33 to give:

$$\pi\rho U^2 \left(C_{pb} + \eta 02 + \left(C_{p34} - \eta_{02}\right)(1-a)^2\right) rdr = \frac{1}{2}\rho W^2 N_b c C_x dr \tag{2.52}$$

Rearranging to:

$$\frac{\left(C_{pb} + \eta_{02} + \left(C_{p34} - \eta_{02}\right)(1-a)^2\right)}{(1-a)^2} = \frac{\sigma_r C_x}{\sin^2(\phi)} \tag{2.53}$$

Where the duct parameters are solved using empirical formulae defined in Section 2.2.2.3.

2.5.4 Resolving the torque

Similarly, the torque from the angular momentum theory (dQ_1) given by Equation 2.38) can be equated to the torque derived in blade element theory (dQ_2) in Equation 2.48 to give:

$$dQ_1 = dQ_2 \tag{2.54}$$

$$4\pi\rho\Omega U a'(1-a)r^3 dr = \frac{1}{2}\rho W^2 N_b c C_y r dr \tag{2.55}$$

Which can be rearranged to solve the tangential induction factor:

$$\frac{a'}{(1+a')} = \frac{\sigma_r C_y}{4\sin(\phi)cos(\phi)} \tag{2.56}$$

2.5.5 Solving the BEMT equations

These equations are arranged in a convenient form to allow values for the flow induction factors a and a' to be solved using 2-D hydrofoil characteristics. This is an iterative process due to the non linear functions of hydrofoil characteristic with regard to α.

2.5.6 Power, thrust and tip speed ratio

The torque and the axial force at each element can be calculated and integrated over the rotor area to attain overall turbine values.

The power can be simply calculated as the product of the torque and rotor angular velocity, representing the pure hydrodynamic power, not accounting for generator

efficiency or any losses such as through the drive shaft, which would need to be included in any electricity generation analysis.

Overall turbine C_T and C_P are defined as:

$$C_T = \frac{\sum_{r_h}^{R} dF_{ax}}{\frac{1}{2}\rho A U^2} \tag{2.57}$$

$$C_P = \frac{\sum_{r_h}^{R} dQ\Omega}{\frac{1}{2}\rho A U^3} \tag{2.58}$$

The reference area A is usually taken as the rotor area $A = \pi R^2$. Hansen (2008) also uses the rotor area in the case of ducted turbines when calculating C_T and C_P. However, Belloni et al. (2016) argues that in order to compare the performance of a ducted with a bare turbine relative to the amount of space they require, the duct inlet area should be taken. Although this is not an objective of the present study, the duct area is used as per Belloni et al. (2016) in order to gain directly comparable results for validation.

These coefficients are frequently quoted in the literature and manufacturers specifications, varying with TSR (tip speed ratio), given by:

$$TSR = \frac{\Omega R}{U} \tag{2.59}$$

The ducted case also uses the rotational velocity at the outer radius of the rotor, despite the fact that this is no longer seen as the 'tip'.

Accuracy in the measuring equipment are usually quoted as force and torque values, taken directly from the manufacturer. These can be converted into coefficients of power and thrust, and incorporated into the experimental measurement results using the following equations:

$$C_{T_{error}} = \frac{T_{error}}{\frac{1}{2}\rho U^2 A} \qquad C_{P_{error}} = \frac{Q_{error}\Omega}{\frac{1}{2}\rho U^3 A} \tag{2.60}$$

2.6 Limitations and correction factors

There are some simplifying assumptions inherent to the BEMT method that do not account for some of the flow physics. This can reduce the accuracy of the model predictions, as well as in some scenarios even cause the model to break down. These are typically addressed by the use of correction factors, which are incorporated into the model to approximate the effects of phenomena that are neglected within the underlying principles.

2.6.1 Model assumptions

The main modelling assumptions that can be corrected for concern the representation of the actuator disc, 2-D assumptions, and the stream tube representation of the flow neglecting mixing with the external free stream fluid. There are a number of proposed factors devised within the literature, the most appropriate of which are selected and discussed here. These corrections are implemented directly into the BEMT equations, which can be optionally activated depending on the requirements of the application case.

2.6.2 BEMT correction factors

This section details and justifies the following three corrections used in this thesis: i) the Prandtl tip and hub loss factor based on the approximations of helical wake shedding; ii) the Buhl variant of the Glauert factor to account for the higher thrust seen in highly loaded conditions; iii) the blockage correction for flow within a channel section, based on expressions by Bahaj, Molland, Chaplin and Batten (2007) which are detailed in Appendix 1.

2.6.3 Effects of a discrete number of blades

The momentum theory resolves forces for each annular ring: it does not consider the flow around the individual blades. The assumption is that all of the fluid in each annular ring interacts with a blade. The method therefore assumes an infinite number of blades of infinite length, meeting at a single point at the rotor axis. This results in over prediction of the forces calculated within the momentum equations, and creates a disparity with the blade element theory.

2.6.3.1 Tip losses

The effects of individual blades can be approximated through considering the flow at the outer and inner boundaries of the blade (at the tip and hub). Analytical approaches can be used to correct for this effect within the momentum equations. These have been successfully applied in wind turbine applications in order to approximate the reduction in hydrodynamic efficiency to account for the finite length and number of blades.

This effect is thought to be of greater influence in the case of TSTs, where blades are designed shorter to withstand the higher force per unit blade length of the higher density working fluid. In the case of a high solidity turbine however, finite blade assumptions will be less influential due to the smaller spaces between blades.

2.6.3.2 Modelling tip losses

Although exact solutions exist such as proposed by Bessel and Biot-Savart, issues arise for integrating them into the BEMT method Burton et al. (2011). The Prandtl approximation solution yields a relatively simple analytical function which has been previously employed to account for the effects of the tip losses (Chapman et al., 2013), and can be easily implemented into BEMT.

Flow shedding at each of the blade tips leads to rotating helical structures in the wake. Prandtl conceptualises these ‘helical sheets’ as a succession of

discs travelling at a constant, axial central wake velocity of $U(1-a)$ with separation distances matching the normal length between vortex sheets, as shown in Figure 2.11a. The fluid surrounding the outer edges of these sheets will be travelling at a greater free stream velocity U, which weaves between the discs, increasing the velocity of the fluid in these areas. This therefore simulates a reduction in the change of momentum at the blade limits, which can be considered a reduction in the hydrodynamic efficiency.

The average velocity of a line at a radial point below the rotor (or wake) radius can be taken as: $U_{av} = U(1-aF(r))$ where F(r) is the tip loss function equal to 1 when the external fluid cannot penetrate the wake and decreases towards zero at the wake boundary where the unattenuated flow dominates.

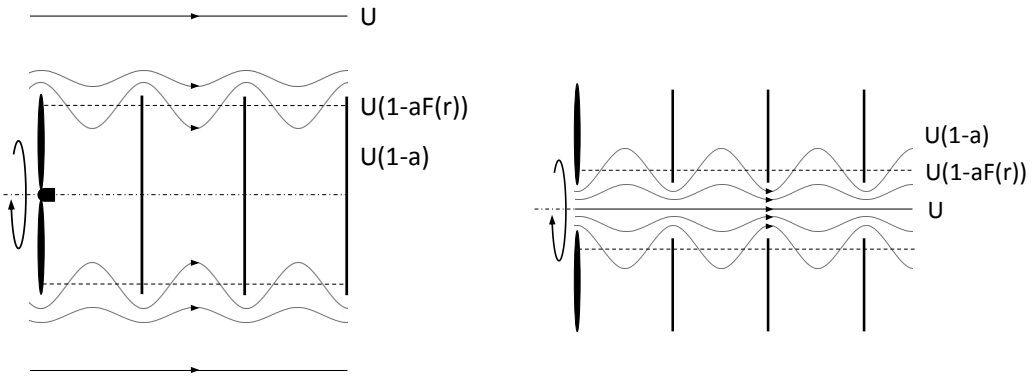

(a) A conventional bare type TST (b) An open centre TST

Figure 2.11: Depiction of the Prandtl concept wake discs for two designs of TST

A similar conceptualisation for the case of the open centre rotor is made, where the tips are inward facing towards the centre as shown in Figure 2.11b.

One assumption of this is that the velocity at the rotor axis is equal to that of the free-stream. This is likely inaccurate, as velocity through the centre is predicted to increase due to flow augmentation. The result of this assumption is that smaller losses are predicted, which lead to larger forces. To determine the actual velocity requires a more complex flow model, which is incompatible with

the BEMT method. This is therefore a limitation in this present study, the effects of which are explored in Chapter 5.

2.6.3.3 Tip/hub loss correction factor

The loss factor can be expressed in the closed solution form proposed by Prandtl:

$$F_{tip} = \left(\frac{2}{\pi}\right) \cos^{-1} e^{-f_{tip}} \tag{2.61}$$

$$\text{where: } f_{tip} = \pi \left(\frac{R_w - r}{d}\right) \tag{2.62}$$

Where R_w is the distance from the centre to the wake edge and d is the normal distance between successive vortex sheets:

$$\begin{aligned} d &= \frac{2\pi R_w \sin(\phi_s)}{N_b} \\ &= \frac{(2\pi R_w)}{N_b} \frac{U(1-a)}{W_s} \end{aligned} \tag{2.63}$$

This is related to the angle between the vortex sheets (ϕ_s) intertwining from N_b number of blades. The Betz-Prandtl approach assumes the flow is inviscid, with no wake rotation, such that the resultant wake velocity $W_s = \sqrt{U(1-a)^2 + (\omega R)^2}$. However, the discs may spin at rotor speed without affecting the flow. Using the Glauert adjustment such that $R_w/W_s \approx r/W$ (Glauert, 1948), the tip loss is rewritten as:

$$f_{tip} = \frac{N_b}{2} \left(\frac{R - r}{r}\right) \frac{1}{\sin(\phi)} \tag{2.64}$$

The circulation at the root of the blade must also fall to zero, and so the hub losses can be approximated similarly to the tip loss methodology.

$$F_{hub} = \left(\frac{2}{\pi}\right) \cos^{-1} e^{-f_{hub}} \tag{2.65}$$

$$\text{where: } f_{hub} = \pi \left(\frac{r - r_h}{d}\right) \tag{2.66}$$

$$d = \frac{2\pi r_h \sin \phi_s}{N_b}$$

using r_h as the hub radius. Again rearranging, and taking the Betz-Prandtl approach of inviscid flow with no wake rotation, the exponent can be expressed:

$$f_{hub} = \frac{N_b}{2} \left(\frac{r - r_h}{r_h}\right) \frac{1}{\sin(\phi)} \tag{2.67}$$

This can be applied to scenarios where a hub is present within the design.

These two factors can subsequently be combined to give an overall loss correction factor defined by:

$$F = F_{tip} F_{hub} \tag{2.68}$$

2.6.3.4 Implementation into the momentum equations

The combined tip/ hub loss factor can then be input directly as a multiplication factor into the expressions thrust and torque from momentum theory. This is a typical methodology used in other BEMT models such as Masters et al. (2011), Chapman et al. (2013) and Moriarty and Hansen (2005).

For a bare turbine, Equation 2.32 becomes:

$$dF_{ax} = 4\pi\rho U^2 a(1 - a) r dr F \tag{2.69}$$

Whilst in the case of a ducted turbine, Equation 2.33 can be written:

$$dF_{ax} = \pi\rho U^2 \left(\eta_{02} + C_{pb} - (\eta_{02} - C_{p34})\,(1-a)^2\right) r dr F \tag{2.70}$$

Similarly, the torque from Equation 2.38 becomes:

$$dQ = 4\pi\rho\Omega U a'(1-a) r^3 dr F \tag{2.71}$$

2.6.4 Highly loaded conditions

From the representation of turbine as an actuator disc, the downstream velocity is expressed as a function of the inflow velocity and the axial induction factor, such that: $U_4 = U(1-2a)$. In highly loaded conditions, where $a > 0.5$, the model predicts a negative downstream velocity, such that there is a flow reversal in the wake. This is not physically possible, and is a known limitation of the method.

As the tip speed ratio increases, the permeability of the disc reduces until the axial induction factor approaches 1 and the disc effectively behaves like a solid plate. This is similarly true if more blades are added to the rotor, increasing the turbine solidity.

Under these conditions, the fluid is pushed radially outwards until separation occurs at the tip which causes a drop in static pressure to develop behind the rotor, which is proportional to tip speed ratio increase. The fluid in the far wake must return to the free stream pressure, which can only be achieved by re-energising from turbulent mixing, the source of this being the unstable boundary layer that develops at the front of the disc. In this scenario, the wake becomes turbulent which entrains fluid external to the wake by a mixing process that injects energy into the slow moving fluid. The low static pressure downstream of the rotor, coupled with the high static pressure at the stagnation point on the upstream face results in increased thrust.

This effect has been observed in physical experiments conducted with flat circular plates, which report significantly higher axial forces than those predicted by BEMT (Burton et al., 2011). Experiments with rotors have shown even higher values, due to energy being dissipated in a thicker, rotating boundary layer which gives rise to an even lower downstream pressure. Data from experiments on helicopter rotors by Glauert (1926) is shown in Figure 2.12a. Here it can be seen that the thrust under higher axial flow induction factors exceed those predicted by BEMT (Hansen, 2008).

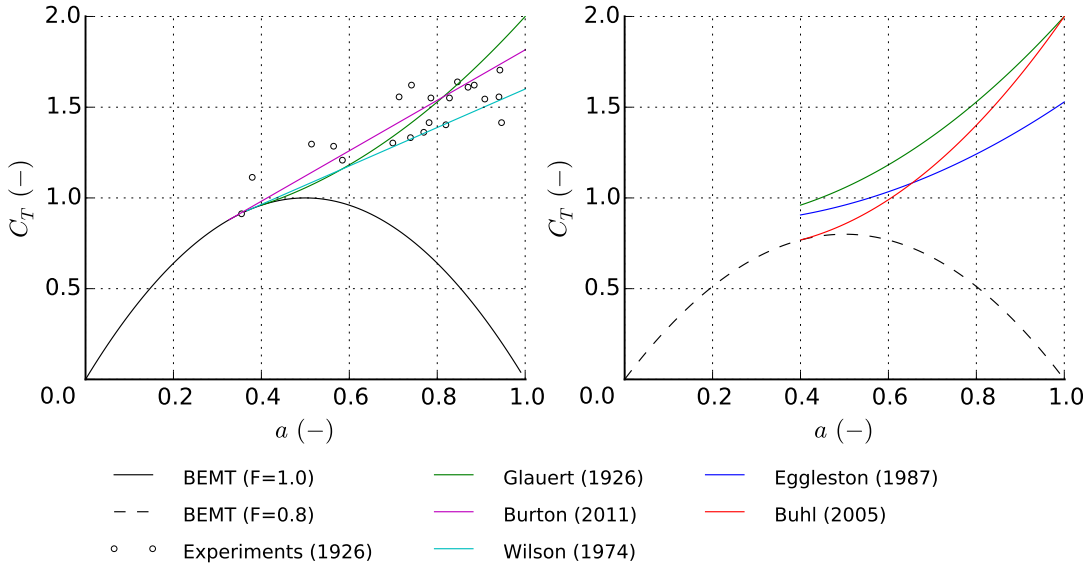

Figure 2.12: Thrust coefficient against axial induction factor, showing comparisons of BEMT against: a) experiments and semi-empirical corrected values under highly loaded conditions (left) and b) highly loaded corrected values with an arbitrary tip/hub loss of 0.8 applied

2.6.4.1 Highly loaded correction factors

At low axial induction factors, C_T can be found with the general expression used in BEMT based on 2-D conservation of momentum equations applied to an actuator disc in a stream tube:

$$\text{When } a < a_T: \qquad C_T = 4a(1-a)$$

Where a_T is the axial induction factor at the transition to a 'highly loaded regime', when the disc no longer follows the classical BEMT approach and instead follows the highly loaded rotor correction.

Various semi-empirical approximations have been proposed based on this observation, in order to account for the effects of high loads on the rotor. A straight line fit to the data can be applied, assuming a value of coefficient of thrust C_{T1} at $a = 1$. There must then be a straight line tangent at the intersection with the momentum theory parabola known at the transition point.

$$\text{When } a \geq a_T: \qquad C_T = C_{T1} - 4\sqrt{(C_{T1} - 1)(1 - a)}$$

Where: $C_{T1} = 4(1-a_T)^2$. The value of C_{T1} is arbitrary and varies in the literature. $C_{T1} = 1.816$ giving $a_T = 0.326$ is the best fit of Glauert data, as suggested by Burton et al. (2011), whereas a value of $C_{T1} = 1.6$ giving $a_T = 0.368$ is used by Wilson and Lissaman (1974).

Glauert, on the other hand, employs a parabolic curve to determine the coefficient of thrust after a_T used in the application of an airscrew. This has the equation in the following form, using $a_T = 0.4$:

$$\text{When } a \geq a_T: \qquad C_T = 0.889 - \frac{\left(0.0203 - (a - 0.143)^2\right)}{0.6427} \tag{2.72}$$

2.6.4.2 Combining with the tip/ hub loss correction

The addition of the tip/hub loss factor can be made to the original thrust curve equation: $C_T = 4Fa(1-a)$. If an arbitrary tip/hub loss factor of 0.8 is applied, it can be seen from Figure 2.12b that the Glauert corrected curve no longer intersects the BEMT thrust coefficient curve, resulting in numerical instability in BEMT solvers (Moriarty and Hansen, 2005). One study reports close to transitional axial induction factors in blade elements at the tip (Chapman et al., 2013), highlighting the necessity to eliminate this source of instability. A simple modification to the

Glauert equation to include the tip/hub loss was proposed by Eggelston and Stoddard (Buhl, 2005):

$$\text{When } a \geq a_T: \qquad C_T = 0.889 - \frac{\left(0.0203 - (aF - 0.143)^2\right)}{0.6427} \tag{2.73}$$

This reduces the gap between the BEMT theory and highly loaded turbine correction lines, however a discontinuity is still seen. Buhl devised an alternative form of the equation using a simple methodology of taking the correction parabola as a quadratic formula (complete derivations can be found in Buhl (2005)):

$$C_T = b_0 + b_1 a + b_2 a^2 \tag{2.74}$$

Where the slope can be defined as:

$$\frac{dC_T}{da} = b_1 + 2b_2 a$$

And the boundary conditions to satisfy:

$$\begin{aligned} \text{At } a = 0.4: \qquad & C_T = 4aF(1-a) = 0.96F \\ & \frac{dC_T}{da} = 4F - 8aF = 0.8F \\ \text{At } a = 1.0: \qquad & C_T = 2 \end{aligned}$$

Solving this gives the expression:

$$C_T = \frac{8}{9} + \left(4F - \frac{40}{9}\right) a + \left(\frac{50}{9} - 4F\right) a^2 \tag{2.75}$$

The variant now ensures the intersection of the classical BEMT thrust curve with the highly loaded correction when the tip/hub losses have been accounted for, as seen in Figure 2.12b. As there is a smooth transition and reasonable agreement with experimental data, this correction is considered most appropriate to this application. The upper limit at a=1 is analogous to flow on a solid plate, and therefore gives a higher level of confidence in this model (Masters et al., 2010).

2.6.4.3 Axial force in the highly loaded condition

As this new expression for C_T is related to the overall rotor, it can be simply translated back to the axial force within each annular ring as:

$$\text{When } a \geq 0.4: \qquad dF_{ax} = \pi \rho U^2 r dr \left(\frac{8}{9} + \left(4F - \frac{40}{9} \right) a + \left(\frac{50}{9} - 4F \right) a^2 \right) \tag{2.76}$$

2.6.5 Channel flows

Sites for deployment of TSTs are typically characterised by the tidal stream velocities, where higher flow rates are desirable to raise the kinetic energy potential available for extraction. The coastal landscape in particular locations offer channels where flow is accelerated, such as between islands and mainlands (e.g. the Pentland Firth, Scotland). These areas are often selected in order to exploit the higher power potential, and therefore will be subjected to the constraining effects of the channel walls. This is also the case when performing scale model tank tests, where boundaries are located in the near vicinity of the rotor.

Fluid flowing through the turbine decreases in velocity, and so will expand in volume in order to conserve mass. The presence of external boundaries constrains the amount of expansion permitted in the wake, and therefore affects the assumptions of the streamtube. The effect of this channelling has been investigated by Garrett and Cummins (2007), as detailed in Appendix 1, Section 1. A blockage correction factor to convert measurements in a test tank to 'equivalent open water' is proposed by Bahaj, Molland, Chaplin and Batten (2007), and is described in Appendix 1, Section 2.

2.6.6 Corrected BEMT

The new formulations of the axial force and torque incorporating the correction factors can be used to define a new set of combined BEMT equations.

2.6.6.1 Resolving corrected axial force

The axial force incorporating the tip/hub loss correction from Equation 2.69 now defines F_{ax1}, which is equated to the blade element force dF_{ax2} to give:

$$4\pi\rho U^2 a(1-a)rdrF = \frac{1}{2}\rho W^2 N_b c C_x dr \tag{2.77}$$

Rearranged to solve for the axial induction factor:

$$\frac{a}{(1-a)} = \frac{\sigma_r C_x}{4F\sin^2(\phi)} \tag{2.78}$$

In the case of ducted turbines, Equation 2.70 defines F_{ax1}, which is equated to the blade element force dF_{ax2} to give:

$$\pi\rho U^2 \left(C_{pb} + \eta 02 + \left(C_{p34} - \eta_{02}\right)(1-a)^2\right) rdrF = \frac{1}{2}\rho W^2 N_b c C_x dr \tag{2.79}$$

Rearranging to:

$$\frac{\left(C_{pb} + \eta_{02} + \left(C_{p34} - \eta_{02}\right)(1-a)^2\right)}{(1-a)^2} = \frac{\sigma_r C_x}{F\sin^2(\phi)} \tag{2.80}$$

These are valid when the turbine is not considered highly loaded, for all $a < 0.4$.

2.6.6.2 Resolving corrected highly loaded axial force

For the highly loaded condition, the Buhl correction factor is incorporated into the axial momentum equations shown in Equation 2.76, therefore it can be stated

that:

$$\pi\rho U^2 r dr \left(\frac{8}{9} + \left(4F - \frac{40}{9}\right) a + \left(\frac{50}{9} - 4F\right) a^2\right) = \frac{1}{2}\rho W^2 N_b c C_x dr \tag{2.81}$$

Which can be rearranged to:

$$\frac{\left(\frac{8}{9} + \left(4F - \frac{40}{9}\right) a + \left(\frac{50}{9} - 4F\right) a^2\right)}{(1-a)^2} = \frac{\sigma_r C_x}{\sin^2(\phi)} \tag{2.82}$$

Which is imposed for $a \geq 0.4$.

2.6.6.3 Resolving corrected torque

Similarly, the corrected expression for torque from Equation 2.71 is used to define dQ_1. Equating, as before, to the blade element torque dQ_2 yields:

$$4\pi\rho\Omega U a'(1-a) r^3 dr F = \frac{1}{2}\rho W^2 N_b c C_y r dr \tag{2.83}$$

Rearranged to solve the tangential induction factor:

$$\frac{a'}{(1+a')} = \frac{\sigma_r C_y}{4F\sin(\phi)cos(\phi)} \tag{2.84}$$

2.7 Inflow conditions

The momentum of the fluid available for extraction is dependent on the flow velocity. Additionally, the hydrodynamic lift and drag forces along the blade are dependent on the blade element coefficients, which vary as a function of the chord based Reynolds number, also dependent on flow velocity.

The upstream depth varying velocity field in the perpendicular plane to the rotor can be defined as the inflow profile. These are dependent on the environmental conditions, such as the proximity of the external boundaries. The location dependent velocities can be input into the BEMT model as a series of vectors.

Here only steady profiles that are 'frozen' in time are considered. 'Quasi-steady' inflow conditions can also be applied, where varying velocity profiles can be input using a time-stepping scheme. The methodology is readily available to accept any time varying velocity vectors, where unsteady can be imposed using dynamic inflow conditions such as described in (Moriarty and Hansen, 2005).

2.7.1 Element coordinates

In order to calculate the spacial variation, the local position of each element is required, relative to a static reference point which is taken to be the sea bed. The vertical location of each element can be specified as:

$$z_i = z_{ref} + r_i \sin(\Phi) \tag{2.85}$$

$$x_i = -r_i \cos(\Phi) \tag{2.86}$$

As shown in Figure 2.13, z_i is the vertical height in the water column (m) of the element i above the boundary; x_i is the horizontal distance from the centre (m); r_i is the elemental radius (m); z_{ref} is the height of the reference above the seabed (m), taken as the hub (or turbine axis); and Φ is the azimuthal angle (radians).

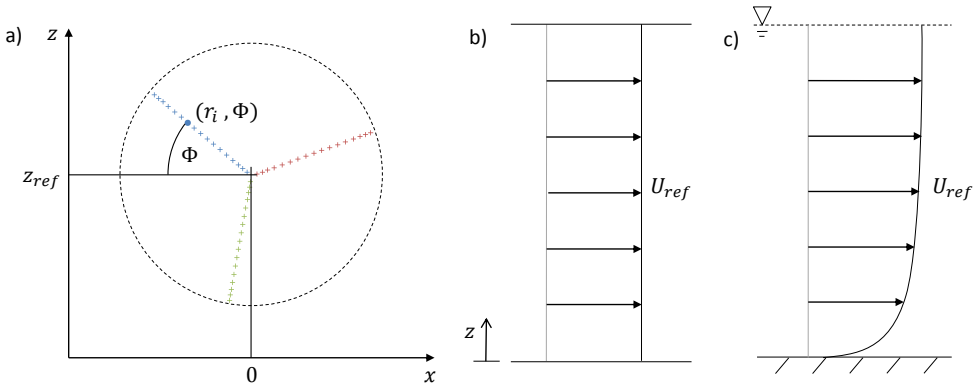

Figure 2.13: a) diagram of elemental coordinates at a given radius and azimuthal angle; b) uniform inflow velocity profile; c) non-uniform inflow velocity profile including viscous shear from a single boundary

2.7.2 1-D inflow velocity profiles

Figure 2.13 b and c show representations of two different 1-dimensional inflow profiles varying with vertical position. Various expressions are used to describe the velocity U at a specific element i. The most basic inflow profile is uniform, where a constant velocity is seen at all vertical positions, thus: $U_i = U_{ref}$.

Viscous effects from the presence of a single boundary, such as the seabed, cause a vertical velocity distribution. This can be approximated using a power law given by:

$$U_i = U_{ref} \left(\frac{z_i}{z_{ref}} \right)^{\zeta} \tag{2.87}$$

Where ζ is the exponential of the power law, taken as $\frac{1}{7}$ in wind turbine analyses; U_{ref} and z_{ref} are the velocity and corresponding height of the reference, usually taken as an average at the hub height (the turbine axis).

Here the influence of the free surface are not assessed, however it can be applied to BEMT as shown by Whelan et al. (2009). Additionally, the presence of any side walls are not taken into account, and therefore there are no x-direction variations.

2.7.3 Reynolds number

The Reynolds number can be given by the expression:

$$Re = LW/\nu \tag{2.88}$$

Where L is the characteristic length (m), W is the fluid velocity (ms^{-1}) and ν is the kinematic viscosity ($\mathrm{m}^2\mathrm{s}^{-1}$).

Considering flow in a test tank, the Re_{tank} uses a characteristic length being the smallest dimension of working cross section of the channel, and the average inflow velocity (U).

Considering the Reynolds number more localised to the blade, Re_{ch} can be calculated using the characteristic length taken as the individual element chord (c_i), which varies along the blade length. If the local fluid velocity over the section is considered, the effect of rotation can be included. This can be extended to using flow velocity over the elements that consider the changes in momentum (illustrated in Figure 2.8) to give:

$$W_i = \sqrt{(U_i(1-a_i))^2 + (\Omega r_i(1+a'_i)^2} \tag{2.89}$$

As this expression now depends on the elemental axial (a_i) and tangential (a'_i) induction factors, which are unknowns, the Reynold's number calculation needs to be incorporated into the iterative loop.

The chord based Reynolds number is therefore dependent on the elemental geometry (as a function of radial position), inflow velocity and rotational velocity. Lift and drag coefficient curves for particular Reynolds numbers are not always readily available and somewhat cumbersome to generate. In previous studies, a single Reynolds number is typically assumed, where the resultant velocity does not account for induction factors, such that:

$$Re = \frac{c_{75\%}\sqrt{(U)^2 + (\Omega_{peak} r_{75\%})^2}}{\nu} \tag{2.90}$$

Where the angular velocity Ω_{peak} is taken at optimal TSR; with $r_{75\%}$ and $c_{75\%}$ corresponding to a location 75% along the blade span. The effects of this approximation is minimal for overall rotor calculations, as the forces are averaged over the blades. However, when more detailed analysis of the blade variation forces is required, Reynolds numbers at each element is instead determined.

2.8 Numerical implementation

This section describes the structure of the BEMT code, built specifically to perform analysis of 'conventional' bare and ducted open centre TSTs. The model

is built using programming language Python, where blade element forces are resolved taking into account various correction factors.

2.8.1 Construction of the BEMT code

The BEMT equations are expressed in terms of two unknown induction factors a and a', and hydrodynamic coefficients of lift and drag, which are a non-linear function of the inflow angle. It is therefore necessary to solve these unknowns iteratively.

The general structure of the code as shown in Figure 2.14, is an iterative procedure in determining elemental, blade and rotor forces. The convergence criteria g is prescribed along with user defined tolerances and limits as a compromise between stability, running time, and solution accuracy. Initial input conditions are applied to encourage model initiation in the correct direction.

The framework of this model is based on a code previously developed by EDF R&D as part of its wind energy assessment project (Levy, 2013). The script was written in programming language Python, version 2.7 (van Rossum, 1995), and applied to a 5 MW horizontal axis turbine (Jonkman et al., 2009). It should be noted that the aim of this previous EDF study was to assess the applicability potential of the methodology to be coupled to an Finite Element Analysis (FEA) software, and therefore no validation or benchmarking with experimental data had yet been performed.

2.8.2 BEMT code for bare turbines

The classical BEMT code for conventional turbines uses the corrected axial force and torque expressions from Equations 2.78, 2.82 and 2.84.

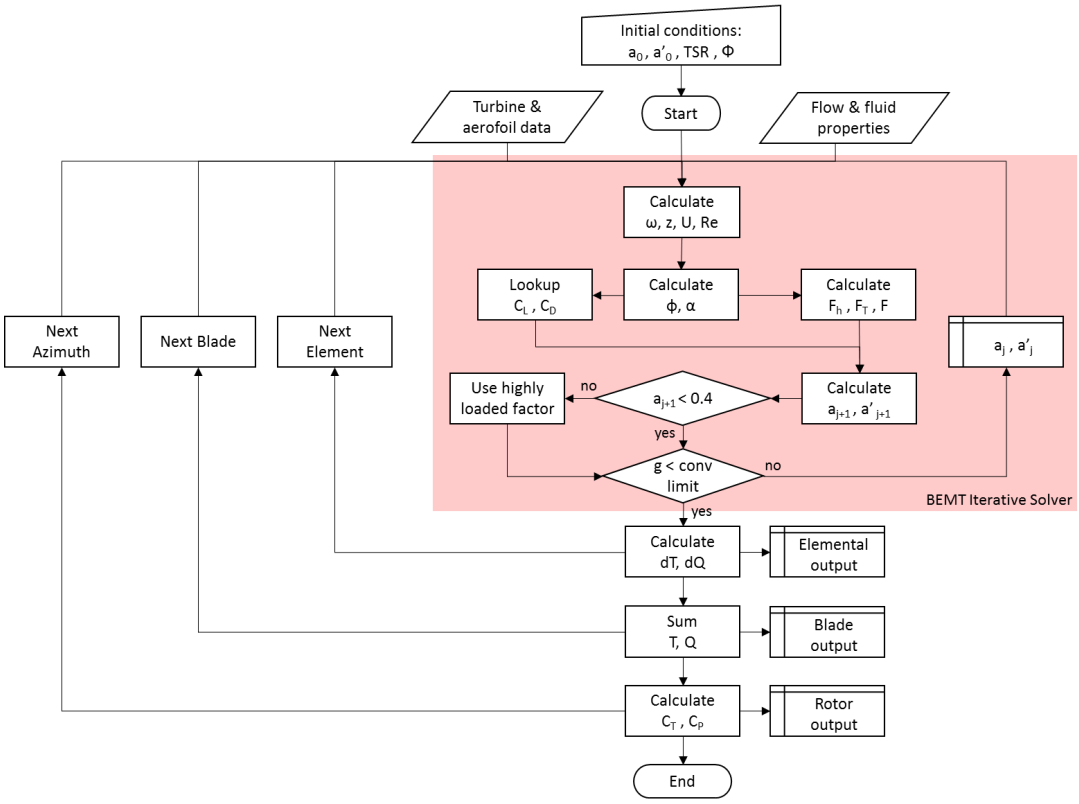

Figure 2.14: Construction flow diagram of the BEMT code

2.8.2.1 Basic iterative procedure

A basic method has been used by various codes detailed in the literature, including Bahaj, Molland, Chaplin and Batten (2007) where the iterative procedure is:

1. Set initial conditions, including a value for axial induction factors a and a′
2. Calculate the local flow angle
3. Lookup hydrodynamic coefficients C_L and C_D based on Re_{ch} and α
4. Calculate new induction factors a_{j+1} and a'_{j+1}
5. Assess if these are within convergence limits
6. Loop if step 5 is not satisfied, otherwise output blade forces.

It is useful to define a factor K to simplify the expressions, given by:

$$K = \frac{4F\sin^2(\phi)}{\sigma_r C_x} \tag{2.91}$$

And therefore it can be stated that:

$$\text{When } a_j < 0.4: \qquad a_{j+1} = \frac{1}{1+K} \tag{2.92}$$

For the highly loaded condition, a second order equation is obtained, which takes the positive root form to attain a real solution between 0 and 1, so that:

$$\text{When } a_j \geq 0.4: \qquad a_{j+1} = \frac{-B + \sqrt{B^2 - 4AC}}{2A} \tag{2.93}$$

$$\text{Where:} \qquad A = \left(\frac{K}{4F}\right)\left(\frac{50}{9} - 4F\right) - 1$$
$$B = \left(\frac{K}{4F}\right)\left(4F - \frac{40}{9}\right) + 2$$
$$C = \left(\frac{K}{4F}\right)\left(\frac{8}{9}\right) - 1$$

The new tangential induction factor is more simply:

$$a'_{j+1} = \frac{1}{\frac{4F\sin(\phi)cos(\phi)}{\sigma_r C_y} - 1} \tag{2.94}$$

2.8.2.2 Iterative function

The induction factors are deemed converged if:

$$|a_{j+1} - a_j|^* |a'_{j+1} - a'_j| \leq \delta |a_j a'_j| \tag{2.95}$$

Where $\delta = 1.0E-8$ is set as the convergence limit. Initial conditions are set as

per (Moriarty and Hansen, 2005), where:

$$a_0 = \frac{1}{4}\left(2 + \pi\sigma_r\frac{\Omega r}{U} - \sqrt{4 - 4\pi\sigma_r\frac{\Omega r}{U} + \pi\sigma_r\left(\frac{\Omega r}{U}\right)^2(8\beta + \pi\sigma_r)}\right); \quad a_0' = 0 \tag{2.96}$$

To avoid infinite loops, a maximum number of iterations is defined ($N_{itermax} = 1,000$). Generally, when iterations exceed this, cyclic behaviour of the induction factor is observed. In these occurrences, the last values are averaged.

2.8.3 BEMT code for ducted turbines

The BEMT code for ducted turbines is constructed from the corrected forms of axial force and torque given in Equations 2.80, 2.82 and 2.84. Duct parameters η_{34}, η_{34}, C_{p34} and C_{pb} are calculated from the empirical expressions in Equations 2.28- 2.31, given in Section 2.2.2.3.

2.8.3.1 Minimise function

An alternative method is to use an optimisation function, which was found to give higher stability convergence, particularly in the ducted BEMT model. An objective function defined in Matlab minimisation package $fmincon$ has been previously successfully applied in other codes (Masters et al. (2011); Shives and Crawford (2011)). The thrust and torque from each theory is considered equal, therefore convergence is achieved when $dF_{ax1} - dF_{ax2} = 0$ and $dQ_1 - dQ_2 = 0$. the minimisation value (g) combines these together to form:

$$g = [dF_{ax_1} - dF_{ax_2}]^p + [dQ_1 - dQ_2]^p \tag{2.97}$$

Where $p = 2$ is imposed to avoid convergence to an incorrect solution. The model then iterates for $g \to 0$. The *minimise* function within *SciPy* offers a

variety of optimisation algorithms, which can be selected based on the nature of the problem (SciPy Community, 2016). In this case, the *Sequential Least Squares Programming (SLSQP)* gives the best compromise between running time, convergence and operational constraints.

2.8.3.2 New equation forms

Rearranging Equation 2.80, the first term can be written:

$$dF_{ax_1} - dF_{ax_2} = \left(\eta_{02} + C_{pb} + (C_{p34} - \eta_{02})(1-a)^2\right) F \sin^2(\phi) - \sigma_r (1-a)^2 C_x \tag{2.98}$$

Incorporating the Buhl correction factor for highly loaded conditions, using Equation , 2.82, when $a \geq 0.4$:

$$dF_{ax_1} - dF_{ax_2} = \left(\frac{8}{9} + \left(4F - \frac{40}{9}\right) a + \left(\frac{50}{9} - 4F\right) a^2\right) \sin^2(\phi) - \sigma_r (1-a)^2 C_x \tag{2.99}$$

Similarly, torque can be expressed using Equation 2.84.:

$$dQ_1 - dQ_2 = 4a' F \sin(\phi) \cos(\phi) - \sigma_r (1 + a') C_y \tag{2.100}$$

It was found that if the exponential value is raised to $p = 4$, a higher stability is achieved in the convergence search. The iterative loop steps through the induction factors searching for equilibrium between the momentum and blade element theories. The higher stability is thought to occur with the larger exponent value due to smaller increments imposed when approaching equilibrium. This increases the number of steps taken to reach convergence, however does not noticeably affect the running time.

2.8.3.3 Convergence criteria

Sensitivity studies on convergence criteria gave the following optimal parameters: a maximum iteration limit was set to 1,000 and a tolerance for the value g of 1.0E-08. Boundary constraints were set to ensure that induction factors stay within reasonable limits, with tangential values being less than 0.5, and axial values between -0.8 to 0.8.

Chapter 3

Two-dimensional analyses of hydrofoil sections

This chapter presents an assessment of two numerical methods to analyse the hydrodynamic behaviour of two-dimensional hydrofoil sections. The overall aim of this work is to generate hydrodynamic coefficients of lift and drag of blade elements, which are used in BEMT calculations of TSTs in Chapters 4 and 5.

Blade forces are dependent on the hydrodynamic properties of the individual blade elements. These can be measured experimentally or generated using numerical models. Results from a panel code and RANS CFD are assessed, comparing accuracy, applicability and computational efficiency.

The main objectives of this work are: 1) identify limitations and sensitivities of the XFoil method that could impact application to different TSTs designs; 2) assess the accuracy and running time of the two numerical methods for standard NACA foil analysis; 3) assess the capabilities of the two numerical methods in the application of rounded edge flat plate foil.

3.1 Introduction

BEMT assumes changes in momentum are accountable solely from hydrodynamic forces on the blade elements, and as such relies on the hydrodynamic coefficients of lift and drag that are input into the model. This highlights the importance of attaining reliable data, as this will have a direct impact on the turbine performance predictions.

It has been found in one study comparing blade performance predictions generated using BEMT based programme GH Tidal Bladed, that uncertainty in results is largely due to uncertainties in the lift and drag data (Buvat and Martin, 2010). This is particularly influential in scale model tests due to the limited data availability of information at low Reynolds number flow conditions.

Foil characteristics can be measured experimentally or generated through various numerical methods.

3.1.1 Aerofoils vs hydrofoils

Aerofoils (operating in air) and hydrofoils (operating in water) are specifically shaped profiles designed principally to generate lift. The advancement of the aeronautical and automotive industries have greatly contributed to improved techniques for modelling aerofoil behaviour. Hydrofoil behaviour within the marine environment has been studied to a lesser extent, where methodologies have mainly developed for naval applications such as ship propeller design.

Lift and drag coefficients are non-dimensional values which can be used to determine the lift and drag forces that will be exerted on a foil under a specific set of operating conditions. They are a function of the Reynolds number, defined as the ratio of inertial to viscous forces. Although the kinematic viscosity of water is around an order of magnitude lower than air, the dimensions of hydrofoils in TSTs are smaller, and therefore Reynolds numbers are very similar to those seen

in wind turbines. This enables the use of two dimensional aerofoil analyses, for example in wind tunnel tests, within hydrofoil studies.

3.1.2 Foil design for TST application

A key parameter in foil design for general turbine applications concerns optimising lift to drag ratio, in order to maximise the productivity whilst minimising structural forces and bending moments. Turbine blades are then designed to have sufficient strength and stiffness properties to resist all operational loadings.

The nature of the operating environment means that the blade profiles of TSTs are quite different to those designed for wind applications. Wind turbine blades have strict design requirements in order to minimise weight. Whereas for TSTs, the focus shifts on to withstanding the higher forces associated with higher density fluid. This generally means that hydro foils tend to be much thicker at the roots. Additional considerations such as ease of manufacture and reliability are of high importance, due to the extremely high costs if a blade failure occurs.

3.1.3 Foil profiles

The National Advisory Committee for Aeronautics (NACA), has been developing aerofoils and analysing their behaviour since 1915, until their transfer to the National Aeronautics and Space Administration (NASA) (Abbott et al., 1945). A series of different foil profiles have been developed, with various geometric complexity and aerodynamic properties.

NACA foils are specified into different series, defined by the profile shape. A number of these are seen in the designs of test scale devices, such as the 4-series in Buvat (2011) and the higher complexity 6-series in Bahaj, Molland, Chaplin and Batten (2007). 6-series profiles are seen to be used in the design of full scale TST blades (McNaughton, 2013), however they vary more in terms of their thickness to chord ratios.

On the opposite end of the scale, profiles based on simple, symmetrical flat plate designs are less hydrodynamically efficient, but offer advantages in other respects, such as lower manufacturing complexity. These can also be incorporated into blade designs to negate the need for pitch or yaw systems, which simplifies the system design and has implications on overall turbine reliability.

3.2 Experimental wind tunnel tests

One method of generating lift and drag coefficient curves of aerofoils is through physical measurements in experimental wind tunnel tests. A large amount of aerofoil data has been collected experimentally and published in sources such as in reports from NACA (Abbott et al., 1945), which detail investigations in a low turbulence wind tunnel (Abbott and Von Doenhoff, 1959). These publications give useful information specific to a finite number of aerofoil types, geometries and Reynolds numbers. For example, experiments on a NACA 6-series profile is reported in NACA document 647 (Goett and Bullivant, 1939) for a Reynolds number of 3.4E+06.

Additional databases have been compiled investigating the effects of varying test conditions such as the Reynolds number, surface roughness and flow turbulence (Miley, 1982).

3.2.1 NACA 4-series reference experimental set-up

Reference measurements used to compare numerical model results are sourced from Timmer (2008), where experiments are performed at the Delft University Low-speed Wind Tunnel. Forces and moments are taken using a six component mechanical balance. A wake rake consisting of 12 static pressure tubes, with a reading accuracy of 2 Nm^{-2} is used to determine aerodynamic drag. The aerofoil model with a 0.25 m chord is constructed from milled steel, and spans the whole 1.8 m width tunnel, with a gap <0.5 mm at either end. A parasitic drag is induced,

caused by the interaction of flow over the wing with boundary layers formed by the walls of the tunnel section. As the small gaps essentially convert the 2-D model into a large aspect ratio wing, this drag can be calculated using wing theory along with the drag measured by the wake rake and balance. Standard wall corrections have been applied as per defined in the literature. Average turbulence intensity is recorded between 0.02 - 0.07 %.

3.2.2 Flat plate reference experimental set-up

The reference experimental data used to validate the numerical model results of flat plate foils is sourced from Munshi et al. (1999). This details a study aimed to assess the effects on aerodynamic performance of attaching rotating cylinders to the ends of flat plate aerofoils. The cylinders at each end rotate in order to influence the boundary layer attachment with the aim of reducing aerodynamic drag. A control experiment where the cylinders are stationary provides a case which is essentially a flat plate aerofoil with rounded edges, of interest for TST applications.

The aerofoil model has a t/c ratio of 0.27, which is installed in a low speed, low turbulence wind tunnel at an ambient turbulence intensity below 0.1%. The test piece is fitted with end plates, and spans the entire 2.9 m tunnel section to create a 2-D condition. The foil is supported by an Aerolab six-component strain gauge balance. Pressure distributions were recorded using a 48 channel pressure transducer, with a reported accuracy of 2.54E-03 mV/N/m^2. A large range of angles of attack is assessed, from $0° \rightarrow 90°$ at increments of between 5° and 10°. The tunnel has a cross section of 0.91 x 0.68 m, however due to the reported complex nature of the experimental set-up, a correction factor to account for flow interactions of the walls is not applied Munshi et al. (1999), and therefore results are presented in their uncorrected form. Tests were performed at a relatively low $Re_{ch} = 3.0E + 04$.

3.3 Numerical analysis of NACA foils using XFoil

In this section, a procedure for generating lift and drag curves of foils using XFoil is described. The application of associated pre processing tools is also illustrated.

Although analyses have been performed on many different NACA profiles within this thesis, the results reported here are limited to a 6-series profiles under the designation NACA63_3-4xx. This type of hydrofoil is incorporated into the design of the TGL 1 MW turbine (Gretton, 2010) and therefore represents a real TST case. A sensitivity analysis is presented to test the dependence of lift and drag predictions on various model input parameters.

3.3.1 Panel code with viscous model

Various numerical programmes are available to predict (and optimise) the performance of foils at given Reynolds and Mach numbers. One popular example used in engineering studies of wind turbines, and more recently in tidal turbines (Bahaj, Molland, Chaplin and Batten, 2007), is the Fortran based programme XFoil (Drela, 1989). Developed by MIT, this is an analytical tool for subsonic flow around isolated foils.

The programme consists of a number of routines which calculate the pressure distribution on the aerofoil surface, which are then used to determine the lift and drag forces as a function of angle of attack. The model combines the linear vorticity stream function panel method with a viscous boundary layer and wake model. Both laminar and turbulent boundary layers are solved simultaneously with transition equations, using a global Newton method.

Details of the method, along with design procedure examples can be found in Drela (1989), with application studies for example in Timmer and Bak (2013).

3.3.2 XFoil set-up

Coordinate data files are read into the model and a smoothing function is used in order to 'clean up' the distribution of coordinate points. This is achieved using a Hanning filter which operates globally and aims to alleviate any noise present due to geometrical imperfections on the foil surface (Drela and Youngren, 2001).

Analyses are restricted to high Reynolds numbers from 1.0E+05, below which the model is found to become unstable and cannot generate repeatable results. Additionally, when assessing extreme angles of attack, separation of the boundary layer occurs and the algorithm fails to converge. This can be improved to an extent by increasing the iteration limit, however this only delays the onset of convergence issues. The limits found in this study occurred around $\alpha = \pm 20^{\circ}$ with an angle stepping interval of 0.25°.

A value to represent the ambient disturbance level of the operating environment 'Ncrit' also needs to be selected. A value of NCrit=3 is chosen as representative of applications in water tanks and for propellers operating in water (Drela, 1989).

3.3.3 Sensitivity analysis

Various studies using different flow parameters have been performed in this thesis in order to better understand the influence of certain parameters on the hydrodynamic characteristic predictions.

3.3.3.1 NACA 6-series geometry

NACA 6-series foils are designated by a six digit number which represents the shape characteristics. The NACA63_3-418 has the following profile characteristic designation (in order of appearance): 6 denotes the series; 3 represents the chord wise position of minimum pressure in tenths of chord from the leading edge as a reference; $_3$ signifies the range of lift coefficient in tenths above and below

the design in which favourable pressure gradients exist on the upper and lower surfaces; −4 represents the design lift coefficient in tenths and finally the 18 indicates the thickness as a percentage of the chord. Additionally, the mean line is designated with a, which indicates the percentage of the chord which experiences uniform pressure distribution. However if this is not specified then it is understood that the uniform-load mean line (a=1) is used (Abbott et al., 1945).

Foil contours are specified by defining two sets of x-y coordinates corresponding to the upper and lower surfaces, and typically normalised against blade chord. XFoil has an in built database of coordinates which can be called within the programme, however does not include NACA 6 series data. These ordinates can be obtained from texts such as Abbott et al. (1945), or more recent on line databases such as UIUC Applied Aerodynamics Group (2015) compiled by the University of Illinois.

3.3.3.2 Reynolds number

In standard chord based Reynolds number calculations, there are some simplifications made to reduce the number of analyses required. Typically, single values of chord, inflow velocity, rotational velocity, fluid temperature are assumed. The Reynolds number then depends on what values are assumed. Within the literature, different sources quote Reynolds numbers for TST applications at: 3.0E+06 (Gretton, 2010), 5.0E+06 (Evans et al., 2013), above 5.0E+06 (Whelan and Stallard, 2011) and as high as 1.1E+07 (Buvat and Martin, 2010).

The comparative study of these Reynolds numbers is shown in Figure 3.1. The non-symmetrical profile of the foil causes a lift force seen at $\alpha = 0°$. There appears to be little difference in the linear lift predictions at low angles of attack ($-7° < \alpha < 7°$). However outside of this region, there is a higher dependency on the Reynolds number. At $\alpha = 20°$, increasing the Re by an order of magnitude from 1.0E+06 to 1.0E+07 results in an increase in C_L of 0.36 (25.1%), and a reduction in C_D of 0.05 (47.0%). It can also be observed that linear changes in Reynolds number results in non-linear changes in lift and drag.

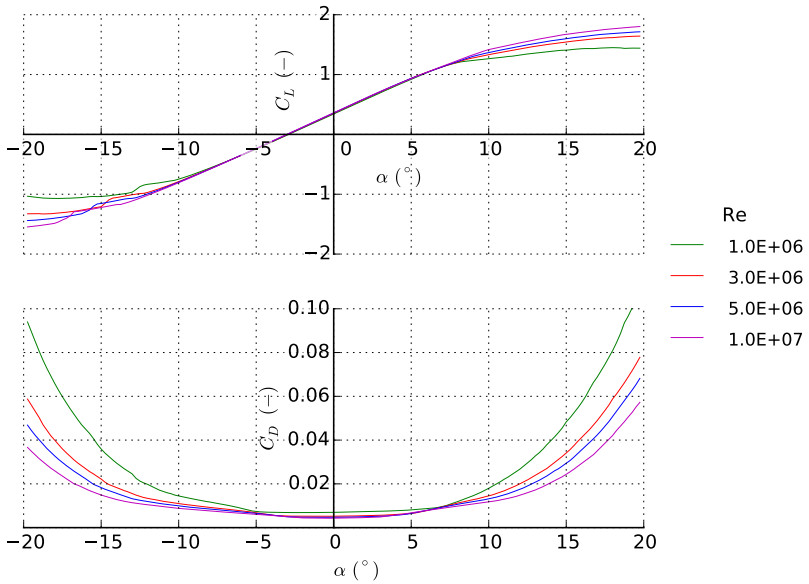

Figure 3.1: NACA63$_3$-418 hydrofoil coefficient curves of lift (top) and drag (bottom), generated with XFoil at various Reynolds numbers

3.3.3.3 Ncrit

The programme treats both laminar and turbulent layers with an e^n amplification formulation, which is used to determine the point of transition. Further explanation is given in XFoil documentation Drela (1989). This has a user specified parameter 'Ncrit' which describes the log of the amplification factor that induces transition. This value is dependent on the ambient disturbance level of the operating environment of the foil with the following recommended values for specific applications (Drela and Youngren, 2001): sail plane 12 - 14; motor glider 11 - 13; clean wind tunnel 10 - 12; average wind tunnel 9; dirty wind tunnel 4 - 8. A sensitivity test shown in Figure 3.2 indicates a very small impact on the lift coefficients, with a slightly higher effect on drag.

3.3.3.4 Source of ordinate points

There are multiple sources of coordinate data, and a study was made to observe if any disparity lies in the different datasets. Inspection of hydrofoil coordinates

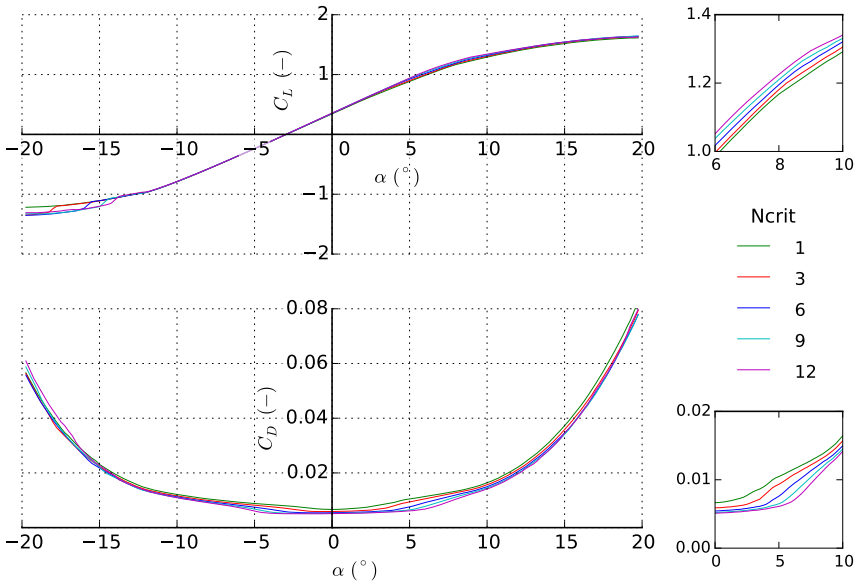

Figure 3.2: NACA63_3-418 hydrofoil coefficient curves of lift (top) and drag (bottom), generated with XFoil at Re=3.0E+06 with various values of Ncrit

from two different sources: the UIUC Applied Aerodynamics Group (2015) database and an older paper Abbott and Von Doenhoff (1959). Although the dataset from UIUC contains many more points, it can be seen that there is negligible difference in the predicted lift and drag coefficients. This shows little sensitivity or a good functionality of the smoothing filter.

3.3.4 3-D stall and extrapolation

As XFoil calculations and experiments are based on 2-D static wind tunnel measurements, the 3-D nature of flow due to the rotation of the blade is not accounted for. In reality, radial forces in the fluid induce a Coriolis Effect, acting in the direction of the trailing edge which effectively delays the onset of boundary layer separation. This delayed stall phenomenon varies as a function of chord and radius, and can be accounted for by applying a Du-Selig (Tangler and Selig, 1997) model to the lift coefficients, and an Eggers (Hansen 2004) adjustment to the drag. Further details on the theory can be found in Appendix 2.

Analysing angles of attack exceeding the point of stall is beyond the capabilities of XFoil, however can be approximated using an extrapolation function as proposed by Viterna and Janetzke (1982). The NREL 'AirfoilPrep' python routine (Ning, 2013) is used to apply these functions.

3.3.4.1 Application of corrections to XFoil predictions

The Du-Selig method within AirfoilPrep requires a number of user specified parameters which are taken as single values: Element radius ratio ($r/R = 0.75$); element chord to radius ratio ($c/r = 0.15$) and tip speed ratio ($TSR = 5$). The Viterna extrapolation also uses the hydrofoil aspect ratio (R/c), where the chord is taken at 75% down the length of the blade.

2-D XFoil generated lift and drag data in the range of $\pm 20°$ are extrapolated to $\pm 180°$. Also 3-D corrected and subsequently extrapolated as shown in Figure 3.3. Generally across the entire range, the effects of the 3-D correction are relatively small. The gradients of linear lift are very similar, but as the foil approaches stall, the largest difference can be seen. The 3-D correction increases C_L by 0.13 (7.7%) and C_D by 0.029 (37%) at $\alpha = 20°$. It is noted that the stall delayed effects only appear to increase the magnitude of lift and drag, but does not impact the angle at which stall occurs.

After the stall conditions, the extrapolation function approximates a C_L curve which gradually tends to zero at $\alpha = \pm 90°$. The C_D curve slopes upwards to a peak at $\alpha = \pm 90°$ and takes the approximate form of a sine wave.

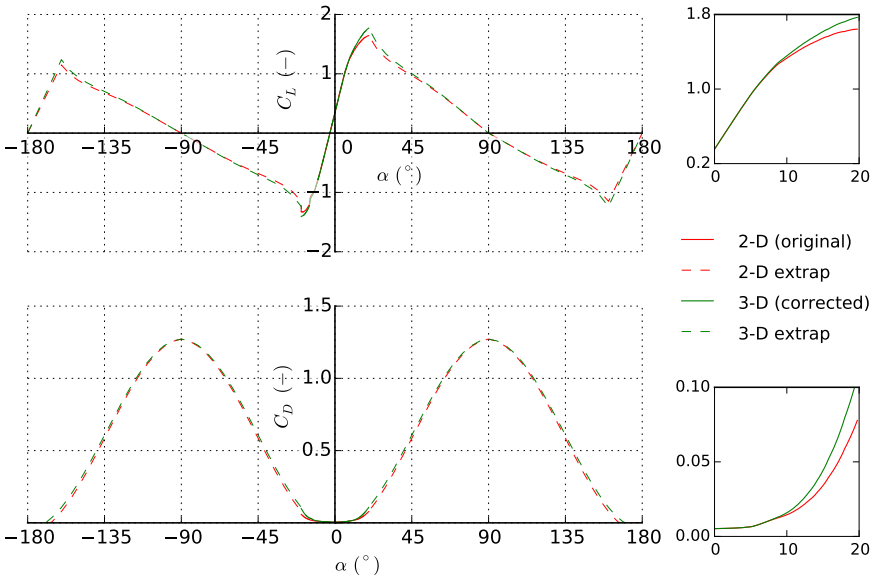

Figure 3.3: NACA63$_3$-418 hydrofoil coefficient curves of lift (top) and drag (bottom) generated with XFoil at Re=3.0E+06, with and without 3-D correction and extrapolation functions applied

3.3.5 High thickness ratio foils

A 'generic' TST is defined in the ReDAPT project to enable comparisons of a standardised design as a reference (Gretton, 2010). The full scale rotor design is a 3 bladed, horizontal axis, pitch controlled rotor designed and manufactured by Alstom TGL. The device is rated at 1 MW at 2.5 ms^{-1} current flow, has a rotor diameter of 18 m, with blades of a NACA63$_3$4xx hydrofoil profiles. The thickness to chord (t/c) ratios vary down the blade length from 0.18 to 0.55. This study has identified a limited availability of data in the literature specifically for thicker profiles, with coefficients only available for the NACA 6-series up to t/c = 0.21 (Ingram, 2012). Due to a lack of data, studies typically assume a constant foil section of t/c=0.18 throughout the entire blade length (Gretton, 2010).

Coordinate points of thicker foils are also not available in standard aerofoil databases. A Fortran code 'NACA546' (Ladson et al., 1996) developed by NASA in the 1970's can be used to generate ordinates of any thickness, thickness

distribution and camber in the NACA series. This was used to generate coordinates for t/c from 18% to 55%, which are illustrated in Figure 3.4.

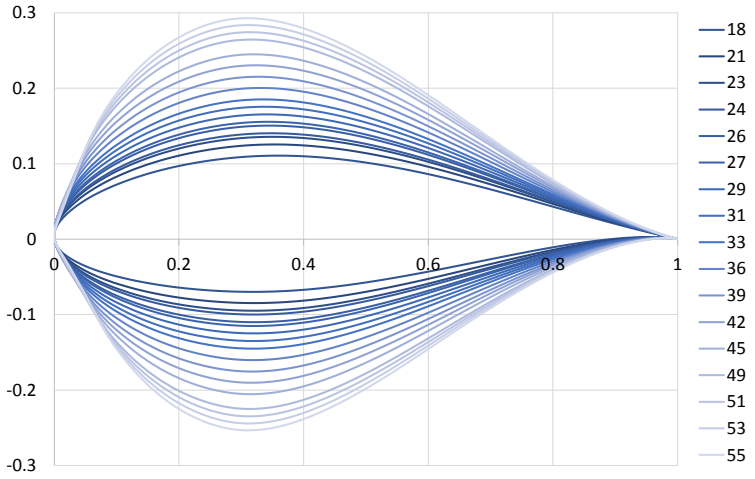

Figure 3.4: Normalised NACA63$_3$4xx hydrofoil geometry for t/c ratios from 18 - 55%

The ordinate data files are imported into XFoil as before, and computations run to determine the lift and drag coefficient curves. These are shown in Figure 3.5.

For small increases in thickness, (t/c $\leq$0.31) the gradient of the linear lift section remains almost constant and there is little change in the drag at low angles of attack. After $\alpha = 10°$, a drop in the lift is seen, and increase in the drag. At $\alpha = 20°$ for t/c = 0.31, C_L reduces by 0.04 (24%) and C_D increases by 0.03 (38%), comparing against t/c = 0.18. This seems reasonable, as the foil surfaces are steeper and thus are less hydrodynamically efficient.

Extending to greater thickness ratios (0.31<t/c$\leq$0.39) the gradient of linear lift become less steep, peaking at a lower value. It also seems that the foil is entering stall, which is beyond the capacity of XFoil to accurately predict.

Extreme thickness foils (t/c $\geq$ 0.4) exhibit significantly different hydrodynamic properties, where lift is positive at negative angles of attack, and drag curves experience large jumps in magnitude. This is due to the higher amounts of boundary layer separation, as the leading edge surfaces become steeper and the foil

behaves more like a cylinder. Clearly the fluid dynamic behaviour is considerably different for these thicker foils, and is thought to depend heavily on dynamic effects from boundary layer separation. It was noted that the stability of convergence is significantly reduced in the simulations, suggesting that the code struggles to effectively predict the surface pressure distribution under these conditions. Due to restrictions in the model under these conditions, these predictions are thought to be non physical, highlighting a limitation of the method.

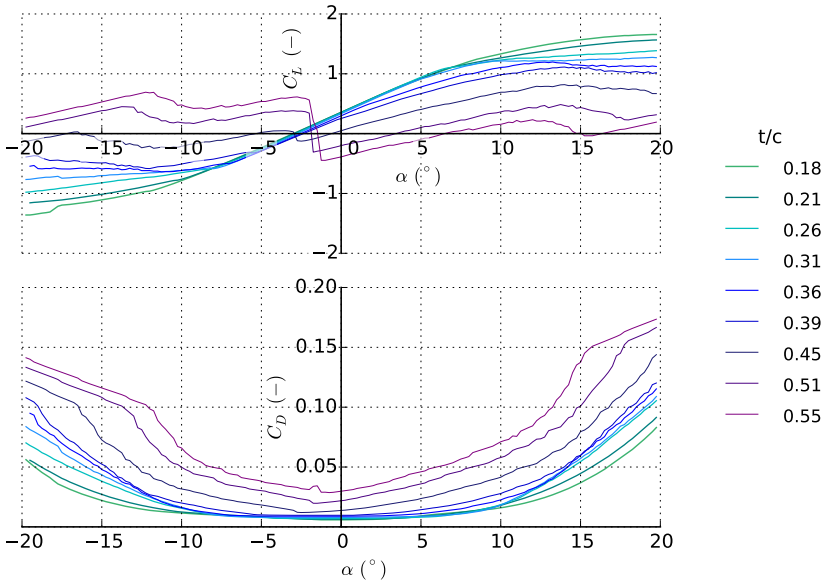

Figure 3.5: NACA63$_3$-4xx hydrofoil of varying t/c ratio coefficient curves of lift (top) and drag (bottom), generated with XFoil at Re=3.0E+06

This study suggests that thickness does have a large influence on the foil hydrodynamic properties, which could lead to large impacts on the TST blade performance. However, limitations in the XFoil model mean that these cannot be represented accurately, and therefore an alternative method is recommended.

3.4 CFD analysis of NACA aerofoils

This section details the development of a 2-D RANS CFD model of a conventional aerofoil based on a NACA0018 profile. The aim is to compare numerically derived

lift and drag curves from CFD and XFoil against wind tunnel experimental measurements. These comparisons are used to assess the accuracy of each method compared with the computational demand. Dependency studies on CFD parameters such as mesh size and time step length are additionally performed.

3.4.1 Computational Fluid Dynamics

CFD is a highly sophisticated and high fidelity tool that can be used to perform detailed aerodynamic and hydrodynamic analyses. This methodology gives the user an insight into complex flow behaviour that are beyond the capabilities of the BEMT model, and provide a better understanding of physical processes that are difficult and expensive to measure experimentally.

Code_Saturne is a CFD software which is used to simulate turbulent and laminar flows in both 2-D and 3-D complex geometries (Archambeau et al., 2004). The code has been developed by EDF R&D since 2000, where it was initially used for nuclear applications. It has been made available since 2007 under an open source licence, and is now a well known industrial standard tool used in a wide range of engineering applications. This is seen in the annual user meetings (such as Code_Saturne (2014)) where industrial test cases provide continuous model validation and improvements to the code robustness.

The code solves the Navier Stokes equations for an incompressible viscous fluid using various turbulence models. Spacial discretisation is performed using a finite volume method through structured or unstructured meshes.

3.4.1.1 Governing equations

Here, the governing Navier-Stokes equations and main CFD methods into solving these are presented, where full derivations can be found detailed in fluid dynamics texts (such as Kundu and Cohen (2002)), where specific information regarding the *Code_Saturne* code found in its dedicated theory manual EDF R&D (2015).

The Navier-Stokes equations are based on formulations for the conservation of mass and momentum. For a compressible fluid, the continuity equation is given by:

$$\frac{\partial \rho}{\partial t} + \frac{\partial}{\partial x_i}(\rho u_i) = 0 \tag{3.1}$$

where u_i is the fluid velocity in tensor form. Conservation of momentum using Newton's second law yields:

$$\frac{\partial}{\partial t}(\rho u_i) + \frac{\partial}{\partial x_j}(\rho u_i u_j) = \rho f_i - \frac{\partial p}{\partial x_i} + \frac{\partial}{\partial x_j}(2\mu S_{ij}) \tag{3.2}$$

Where f_i is the force on the body per unit mass, p is the fluid pressure, μ is the dynamic viscosity and S_{ij} is the viscous strain rate, given for a Newtonian fluid by:

$$S_{ij} = \frac{1}{2}\left(\frac{\partial u_i}{\partial x_j} + \frac{\partial u_j}{\partial x_i}\right) \tag{3.3}$$

3.4.1.2 Reynolds Averaged Navier-Stokes

Fluid dynamics problems often involve turbulence, which exist in almost all natural flows. The chaotic nature of turbulent flow leads to complex and rapid variations of a velocity field in space and time. The Navier-Stokes equations as defined above can be solved using Direct Numerical Simulation (DNS), which resolves all length scales (temporal and spatial). This usually requires a very fine mesh and small time-steps, leading to extremely high computational times which are not suitable for the majority of engineering applications (Leroy, 2015). Other methods include the use of turbulence models, which remove the need to solve all flow scales. Large Eddy Simulation (LES) and Detached Eddy Simulation (DES) methods use a filtering approach which is less computationally intensive. However these are, at present, considered too costly for industrial applications (Baker, 2009), particularly in complex geometries.

As a compromise between accuracy and computational time, a Reynolds Averaged (RANS) approach has been developed. The highly variable turbulent flow field can be time averaged to present a less variable mean. Therefore the instantaneous velocity can be decomposed into a mean and a fluctuating component such that:

$$u = U + u' \tag{3.4}$$

where: $U = \overline{U}$ is the mean velocity and u' is the fluctuating velocity component, where $\overline{u'} = 0$. The RANS equations are obtained by decomposing the velocity field within the Navier-Stokes equations into the mean and instantaneous values, then taking the time average. Full derivations can be found in Kundu and Cohen (2002). One consequence of this averaging is the incorporation of a Reynolds-stress tensor:

$$\tau_{ij} = \rho\overline{u_i' u_j'} \tag{3.5}$$

Which represents the stresses on the mean flow from the turbulent fluctuations. This would require a further six transport equations to provide closure to the Navier-Stokes equations, which are obtained through applying a turbulent model, of which there are numerous solutions proposed.

3.4.1.3 Turbulence modelling

This study does not provide an investigation into the different types of turbulence model available, where the reader is directed to studies such as (El-behery and Hamed, 2009) for more detailed information. Rather, the two-equation Shear Stress Transport (SST) model is employed as proposed by Menter (1994) for turbulent closure. This model has shown improved predictions compared with standard $k - \varepsilon$ models for flows with strong adverse gradients and boundary layer separation. For this reason, it is typically used for two-dimensional bluff body problems (such as Baker (2009)) and in tidal industry applications (such

as McNaughton (2013) and Mercier (2014)), therefore was considered a suitable selection for this case.

A brief formulation of the two equation model can be found in Appendix 3, Section 1.

3.4.1.4 Simulation parameters

To solve the Navier-Stokes equations spatially, a mesh of volumetric elements is constructed. The 'quality' of the mesh refers to various geometrical properties of elements, such as the orthogonality (skewness) and aspect ratio.

Walls where the velocity tends to zero are known as no-slip boundaries, which increases the production of turbulence through viscous shear effects. This is a critical region where a higher level mesh control is required to correctly model the large velocity gradients associated to the boundary layer. In the case of flow around a 2-D foil, the large influence of boundary layer separation means that the treatment of the viscous sub layer is of high importance. Sufficient representation can be ensured by using a dimensionless wall distance, given by the equation:

$$y^+ = \frac{u_* y}{\nu} \tag{3.6}$$

Where u_* is the friction velocity at the wall and y is the vertical height of the first cell nearest the wall. The mesh is constructed so as to achieve certain y^+, based on the flow problem to be solved and turbulence model selected.

The Courant, or Courant-Friedrichs-Lewy (CFL) number is used to assess appropriate time-step lengths, and is given by:

$$CFL = \frac{u\Delta t}{\Delta x} \tag{3.7}$$

Where Δt is the time step and Δx is the length interval.

3.4.2 CFD simulation parameters

3.4.2.1 Geometry

The NACA0018 aerofoil is a 4-series NACA symmetrical foil, with a thickness to chord ratio of 0.18 located 30 % down the length of the chord (Jacobs et al., 1935). The overall geometry is detailed in Table 3.1.

Table 3.1: NACA0018 aerofoil overall geometrical parameters

Parameter	Value	Units
Chord	3.7	m
Thickness	0.67	m
Span	0.1	m

The geometry is constructed in SALOME (version 7.5.1), using coordinates of the suction (top) surface based on the following equation (Jacobs et al., 1935), which is then mirrored to construct the pressure (bottom) surface:

$$y(x) = \left(0.18\left(\frac{c}{0.2}\right)\right)\left[0.2969\sqrt{\frac{x}{c}} - 0.126\left(\frac{x}{c}\right) - 0.3516\left(\frac{x}{c}\right)^2 + 0.2843\left(\frac{x}{c}\right)^3 - 0.1015\left(\frac{x}{c}\right)^4\right]$$

x is the horizontal coordinate from 0 to the chord length, where 500 divisions are prescribed, selected to produce a sufficiently smooth curve, shown in Figure 3.6. The trailing edge condition is not specified within this coordinate equation, and is user prescribed. Studies typically analyse one of three conditions: sharp point, flat chamfer or rounded edge. As the boundary layer separation is initiated in this region, the condition of the trailing edge is expected to have an influence on the aerodynamic forces. In reality, the process of constructing a TST blade from composite layers would mean creating a pointed or flat edge would be physically restricted. Therefore the most logical profile was assumed to be rounded, which

was selected as the more physically realisable solution. This is applied as a semicircle as shown in Figure 3.6.

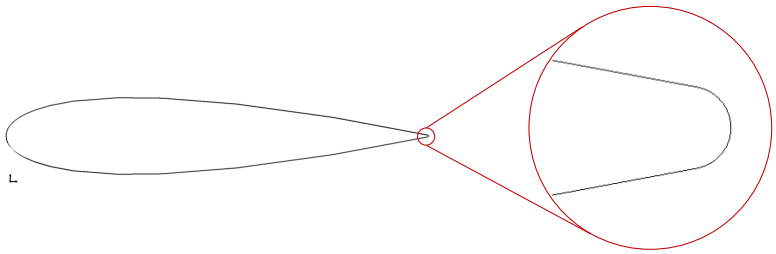

Figure 3.6: NACA0018 aerofoil geometry, with magnification on the trailing edge

3.4.2.2 Mesh construction

An 'O-type' structured mesh is constructed in Salome, using 3-D volumetric rectangular section elements (hexahedrons), with a single cell thickness. Higher densities of smaller elements are localised around areas where more detail is required, which then increase in size towards the domain exteriors in order to reduce the computational time. The aerofoil surface is discretised to achieve an even distribution of radial elements, and an exponential growth rate ensures higher resolution towards the foil surface to better capture the complex interactions around the boundary layer. The trailing edge is also discretised to achieve a higher element density, where flow entrainment from the suction and pressure surfaces occurs. The aerofoil mesh at 0° is shown in Figure 3.7.

3.4.2.3 Boundary conditions

In order to test different angles of attack, the aerofoil mesh is merged within a circular 'control mesh', which is then merged within a 'tunnel mesh', representing the conditions of a wind tunnel. The outer circle of the control mesh is radially discretised into 360 sections which matches with the circular cut out section in the tunnel, enabling conformal merging between the interfaces for each integer angle of attack. Meshes for α=0° and 30° are shown in Figure 3.8.

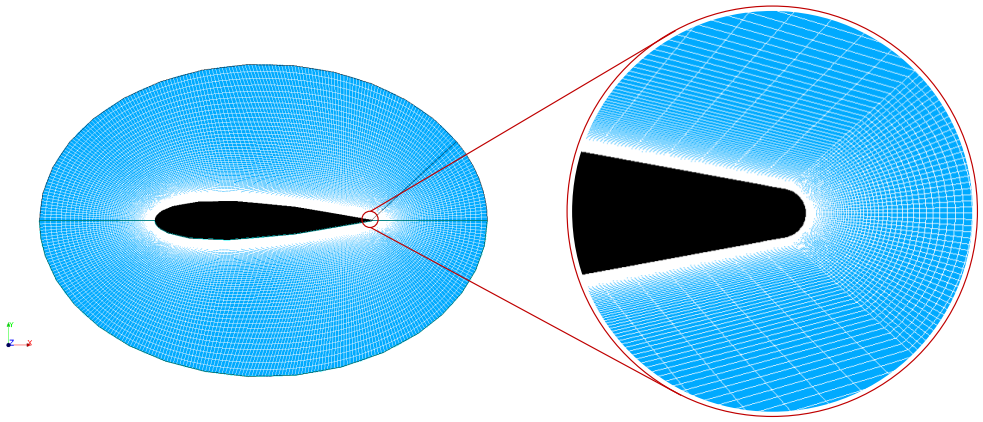

Figure 3.7: NACA0018 aerofoil mesh, with magnification on the trailing edge

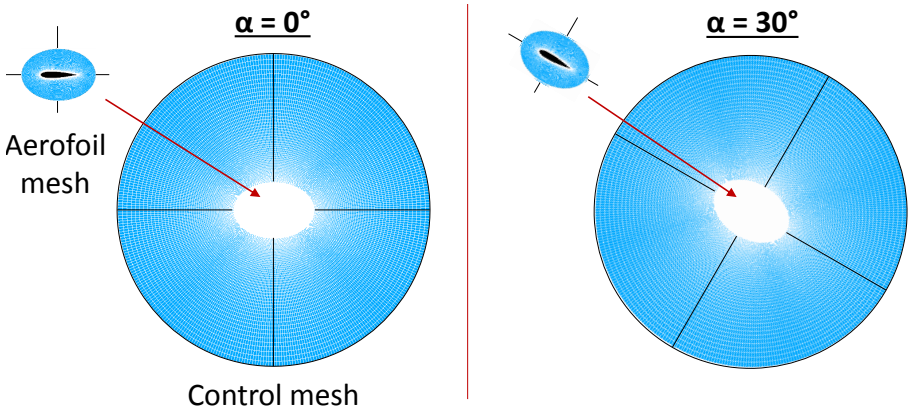

Figure 3.8: NACA0018 aerofoil and control meshes for α=0° and α=30°

The overall domain is shown in Figure 3.9. The flow at the inlet is of constant uniform profile in the direction normal to the boundary, located ∼13 c (where c is the chord length) upstream of the foil. A constant pressure gradient is selected for the outlet boundary condition located ∼50 c downstream. Top and bottom boundaries are also situated ∼13 c distances away. These are sufficiently far away to ensure established flow with no influences from boundary presence, similar to analysis from the literature (e.g. Yao et al. (2012)). To represent a 2-D flow, all surfaces including front, back and sides are prescribed with symmetrical boundary conditions. A smooth 'no-slip' wall condition is applied to the aerofoil surface.

The interfaces for the aerofoil to control mesh, and control to the tunnel mesh are fully merged.

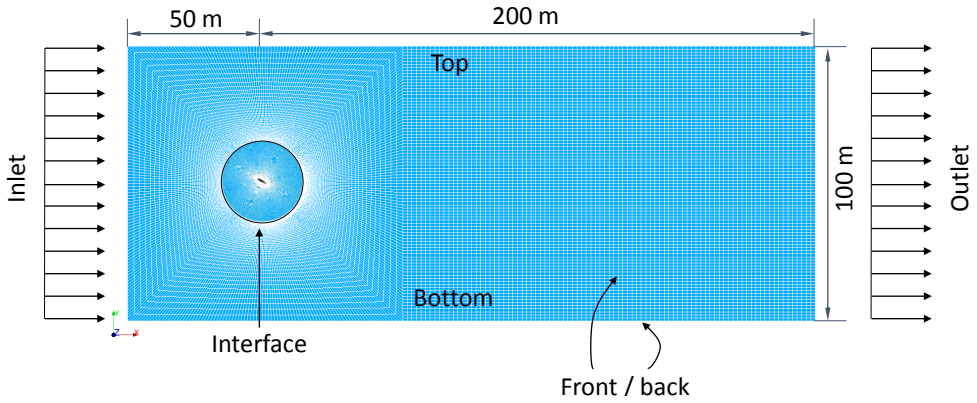

Figure 3.9: NACA0018 aerofoil complete mesh set up, indicating domain size and surface labels

3.4.2.4 Code_Saturne simulation set-up

This study uses EDF in-house developed and open source CFD suite *Code_Saturne* version 4.0.3 (Archambeau et al. (2004), EDF R&D (2015)). The fluid properties are detailed in Table 3.2. A RANS kω-SST turbulence model is selected for all cases. Default settings conserved in the model include solver precision of pressure, velocity, k and ω set to 1.0E-08, and extrapolation of pressure gradient on domain boundary set to Neumann 1st order. Simulations use an unsteady flow algorithm where an upwind scheme is selected, found to give better overall convergence than when using a centred scheme.

Table 3.2: NACA0018 test: fluid flow properties

Parameter		Value	Units
Density	ρ	1.17862	kgm^{-3}
Dynamic viscosity	μ	1.83E-05	$\mathrm{kg(ms)}^{-1}$
Inlet velocity	U	4.2	ms^{-1}
Reynolds number (chord)	Re_{ch}	1.0E+06	-
Turbulence intensity	TI	0.05	%

3.4.3 Dependency studies

3.4.3.1 Mesh independence study

In order to reduce the dependence of aerofoil forces on the mesh size, a convergence study is performed using different numbers of elements within the domain. Table 3.3 shows the lift and drag coefficients from 4 meshes from 35,000 to 700,000 elements, at an angle of attack $\alpha = 20°$. The Δ values describe the coefficient range over the final few timesteps, as there are small fluctuations seen in the aerodynamic forces.

Table 3.3: NACA0018 mesh convergence study results

Mesh	Elements	y^+	C_L	ΔC_L	C_D	ΔC_D
m1	35,100	1.77	1.019	0.027	0.345	0.000
m2	91,900	0.93	0.932	0.102	0.359	0.021
m3	283,200	0.92	0.914	0.081	0.353	0.016
m4	702,800	0.91	0.901	0.076	0.351	0.016

It can be seen that results appear converged around mesh 3, which is selected as a good compromise between accuracy and computational time. This mesh has quality values of: skewness $< 45°$, aspect ratio < 40 at the leading edge and < 10 at the trailing edges; and a critical zone $y^+ \sim 1$ at $\alpha = 0°$ rising to a maximum of 2.8 at $\alpha = 20°$.

3.4.3.2 Time step convergence

Figure 3.10 shows the temporal variation of lift and drag for different time-steps, at a fixed $\alpha = 15°$. All the results converge approximately at a $C_L = 1.22$ and $C_D = 0.069$, however the largest time-step (with a corresponding final Courant number ~ 200) is seen to experience low amplitude, high frequency oscillations throughout the simulation. At the initiation stage, there also appear to be small instabilities. This is a due to the time steps being too large to allow forces to be effectively resolved, where all other curves show smoother transitions and

no oscillations. Reducing the time-step reduces the initial overshoot and the time taken for convergence to be achieved, however also increases the simulation running times. As a compromise, time-steps between 1.0E-03 and 5.0E-04 s are taken as the optimal, with a corresponding Courant number of ~ 20. Here, only one angle of attack is assessed, which may not necessarily be the optimal at other angles to be analysed.

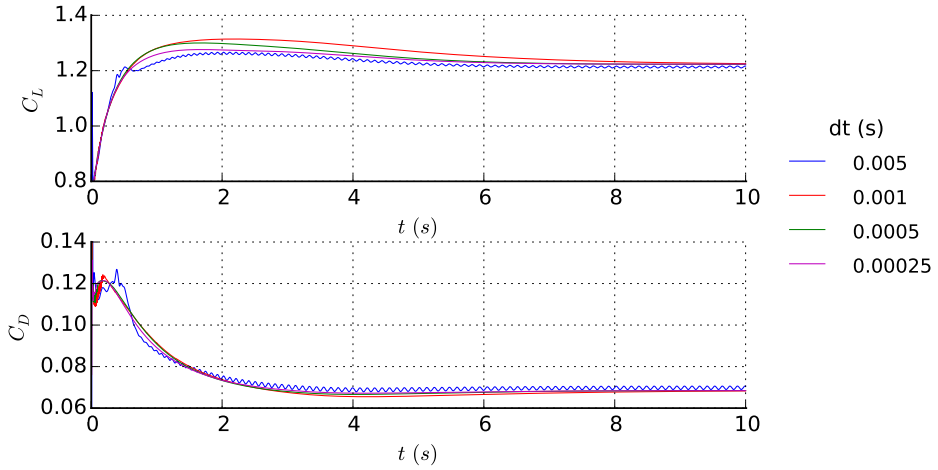

Figure 3.10: NACA0018 aerofoil coefficients of lift (top) and drag (bottom) variation with time (t), generated from RANS CFD at Re_{ch}= 1.0E+06, comparing different time step values (dt) at $\alpha = 15°$

3.4.3.3 Turbulence model testing

A test was performed to compare the temporal lift and drag predictions from various turbulence models, where results are presented in Appendix 3, Section 2. This shows some dependency on the selection of turbulence model, however a more in depth analysis with separate meshes would be required to make a full comparative assessment.

3.4.4 Code_Saturne results

3.4.4.1 Temporal variations

Figure 3.11 shows the temporal variation of lift and drag at fixed angles of attack from 0° to 30° at 5° increments. It can be seen that for $\alpha < 25°$, smooth convergence to a steady state is achieved within 15 s. At $\alpha \geq 25°$, significantly different profiles are seen at the initiation, signifying a difference in behaviour of the flow around the aerofoil associated to higher angles of attack. A maximum steady lift coefficient occurs at $\alpha = 15°$, after which the blade stalls and a reduction is seen along with a step increase in drag. Regular oscillations also develop as the simulation progresses. At $\alpha = 30°$, these oscillations reduce in amplitude, however do not level out completely within the simulation time.

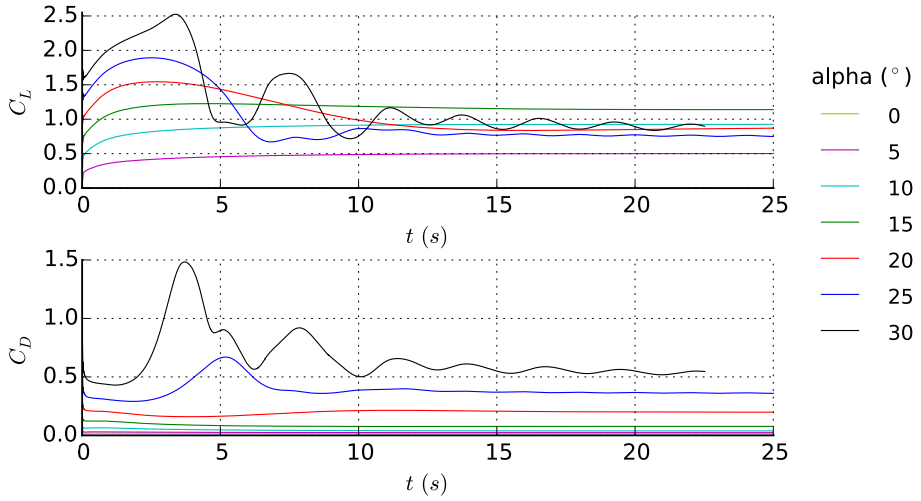

Figure 3.11: NACA0018 aerofoil coefficients of lift (top) and drag (bottom) with time (t) at Re_{ch}= 1.0E+06, for different angles of attack

3.4.4.2 Flow field analysis

Figure 3.12 shows the flow velocities and pressures around the aerofoil at a time t = 20 s. It can be seen that the pressure contours become larger on both the suction and pressure surfaces from $0° \leq \alpha \leq 15°$, which results in increased lift.

At $\alpha = 15°$, the section reaches a suction peak. When this is exceeded the foil enters the stall regime, whereby the boundary layer starts to separate from the suction surface, reducing the area of negative pressure in this zone and thereby decreasing the amount of lift. The wake can be seen to extend further downstream represented by the area of lower velocity behind the foil with higher associated drag forces. After $\alpha = 25°$, the foil experiences 'deep stall' whereby the adverse pressure gradient reaches the critical level where the boundary no longer is stable and detaches from the leading edge. The flow is then unstable, seen in by the velocity streamlines as well as in the pressure contour plot, where periodic vortex shedding occurs.

Analysing the temporal flow field for $\alpha = 30°$, Figure 3.13 shows the velocity vectors at different times, where the vortex shedding can be more clearly seen. Step 1) starting at the top at 2.5 s and 7.5s, the peak lift occurs where the boundary layer at the leading edge is attached. Step 2) the boundary layer at the leading edge becomes unstable and separates, causing flow entrainment with the surrounding fluid in a circulatory motion. The fluid rotation in the wake then disturbs the boundary layer further along the foil surface, initiating further separation and flow reversal along the suction surface, reducing lift. Step 3) the circulatory motion draws fluid from the pressure surface until this also becomes unstable at the trailing edge, resulting in a vortex shed rotating in the opposite direction. Step 4) as the vortices flow further down stream, the boundary layer at the leading edge becomes reattached and lift increases.

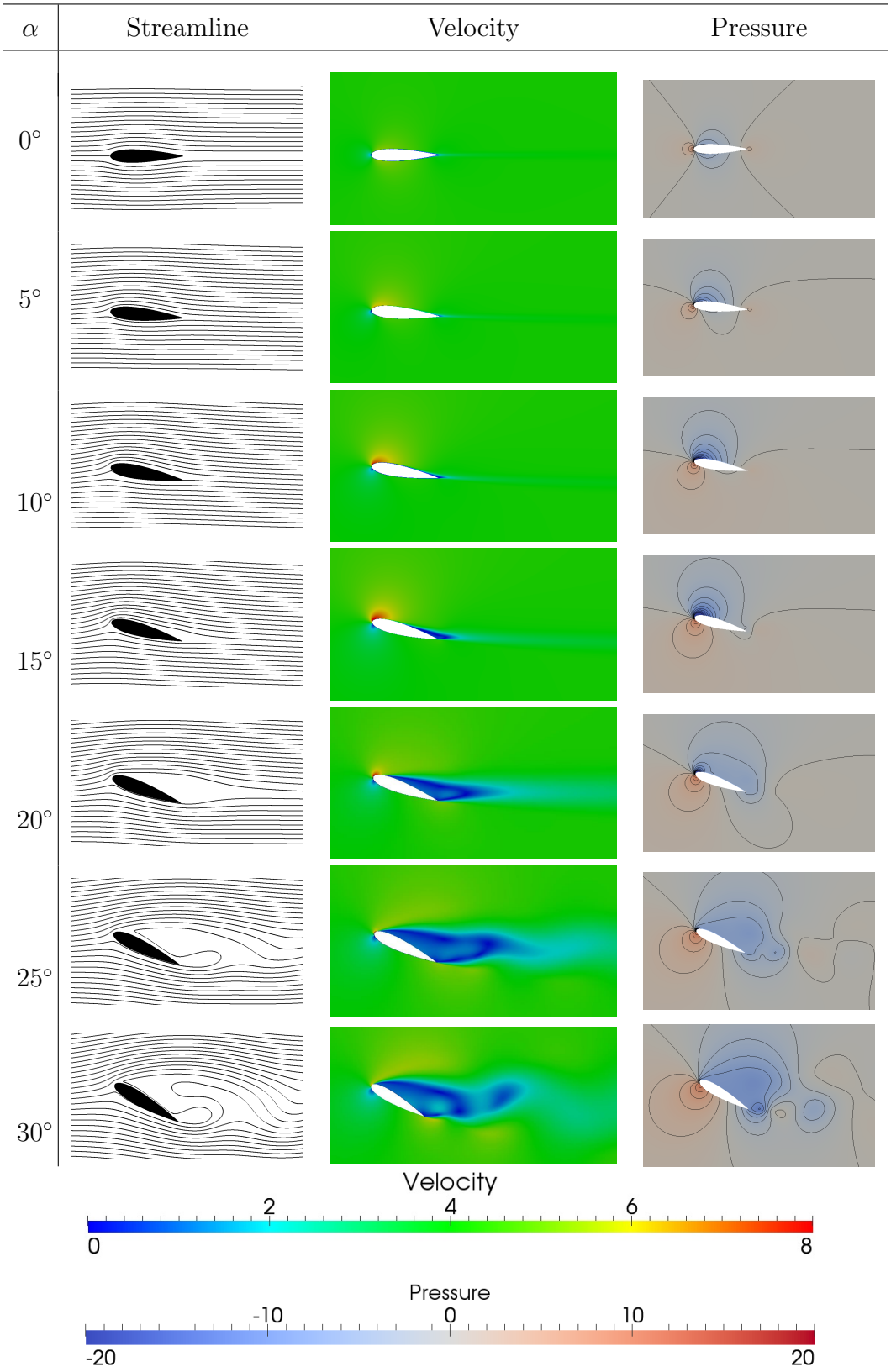

Figure 3.12: NACA0018 aerofoil flow streamlines, velocities (ms^{-1}) and pressure (Pa) contours at Re_{ch}= 1.0E+06 for α=0° to 30° at fixed time t = 20 s

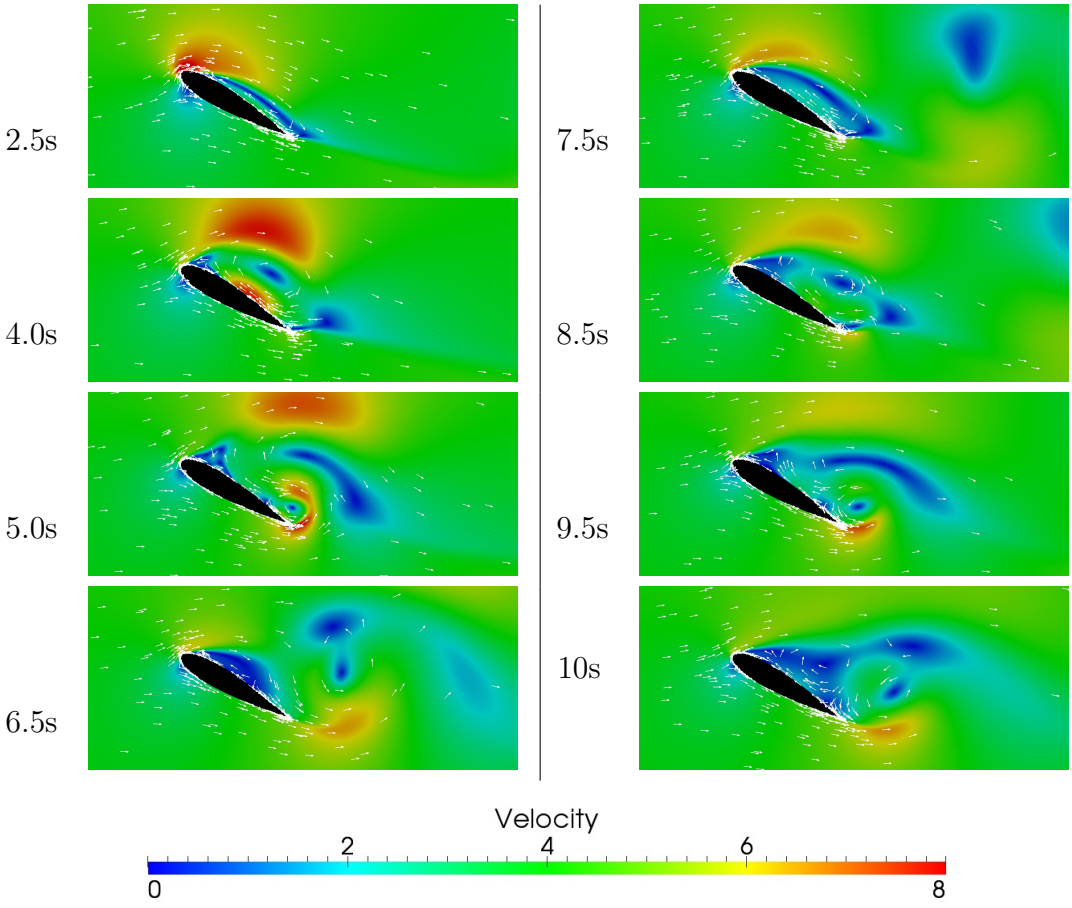

Figure 3.13: NACA0018 aerofoil time evolution of flow velocity (ms^{-1}), at Re_{ch}= 1.0E+06 for α=30° with arrows representing velocity vectors

The shedding and reattachment of the boundary layer causes fluctuating surface pressure forces, which results in periodic oscillations in lift and drag. The turbulent viscosity of the wake at the final time-step for $\alpha = 30°$ is shown in Figure 3.14. This illustrates the vortices shed alternately from the leading and trailing edges, where a steady state solution is not achieved. In these situations, average values of lift and drag are taken over the final few cycles.

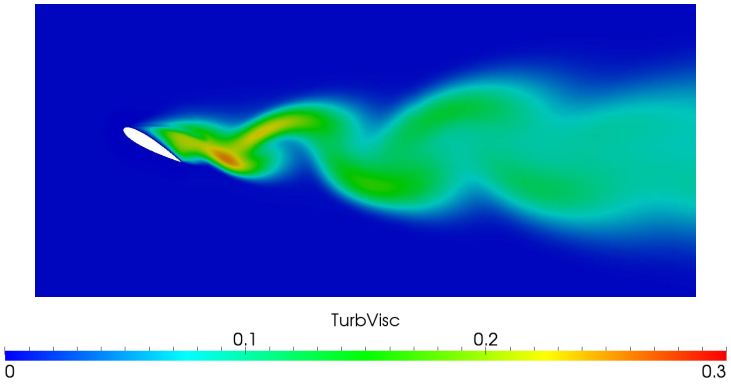

Figure 3.14: NACA0018 aerofoil wake turbulent viscosity, at Re_{ch}= 1.0E+06 with $\alpha = 30°$ at t=25 s

3.4.4.3 Comparison: lift and drag coefficient curves

Lift and drag coefficient curves comparing output from these CFD studies with XFoil and experimental measurements from Timmer (2008) are presented in Figure 3.15a. Generally, the CFD shows better agreement to the experimental data, which is expected due to the higher complexity of the model.

At low to moderate angles of attack, the linear section of the lift is well represented by the CFD, matching both the gradient and the peak of 1.2 for $\alpha = 15°$. The panel method however predicts a steeper gradient, peaking at 1.4. The drag is better represented by the panel method, where CFD predicts values almost two times as large as the experiments up to $\alpha = 13°$.

A large hysteresis loop is seen in the experimental measurements, where leading edge stall occurs at 27° for increasing α, and around 17° for decreasing α. The

hysteresis was seen to be the largest of all Reynolds numbers considered in the experimental campaign. The numerical models are static analyses at fixed angles, where the CFD is re-initiated at each attack angle interval, imposing a flow velocity at the inlet until convergence is reached. Therefore this hysteresis is not modelled.

A repeat of the analysis was performed at a higher Re=3.4E+06, where a new mesh was constructed to give a similar quality to the previous one. An additional comparison with measurements from an older set of experiments reported in NACA document 647 (Goett and Bullivant, 1939) is shown in Figure 3.15b, where similar trends are seen. It is noted that no hysteresis loop is present, as the experiments only run in one direction. Again an over prediction in drag from the CFD is observed at low angles of attack, along with over predictions of lift by up to 30%. Better agreement is however seen in the linear lift region and at extreme angles than results from XFoil.

3.4.5 Discussion

This study has analysed a NACA0018 aerofoil with two numerical models using a panel method and RANS CFD. Generally, a better agreement is seen between experimental measurements with CFD results, particularly at higher angles of attack. This is due to the more precise representation of the unsteady flow from boundary layer separation and formation of separation bubbles through solving Navier Stokes equations, which is a known limitation in XFoil. The hysteresis seen in the experiments show a dependency on either increasing or decreasing attack angles, and is attributed to the relatively thick aerofoil leading edge.

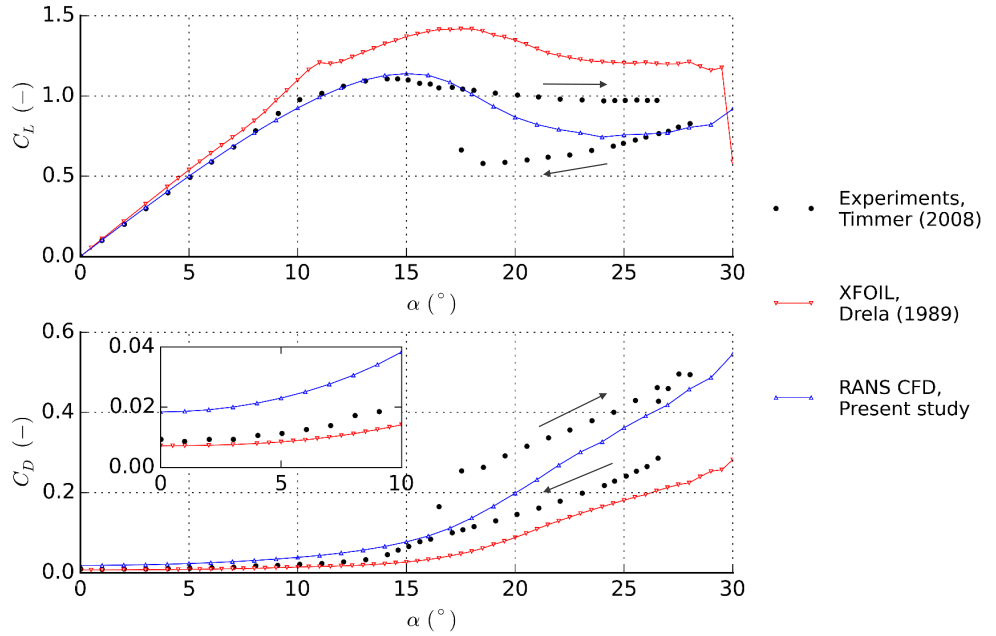

(a) Re_{ch}= 1.0E+06, experimental data from Timmer (2008)

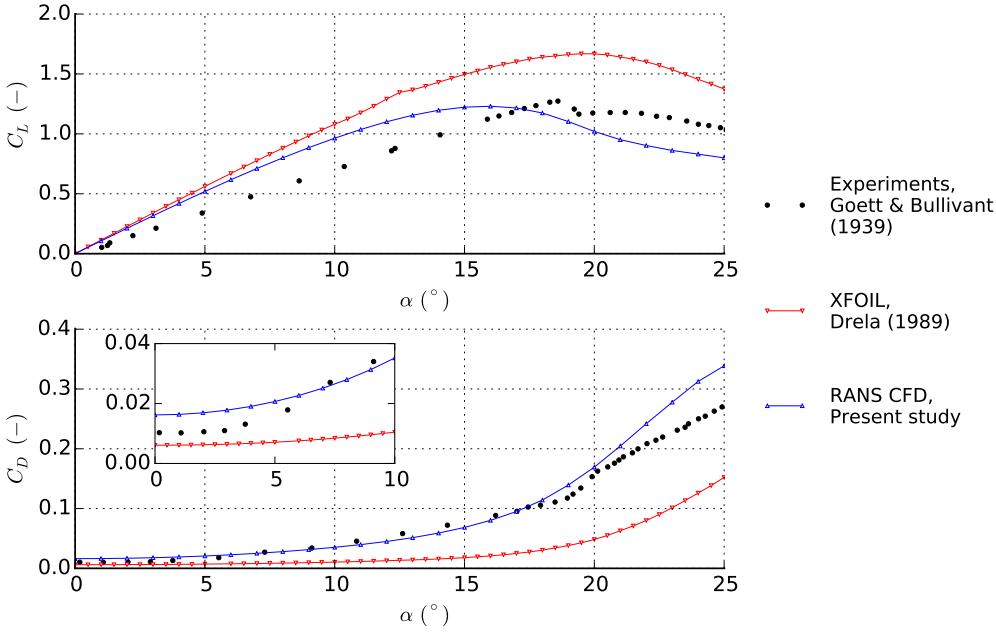

(b) Re_{ch}= 3.4E+06, experimental data from Goett and Bullivant (1939)

Figure 3.15: NACA0018 aerofoil coefficient curves of lift (top) and drag (bottom), comparing results generated from RANS CFD and XFoil with wind tunnel experiments at two Reynolds numbers

3.4.5.1 Experimental sources of error

The CFD is seen to predict higher drag forces than seen in the experiments at low angles of attack. Experiments under Re=1E+06 quote static pressure tube measurements accuracy of 2 Nm^{-2} (Timmer, 2008). As drag coefficients are in the order of 0.01, a small change due to measuremental error could have a large impact. An additional possible influence is from the formation of laminar separation bubbles on the pressure surface. These were observed in the experiments under certain operating conditions, and found to have dominated the trailing edge flow conditions. This lead to high levels of span wise flow, which were found to be reduced through the application of 0.48 mm thick zigzag tape on the pressure surface 80% along the chord.

Due to uncertainty in the drag over predictions, a secondary comparison was made with an additional set of experiments at Re=3.4E+06 (Goett and Bullivant, 1939). Again, a smaller but sizeable difference is seen between CFD generated results and measurements from a wake rake. The accuracy of these experiments report $C_D \pm 0.0002$, which is considered negligible even at low α.

3.4.5.2 Trailing edge condition

The reason for the disparity in drag predictions is thought to be due to the geometry of the aerofoil, specifically concerning the trailing edge. The geometry created within the CFD uses a rounded trailing edge, thought to be a more realistic case in the construction of carbon fibre blades. However in the experiments, scale model foils are fabricated from milled steel. This is in order to achieve higher tolerances in order to minimise surface roughness and reduce scaling effects.

The first set of experiments does not provide any detailed aerofoil geometry, however the secondary experiments report using a 'blunt' trailing edge (Goett and Bullivant, 1939). This would affect the formation of the wake, and interactions where flow over top and bottom surfaces meet, particularly for low angles of

attack. Default XFoil aerofoil coordinates have a blunt trailing edge condition (Drela, 1989), which would explain a better agreement seen for low angles. At higher angles of attack, the drag becomes dominated by the forces on the pressure surface.

3.4.5.3 CFD modifications

In order to get a more representative comparison, the CFD should be repeated with a blunt trailing edge. Additionally, the mesh could be improved by instead using a 'C-type' mesh, which is more highly refined just behind the trailing edge. This is thought to have a better capability to capture the flow behind the foil at low angles of attack.

Also, although mesh and time-step independence studies were performed, the aspect ratio across the surfaces and Courant numbers are quite high. Improving these could see some better agreement to the experiments.

An additional direction of work regarding this subject would be to assess the accuracy of RANS turbulence models in representing the turbulent boundary layer separation at high angles of attack. Studies using Large Eddy Simulation (LES) are well known to have better wake modelling capabilities, however have a significantly higher computational demand.

3.4.5.4 Computational requirements

It is well understood that due to the higher complexity of solving Navier Stokes equations, the CFD method is more computationally demanding than the simpler panel code. This highlights the main benefit to using models such as XFoil, and the basis of its widely spread use despite the inherent limitations and lower accuracy. In order to quantify the magnitude of this difference in demand, the following computational set up and times were recorded.

The RANS simulations were performed using EDF cluster 'Athos', made up of

$Intel^{®}$ $Xeon^{®}$ E5-2697v2 2.7 GHz Processors. A single node made up of 12 cores was used for each simulation, which converged within approximately 40 minutes. Therefore, each angle of attack analysed required equivalent to approximately 8 core hours.

The XFoil simulations were performed on a laptop running an $Intel^{®}$ $Core^{™}-i5$ 2.9 GHz dual core processor with 8 GB RAM, which converged within one minute for all angles of attack.

3.5 CFD analysis of flat plate foils

This section details the development of 2-D RANS CFD simulations of simple flat plate type foil sections. Although data and simple models exist concerning the hydrodynamic properties of these type foils, they are restricted to geometries with blunt chamfered or sharp edges. Information regarding foils with rounded leading and trailing edges for a large range of angles of attack is, on the other hand, less available in the literature.

The aim here is to compare lift and drag cures generated using CFD, with XFoil and experimentally measured values, in order to assess the difference in performance of each numerical model. This is labelled as the 'validation case'. CFD models are then constructed for hydrofoil sections of two different thickness to chord ratios, analysed at two much higher Reynolds numbers. These are labelled the 'application' cases, as they are to be applied to the ducted BEMT simulations in Chapter 5.

3.5.1 CFD simulation parameters

3.5.1.1 Geometry

The rounded edge flat plate foils are of simple geometry, with parameters defined in Figure 3.16. The chord is set to unity, where the thickness is then modified

to suit the required thickness to chord (t/c) ratio. The length in the span-wise direction is set at 0.01 m. The validation case has a t/c = 0.27, whereas the two application cases are made up of much lower ratios of 0.04 and 0.09.

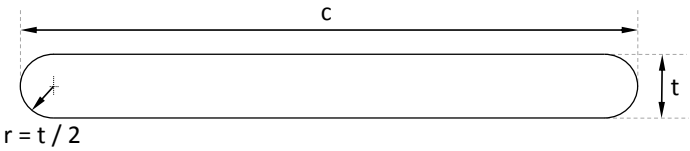

Figure 3.16: Flat plate foil general geometrical layout

3.5.1.2 Mesh construction

'O-type' structured meshes similar to the NACA foil case were constructed in Salome, using 3-D volumetric rectangular section elements of single cell thickness. The meshes for each of the different thickness to chord ratio cases are shown in Figure 3.17.

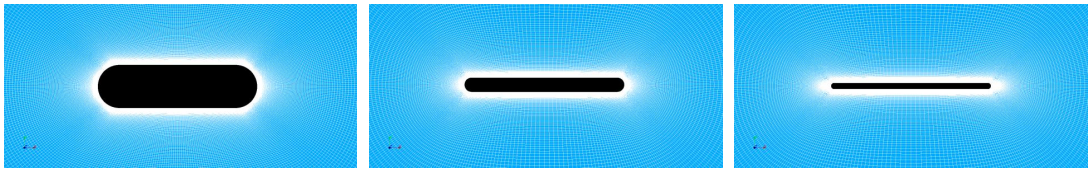

Figure 3.17: Flat plate foil magnified view of meshes for 3 thickness to chord ratios (t/c): 0.27 (left) 0.09 (centre) and 0.04 (right), at $\alpha = 0°$

For this case, there is no control mesh, rather the foil mesh for each angle of attack is merged directly with the tunnel mesh, as shown in Figure 3.18. A new tunnel mesh is constructed, based on the same dimensions as previously used in the NACA case, however with a higher density of elements down the transverse central section. This is in an attempt to better capture the wake behind the foil section, without dramatically increasing the computational time.

The combined meshes for each t/c contain 280,000 elements, deemed appropriate from mesh independence studies that were performed, similarly to those for the

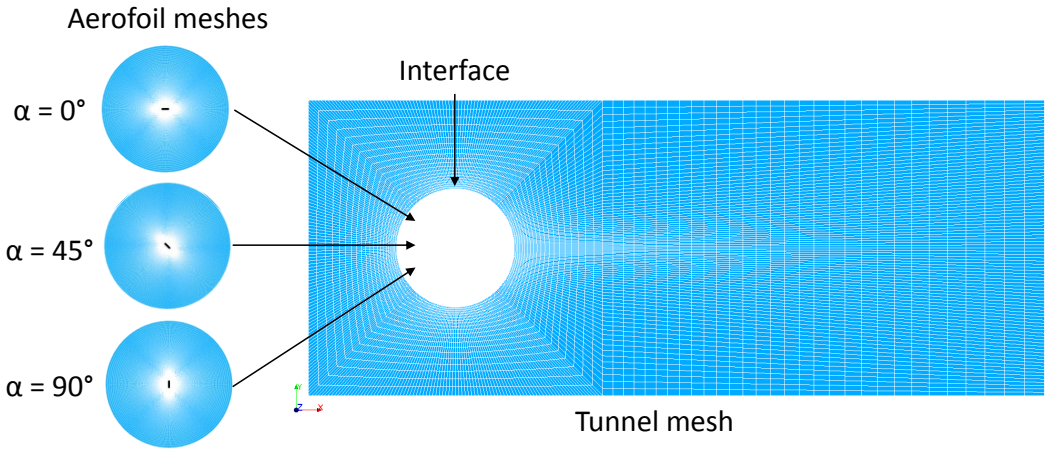

Figure 3.18: Flat plate foil meshes for t/c=0.27 at different angles of attack, indicating interface with tunnel mesh

NACA case reported in Section 3.4.3.1. Each mesh had slightly different quality values, however globally: skewness $< 45°$ and aspect ratio < 50 at the leading and trailing edges. The thickness of the first cell from the foil surfaces was specifically tuned for each t/c and for each Reynolds number to achieve a critical zone $y^+ \sim 1$ at $\alpha = 0°$.

3.5.1.3 Boundary conditions

The flow at the inlet is of constant uniform profile, prescribed in the direction normal to the boundary, located a minimum of ∼13 c (where c is the chord length) upstream of the foil. A constant pressure gradient is selected for the outlet boundary condition located ∼50 c downstream. Top and bottom boundaries are also situated ∼13 c distances away. All surfaces including the top, bottom and sides are prescribed with symmetrical boundary conditions. A smooth 'no-slip' wall condition is applied to the foil surface. The interfaces between the foil and tunnel meshes are fully merged.

3.5.1.4 Code_Saturne simulation set-up

These studies again use EDF in-house developed CFD suite *Code_Saturne*, version 4.0.5 (Archambeau et al. (2004), EDF R&D (2015)). The fluid properties prescribed to the validation and application cases are detailed in Table 3.4. Air was selected for the validation case, to be consistent with the reference source. Although water was selected for the application case, the hydrodynamic behaviour of the foil is dependent on the ratio of viscous to inertial forces, which is defined by the Reynolds number. Turbulence intensity is taken as arbitrary percentage, and although not assessed as a variable within this study, could provide an opportunity for future work investigating the turbulent nature of flows.

Table 3.4: Flat plate foils: fluid properties used in validation and application studies

Parameter		Validation	Application	Units
Density	ρ	1.17862	1024.0	kgm^{-3}
Dynamic viscosity	μ	1.83E-05	1.07E-03	$\mathrm{kg(ms)}^{-1}$
Turbulence intensity	TI	0.05	0.05	%
Inlet velocity	U	4.2	1.05 - 10.5	ms^{-1}
Reynolds number	Re_{ch}	3.0E+04	1.0E+06 - 1.0E+07	-

All other parameters are conserved from Section 3.4.2.4

3.5.2 Results: Validation case

3.5.2.1 Lift and drag coefficient curves

Figure 3.19 shows the comparison of lift and drag curves generated by the RANS CFD against reference experiments from Munshi et al. (1999). In general results are reasonably similar in trend, however it is seen that the CFD generated lift forces are higher for all angles of attack considered, which is particularly pronounced around where the foil enters stall ($\alpha \sim 10°$). Thin aerofoil theory follows the linear lift region quite comparably to the CFD, but this method is only valid at low attack angles. There are limited measurement points in which

to make a detailed comparison and smaller increments in attack angle are required to better define the stall condition. Drag shows excellent agreement at low angles of attack, before over predictions are seen in the CFD. This is mainly caused by a jump in both lift and drag at $\alpha = 39°$, an occurrence which is not observed in the experimental data.

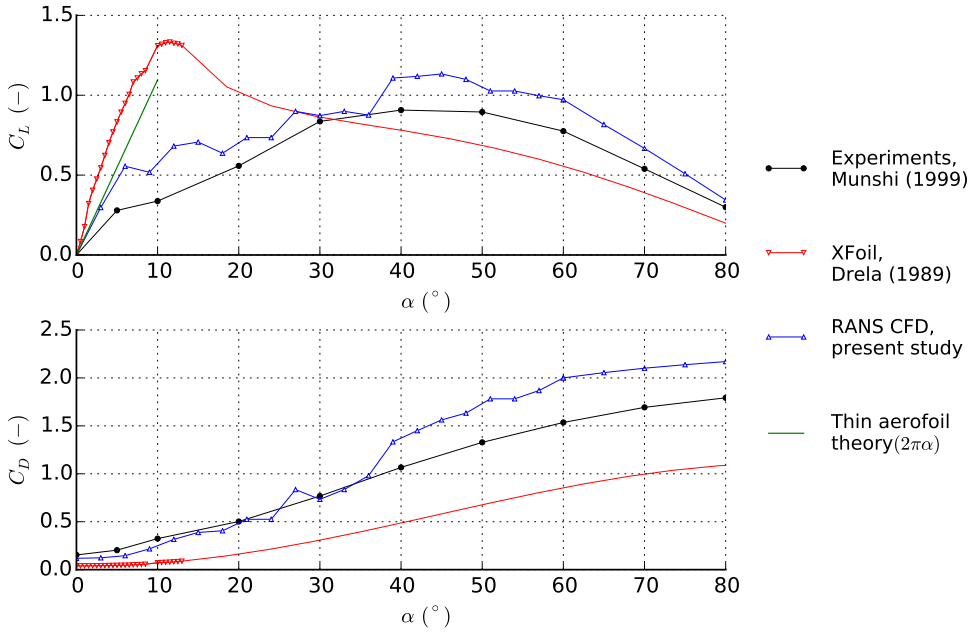

Figure 3.19: Flat plate foil coefficient curves of lift (top) and drag (bottom) for t/c=0.27 at Re=3.0E+04, comparing (uncorrected) experimental measurements (Munshi et al., 1999) with RANS CFD and XFoil

XFoil is found to be unstable for the majority of angles, where convergence is forced by raising the iteration limit and restarting simulations at different stepping intervals. The results show a significantly steeper linear section of lift, resulting in a peak much higher than those of the CFD or experiments. Drag coefficients are also considerably lower. The extrapolation function is applied to extend curves beyond stall, which appear to give a reasonable representation of foil properties at larger angles, considering the simplicity of the calculation. These results suggest that XFoil is not suitable for analysing these type foils. However, it is also noted that the Reynolds number is lower than the minimum value of 1.0E+05 as recommended for XFoil, where the model is known to become unstable.

3.5.2.2 Temporal analysis

Figure 3.20 shows the CFD generated lift and drag coefficient evolution over time for different angles of attack. Fluctuations are seen at $\alpha \geq 10°$, indicating periodic vortex shedding as discussed in the case of the NACA foil. Again the average values are taken over the final 20% of the time steps, as indicated by the thicker lines. Here it is assumed that simulations have sufficiently progressed such that steady periodic oscillations are exhibited. At $\alpha = 40°$, multiple peaks in lift and drag are seen. This is thought to raise the average lift and drag forces, and responsible for the jump observed in the coefficient curves. These additional peaks are seen to reduce in amplitude with increasing attack angle until 80°.

An inspection of the flow field for $\alpha = 30°$ and $\alpha = 40°$ shows the vortex formations over time, and their impacts on the flow over the foil. Figure 3.21 shows vortices shed from both the leading and trailing edges, rotating in opposite directions as seen in the NACA foil analysis. However for the larger angle of $\alpha = 40°$, the vortex shed at the trailing edge is larger, causing flow entrainment back towards the foil. This results in some flow reversal on the suction surface, thought to be responsible for the additional peaks in the fluid dynamic forces.

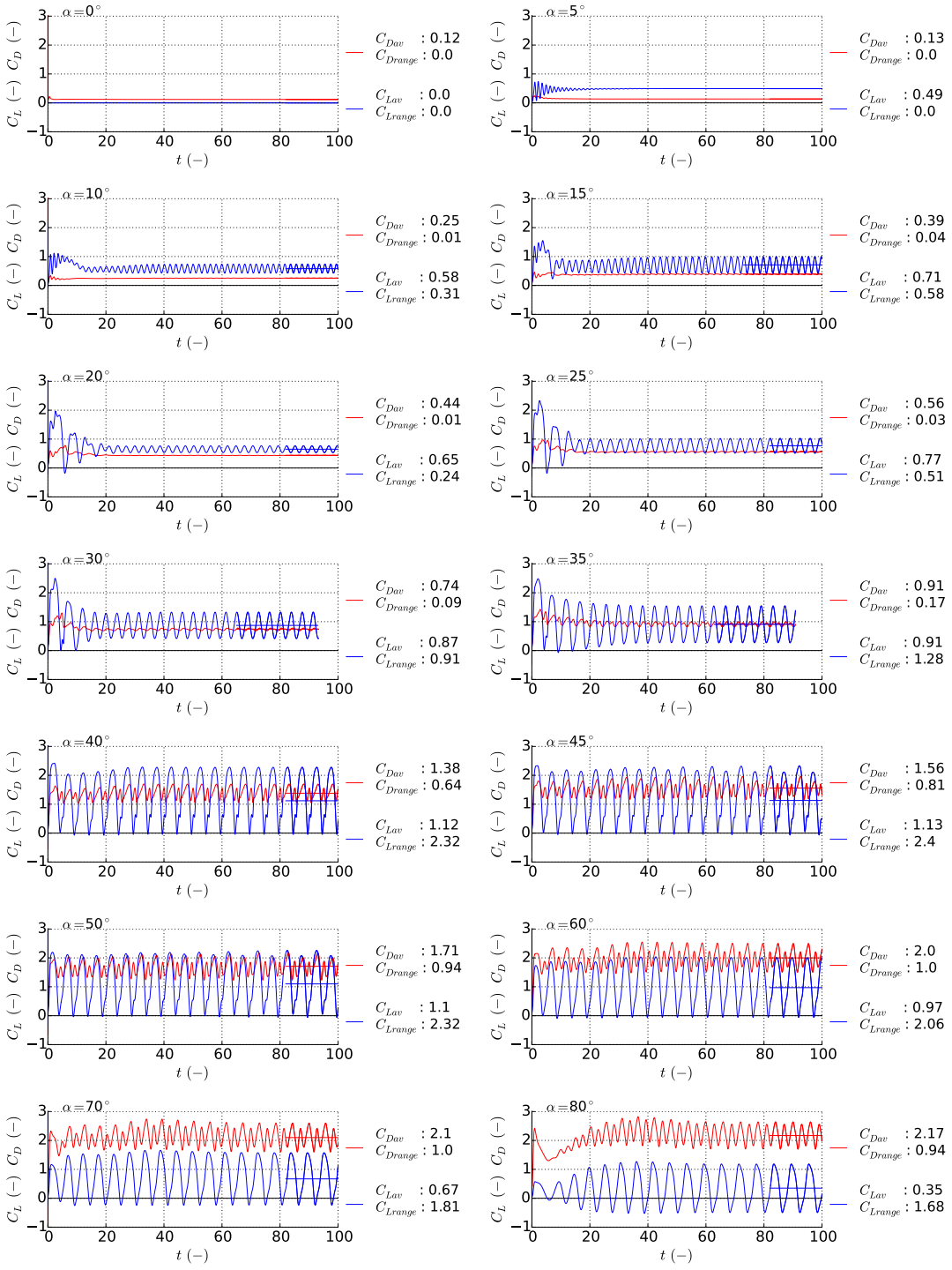

Figure 3.20: Flat plate foil time evolution of lift and drag coefficients with t/c=0.27 generated from RANS CFD at Re=3.0E+04, for various angles of attack

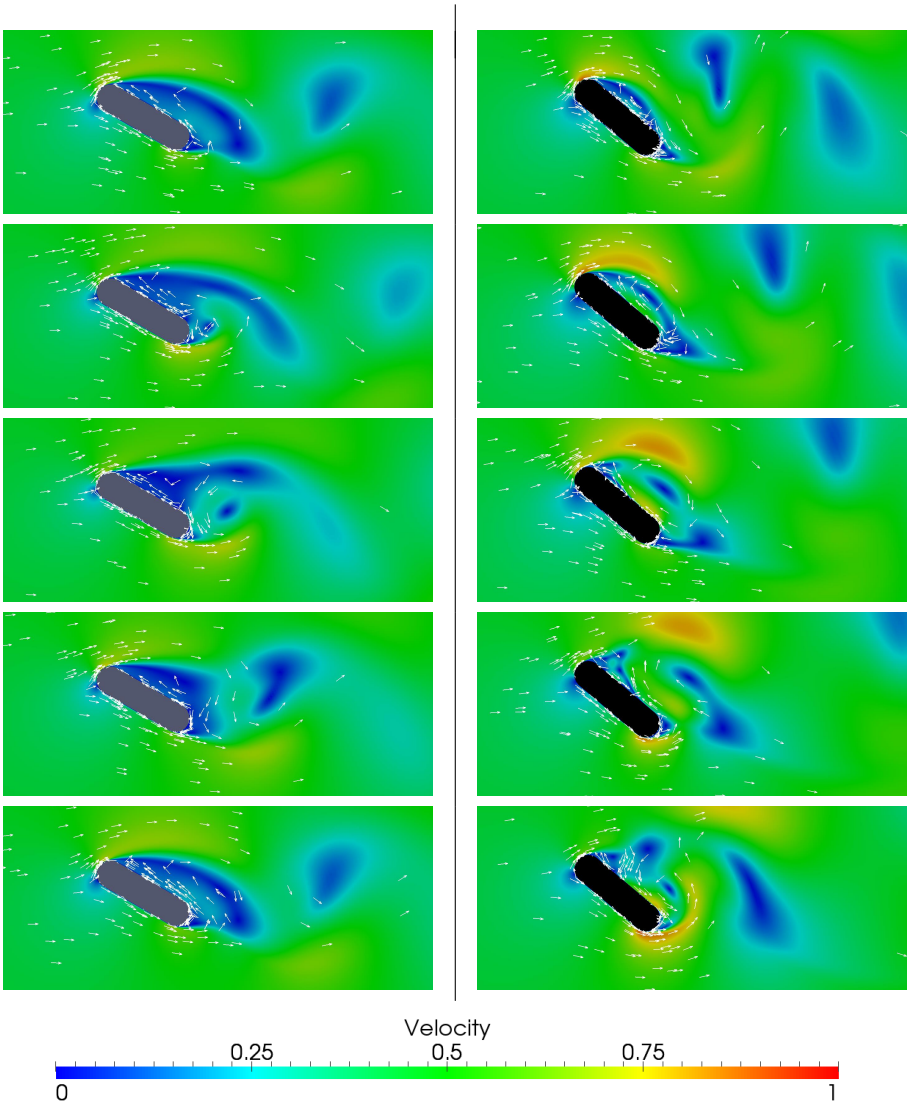

Figure 3.21: Flat plate foil of t/c=0.27 time evolution of flow velocity (ms^{-1}) from RANS CFD at Re = 3.0E+04 for $\alpha = 30°$ (left) and $\alpha = 40°$ (right), with arrows representing velocity vectors

3.5.3 Results: application case

3.5.3.1 Lift and drag coefficient curves

Having compared results to experimental data, simulations of additional t/c ratio foils are now presented. Two t/c ratios of 0.04 and 0.09 are tested, where

results for Reynolds numbers of 1.0E+06 and 1.0E+07 are shown in Figure 3.22a and Figure 3.22b respectively. Angles between $0° \leq \alpha \leq 30°$ are analysed at increments of 1° to capture the stall condition in sufficient detail. The less critical range $30° < \alpha \leq 70°$ are analysed at increments of 5° to reduce the number of simulations required. A linear interpolation is applied in order to estimate curves between the t/c ratios at increments of 0.01 (1%).

Comparing the two thickness ratios, it can be seen that lift and drag are very similar at low angles of attack, within the linear lift region. There is then a difference in the angle at which the foil stalls, seen by the sharp drop in lift and the sharp increase in drag. Stall angles are defined in Table 3.5.

Table 3.5: Flat plate foil stall angles

t/c ratio	Re=1.0E+06	Re=1.0E+07
0.04	7°	8°
0.09	10°	14°

After stall, both foils predict similar trends up to $\alpha = 40°$. For $40° \leq \alpha < 70°$ there are larger differences seen, showing some larger dependency on the thickness. This is largely due to a jump in lift and drag, similar to that previously observed in the validation case, which occurs only for the thicker foil. This sharp change occurs at 55° for $Re_{ch} = 1.0E + 06$, and more dramatically at 45° for $Re_{ch} = 1.0E + 07$. Inspection of the temporal variations in flow fields shows that the cause of this is again disturbances in the boundary layer from vortex shedding as described in Section 3.5.2.2.

In order to limit the number of CFD analyses, a linear interpolation can be used to approximate curves for intermediate t/c ratios. However, as seen in the figures, the main issue concerns the stall condition. Although peak lift and drag values seem well approximated between the upper and lower limits of t/c = 0.04 and 0.09, the angle of stall does not change appropriately. In reality, this is expected to increase gradually with increasing thickness.

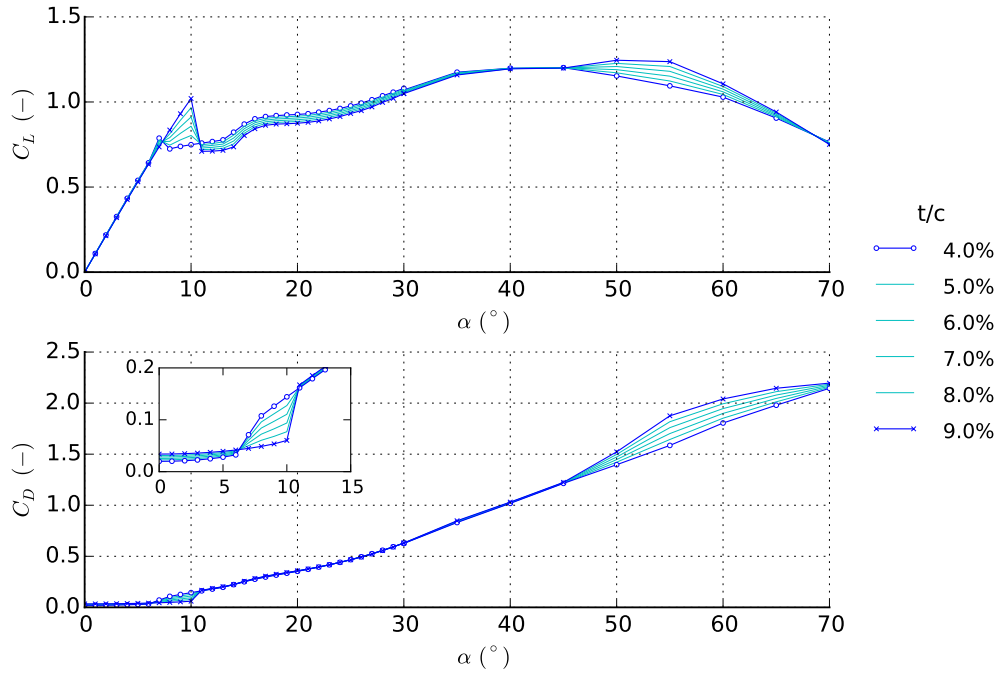

(a) Re_{ch}=1.0E+06

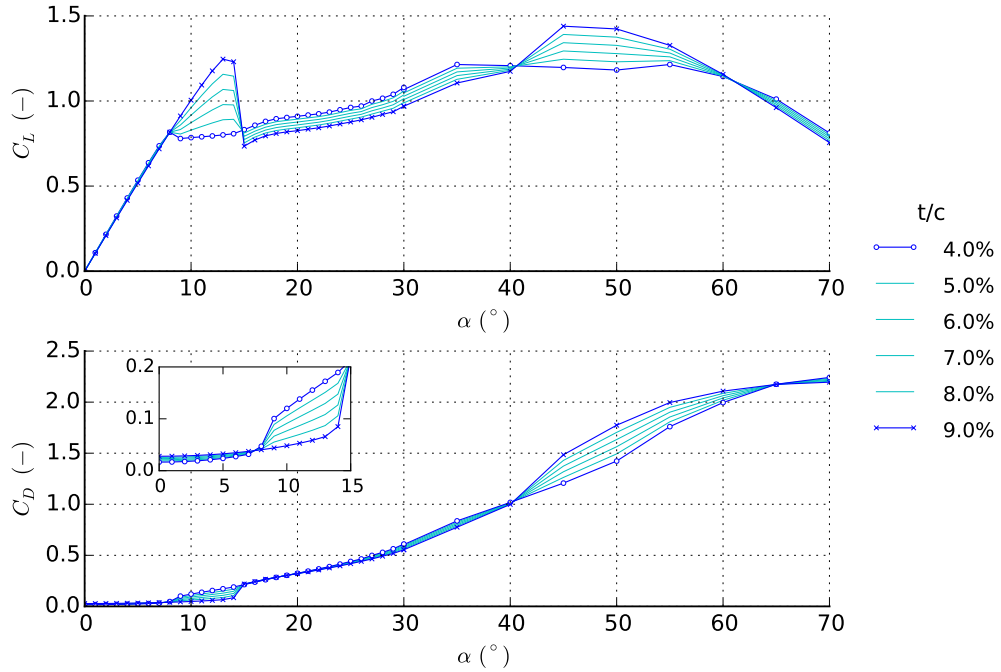

(b) Re_{ch}=1.0E+07

Figure 3.22: Coefficient curves of lift (top) and drag (bottom) from 2-D RANS studies of rounded edge flat plate foils with varying thickness to chord ratios, for two different Reynolds numbers

3.5.3.2 Temporal analysis

The time evolution of lift and drag coefficients is considered for a single case of t/c = 0.09 at Re = 1.0E+07. This is shown in Figure 3.23 for low angles of attack. At each angle, the evolution with non-dimensional time ($t = t_{actual}U/c$) is plotted. Initially, rapid fluctuations occur until the flow is stabilised, and coefficients converge to steady state values. Increasing α up to stall shows steadily increasing lift, whereas drag remains almost constant. Once stall is exceeded (at $\alpha = 14°$) the boundary layer separates, initiating the onset of vortex shedding, as previously discussed, which results in the periodic oscillations in hydrodynamic forces.

3.5.4 Computational requirements

XFoil simulations were again performed on a laptop running an $Intel® Core^{TM} - i5$ 2.9 GHz dual core processor with 8 GB RAM. Simulations required slightly more time to converge than in the NACA case, however still converged in under 3 core minutes.

The RANS simulations were performed using EDF cluster 'Porthos', made up of $Intel® Xeon®$ E5-2697v3 2.6 GHz Processors. A single node made up of 14 cores was used for each simulation, which converged within approximately 30 minutes. Therefore, each angle of attack analysed required the equivalent of approximately 7 core hours.

3.6 Summary

Lift and drag coefficients are required by BEMT codes to compute the hydrodynamic forces on the blade elements.

As these are a function of Reynolds number, which are found to be in the same order of magnitude to wind turbines, experimental measurements from wind

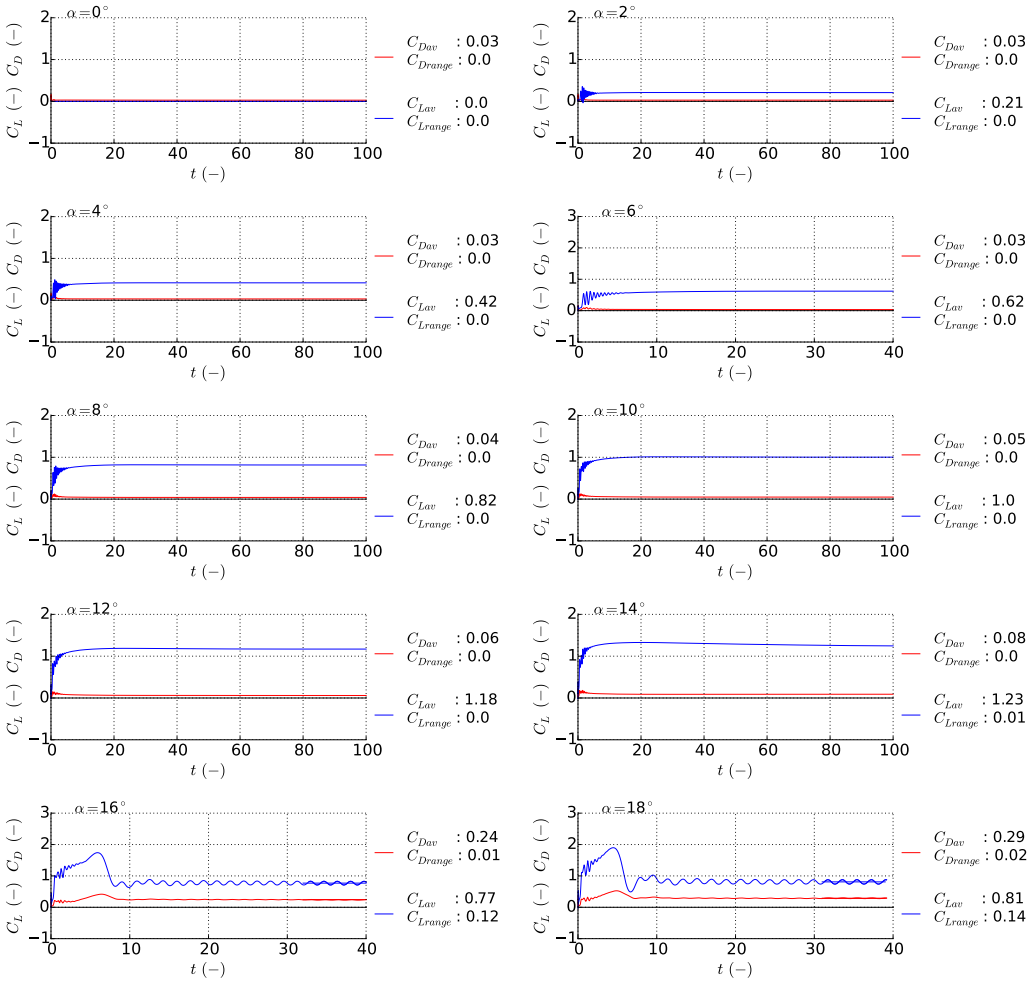

Figure 3.23: Time evolution of lift and drag coefficients for a flat plate foil with t/c=0.09 generated from RANS CFD, at low angles of attack ($0° \leq \alpha \leq 18°$) for Re=1.0E+07

tunnel tests can be used. However, these are only available for specific foil profiles and only available for some Reynolds numbers.

To generate curves for the specific hydrofoils and under the specific operational conditions seen for TSTs, numerical methods are adopted. This chapter has presented findings from 2-D analyses for a range of foil profiles using two very different numerical methods: one incorporating a panel code with viscous model XFoil; and the other solving Reynolds averaged Navier-Stokes equations using CFD software *Code_Saturne*.

3.6.1 XFoil

The panel code method used in XFoil is able to calculate lift and drag curves for NACA foils with reasonable agreement to wind tunnel measurements. Limitations have been shown in representing complex flows such as boundary layer separation. This can be resolved through the use of an extrapolation function which has shown to successfully extend the range of angles of attack.

The code is also seen to be restricted when assessing alternative foil profiles, such as with large thickness to chord ratios and for rounded edge flat plate type hydrofoils.

Simulations are run with extremely little computational demand, which is the basis of its widely spread use in similar applications. Set-up times are also relatively extremely short, as there is no requirement for geometry or mesh construction.

3.6.2 RANS CFD

RANS CFD analysis using *Code_Saturne* show better overall accuracy for NACA profiles. This method is also shown to be capable of analysing rounded edge flat plate foils, with reasonable agreement to experimental data (although limited measurement data is available for comparison).

The model appears to capture well the complex flow effects from separation of the boundary layer under the stall condition. Assessing the temporal variations in hydrodynamic forces shows the appearance of periodic fluctuations, which result from alternating vortex shedding at the edges at larger angles of attack. The full range of angles of attack can be assessed, which neglects the requirement to apply any extrapolation function.

This higher accuracy and adaptability however comes at the cost of much higher

computational demand to run the simulations, in addition to longer preparation times. To circumvent this, the number of analyses of flat plate foils can be limited through the use of linear interpolation functions to extend curves to a range of t/c ratios and Reynolds numbers.

3.6.3 Sensitivity to Reynolds number

The Reynolds number also has a large influence on fluid dynamic behaviour of the foils. For the case of TSTs, the Reynolds number can vary by an order of magnitude, depending on the selected rotational velocity and chord length.

As the blade forces are directly influenced by the hydrodynamic properties of the elements, the BEMT predictions could be improved if the lift and drag coefficients took into account the specific geometric and flow parameters of each blade element. For example, C_L and C_D curves corresponding to a specific chord and Reynolds number could be used at a given rotational velocity.

3.6.4 Application to BEMT

XFoil analysis of NACA 6-series foils was found to show reasonable agreement to experimental values, and able to generate full coefficient curves in a matter of minutes on a single CPU. Extrapolation functions are also used to extend the range of angles of attack to required values. This method is therefore used to generate datasets to be read into the BEMT simulations applied to conventional turbines in Chapter 4.

RANS CFD using *Code_Saturne* is capable of analysing rounded edge flat plate foils, with reasonable agreement to experimental data. This method is therefore selected to generate datasets to be applied to Ducted BEMT simulations in Chapter 5.

Chapter 4

Classical BEMT for conventional TSTs

This chapter presents the application of the 'classical' BEMT model to a 'conventional' style device consisting of a low solidity, bare, horizontal axis rotor, similar to that of most popular wind turbine designs. The model is here validated through comparing predictions of thrust and power against physical data, in the form of scale model experimental measurements, as well as indirectly validated with numerical results from other BEMT models and CFD studies.

The main objectives from the work detailed in this chapter are: 1) to confirm the BEMT principles are well implemented in the code; and 2) to assess the capabilities and validity of the model for this specific application. In the process of addressing these, a number of intermediate tasks are carried out including: the development of pre and post processing tools to standardise the procedure; identifying and resolving any numerical instabilities; optimising the programming loops to minimise running times; testing sensitivities to various imposed empirical factors. This work is partly published in Allsop et al. (2016)

4.1 Overview

Numerous experimental scale model tank tests have previously been performed, with published data available in the literature. Here three case studies are selected, each based on different experimental layouts and device scales, to test the model capabilities under different operating conditions.

For each case, the input data is collated into text file formats and prescribed as inputs into the classical BEMT model through various read-in functions. All input data is defined as close as possible to those described in the experimental procedure from the literature. However, some modelling decisions are made (mainly due to data availability issues from the references), the choice of which has impacts on the model predictions. Every attempt is made to justify approaches taken in these cases, with consideration taken into their influence on the results.

Individual cases are briefly discussed at the end of each section, with an overall discussion combining the assessments presented at the end of the chapter.

4.1.1 General BEMT structure

Recalling from Chapter 2 (the BEMT equations) and Chapter 3 (the method of generating hydrofoil coefficients), the structure of the model used in this chapter uses the following general principles:

1. Classical BEMT equations are applied using a simple iterative loop
2. Correction factors based on:
   - The Prandtl tip and hub loss correction factors are implemented
   - The Buhl correction in highly loaded conditions
   - The Bahaj blockage correction factor for channel flows
3. XFoil generated lift and drag coefficient curves, corrected with:
   - Du-Selig and Eggers adjustments for a rotating foil
   - Viterna's extrapolation function for post stall angles

4.1.2 Process

The model is initiated for each individual inflow velocity and pitch angle, where the turbine rotational velocity is varied via a stepping function. Intermediate calculation steps are inspected in order to assess the model performance, to ensure convergence is well established and to gain indications of the magnitude and location at which correction factors are being applied. Elemental and blade forces can be analysed, however only non-dimensionalised values of rotor thrust and power are available for comparison at this stage.

4.2 Case 1: 1/20th scale cavitation tunnel experiments

The experiments used for this Validation Case 1 have been performed by Bahaj, Molland, Chaplin and Batten (2007). Tests are carried out on a 1/20th scale rotor in a fully enclosed cavitation tunnel. These were developed primarily to assess the power and thrust of a three bladed, horizontal axis turbine, with results also used to validate the in house BEMT code created by the Sustainable Energy Research Group (SERG) at the University of Southampton, as an extension of the same study. Therefore all required input parameters specific to this method are detailed, making it fully replicable. Turbine parameters, hydrofoil coefficients, flow conditions and test set-ups, as well as performance and thrust curves are taken from the following sources: Batten et al. (2006); Bahaj, Molland, Chaplin and Batten (2007); Bahaj, Batten and McCann (2007); Batten et al. (2007).

The source data, which also includes towing tank experiments not used in this study, has been used in numerous studies to assess the performance of various numerical models, for example: Turnock et al. (2011) and Olczak et al. (2016).

4.2.1 Experimental set-up

Tests are performed in a cavitation tunnel at QinetiQ, Haslar, with the working section dimensions and flow conditions as detailed in Table 4.1 (Bahaj, Molland, Chaplin and Batten, 2007).

Table 4.1: Case 1 cavitation tunnel parameters

Parameter	Value	Units
Length	5.0	m
Width	2.4	m
Height	1.2	m
Max flow velocity	8.0	ms^{-1}
Pressure range	0.2 - 1.2	ATM

This experimental set-up benefits from reduced boundary influences and no free surface effects, as the working section is completely enclosed (see Figure 4.1).

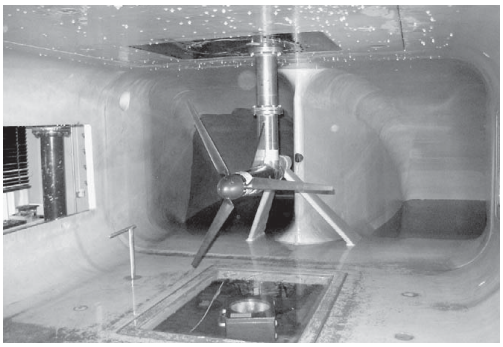

Figure 4.1: Case 1 image of cavitation tunnel experimental set-up, with installed turbine and test rig, taken from Bahaj, Molland, Chaplin and Batten (2007)

4.2.2 Flow conditions

Four experiments are performed at different inflow velocity and blade pitch combinations, as defined in 4.2. Measurements are taken at various rotational velocities of the turbine. (Note that Bahaj (2007) quotes pitch with reference to

the rotor plane. Values are therefore are a combination of the real pitch angle and the blade twist at the root, and so are offset by 15°). No turbulence intensity values are quoted.

Table 4.2: Case 1 test conditions

Case	Velocity (ms^{-1})	Pitch (°)
1a	1.30	12.0
1b	1.40	0.0
1c	1.54	10.0
1d	1.73	5.0

Figure 4.2 shows the depth distribution of velocity based on uniform and shear profiles using a $1/7^{th}$ power law, with the turbine depth range shown in the grey box to highlight the velocities seen by the turbine. The velocity is non uniform over the turbine area, particularly at the highest velocity, and therefore will have some effects on the rotor averaged thrust and power prediction. More significant impacts will be on the distribution of the forces along the blade at different azimuthal positions within the water column.

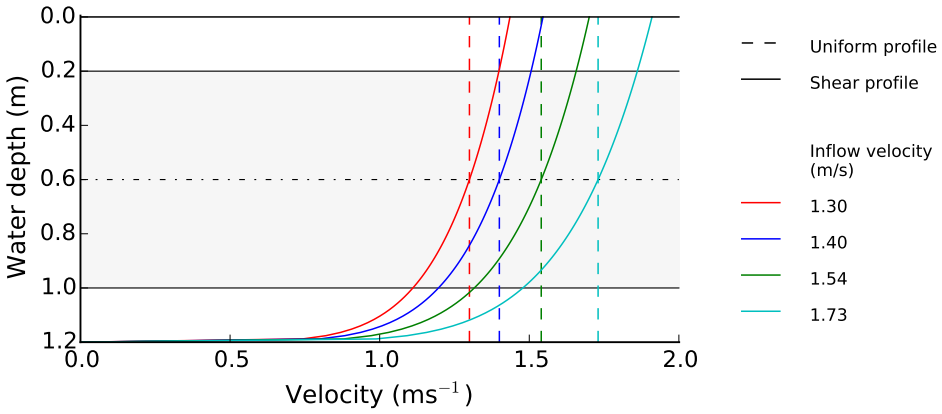

Figure 4.2: Case 1 inflow velocity profiles for each test, showing water depth distributions based on uniform and $1/7^{th}$ power law shear profiles. The grey shaded area represents the extents of the turbine.

Figure 4.3 shows a two dimensional section of the channel at the rotor plane, showing the turbine frontal area within the constraints of the channel walls. As

the cavitation tunnel height is 1.5 D (where D is the turbine diameter), and the width is 3 D, there are thought to be influences from the presence of all the boundaries affecting the flow into the turbine.

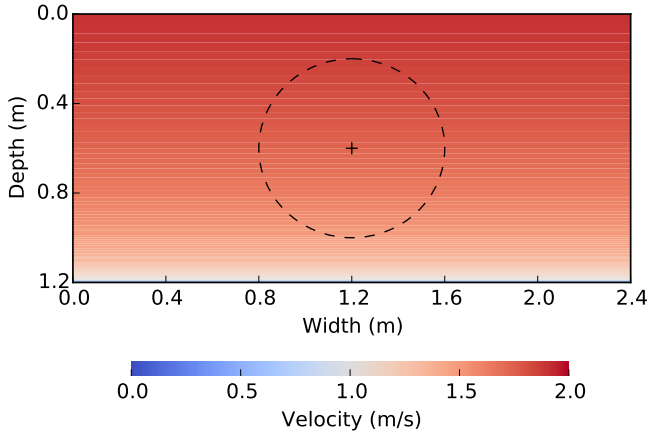

Figure 4.3: Case 1d theoretical 2-D inflow velocity profile within the channel working section at the rotor plane, showing vertical distributions based on a $1/7^{th}$ power law for U_{hub} =1.73 ms^{-1}. Dashed line represents the turbine circumference when installed.

There is a lack of data regarding the flow velocities at different positions in the channel, and no information concerning the influence of the viscous shear from the surrounding walls, within the source data. Therefore a $1/7^{th}$ power law is applied, to approximate the influence of the bottom friction only, to be consistent with the similar flume parameters detailed in Validation Case 3.

4.2.3 Turbine parameters

The turbine consists of a 3-bladed, horizontal axis rotor with a diameter of 800 mm and a hub diameter of 100 mm. Radial distributions of blade geometrical parameters are detailed in Table 4.3. The circle represents the shape of the blade root connection to the hub, before transition to the NACA blade hydrofoils.

Table 4.3: Case 1 1/20th scale model turbine geometry

r/R (-)	β (°)	c/R (-)	foil	t/c (%)
0.20	15.0	0.125	Circle	24.0
0.25	12.1	0.120	NACA63-8xx	22.5
0.30	9.5	0.116	NACA63-8xx	20.7
0.35	7.6	0.111	NACA63-8xx	19.5
0.40	6.1	0.106	NACA63-8xx	18.7
0.45	4.9	0.102	NACA63-8xx	18.1
0.50	3.9	0.097	NACA63-8xx	17.6
0.55	3.1	0.092	NACA63-8xx	17.1
0.60	2.4	0.088	NACA63-8xx	16.6
0.65	1.9	0.083	NACA63-8xx	16.1
0.70	1.5	0.078	NACA63-8xx	15.6
0.75	1.2	0.073	NACA63-8xx	15.1
0.80	0.9	0.069	NACA63-8xx	14.6
0.85	0.6	0.064	NACA63-8xx	14.1
0.90	0.4	0.059	NACA63-8xx	13.6
0.95	0.2	0.055	NACA63-8xx	13.1
1.00	0.0	0.050	NACA63-8xx	12.6

4.2.4 Reynolds number

Considering the tank, the characteristic length can be taken as the width of the tank (2.4 m), and using the average inflow velocity (U) for each case, ranging from 1.3 - 1.73 ms^{-1}, Re_{tank} ranges from 3.1E+06 - 4.1E+06.

Considering the Reynolds number more localised to the blade, the chord based Reynolds number can be calculated using the characteristic length taken as the chord, which varies along the blade length from 0.02 - 0.05 m. This means for an inflow velocity of 1.73 ms^{-1}, Re_{ch} ranges from 3.5E+04 - 8.7E+04.

If then the fluid velocity accounts for the rotation of the blade, the resultant velocity is used, which varies depending on angular velocity and element radius. For Case 1d (defined in Table 4.2), Re_{ch} was found to vary by an order of magnitude from 3.0E+04 - 4.0E+05, as presented in Figure 4.4. In order to

reduce the number of calculations, a single value is taken at optimal TSR of 5 and at a position three-quarters of the blade span, Re_{ch} = 2.0E+05. This value is used in all other velocity cases within this study, the implications of which are discussed in Section 4.5.2.

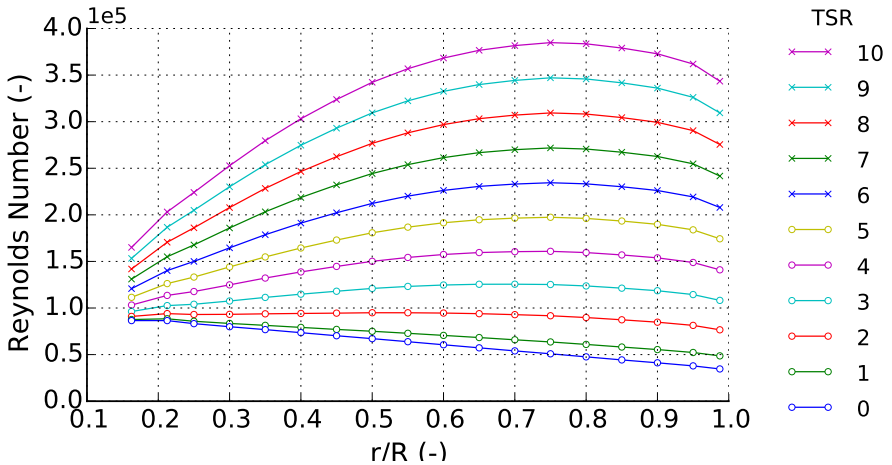

Figure 4.4: Case 1d variation of chord based Reynolds number with normalised radius (r/R) for various TSR

4.2.5 Hydrofoil characteristics

Hydrofoil profiles are based on a NACA63-8xx, where xx is the thickness to chord ratio varying along the blade length, detailed in Table 4.3. The lift and drag coefficients are generated with XFoil (Drela and Youngren, 2001), as detailed in Chapter 3. It is noted that thickness ratios are in the range capable of being solved by the panel code.

Data is preprocessed using NREL software Airfoilprep (Ning, 2013) by applying a Du-Selig and Eggers correction (detailed in Appendix 2, Section 1) factor for stall delay of a rotating blade (Brenton et al., 2007), which also depends on the radial location. A Viterna extrapolation function (Viterna and Janetzke, 1982) is applied (details of which are found in Appendix 2, Section 2) to increase the range of angles of attack past the capability of XFoil.

Lift and drag curves as a function of angle of attack are shown in Figure 4.5 for

a Reynolds number of 2.0E+05. To model the connection to the hub, the blade root is represented by a cylindrical element, with an associated drag coefficient of 0.5 for all angles of attack.

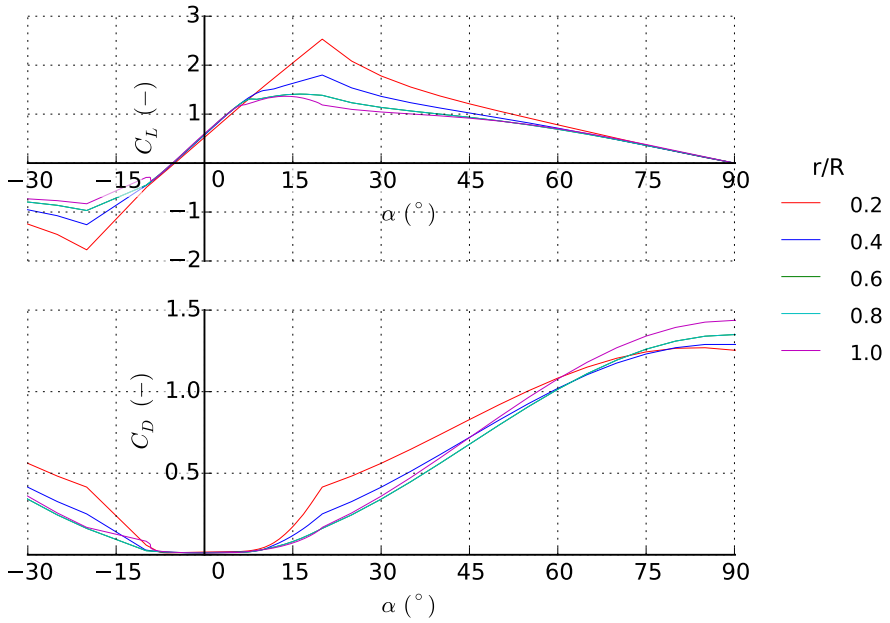

Figure 4.5: NACA63-8xx hydrofoil C_L (top) and C_D (bottom) curves at Re_{ch}= 2.0E+05, at various normalised radii (r/R)

4.2.6 Blockage correction

The global blockage, as a ratio of the rotor swept area to the channel section area is relatively high, at 17%. This has associated blockage correction factors (as derived in Section 2.6.3) as detailed in Table 4.4. These have been previously applied to the raw experimental data by the author (Bahaj, Molland, Chaplin and Batten, 2007), and therefore TSR, thrust coefficients and power coefficients are quoted in their 'equivalent open water' form, and can be directly compared with the BEMT results.

Table 4.4: Case 1 blockage correction factors, using tunnel thrust coefficient C_T=0.8

Parameter	Blockage Correction Factor
TSR	0.94
C_T	0.89
C_P	0.82

4.2.7 Numerical implementation

Figure 4.6 shows the distribution of axial and tangential induction factors as well as the tip/hub loss correction factor along the blade length for each inflow velocity and blade pitch angle. As there is a shear inflow applied to the model, the values will vary azimuthally, therefore averages are taken over one turbine rotation.

The axial induction profiles are seen to vary quite significantly with inlet velocity and blade pitch, where values exceed the transition to the highly loaded regime (> 0.4) only in Case 1b and very slightly in Case 1d. These occurrences are seen to be localised at the blade tips, demonstrating a very small dependence on the Buhl correction factor based on semi-empirical formulae (detailed in Section 2.6.2).

In contrast, the tangential induction factors appear to be very similar in trend for each of the cases, with only slight variations in magnitude. For the majority of the blade sections, the tangential induction factor is low, for the most part < 0.1.

The tip/hub loss describes the reduction in hydrodynamic efficiency along the blade, becoming more influential towards the tip and hub as per its definition. The magnitude of this efficiency decreases with TSR, and the distributions are non-symmetrical where the tip losses are clearly more significant in all cases considered.

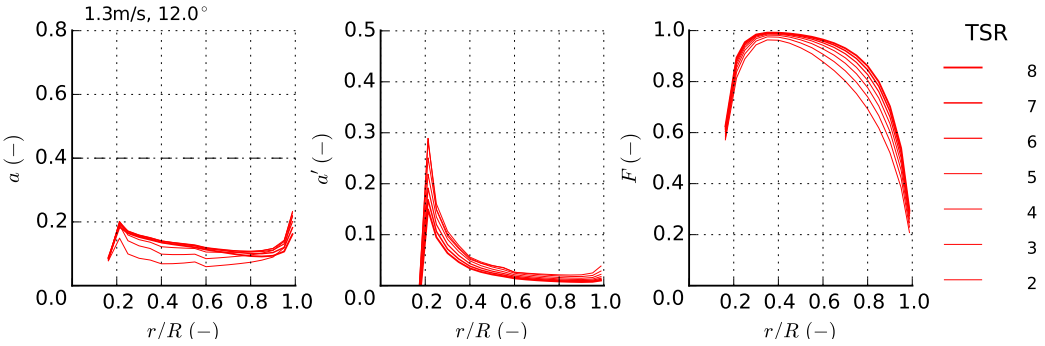

(a) 1.3 ms^{-1}, 12° pitch

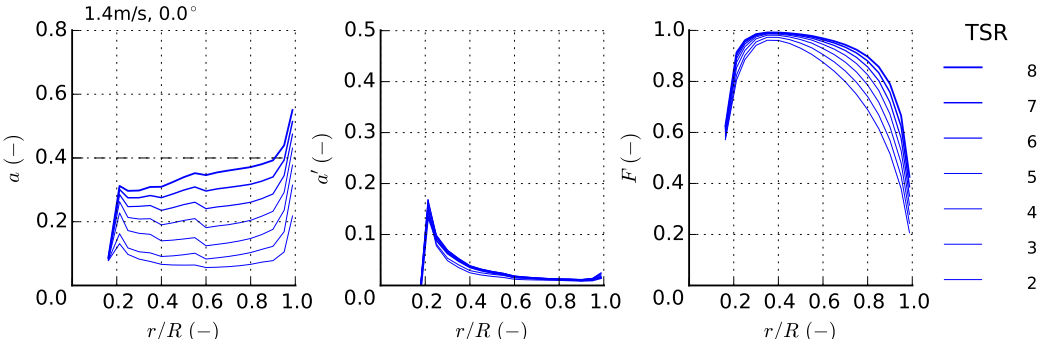

(b) 1.4 ms^{-1}, 0°pitch

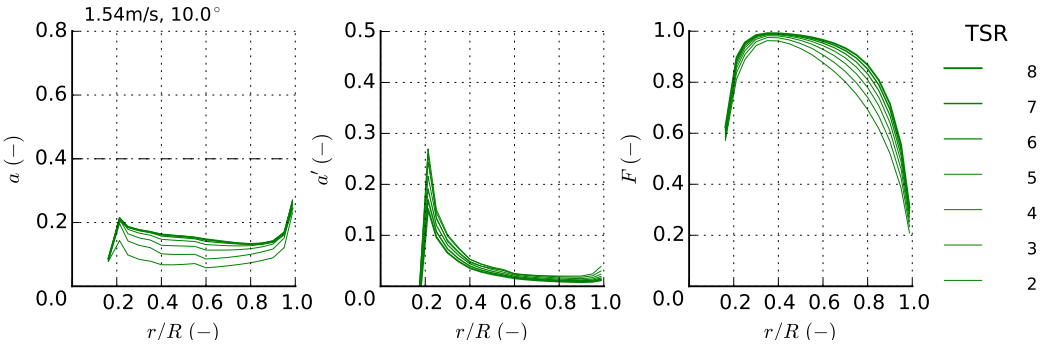

(c) 1.54 ms^{-1}, 10° pitch

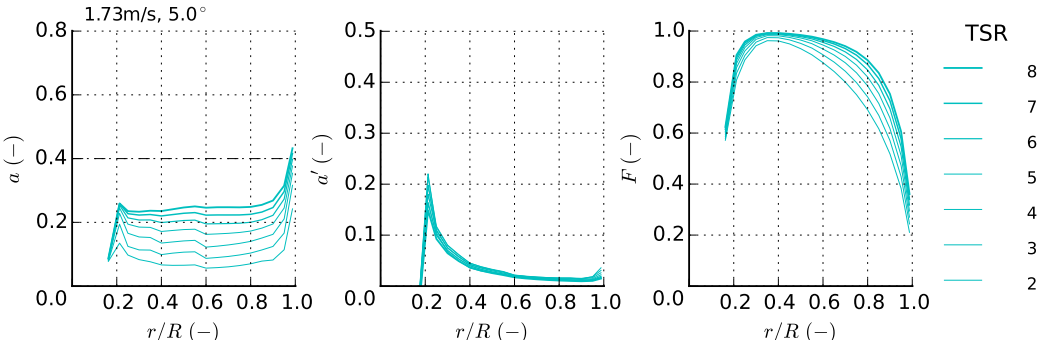

(d) 1.73 ms^{-1}, 5° pitch

Figure 4.6: Cases 1a - 1d distribution of axial induction (left), tangential induction (centre) and tip/hub loss (right) factors with normalised radius

4.2.8 Validation

Figure 4.7 shows the results of the Case 1 validation, where the coefficients of power and trust curves against tip speed ratio are presented. In general, the results of the present study are very similar to the BEMT models from academic code from The University of Southampton SERG. Good agreement is also seen with DNV-GL Tidal Bladed (DNV GL Garrad Hassan, 2012*b*), however there are some disparities seen in power predictions at higher TSR. There are limited published details regarding the input conditions used in this DNV Bladed analysis, therefore the cause of the discrepancies cannot be determined.

The present study also shows very good agreement with the physical model data points. The overall trend of each case is well matched, and the peak values well captured, particularly for Cases 1a, 1c and 1d. For these cases, at TSR < 6, thrust predictions are within +1/-10% and power predictions within +1/-7 % of the experimental data.

For TSR > 6, beyond the optimal operational point of the turbine, less agreement is seen, with under predictions in thrust of up to 20 %, and over predictions in power of up to 23 %.

Experimental data points for Case 1b show more spread, a sharper peak power compared with the other cases, and a steeper drop off as the rotational velocity exceeds the optimal TSR. Thrust forces are also comparatively high, which is thought to be due to the 0° pitch angles of the blades. As a small pitch leads to lower inflow angles, a resulting higher axial induction factor is experienced, as can be seen in Figure 4.6. The BEMT model predicts a higher optimal TSR where peak power occurs, and follows a less steep reduction as the rotational velocity increases. Thrusts also can be seen to follow a steady increase past the optimal operating condition.

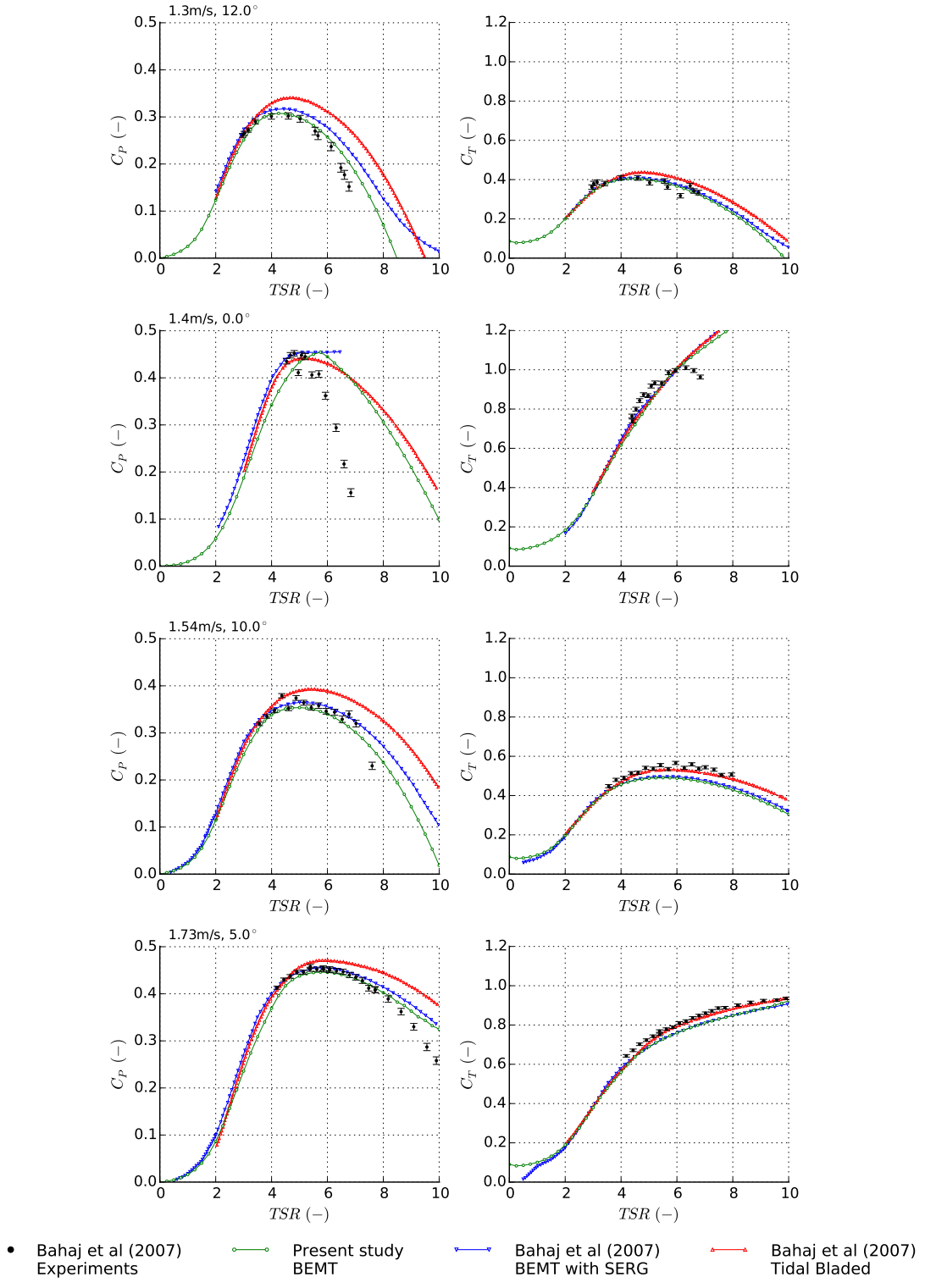

Figure 4.7: Rotor coefficients of power (left) and thrust (right) variation with TSR for Cases 1a) 1.3 ms^{-1}, 12° 1b) 1.4 ms^{-1}, 0° 1c) 1.54 ms^{-1}, 10° 1d) 1.73 ms^{-1}, 5° (top to bottom respectively) comparing against experimental measurements and output from two other BEMT models (Bahaj, Molland, Chaplin and Batten, 2007)

4.2.9 Case discussion

4.2.9.1 Experimental parameters

Measurement accuracy of torque and thrust are quoted at ±0.25 Nm and ±5 N respectively (Bahaj, Molland, Chaplin and Batten, 2007). These can be converted into non-dimensional coefficients of thrust and power, and included in the validation shown as vertical error bars seen in Figure 4.7. As power is a function of turbine rotational velocity, the errors increase with TSR. As C_T is a function of $1/U^2$, and C_P a function of $1/U^3$, the magnitude of the error reduces with increasing flow rate.

Flow velocities are measured using a pitot-static tube, taking pressures at the side wall, where errors are estimated to be below 1% (Bahaj, Molland, Chaplin and Batten, 2007). Velocity taken at this position close to the wall surface are likely to be within the turbulent boundary layer. With no detailed information regarding the flow, the quoted velocity is applied at the hub height within the model, however in reality this value would be greater, as it is further from the boundary. This would result in a higher Reynolds number than that used to generate the hydrofoil lift and drag curves, which would in turn lead to different blade forces, leading to convergence upon different induction factors, and hence different power and thrust values.

The blades are manufactured using a 5-axis CNC machine, within an accuracy of ±0.05 mm. This error in hydrofoil geometry is negligible relative to the size of blade elements, where the average properties of each section are input and interpolated in the numerical analysis. The blades are brought to a smooth finish and anodised. Despite the effects of the blade surface roughness on boundary layer formation, hydrodynamic coefficients predicted by XFoil have larger associated uncertainties.

4.2.9.2 BEMT model conditions

The fluid velocity will be influenced by the friction effects of all the surrounding boundaries, which is not taken into account in the model. Due to the complex interactions of the boundaries on one another, this was simplified to the application of just one shear profile, due to surface friction of the bottom surface. This was considered most appropriate, as the model will be later used to assess full scale turbines in an operational environment, where boundary layers from the sea bed will be the highest contributing factor.

Turbulence intensity is not measured within the experiments, which will change the level of turbulent kinetic energy in the flow, affecting the flow over the blade surfaces, and hence the blade forces and wake formation. The current BEMT model is not capable of modelling such turbulent inflows.

The effects of tower shadowing are not considered in the current BEMT model. In reality, the presence of a structure behind the turbine would cause various levels of wake interference, which would vary depending on the velocity of the fluid as well as the rotational velocity of the turbine.

4.2.9.3 Tip loss effects

To get an approximation of the impact of tip/hub losses on the thrust and power predictions, Cases 1a, 1c and 1d are re-run, with tip and hub loss factors deactivated. Results shown in Figure 4.8 shows that incorporating this factor leads to a reduction of up to 10 % in power and 7 % in thrust.

This shows that accounting for the discreet blade effects is an important factor, which should not be neglected.

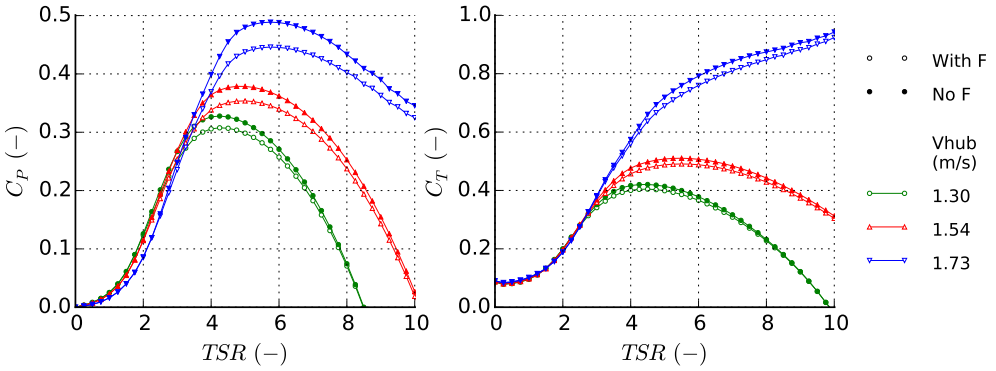

Figure 4.8: Rotor coefficients of power (left) and thrust (right) variation with TSR for cases 1a) 1.3 ms^{-1}, 12° 1c) 1.54 ms^{-1}, 10° 1d) 1.73 ms^{-1}, 5° comparing effects of including a tip/hub loss correction factor (F)

4.3 Case 2: 1/60th scale, low blockage tank experiments

This test case uses experiments from Stallard, Feng and Stansby (2015), which are smaller in scale in order to test array scale models in subsequent studies. As the channel is large compared to the rotor diameter, there is lower blockage, and therefore the results are less impacted by the constraining effects on the wake expansion and velocity shear by the surrounding walls. Input parameters and measurements are taken from Stallard, Feng and Stansby (2015), with additional details of the test set-up found in Stallard et al. (2013). The results from this single turbine arrangement is used in other validation studies of different numerical models from BEMT, RANS-BEM and blade resolved RANS models: Olczak et al. (2016); Masters et al. (2015); Shives and Crawford (2016). These studies are then further developed to assess array interactions, which are also experimentally investigated using this flume and rotor type.

4.3.1 Experimental set-up

The tests are performed in a wide flume situated at the University of Manchester, with a width ten times greater than the depth, and therefore low associated blockage. The working section dimensions and flow conditions are detailed in Table 4.5 (Stallard, Feng and Stansby, 2015)

Table 4.5: Case 2 Manchester flume geometry

Parameter	Value	Units
Length	12.0	m
Width	5.0	m
Height	0.45	m

4.3.2 Flow conditions

The nature of the flume geometry means there are fewer effects from the presence of the boundaries on the inflow profile, minimal restrictions in the transverse wake development, and reduced behaviour of large turbulent structures. Various installations are used to restrict large eddy formation and produce a uniform turbulence intensity, with the longitudinal average measured at 12 % at the rotor plane.

Mean inflow velocity is reported in the reference as 0.463 ms^{-1}, however this is located at height above the channel of 0.315 m. The velocity at the hub height of 0.225 m was 0.45 ms^{-1}, taking the average from the measuremental data.

Figure 4.9 shows the comparison of a uniform inflow and shear profile based on various power laws with velocities measured at 40 depth ordinates within the flume. It can be seen that a power law based on an exponent of 1/10 shows the best agreement with the experimental values.

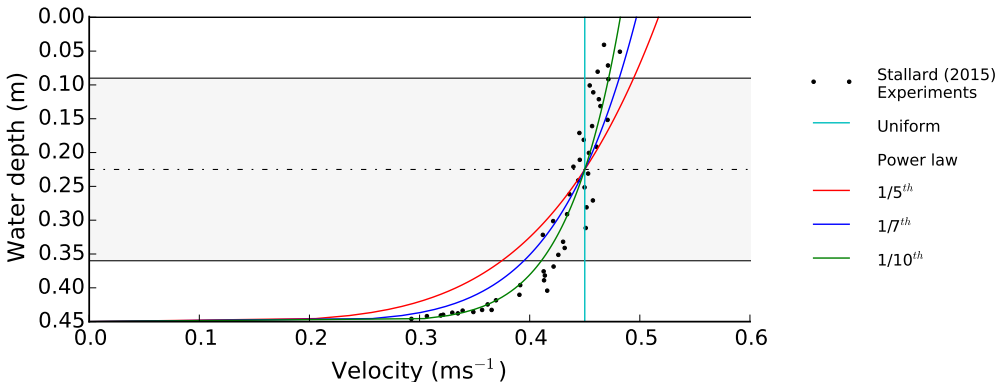

Figure 4.9: Case 2 inflow velocity profiles, showing water depth distributions based on uniform and power law shear profile of various exponents, comparing with measured flume data taken from Stallard, Feng and Stansby (2015). The grey shaded area represents the extents of the turbine.

Figure 4.10 shows a cross sectional view of the channel, with the velocity distribution varying in the vertical direction as a 1/10th power law. Here it can be seen that the turbine is influenced by the presence of the channel base. However, as the channel walls are 5 rotor diameters away from the turbine, it can be seen that even if a non-uniform profile was applied to account for their presence, there would be little influence on the velocity distribution on the disc frontal area and therefore is unlikely to have any real effects on the turbine performance.

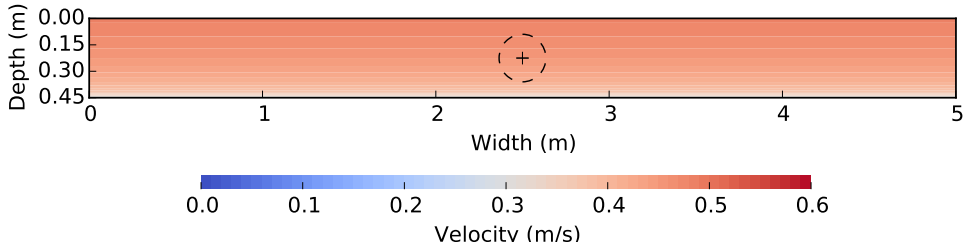

Figure 4.10: Case 2 theoretical 2-D inflow velocity profile within the channel working section at the rotor plane, showing vertical distributions based on a 1/10th power law with U_{hub} =0.45 ms^{-1}. Dashed line represents the turbine circumference when installed

4.3.3 Turbine parameters

The turbine is a 3-bladed, horizontal axis turbine of diameter 270 mm, with a hub diameter of 30 mm. The turbine geometry was selected in order to replicate full scale rotor thrust. Radial geometrical parameters are detailed in Table 4.6.

Table 4.6: Case 2 1/60th scale model turbine geometry

r/R (-)	β (°)	c/R (-)	foil
0.13	38.0	0.111	Gottingen 804
0.18	30.5	0.129	Gottingen 804
0.24	23.0	0.148	Gottingen 804
0.29	19.5	0.185	Gottingen 804
0.33	16.0	0.222	Gottingen 804
0.41	13.7	0.213	Gottingen 804
0.48	11.3	0.204	Gottingen 804
0.54	9.0	0.185	Gottingen 804
0.63	7.5	0.165	Gottingen 804
0.73	5.8	0.144	Gottingen 804
0.83	4.1	0.130	Gottingen 804
0.93	3.1	0.115	Gottingen 804
0.97	2.6	0.096	Gottingen 804

4.3.4 Reynolds number

The tank based Reynolds number (Re_{tank}), based on average inflow and flume height is approximately 2.1E+05. The chord based Reynolds number (Re_{ch}) varies down the length of the blade, and is additionally dependent on the rotational velocity. As before, a single set of parameters is taken to simplify to one Reynolds number of 3.0E+04, based on the chord at three quarters of the blade span (19 mm), and the optimal TSR of 4.5.

4.3.5 Hydrofoil characteristics

The blades comprise of Gottingen 804 hydrofoils, which have associated lift and drag coefficient curves as detailed in Figure 4.11. Here the data is taken directly

from the validation source, where the Viterna extrapolation function was not included as angles of attack do not exceed the quoted values in this case. It can be seen that the data is quite sparse, and the section stalls very abruptly at a relatively low angle of attack of 8°. Values are not corrected for the stall delay of rotating foils, where the Du-Selig and Eggers model detailed in Appendix 2 Section 1 is not applied. A single set of values is therefore used down the entire length of the blade.

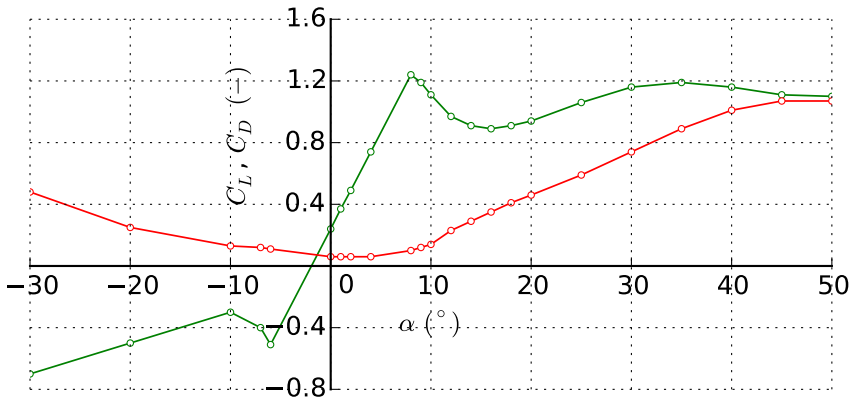

Figure 4.11: Gottingen 804 hydrofoil C_L (green) and C_D (red) curves at Re_{ch} = 3.0E+04, taken from Stallard, Feng and Stansby (2015)

4.3.6 Blockage correction

The global blockage, as a proportion of the rotor swept area to the channel section area, is only 2.5 %. The wake development is therefore considered unconstrained by the walls in the transverse direction, as width = 18.5 D. Therefore no blockage correction is required.

4.3.7 Numerical implementation

Figure 4.12 shows the azimuthal average blade distributions of induction factors, where it again can be seen that the transition to the highly loaded regime is exceeded at the highest TSR, localised to the blade tips. This shows there is a use

of the highly loaded correction factor, but due to the irregularity and magnitude, these effects are thought to be minimal. At a TSR of 4, a step increase of induction factor is seen around 1/3rd of the way down the blade. Scrutinising the angles of attack for this region reveals values around 8-10°, where a peak in the lift coefficient is seen from Figure 4.11. As with Case 1, the tip/hub correction is being applied effectively, again more influential at the tips at lower TSR.

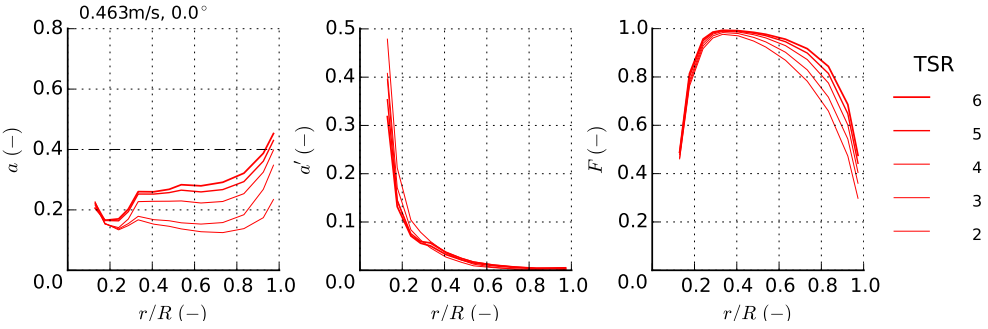

Figure 4.12: Case 2 azimuthal average radial distribution of axial induction (left), tangential induction (centre) and tip/hub loss (right) factors at various TSR

4.3.8 Validation

Figure 4.13 shows the results of the validation, again based on non-dimensional C_P and C_T against TSR. The results of the present study show good agreement to those generated using a BEMT commercial code Tidal Bladed (DNV GL Garrad Hassan, 2012*b*) confirming the theory is well implemented into the code. The largest difference is seen at optimal TSR = 4, where the current study estimates a 10% lower peak power.

The measured data for this experiment contains considerably more spread than other test cases analysed. Thrust variations of up to 8 % are seen, whereas power varies by up to 40 %. This relatively large range within the power data points is thought to be due to the variation seen in the inflow velocity profile, as shown in Figure 4.9.

The BEMT model predicts power comparable to that measured in the experiments, however are usually in the lower limit of the range. Thrust trends are generally well matched, with some under prediction of up to 12 % seen at higher TSRs.

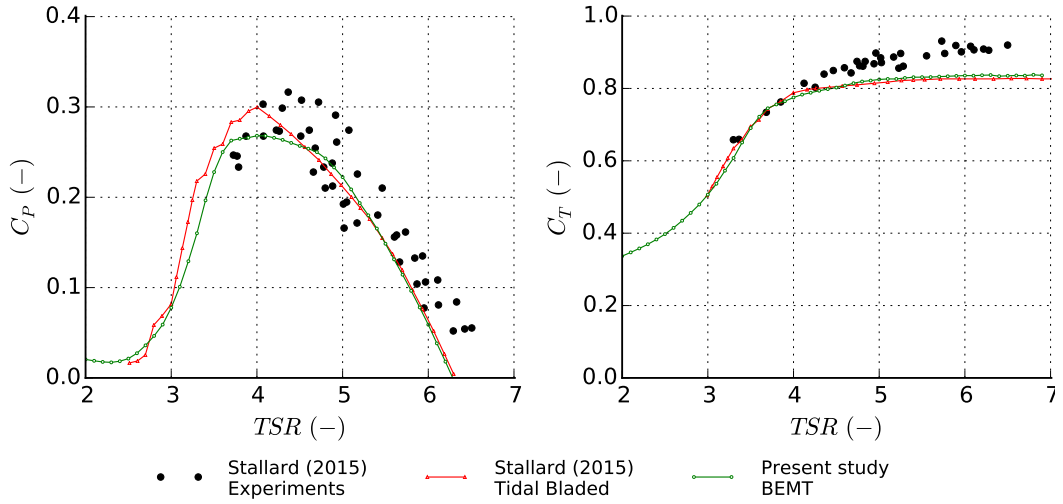

Figure 4.13: Case 2 rotor coefficients of power (left) and thrust (right) variation with TSR, with comparisons against experimental measurements and output from BEMT model Tidal Bladed (Stallard, Feng and Stansby, 2015)

4.3.9 Radial variations

Up to this point, power and thrust coefficients of the entire rotor are compared. Additionally, the radial distribution of specific parameters can be output from the model, to compare the induction factors predicted for each annular ring, or blade element. As there is a shear inflow applied to the model, the values will vary azimuthally, therefore averages are taken over one turbine rotation.

At the peak power condition, defined by the experiments occurring at TSR = 4.5, a comparison is made with a coupled RANS-BEM (a 2-d method defined in Section 4.4.8) (Olczak et al., 2016), as shown in Figure 4.14. It can be seen

that the axial induction predictions vary significantly at the tip. For the RANS-BEM case, the tip/hub loss corrections are applied to the axial induction factor, hence their lower predictions. In order to make direct comparisons, the axial induction factors from BEMT are multiplied by the tip/hub loss factor, which then gives much better agreement.

The CFD model predicts higher tangential induction factors along the majority of the blade length, which results in higher overall rotor power estimations. This could be related to the turbulence intensity, which is accounted for in the study, which increases the kinetic energy of the flow available for extraction.

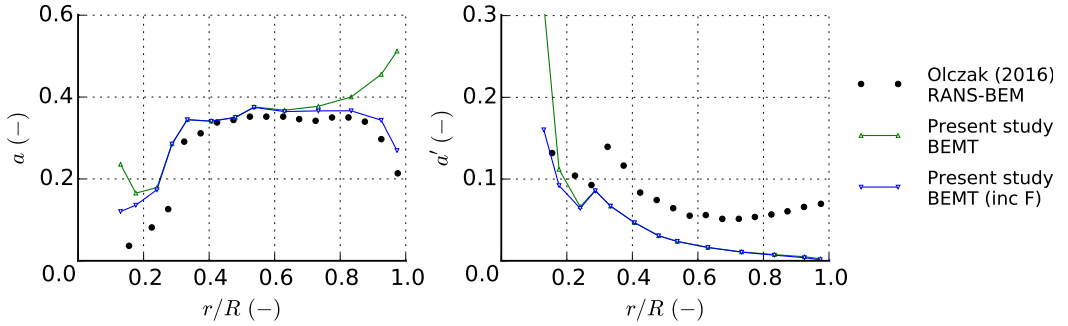

Figure 4.14: Case 2 azimuthal average axial (left) and tangential (right) induction factors against normalised radius, comparing BEMT predictions with data from a RANS-BEM model (Olczak et al., 2016)

4.3.10 Case discussion

In general, results from the BEMT code are in very good agreement to the experimental data. However there is a large spread in measured power points, which makes it difficult to make direct comparisons. There are some under predictions in thrust observed, by up to 10% at the highest TSRs.

4.3.10.1 Hydrofoil coefficients

Lift and drag coefficients for the Gottingen 804 foil reported by the source from wind tunnel experiments are quite sparse, and contains a sharp stall region. As

the BEMT interpolates linearly between the coefficients, discontinuities can occur with a small change in inflow angle (as a result of the convergence procedure within the iterative loop), caused by large jumps in the lift and drag data within the lookup table. A study (Masters et al., 2015) assessing the influence of modifying the lift and drag coefficients by set proportions result in a significant difference in the power and thrust predictions, as well as the optimal TSR. This suggests a high sensitivity to the hydrodynamic coefficient prescribed to the model for this case.

4.3.10.2 Experimental parameters

At positions 2.5 D either side of the turbine centreline, there are some flow reductions attributed to regions of transverse circulation. However, these were found to be low, with an average of the vertical and transverse components $< 0.05U$. Therefore the span-wise variations in velocity are ignored when calculating the average inflow velocity.

Angular displacement is measured to a resolution of $\pi/100$, differentiated to determine the angular velocity Ω. Samples are taken at 200 Hz, and therefore angular velocity is obtained within 0.1 % accuracy.

Strain gauges are used to measure the combined thrust of both the rotor and the tower during the experiments (F_{total}). In order to quote values of the thrust on just the rotor (F_{ax}), tests are run with the rotor removed to assess the axial forces on just the tower (F_{tower}), which averaged at 0.26 N. This value is then removed from the overall thrust such that: $F_{ax} = F_{total} - F_{tower}$. This assumes that the force on the tower will be identical when the rotor is reattached, deemed to be acceptable as forces are one order of magnitude less than those measured on the rotor at around 6 N.

No data is provided on the accuracy of the strain gauges, which could have a high influence on the C_T and C_P due to the low flow inflow velocity.

4.4 Case 3: 1/30th scale experiments

This final case is based on experiments (Buvat and Martin, 2010) aimed to investigate the performance and wake of a scale model TST, with the purpose of validating numerical models. Tests are performed as part of the PerAWaT (Performance Assessment of Wave and Tidal array systems) project, a research and development project funded by the Energy Technologies Institute (ETI). This is a partnership between industrial companies DNV-GL, EDF and E.ON, as well as the Universities of Edinburgh, Oxford, Manchester and Queens, Belfast.

The project is split into four work groups, with WG3 and WG4 involved with tidal energy, focussing on numerical modelling and experimental testing respectively. WG4 is further split into two work packages, the first concerning the 1/30th scale test, further split into 4 work documents which are used in this study: Buvat and Martin (2010); Buvat (2010); Buvat (2011); Buvat (2012).

4.4.1 Experimental set-up

Experiments are carried out in a flume at the Electricité de France (EDF) national research and development laboratory for hydraulics and environment (LNHE) located in Chatou, France. The working section dimensions and flow conditions are as detailed in Table 4.7 (Buvat and Martin, 2010). The experimental set up of the turbine within the flume is shown in Figure 4.15.

Table 4.7: Case 3 EDF flume parameters (Buvat and Martin, 2010)

Parameter	Value	Units
Length	70.0	m
Width	1.5	m
Height (max)	1.2	m
Height (used)	0.8	m
Max flow rate	1000	Ls^{-1}

Figure 4.15: Case 3 images of the flume experimental set-up, with installed turbine and test rig, taken from Buvat and Martin (2010)

4.4.2 Flow conditions

Three inflow velocities are tested, as detailed in Table 4.8 measured using ADV sensors at hub height, 5 D upstream of the rotor.

Table 4.8: Case 3 test inflow velocities

Case	Velocity (ms^{-1})
3a	0.27
3b	0.41
3c	0.55

4.4.2.1 Theoretical velocity distribution

Here, the main interest is in Case 3c, the largest inflow test of 0.55 ms^{-1}, equivalent to 3 ms^{-1} full scale. The average transverse turbulence intensity is relatively low, measured at 6-7 % (Buvat, 2012).

Figure 4.16 shows inflow profiles for Cases 3a and 3c, comparing a uniform inflow for 0.27^{-1} and 0.55 ms^{-1} at hub height, with power law shear profiles of varying

exponent values, and experimental measurements within the flume. It can be seen that there is very little spread in the experimental data, as a single set of time average data is reported in Buvat (2011). The $1/7^{th}$ power law shows the best agreement to the measurements, which will be used within the proceeding study. As no data is available regarding Case 3b at 0.41 ms^{-1}, a similar profile is assumed, so the same power law is applied.

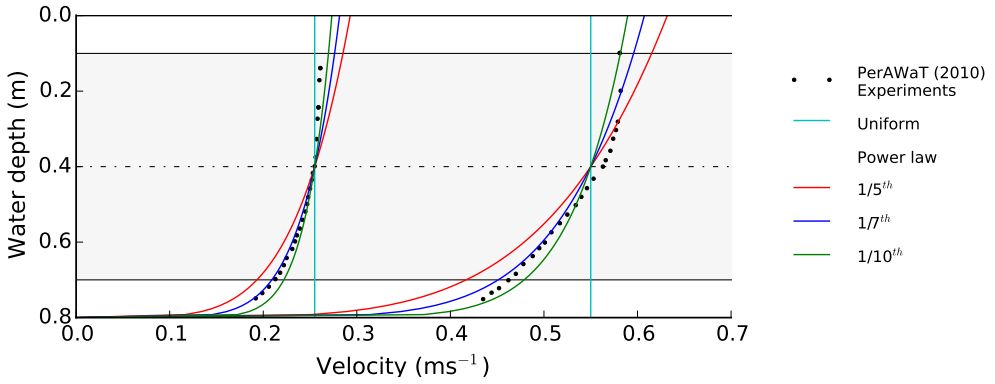

Figure 4.16: Case 3a and 3c inflow velocity profiles, showing water depth distributions based on uniform and power law shear profile of various exponents, comparing with measured flume data taken from Buvat (2012). The grey shaded area represents the extents of the turbine when installed

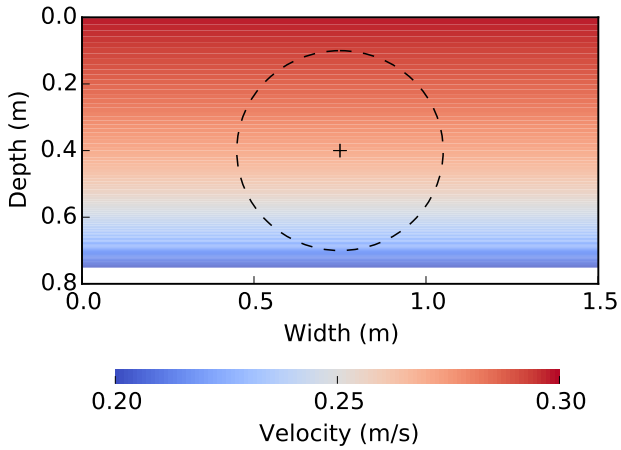

Figure 4.17: Case 3a theoretical 2-D inflow velocity profile within the channel working section at the rotor plane, showing vertical distributions based on a $1/7^{th}$ power law with $Uhub$ =0.27 ms^{-1}. Dashed line represents the turbine circumference when installed

Figure 4.17 is a cross section view of the flume working area, showing a theoretical two dimensional view of the Case 3a flow velocity based on a $1/7^{th}$ power law.

4.4.2.2 Measured velocity distribution

As the flume height is quite small at 1.33 D, there are quite significant influences on the velocity distribution across the rotor frontal area from the bottom friction. As the flume width is 2.5 D, there are also interactions on the flow from the side walls, which have proven to cause significant issues in generating a smooth flow field within the experiments (Buvat, 2011). Additional influences arise from the close presence of a free surface, typical of open channel flows.

The distribution of measured velocity (McIntosh et al., 2010) across the plane parallel to the rotor for Case 3a is shown in Figure 4.18. There are some non-uniform width wise variations seen here resulting from friction at the walls, however these are quite small over the frontal area of the turbine.

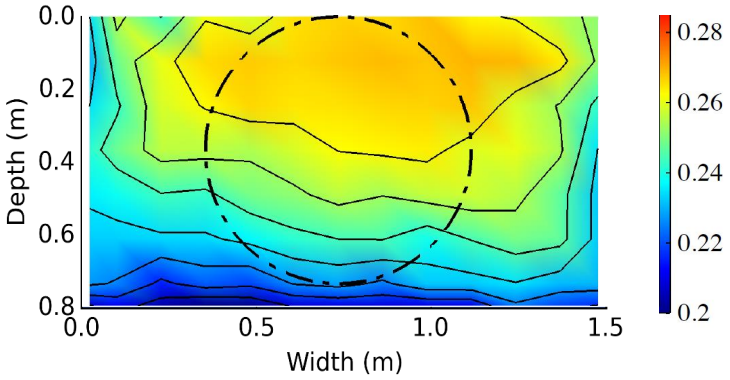

Figure 4.18: Case 3a measured inflow velocity profile within the channel working section at the rotor plane, reconstructed from McIntosh et al. (2010). Dashed line represents the turbine circumference when installed

For faster inflows however, much larger span-wise variations are observed. Case 3c is shown in Figure 4.19, where a velocity deficit can be seen at the base of the tank (note that this figure is taken from tests where a higher turbulence is artificially generated). The deficit was considered due to Prandtl's secondary

flows circulating within the flume, driven by turbulent stresses. Prior to turbine installation, attempts were made to reduce these secondary flows, which improved (to an extent) the flow field uniformity, however it was not possible to completely eliminate the vortices. Each vortex from each side wall were seen to interact with each other, thus preventing dissipation. The reference study concluded these effects were due to the inherent nature of flumes with low width to height ratios (McIntosh et al., 2012). This is thought to have a considerable impact on the blade forces.

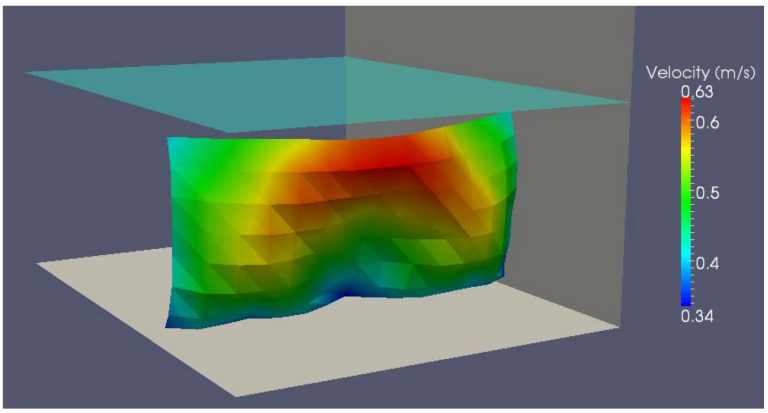

Figure 4.19: Case 3c measured inflow velocity profile within the channel working section at the rotor plane, taken from Buvat (2010), without turbine installed

4.4.3 Turbine parameters

The rotor diameter of 600 mm, and a hub diameter of 86 mm, with radial variations of geometrical parameters detailed in Table 4.9. A blade model is also supplied by EDF, shown in Figure 4.20. The geometry of the device is modified to replicate thrust level variations with TSR seen by the full scale rotor, as justified in Whelan and Stallard (2011).

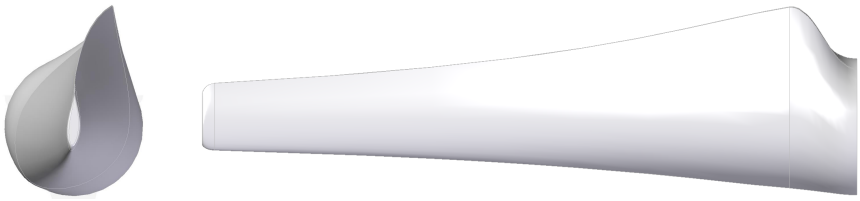

Figure 4.20: Case 3 frontal and side views of full scale TST blade 3-D CAD model

Table 4.9: Case 3 1/30th scale model turbine geometry (Ingram, 2012)

r/R (-)	β (°)	c/R (-)	t/c (%)	foil
0.158	32.00	0.067	100	Circle
0.200	31.04	0.067	15	NACA 4415
0.233	29.22	0.100	15	NACA 4415
0.267	26.62	0.167	15	NACA 4415
0.300	25.78	0.167	15	NACA 4415
0.333	24.16	0.233	15	NACA 4415
0.367	22.60	0.267	15	NACA 4415
0.400	21.10	0.300	15	NACA 4415
0.433	19.67	0.300	15	NACA 4415
0.467	18.31	0.300	15	NACA 4415
0.500	17.01	0.300	15	NACA 4415
0.533	15.77	0.267	15	NACA 4415
0.567	14.60	0.267	15	NACA 4415
0.600	13.49	0.267	15	NACA 4415
0.633	12.45	0.233	15	NACA 4415
0.667	11.47	0.233	15	NACA 4415
0.700	10.56	0.233	15	NACA 4415
0.733	9.71	0.200	15	NACA 4415
0.767	8.92	0.200	15	NACA 4415
0.800	8.21	0.200	15	NACA 4415
0.833	7.55	0.167	15	NACA 4415
0.867	6.96	0.167	15	NACA 4415
0.900	6.44	0.133	15	NACA 4415
0.933	5.97	0.133	15	NACA 4415
0.967	5.58	0.133	15	NACA 4415
0.992	5.11	0.100	15	NACA 4415

4.4.4 Reynolds number

The tank based Reynolds number (Re_{tank}), using average inflow and flume height is between approximately 2.2E+05 - 4.4E+05.

Initially, the chord based Reynolds number (Re_{ch}) was calculated at 4.0E+04, taking just the average inflow velocity in Case 3c. This therefore represents a minimum, as any rotation would increase the velocity of flow over the foil, increasing the Reynolds number. The geometry was changed (as justified in Whelan and Stallard (2011)), to increase the Reynolds number to be more representative of a full scale TST. This had a representative Re_{ch} = 8.0E+04, which was deemed appropriate as it exceeds the transition from laminar to turbulent flow at 7.0E+04, where the hydrofoil characteristics change dramatically.

If the resultant fluid velocity due to turbine rotation is accounted, in consistency with previous cases based on the chord at three quarters of the blade span (60 mm), and the optimal TSR = 3.5 is considered: For Case 3a, a Re_{ch} = 5.0E+04 was calculated, which increases to the transition point of 7.0E+04 only at TSR = 5. This case is therefore thought to be affected by highly complex interactions as the fluid changes from a laminar to a turbulent flow regime. For Cases 3b and 3c, Re_{ch} = 1.0E+05.

4.4.5 Hydrofoil characteristics

The blades comprise of NACA 4415 hydrofoils, which have lift and drag curves as shown in Figure 4.21a for Re_{ch} = 5.0E+04, and in Figure 4.21b for Re_{ch} = 1.0E+05. It can be seen that the Reynolds number does not have a large impact on these curves.

These hydrodynamic characteristics were generated (similarly to Case 1) using XFoil (Drela and Youngren, 2001), applying a Du-Selig and Eggers correction

factor for stall delay of a rotating blade (Brenton et al., 2007) and extrapolated past stall using a Viterna function (Viterna and Janetzke, 1982).

A cylindrical blade section is used to represent the geometry of the root connecting to the hub, which has an assumed drag coefficient $C_D = 0.5$ for all angles of attack (Ingram, 2012).

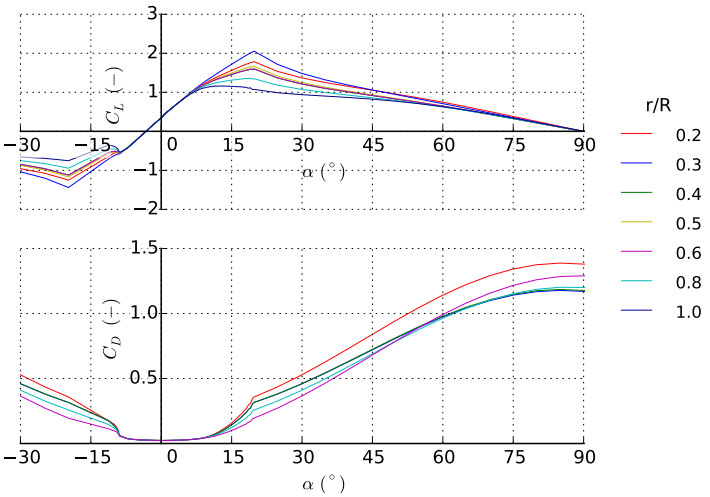

(a) Re_{ch} = 5.0E+04

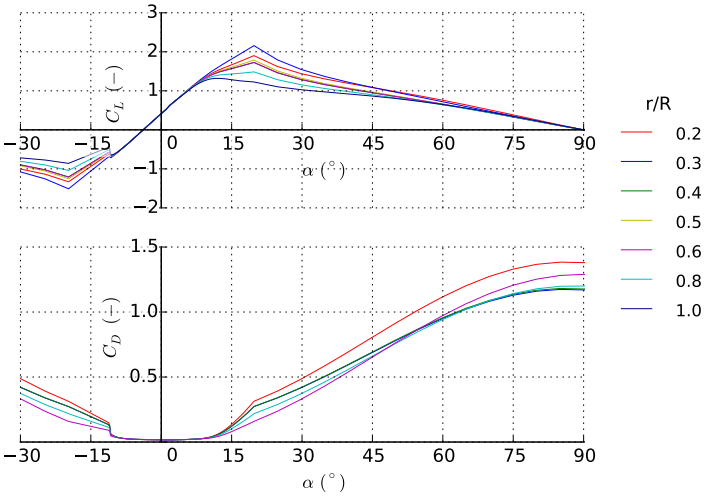

(b) Re_{ch} = 1.0E+05

Figure 4.21: NACA 4415 hydrofoil C_L and C_D curves for various normalised radii

4.4.6 Blockage correction

The global blockage ratio based on the turbine to channel section area is 23.6 %. As recommended by the data source, the experimental measurements are applied with a blockage factor, to convert values into 'open water equivalents', detailed in Table 4.10. The ratio of bounded flow to equivalent open water velocity was determined as $(U/U_f) = 0.94$ using the iterative procedure defined in Appendix 1, Section 2.

Table 4.10: Case 3 blockage correction factors for $C_T = 0.85$

Parameter	Blockage Correction Factor
TSR	0.94
C_T	0.88
C_P	0.83

4.4.7 Numerical implementation

Figure 4.22 shows the blade distributions of induction factors for Case 3c, where it again can be seen that the transition to the highly loaded regime is exceeded only at the blade tips. This again shows minimal dependence on the highly loaded correction factor. At TSR of less than 4, lower axial induction factors are seen, which, when scrutinising the angle of attack for this region, are due to operation in the stall regime. It is noted that tangential induction factors are higher, on average, relative to other cases, which would lead to high affiliated rotor torques. Results corresponding to Cases 3a and 3b are sufficiently similar that they are not shown here.

4.4.8 Reference RANS model parameters

Additional data for the comparison in this case is taken from two CFD studies performed by McIntosh et al. (2010). The first employs a Reynolds Averaged Navier Stokes representation of the flow field, but resolves the blade forces using

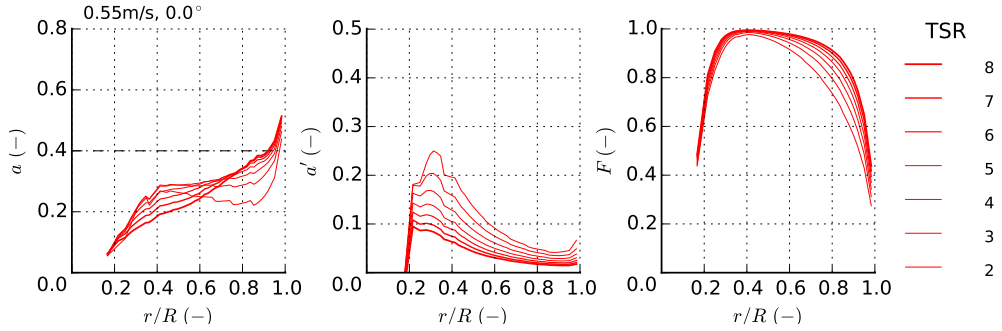

Figure 4.22: Case 3c radial distribution of axial induction (left), tangential induction (centre) and tip/hub loss (right) factors at various TSR

BEM (known as coupled RANS-BEM). The second uses fully blade resolved RANS, where both the flow field and the rotor are modelled using a RANS representation. This method resolves the fluid flow around the blades, including within the viscous boundary sub-layers, and therefore requires a very fine mesh close to the blade surfaces.

The turbine geometry differs slightly, as blade chord and twist distributions are taken from the CAD model used in turbine manufacture, rather than quoted by the source.

The simulations use a k-ω SST turbulence model, account for the hub, nacelle and tower structures, and use a domain representative of that constrained by the flume, where two representations of the free surface are applied (full parameters can be found in (McIntosh et al., 2010)). Power and thrust coefficient curves are published in McIntosh et al. (2012).

4.4.9 Validation

Figures 4.23a - 4.23c show the results of the validation, again based on non-dimensional power and thrust against TSR. Here comparisons are made with experimental data, as well as two CFD models using blade resolved RANS and coupled RANS-BEM models.

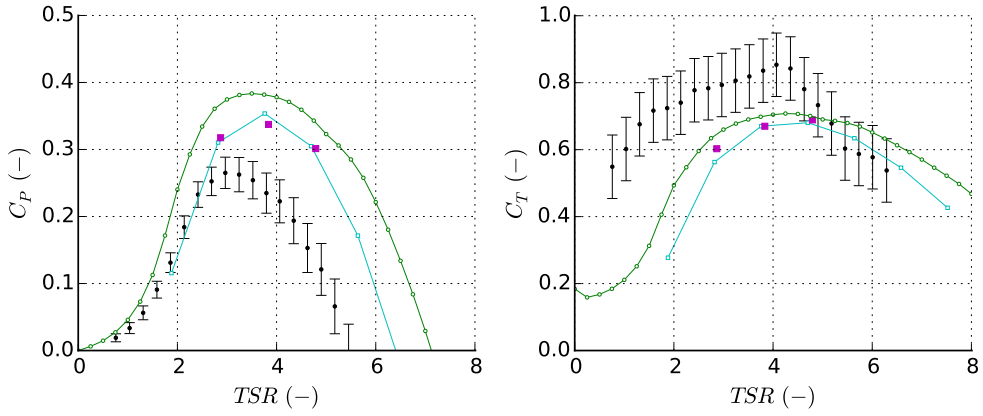

(a) 0.27 ms^{-1}

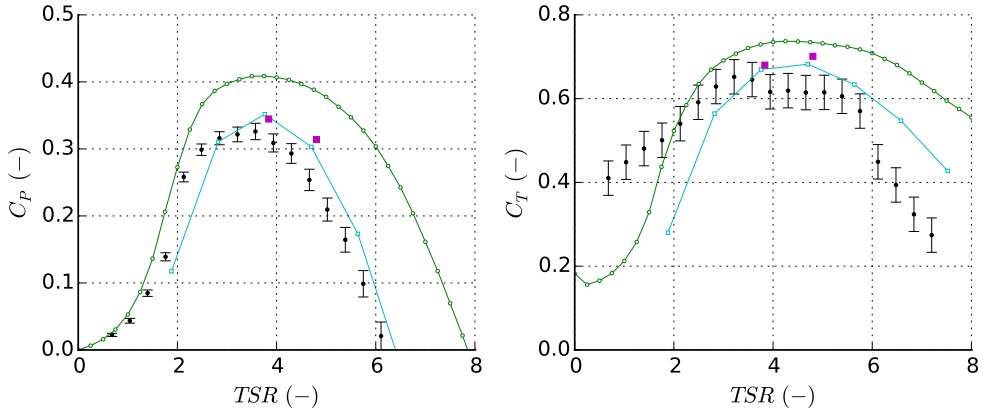

(b) 0.41 ms^{-1}

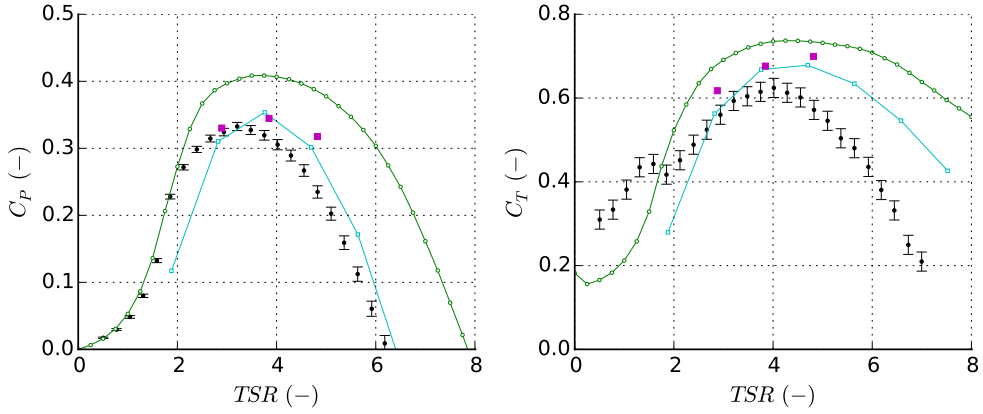

(c) 0.55 ms^{-1}

Figure 4.23: Rotor coefficients of power (left) and thrust (right) variation with TSR, comparing against experimental measurements (Buvat, 2012) and CFD studies using RANS-BEM and RANS blade resolved models (McIntosh et al., 2012)

4.4.9.1 Experimental accuracy

Manufacturers quoted accuracy of measuring instrumentation from Buvat (2011) are taken as worst case at ± 0.025 Nm torque, and ± 1.0 N in thrust. These are translated to C_P and C_T and shown as vertical error bars in Figures 4.23a - 4.23c. The Acoustic Doppler Velocimeters (ADVs) have a precision of ± 0.25 cms^{-1}, equivalent to a maximum of 1 % flow velocity in this case.

As power is a function of turbine rotational velocity, the errors increase with TSR. As C_T is a function of $1/U^2$, and C_P a function of $1/U^3$, the magnitude of the error is highest for Case 3a.

4.4.9.2 Comparison with experiments

Case 3a shows significant differences, thought to be due to the close proximity of the flow to the transition between laminar and turbulence regime, causing complex interactions with the blades, and resulting in varying (and highly difficult to predict) dynamic behaviour of the hydrofoil characteristics. Coupled with the large range due to errors associated with accuracy of measuring equipment (particularly in thrust) there is limited confidence in these results. This is therefore used only as an illustrative case.

Case 3b also has relatively high error ranges, particularly in thrust, due to the low flow velocity. The BEMT model follows a similar trend in power, where the optimal TSR is well captured at around 3.8. However, over predictions are seen in both power and thrust throughout the results, particularly at the higher rotational velocities. At optimal TSR, over predictions are seen in C_P by 27 % and C_T by 6 %.

Case 3c exhibits more reasonable error ranges. The BEMT model again follows a similar trend in power, however over predicts the optimal TSR by 8 %. Over predictions in power and thrust are again observed throughout the data,

particularly at higher TSR At optimal TSR, over predictions are seen in C_P by 20 % and C_T by 16 %.

4.4.9.3 Comparison with RANS BEM

It can be seen that there are few data points from the CFD studies, particularly using a RANS blade resolved model, due to higher associated computational costs. It is reported that each case using the RANS-BEM model were completed in 32 CPU-hours, whereas the blade resolved case within the same study, using the same computational set up, required 100 CPU-hours per turbine revolution (McIntosh et al., 2012). The very few blade resolved data points lie within 6 % in C_P and 4 % in C_T of the coupled RANS-BEM model. This suggests that the blade element theory is able to well replicate results from fully resolving the flow around the blades, whilst requiring only a fraction of the computational time.

For all three cases, the BEMT model shows a very similar trend to that of the coupled RANS-BEM, with an optimal TSR at approximately 3.8. The BEMT model however, consistently predicts higher power and thrust, at a maximum of 17 % in power, and 8 % in thrust at optimal TSR. To put this in perspective in terms of computational requirement, the present BEMT simulations were performed using a laptop running an $Intel\ Core^{TM}\ i5$ 2.9 GHz dual core processor with 8 GB RAM. All points on the power and thrust curves were generated within 3 minutes, equivalent to ∼6 core minutes.

4.4.10 Case discussion

4.4.10.1 Flume flow distribution

Generally, the forces predicted by the BEMT model are higher than those measured in the experiments. The cause is thought to stem from the complex velocity profile measured within the section of the flume.

There is a velocity deficit discovered in the base flow assessments from Prandtl's

secondary flows circulating within the flume. This flow is driven by turbulent stresses, which were attempted to be removed prior to turbine installation, however could not be completely eliminated due to the inherent nature of flumes with low width to height ratios (McIntosh et al., 2012). These effects are seen to disappear only for width to height ratios of 5. This is thought to be the main cause of disparity seen between the numerical and experimental results.

This flume geometry also gives rise to relatively high blockage correction factors applied to the data, which again shows a high dependency on this factor.

4.4.10.2 BEMT model conditions

Over predictions at higher TSR for all cases are thought to be due to the greater influence of rotational velocity on the span-wise flow down the blade lengths. As one of the main assumptions in blade element theory is taking each discrete hydrofoil section independently, 3D flow between sections is neglected. As span wise flow is thought to increase with rotational velocity, this is considered to be one contributing factors to the disparity seen in the results.

For this case, there are relatively large changes in chord and twist along the blade length. As the blade element theory splits the blade into a number of discrete hydrofoils modelled independently, flow parameters are averaged over the length of each element. This could be improved through smaller element sizes, however is restricted in this case due to the availability of more detailed blade data.

In the coupled RANS-BEM model, the effects of the free surface are tested by carrying out two simulations: a rigid lid and volume of fluid treatment of the top surface. Negligible impact on the rotor power and thrust is shown by McIntosh et al. (2012), suggesting minimal dependence on the presence of the free surface.

4.4.10.3 Inflow dependency

One additional observation is that both CFD and BEMT models show very little dependence on inflow velocity. This is due to non-dimensionalising all factors with respect to inflow velocity. BEMT predictions for Case 3b and 3c are identical, however Case 3a shows some differences due to the different lift and drag coefficients used in this case (see Figure 4.21a). Measured data for Cases 3b and 3c show a slight dependency on inflow, where increasing velocity increases C_P and decreases C_T values. Due to the error bars and the large variations in flow velocity measured through the channel section, the reason for this observation is unknown.

4.5 Overall discussion

Hydrodynamic models are used to attain information on how a turbine will operate in its working environment. BEMT is a well established method in the wind industry, and more recently adopted in the field of TSTs. Models based on the BEMT have been shown to successfully predict power and thrust curves, showing good agreements to physical models and more complex CFD studies. General observations show that for all cases, the model over predicts power at high TSR, thought to be associated with fundamental assumptions inherent to the theory.

4.5.1 Summary

The aim of the work performed within this chapter was to develop a hydrodynamic model with the following key attributes: high adaptability to easily implement modifications in order to analyse alternative turbine designs; capability to predict blade distributions of force; ability to apply non-uniform inflow profiles for analysis of cyclic blade forces; low numerical complexity, to enable high numbers of fast running simulations under various inflow conditions. This is believed to have been achieved with the following outcomes:

4.5.1.1 Accuracy

The code is validated against rotor average values of thrust and power against numerous different scale model cases. Results show excellent correlation to other numerical models published in the literature, showing good implementation of the theory.

In general, the BEMT shows very similar trends to those measured in the experiments, capturing the peak power condition well. In two of the three test configurations analysed (Cases 1 and 2), excellent agreement of within 10 % of physical model measurements at optimal rotational speeds. Turbines are designed

to run as close to this optimal TSR as possible, in order to attain the maximum power output under different flow conditions. This confirms the appropriateness of the method and selection of the modelling techniques for this application.

In extremely fast flows the turbine can use over speed control, where the TSR is raised in order to limit the blade forces. BEMT is less able to well predict power and thrust at high TSRs, where disparities against experimental measurements of up to 25% are observed. This suggests a lower suitability for application to turbines employing over speed control, and care should be taken when using BEMT predicted blade forces in these conditions.

Comparison with Case 3 measured data shows less good correlation with differences of up to 27 % in power and 16 % in thrust at optimal TSR. There is improved agreement seen using RANS models, however at significantly higher computational costs. The cause of the differences are thought to stem mainly from flume geometry causing relatively high blockage as well as turbulent stresses driving secondary flows. This cannot be captured by the BEMT method, highlighting a limitation when considering highly complex inflows. In addition, other contributing effects considered influential are: relatively high errors in the measuring equipment and large changes in chord and twist down the lengths of the blades.

4.5.1.2 Adaptability

The code employs various read-in functions designed to accept simple text files defining turbine geometry, blade element geometry, hydrofoil coefficient curves, fluid properties and boundary conditions. User defined functions are included for simple enabling / disabling of correction factors, as well as defining: inflow profile type; acceptable induction factor tolerance and desired output (individual element forces, blade average forces, rotor averaged coefficients). An iterative looping function is applied, which is easily modified depending on the most appropriate routine.

Scripts are written to pre-process hydrofoil data into a format directly readable into the code. Additional scripts are written to post process outputs into a format for direct comparison with validation data, or for entering into stress analysis models.

4.5.1.3 Numerical complexity

In general, the BEMT method has a low computational demand, however there are additional factors which can be implemented to combat the effects of model simplifications, which increase the numerical complexity and therefore the computational intensity of the model. Various corrections and pre processes taken from the literature are assessed and applied to the model where they are believed most appropriate without compromising on numerical stability and running times. Final computational time for generating power and thrust curves using this model is in the order of a few CPU-minutes. In contrast, coupled RANS-BEM models report in the order of CPU-days, and RANS blade resolved studies in the order of CPU-weeks. This shows a high level of appropriateness for use in blade structural integrity analyses, where numerous simulations are required to examine the blade forces under various operating conditions.

4.5.1.4 Non-uniform inflows

Non-uniform inflow profiles can be applied, through incorporating an additional loop, stepping with azimuth during each turbine rotation. Within each loop, the local velocities are calculated, depending on the position of each blade element relative to the sea bed. Elemental axial and tangential forces are then balanced and output as a function of azimuth. The variation of blade forces during one rotation can then be calculated, and from this the cyclic loads. Computational times increase almost linearly with the number of azimuth angles analysed, due to the linear increase in the number of iterative loops to be solved in each simulation. However, with a vertical shear profile, it can be easily seen that maximum forces occur at the top dead centre (12 o'clock position), and minimum at bottom dead

centre (6 o'clock position), thus the range in cyclic loads can be determined simply by running two simulations.

4.5.2 Reliance on BEMT modelling parameters

Performing an in-depth sensitivity analysis to the various input data, correction factors and modelling assumptions is not a main objective of this study. During the construction of the model, however, impacts from using different data were observed, and common themes seen in the literature, giving indications on where sensitivities lie. This gives useful indications on the parameters where most care should be taken.

4.5.2.1 Correction factors

In all cases, the highly loaded regime is only reached during occasional rotational velocities, and is localised at the blade tips. Therefore there is minimal dependency on the highly loaded correction factor. This is considered a positive, as the correction factor is semi-empirical, based upon experimental data from a relatively dated source with considerable scatter (Burton et al., 2011).

The blockage correction is seen to be substantial, reducing experiment power predictions by up to 18%, and thrust by up to 11% to get to open water equivalent values. This shows a substantial reliance on the accuracy of this correction formulation. These effects can be reduced through experiments in larger tanks, such as with Case 2. Although influential in experimental set ups, this correction will no longer be required when performing analyses of full scale turbines in open water.

The tip/hub loss correction is considered extremely important as it is accounts for lower hydrodynamic efficiencies and therefore directly impacts the blade forces. Although the highest losses are seen localised at the tip and hub, most elements

are impacted by these factors at all TSRs. This was seen in Case 1 to reduce power predictions by up to 10% and thrust by 7%.

4.5.2.2 Inflow velocity profile

A non-uniform inflow profile is applied to all cases, based on a vertical shear profile from bottom friction. This velocity does not significantly affect the results compared with a uniform profile. As the velocity profile is almost linear across the rotor area, the average will lie close to that of the uniform profile, taking the average hub height velocity at all depths. As the calculations are of overall rotor power and thrust, which are averaged over one rotation, these are almost identical. The difference lies in the variation of blade forces with azimuth, which is not assessed in this chapter.

Fluid shear from the walls of the channel have not been explored in this study, however could be incorporated into the model. This is a slightly more complicated procedure than purely changing the velocity distribution in the horizontal plane as well as the vertical, as there would be interactions of boundaries upon one another. The position of the blade elements at each azimuth could be determined relative to all boundaries, and the local flow velocity at this location used in the momentum balance, thus predicting reduced forces. However, inclusion would impose additional numerical complexity to the model, and is only relevant to flow in experimental channels rather than in real tidal flows, where the final model is to be applied.

4.5.2.3 Reynolds number and hydrodynamic coefficients

Chord based Reynolds numbers are calculated based on the resultant velocity from the inflow and rotation of the turbine. However, in order to reduce the number of calculations, this is simplified to a single value, based on the hub height flow velocity and one rotational velocity. Additionally, the characteristic length is taken at a single point along the rotor blade. For the entire range of

TSR and chord lengths along the blade, the Reynolds number can vary by an order of magnitude. Although this does not have a direct impact on the model calculation, the hydrodynamic coefficients of lift and drag are dependent on the Reynolds number.

In the design of the turbine for Case 3, Tidal Bladed was used to gain initial performance approximations. It was noted that during this study, there was an uncertainty in predictions, arising mainly from uncertainties in the lift and drag data. An extensive review of the available data for NACA4415 hydrofoils with the Reynolds number range of interest concluded there is a limited amount of data available, and there was "varying reliability" within the datasets (Buvat, 2012).

It can be seen that lift and drag coefficients for Case 3a (Figure 4.21a, $Re_{ch} = 5$ x 10^4) and Case 3b (Figure 4.21b, $Re_{ch} = 1$ x 10^5) are extremely similar. However, there is a considerable difference seen in the power and thrust curves as a result, of 7 % at optimal TSR. This shows a sensitivity to hydrofoil coefficients when predicting rotor performance, and highlights the need to accurately predict lift and drag curves. This is further emphasised in a sensitivity study (Masters et al., 2015), which assesses the impact on Case 2 results when lift and drag coefficients are modified by arbitrary amounts designed to represent changes in surface roughness from degradation or biofouling. Reported here is a 40 % reduction in power when C_D is increased by 50 % and C_L increased by 10 %. Although it should be noted that the Manchester experiments are designed to replicate the full scale thrust, and therefore effects on power are thought to be atypical.

4.5.2.4 Free surface effects

The presence of an open surface in the flume configurations causes a drop in the water height just upstream of the rotor, caused by a reduction in the fluid velocity. RANS simulations of Case 3 test two models comprising of a rigid lid and volume of fluid representation of the flume. The results show negligible difference (McIntosh et al., 2012), demonstrating a lack of influence from the presence of

the free surface. Additionally, in real applications the free surface will be in even lower proximity to the turbine, therefore it is considered acceptable to neglect their effects at this stage.

4.5.2.5 Flow assumptions

The inflow is assumed to be constant, where no dynamic effects are accounted for within this BEMT code. Various levels of turbulence intensity is observed within the experiments, which is thought to have influences on the loading conditions. These may be averaged out over the whole rotor, and thought to have a higher influence when assessing the forces of the individual blade elements. Additionally, the flow is always assumed to be perpendicular to the rotor plane with no yawed effects taken into account.

4.5.2.6 Tower effects

In all physical experiments, the rotor is suspended in the water column by fixing to a vertical tower. In Case 2, thrust forces are measured on the rotor and tower combined, which are corrected using prior measurements of thrust on the tower without the rotor installed. The current BEMT model does not account for the tower shadowing, where interferences in the wake formation is thought to have an impact on the fluid entering the turbine, and therefore the blade forces. As the ducted and open centre turbines do not incorporate such a foundation structure, this effect is not explored further.

Chapter 5

Application of BEMT to bi-directional ducted TSTs

This chapter presents the application of the ducted BEMT model. A comparative study is performed using results from an academic study employing a coupled CFD-BEM model. Here overall rotor power and thrust is assessed as well as the radial distributions to compare the hydrodynamic force computations at a greater resolution. Secondly, two commercial cases designed by OpenHydro are assessed, which are compared with fully blade resolved RANS CFD studies. The modelled blades are symmetrical rounded edge flat plate hydrofoils, where hydrodynamic coefficients have been generated from the 2-D RANS CFD studies detailed in Chapter 3.

The main objectives of the work presented here are to: 1) assess the ability of the duct model to replicate computations using CFD; 2) assess the capability to run a commercial case using hydrofoil data obtained from the 2-D RANS studies detailed in Chapter 3; 3) identify the extent of the computational demand for the different modelling techniques; 4) assess the impact of neglecting 3-D flow assumptions on the BEMT model accuracy.

5.1 Overview

Compared to studies on bare turbines, there are fewer published analyses of ducted and open centre configurations available. This is particularly the case for designs incorporating a bi-directional duct and high solidity rotor, which is the focus of the work in this thesis.

Within this chapter, an indirect validation comparing results of the ducted BEMT model with those from a coupled RANS-BEM study is presented. This uses geometry of a 'generic' type, and a blade design incorporating conventional hydrofoil profiles. Subsequently, an analysis is performed using ducted BEMT applied to two commercial turbines designed by OpenHydro. These are compared with blade resolved studies provided by an external engineering consultant. Lastly, a brief engineering application case is presented, where sacrificial anodes are attached to the rotor for corrosion protection. Their resulting influences on the power and thrust is assessed.

For each case, the input data is collated into text file formats and prescribed as inputs into the ducted BEMT model through various read-in functions. The input data is selected to represent the numerical models detailed in the references to enable direct comparisons to be made.

5.1.1 General ducted BEMT structure

Recalling from Chapter 2 (the ducted BEMT equations) and Chapter 3 (hydrofoil coefficients generated), the structure of the model used in this chapter uses the following general principles:

1. Ducted BEMT equations are applied with Shives' empirical expressions
2. An iterative procedure prescribed using a *SciPy* minimisation function
3. Correction factors based on:
   The Prandtl tip loss correction (only for the PS2 commercial case)

The Buhl correction in highly loaded conditions

4. (Only for commercial cases) RANS CFD generated lift and drag coefficient curves for rounded edge flat plate foils, corrected with:
   Du-Selig and Eggers adjustments for a rotating foil
   Linear interpolation for full range of thicknesses and Reynolds numbers

5.1.2 Process

The model is initiated for each individual inflow velocity, where the turbine rotational velocity is varied via a stepping function.

Intermediate calculation steps are inspected in order to assess the model performance, to ensure convergence is well established and to gain indications of magnitude and location at which correction factors are being applied.

Comparisons are made on rotor coefficients of power and thrust curves for all cases. Radial variations are also compared within the generic case.

5.2 Generic case

A recent study analyses the hydrodynamics of an ducted, open centre TST, using a coupled RANS-BEM model. Full details of the study are published in Belloni et al. (2016), building on extensive work developed during a PhD thesis by the same lead author Belloni (2013), which also makes comparisons with bare, and ducted 'closed centre' configurations. The generic case comparison presented in this Chapter gives an indirect validation of the ducted BEMT model with another numerical code, and has been published in Allsop, Peyrard, Thies, Boulougouris and Harrison (2017).

5.2.1 Reference model set-up

The reference data comes from a study using a RANS-BEM tool, developed by The University of Oxford, embedded in commercial CFD software ANSYS FLUENT (version 12.0), which has previously been verified in separate studies (Fleming and Willden, 2016*b*).

The k-ω SST turbulence model is employed, where the simulation domain consisting of a square section width and height equal to 4.7 D (where D is the diameter of the duct) with a corresponding blockage ratio of 3.6%. The inflow is applied to the inlet located 8.1 D upstream of the disc, and a uniform pressure outlet imposed at the exit boundary 16.2 D downstream of the disc. Symmetry conditions are imposed on all other boundaries. A structured mesh of flat layer prism cells is used at the duct, increasing in size to an unstructured mesh towards the domain extremities. The reported y^+ ranges from 15-200 at the duct walls, where a higher resolution is applied, particularly at the trailing edges of the duct and in the turbine wake (Belloni et al., 2016).

5.2.2 Flow conditions

A single flow condition is considered, as per the reference study (Belloni et al., 2016), with a uniform profile with no bottom friction, at a constant velocity of 2 ms^{-1}. This has a corresponding chord based Reynolds number of approximately 1.0E+06.

5.2.3 Academinc case turbine geometry

The overall geometry is detailed in Figure 5.1, reproduced from Belloni et al. (2016), however the inlet and outlet diffuser surface angles are not provided. These inputs are required by the duct model, (See Chapter 2 Section 2.2.2.3) and not easily defined for bi-directional ducts. A calibration study was thus performed to estimate appropriate values, by applying the model to device, and comparing

the corresponding thrust and power curves with blade resolved CFD simulations (from Section 5.3). This estimation suggests suitable diffuser surface angles of $\theta_{in} = 10°$ and $\theta_{out} = 30°$. A sensitivity analysis on these values is presented in Section 5.2.8.2.

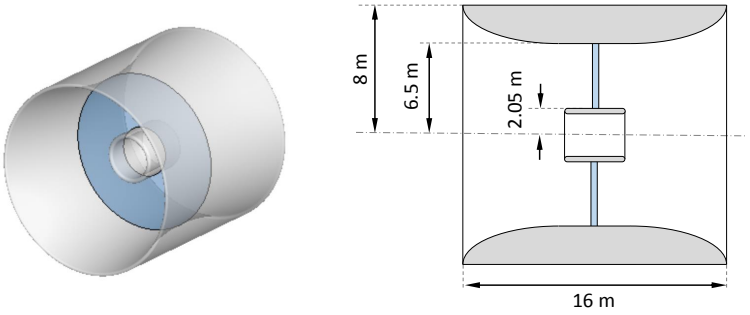

Figure 5.1: Generic turbine overall geometry (reproduced from Belloni et al. (2016))

Detailed radial rotor parameters are as defined in Table 5.1. The blade twist and local solidity are provided, sufficient to perform analyses with the ducted BEMT code.

5.2.4 Hydrofoil coefficients

The blades consist of Risø-A1-24 foils, with lift and drag coefficients as shown in Figure 5.2. These are produced from wind tunnel data at a Reynolds number of 1.6 x 10^6 (Fuglsang et al., 1999) for a range of angles $-5° < \alpha < 35°$.

No 3D stall delay or post stall extrapolation functions are applied. Rather, for angles outside of the wind tunnel data, the following was implemented: $\alpha > 35°$, values at 35° are used and $\alpha < -5°$, values at -5° are used. This was to be consistent with the validation methodology (Belloni, 2013), deemed permissible as there were few occasions where converged angles went outside the range.

Table 5.1: Validation case ducted and open centre TST geometry parameters, detailing radial distributions of blade twist and local rotor solidity of each annular ring (Belloni et al., 2016)

r/R (-)	β (°)	σ_r (-)
0.30	29.7	0.420
0.35	28.3	0.365
0.40	25.6	0.305
0.45	23.0	0.255
0.50	20.8	0.220
0.55	18.9	0.185
0.60	17.2	0.163
0.65	15.6	0.141
0.70	14.2	0.124
0.75	13.1	0.110
0.80	12.0	0.100
0.85	11.1	0.090
0.90	10.3	0.083
0.95	9.5	0.076
1.00	8.4	0.070

5.2.5 Ducted BEMT model set-up

The ducted BEMT model is based on the equations detailed in Chapter 2, Section 2.2.2. This uses the Lawn (2003) analytical expressions for ducted flow, solved using Shives and Crawford (2011) CFD derived empirical coefficients and specific duct geometry.

The open centre turbine connects blade tips in an outer ring that rotates within the stator, and thus restricts the formation of tip vortices. This has implications on the tip-losses that have been observed in conventional turbines. CFD studies have reportedly shown that the change in axial velocity at the tip is small (Fleming and Willden, 2016*b*), and therefore the tip loss factor is set to unity.

This case incorporates an open centre hub which connects the ends of the blades at the centre. This is thought to constrain the vortex shedding which is

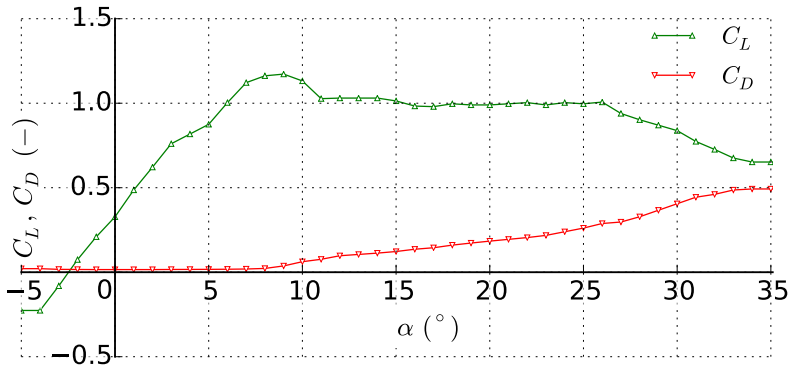

Figure 5.2: Coefficients of lift and drag against angle of attack for a Riso-A1-24 foil from wind tunnel tests, Re = 1.6E+06 (Fuglsang et al., 1999)

the basis of the Prandtl hub loss, and therefore the hub loss correction factor is set to one. This is a limitation of the model, as the complex nature of the flow in this region will have associated 3 dimensional effects and therefore associated hydrodynamic efficiency losses. An alternative correction factor could be proposed, but would require input from extensive blade resolved CFD simulations in order to understand the complex flow mixing through and around the open centre.

A highly loaded correction is applied, based on a factor devised by Buhl (2005) for axial induction factors above 0.4, where transition to the highly loaded regime is defined.

The RANS-BEM domain has symmetrical boundary conditions, assumed to be set sufficiently far from the rotor so that the simulations are run in open water equivalent conditions. Therefore no blockage correction is required.

5.2.6 Validation results

Figure 5.3 shows the results of power and thrust coefficient curves, which follow an increasing trend up to a maximum at an optimal TSR, before reducing at a slower rate. The comparison of the ducted BEMT results with RANS-BEM shows exceptional agreement (within 2%), up to the optimal TSR = 3.0. Beyond

the peak, increasing disparity is seen between the datasets with increasing TSR, where ducted BEMT predicts up to 25 % higher power and 10 % higher thrust at TSR = 5.

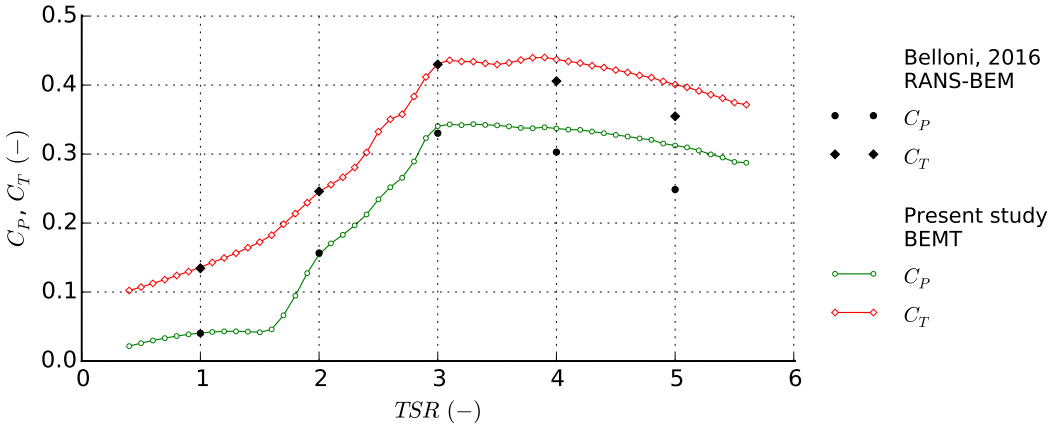

Figure 5.3: Rotor coefficients of power and thrust variation with TSR for a full scale generic open centre and ducted TST, comparing present ducted BEMT with RANS-BEM results (Belloni et al., 2016)

5.2.7 Radial variations

Rotor averaged values give an overall indication to the performance of a turbine, however it is also important to be able to assess the force distributions in greater detail. Figure 5.4 shows the radial distributions of various parameters calculated in the model, namely the normalised velocity at the disc, angle of attack and local element coefficient of thrust.

The thrust coefficient at each annular ring can be calculated as:

$$C_{Tloc} = \frac{dT}{1/2 dA U_d^2} \tag{5.1}$$

Where dA here is the area of each annular ring and the velocity is at the disc.

Comparing the ducted BEMT to RANS-BEM, excellent agreement is seen for angles of attack at all TSRs considered, as well as for velocity and local element thrust up to TSR 3.

Some discrepancies are apparent in the predictions of velocity and local thrust at TSRs 4-5, which explains the disparity seen in the overall rotor results. Here however, the results can be observed in more detail, where the divergences can be identified to localised positions, situated around the hub.

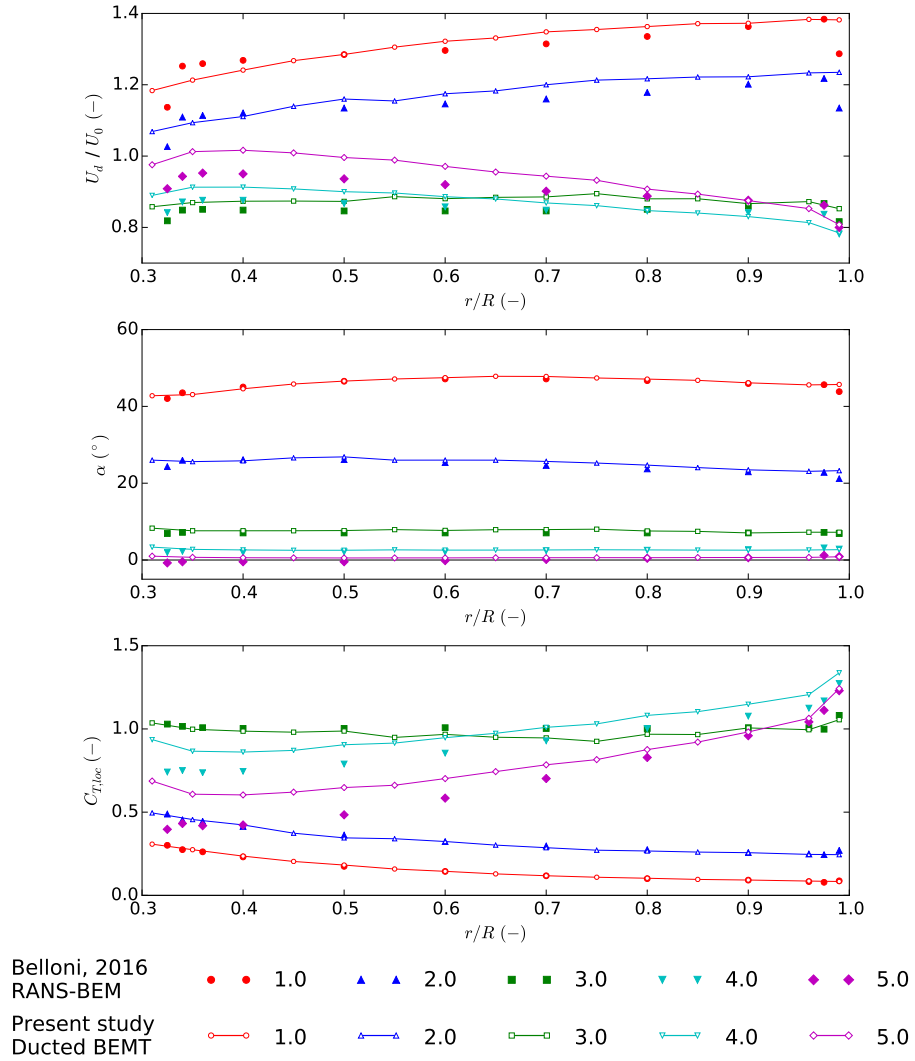

Figure 5.4: Variations of a) normalised flow velocity (top), b) angle of attack (middle) and c) local elemental thrust coefficient (bottom) with normalised radius, for various tip speed ratios, comparing ducted BEMT (lines) with RANS-BEM (points) (Belloni et al., 2016)

5.2.7.1 Detailed analysis

It is interesting to observe that for TSR ≤ 2, the velocity at the disc is greater than that at the inflow ($U_d/U > 1$). This translates to a negative axial induction factor (as $U_d = U(1-a)$).

This is an unexpected result as negative axial inductions not seen in the case of 3-bladed bare turbines. A logical explanation can be devised when one considers the differences in configuration that have been imposed for this case. Considering the main working principle of the duct, the diffuser forces the fluid to expand, which lowers the pressure and augments the flow through the throat. This raises the velocity in this location, where the disc is installed.

This can be related back to the elemental velocity triangles (Chapter 2, Section 2.2.1) to explain why this is only the case for low TSRs. The axial velocity (U_{d_i}) is a function of the relative tangential flow velocity over the element and inflow angle, which is rearranged to:

$$a_i = 1 - \frac{\Omega r_i}{U_i}(1 + a'_i)\tan(\phi_i) \tag{5.2}$$

The elemental tangential induction factor a'_i is seen to stay relatively small and constant for most TSRs and radii. Therefore a_i can only become negative if $tan(\phi_i)$ is sufficiently large. If TSR is small, then the Ω is small, or U_i is large. This translates to a large inflow angle ϕ_i between the two velocity vectors. ϕ_i is a function of α, which, from Figure 5.4, is $> 20°$ for TSR ≤ 2. As $tan(\phi)$ grows exponentially for $0° \leq \phi < 90°$, the higher angles are seen to be sufficiently large as to cause negative a_i.

5.2.8 Case discussion

Power and thrust predictions are almost identical for both models for TSR < 4, which includes the peak operating condition. As both methodologies implement

the blade element theory, based on the same geometrical parameters, hydrofoil lift and drag coefficients and correction factors, this is not considered to be an area of comparison, where differences are attributed only to the treatment of fluid momentum. The suggestion from these results is that the momentum changes calculated within ducted BEMT is very similar to the momentum changes computed by solving the Reynolds averaged Navier-Stokes equations within the CFD study. Further analysis of the computed parameters confirms the calculations are also similar in radial distribution, considering the momentum changes within each annular ring.

This has positive implications for the approach taken, and effectively shows that the modified analytical momentum theory is well representing the flow through the duct. Due to the limited number of data points in the reference study for comparison, the full profiles cannot be fully verified, and a number of additional comparison cases should be analysed to raise confidence in the model.

5.2.8.1 Ducted BEMT model capabilities

Over predictions seen at higher TSRs (TSR ≥ 4) are likely due to the more complex flow characteristics associated to faster rotating turbines, which appear to be better captured using CFD models. Assessment of the radial distributions shows that the over predictions of disc velocity and thrust are located closer to the open centre hub ($r/R = 0.3$). This is thought to stem from flow interactions in and around the hub, with fluid likely being drawn through the open-centre and therefore reducing the hydrodynamic efficiency of the blade elements towards this region. A correction factor could be investigated to improve the accuracy of flow predictions around this specific hub design, however is beyond the scope of the current study.

Although the Buhl factor is applied, axial induction factors converge on values less than the transition to the highly loaded regime. Therefore, under the input conditions considered, the results are always solved as per the ducted

BEMT calculations. This shows a non-dependency on the Buhl correction factor, which has associated uncertainties due to the semi-empirical correction, based on experiments where measurements show a significant amount of spread (Recall Chapter 2 Section 2.6.4).

In order to remain consistent with the inputs of the RANS-BEM model, the lift and drag coefficients at angles of attack above 35° are kept constant. The rationale being that this is a rare occurrence at non-optimal operating conditions. It is seen that for low TSR, the angles of attack are consistently above this limit. A post stall model could be used, such as the Viterna extrapolation function which is commonly employed, in order to improve the accuracy of the hydrodynamic coefficients for low TSRs.

5.2.8.2 Sensitivity to duct model parameters

Additional simulations were performed in order to assess the sensitivity of the model to the selection of particular duct geometries.

CFD derived coefficients used in the duct model depend on the diffuser angles, which are not easy to define for bi-directional duct profiles. A sensitivity test is performed using three sets of diffuser angles, as defined in Table 5.2. The reference is what was used in the current study.

Table 5.2: Diffuser angles for three cases used in a sensitivity analysis

	$\theta_{in}(^\circ)$	$\theta_{out}(^\circ)$
low extreme	0	0
reference	30	10
high extreme	60	20

Figure 5.5 shows that power and thrust predictions using extreme values are within 5 % of those when using the reference in this study, indicating a low sensitivity to these parameters.

Results with no duct are also presented (running what is essentially classical

BEMT), to quantitatively assess the influence of the duct model. This shows that the duct is improving power production for most TSRs due to the flow augmenting effects, as expected. Note that these are still a function of the duct inlet area, and therefore is only indicative to show the influence of the analytical function for ducted flow. It is not to be used to compare the performance of a bare vs ducted TST.

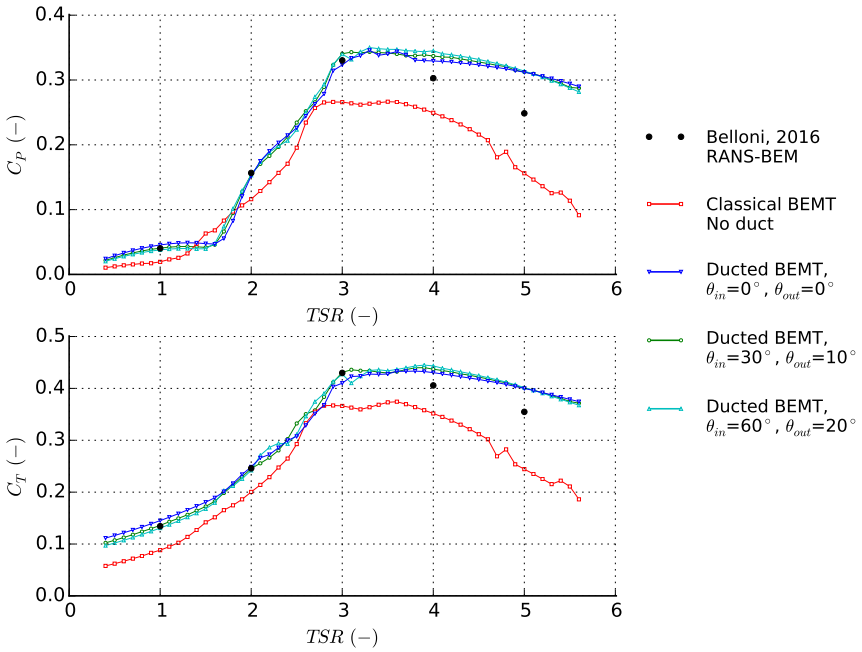

Figure 5.5: Power (top) and thrust (bottom) coefficient curves for a generic full scale open centre and ducted TST, comparing classical BEMT with ducted BEMT with various diffuser parameters

5.2.8.3 Computational requirements

Studies on conventional turbines quoted computational requirement of 100 CPU-hours per turbine rotation using blade resolved RANS CFD and 12 CPU-hours for each simulation using coupled RANS-BEM (McIntosh et al., 2012). No explicit details on the computational set up is given by this reference.

The coupled RANS-BEM study was performed on a 16 node computer cluster,

with 8 cores per node. Steady computations were completed in 8 hours using 4 cores, equivalent to 32 core hours for each of the 5 simulations Belloni (2013). The present ducted BEMT computations were performed using a laptop running an $Intel^{®}\ Core^{™} - i5$ 2.9 GHz dual core processor with 8 GB RAM. Simulations were completed within 3 minutes, generating all 60 points on the power and thrust curves, equivalent to 6 core minutes.

Computational time from separate studies cannot be directly compared, due to dependencies on factors such as the computer used, processor type, number of partitions and clock time. There are also dependencies on certain CFD parameters such as the mesh definition, domain size and time step used. However, differences of several orders of magnitude seen in this study is indicative of substantial computational cost savings when using the proposed BEMT model. This highlights an advantage in the application of performing engineering assessments such as fatigue damage or when making and evaluating multiple design iterations under time or resource constraints.

5.2.9 Limitations

Both the ducted BEMT and RANS BEM models are based on the blade element theory restrictions, where any span wise flow is not considered, and individual hydrofoil sections are analysed as a function of the lift and drag coefficients. In order to reduce the limitations of 2-D analyses, corrections for physical behaviour could be included, such as the delayed stall effects by applying the Du-Selig and Eggers adjustments to lift and drag coefficients. However, the complex flow through the different turbine configuration is likely to have impacts on the Coriolis Effects of flow, and would need to be further analysed.

RANS has the ability to capture the spanwise flow, however this is beyond the capabilities of the momentum equations which are based on independent annular rings, capturing no radial flow between elements. This is thought to be more significant around the open centre hub. As the bending stress is a function of all

forces along the blade, the spanwise flow will have an influence on blade life, and should be considered in any detailed structural analysis.

The incorporation of the duct effects in the BEMT equations are devised from CFD studies of unidirectional duct geometries. When applying this to the bi-directional duct in this case, the inlet and outlet angles are less easy to define, yet are incorporated within the empirical expressions. These angles were empirically calibrated for the OpenHydro device, comparing the resultant C_P and C_T curves with blade resolved CFD studies. There are inevitably inaccuracies with this approach due to the differences in the geometry of machines, as well as calibrating against a methodology that resolves flow around each blade.

Simplifications are inherent in the BEMT, so the method neglects any mixing with fluid surrounding the stream tube. The present study only considers a flow direction perpendicular to the rotor plane, however this could be adapted to additionally assess yaw. The flow is also considered inviscid and steady. Quasi static simulations could be performed, where frozen inflow conditions are applied at each time step, but is considered beyond the scope of the present study.

The analytical ducted momentum method has been verified here with a higher complexity CFD model, however, due to the limited number of data points for comparison, this analysis is somewhat restricted. Assessment against additional cases is recommended, preferably with higher complexity models or experimental measurements, to raise confidence in these results.

5.3 Commercial case application

The analytical ducted BEMT model is now applied to two full scale commercial TSTs as developed by OpenHydro. Two generations of device, as shown in Figure 5.6 are analysed: the 'OCT16' and 'PS2'. Both designs consist of a high solidity, open centre rotor, incorporating a symmetrical bi-directional duct housing a rim induction generator.

This section evaluates the performance of the developed BEMT model against blade resolved CFD studies performed by 'Optydro Concept', as an independent contractor to EDF R&D.

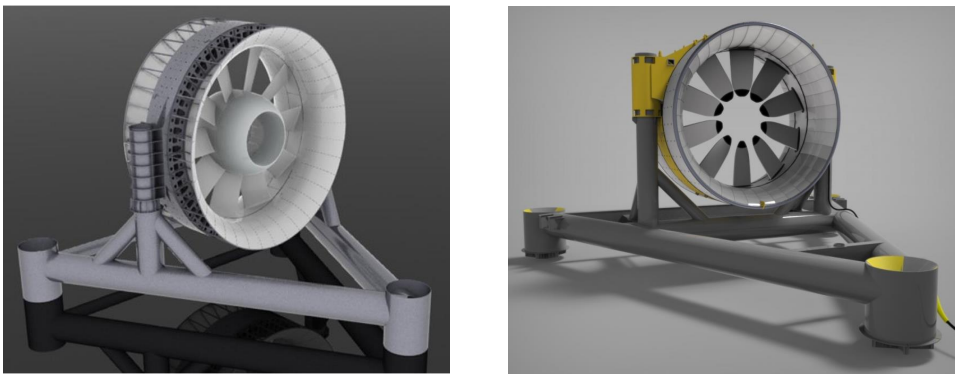

Figure 5.6: OpenHydro ducted, high solidity and open centre TST designs: OCT16 (left) and PS2 (right)

5.3.1 OpenHydro TST designs

This section details the overall designs and blade geometrical properties of the two commercial TSTs.

5.3.1.1 Turbine geometries

The dimensions of each device are shown in Figure 5.7. Both designs are generally very similar incorporating a bi-directional duct of equal overall dimensions, a

high solidity rotor with 10 blades, and a central aperture. Main differences in configuration likely to affect their hydrodynamic behaviour are regarding the condition of the aperture, where the OCT16 device connects the blade tips using an inner venturi. The later generation PS2 device has removed this inner ring, leaving the tips open to the flow. It can be additionally observed that the blade profiles appear quite different as a result of this design change.

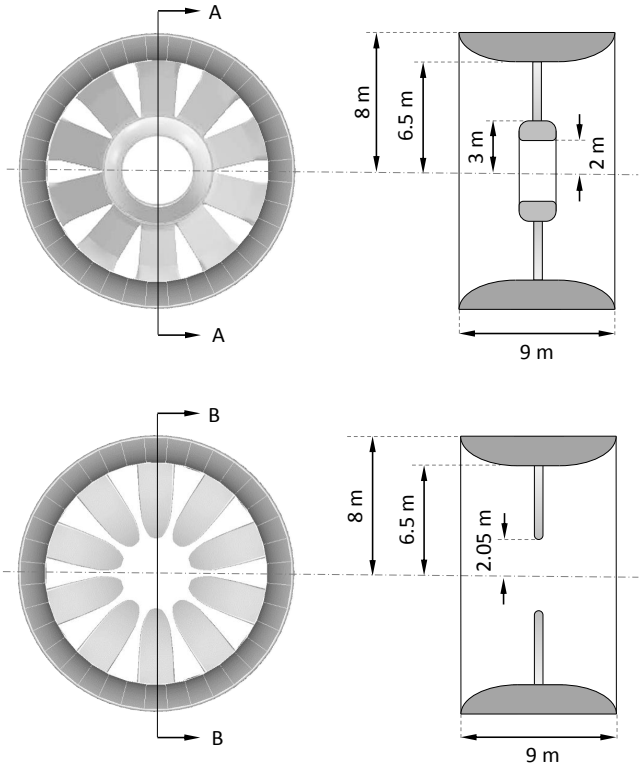

Figure 5.7: Overall turbine rotor and stator dimensions for the OpenHydro OCT16 (top) and PS2 (bottom) devices, showing turbine sub-assembly (support structure / foundation removed) frontal (left) and sectional views (right)

Radial variations of blade parameters for each of the two turbines including chord, thickness and twist are shown in Figure 5.8. Parameters are normalised using maximum values seen in both cases combined, such that $\tilde{c} = c/c_{max}$, $\tilde{t} = t/t_{max}$ and $\tilde{\beta} = \beta/\beta max$. Here the differences between the devices are more apparent. First, there is a difference in the length of the blades (although the central hub is not represented here). The curved profile of the PS2 type blades to the open tip are in contrast to the almost straight profile of the OCT16. The thickness of

OCT16 blades is high at connections to the inner and outer rings, however remains almost constant between. For the PS2 blades on the other hand are thicker at the connection to the other ring, with a gradual tapering towards the tip. Blade twist is almost equal for the two cases at the centre, with a linear decease in OCT16 blades compared with a more asymptotic curve to a much smaller angle at the outer ring.

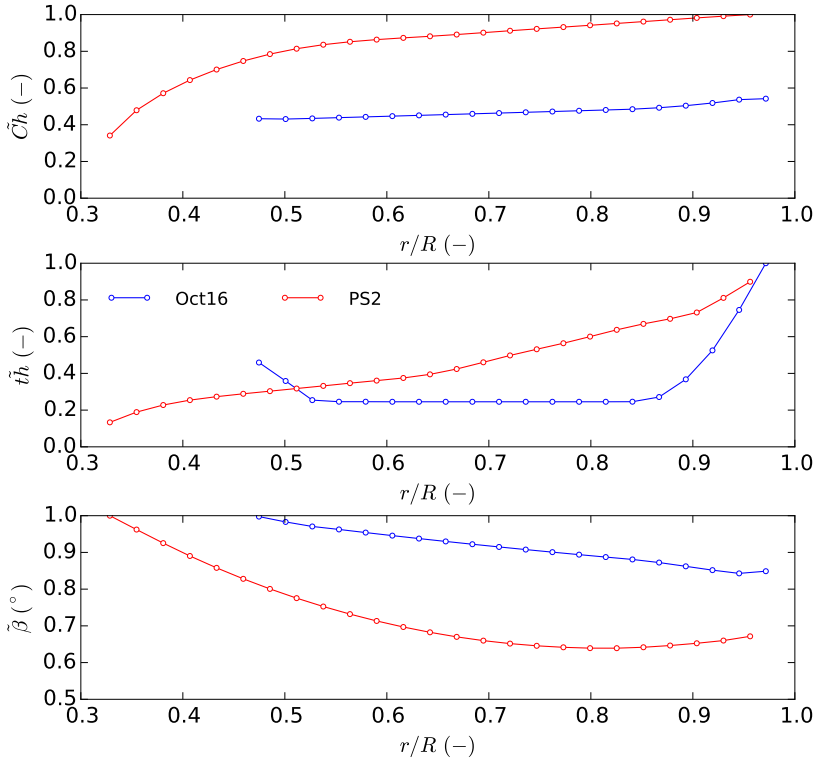

Figure 5.8: Radial distributions of non-dimensional a) chord (top) b) thickness (middle) and c) twist (bottom) for the OpenHydro OCT16 and PS2 devices

5.3.1.2 Blade hydrofoil sections

CAD files for each of the devices were provided by OpenHydro, Figure 5.9 shows the overall assembly for the PS2.

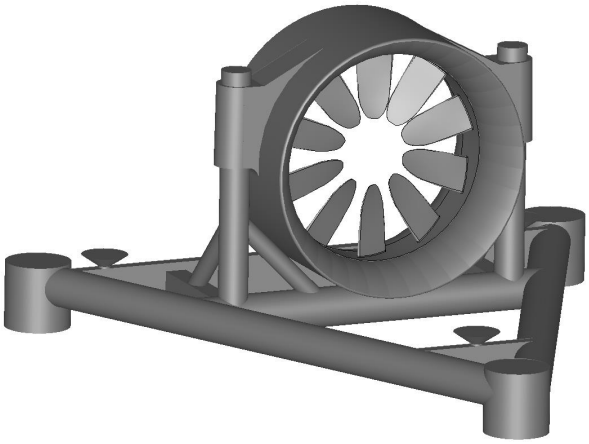

Figure 5.9: CAD model of the overall assembly of the PS2 device

As defined in the blade element theory, the blades are split into a number of discrete hydrofoil sections. Inspection of the blades from the CAD model show these sections consist of flat plate type hydrofoils with rounded edges. A PS2 blade can be seen in Figure 5.10 where the span-wise variations in chord, thickness and twist angles of each element can be clearly seen, aspect ratios of thickness to chord (t/c) varying between 0.04 - 0.09.

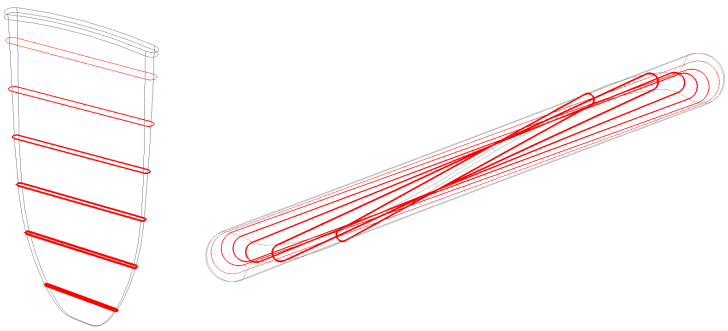

Figure 5.10: Sectional views of a PS2 blade indicating element rounded edge flat plate foil profiles

5.3.2 Reference model set-up

The validation data was provided by *OptydroConcept*, an engineering consultancy with experience in numerical simulations of TSTs for design optimisation (Kueny, 2012). CFD studies of the OCT16 (Kueny, 2015*b*) and PS2 (Kueny, 2015*a*) OpenHydro devices were performed by Professor Kueny, which are used as references throughout this comparative study. The complete set of simulation parameters are detailed in Appendix 4.

This is a fully blade resolved case, assessing a single blade and stator with the foundations removed. Simulations use a RANS $k - \varepsilon$ turbulence model with a scalable wall function. The domain is a 1/10th segment of the turbine (36°), modelling a single blade with periodic boundaries to reduce computational cost.

The domain is a $1/10^{th}$ segment of a cylinder, with external limits set at 6 D from the turbine location (where D is the diameter of the duct). A constant pressure is applied at the boundaries, calculated as the mean pressure at the outlet. A constant velocity inlet is located 1.5 D upstream and outlet 6 D downstream of the turbine.

The domain is split into rotating and stationary sections, with a 'stage' (or 'mixing plane') imposed at the interface. This calculates average circumferential exchange of azimuthal pressure and flow velocity.

The structured meshes consist of 2.1 million nodes (OCT16) and 4.2 million nodes (PS2). These are refined at the blade surfaces and report $y^+ < 30$ (OCT16) and < 50 (PS2) in critical zones.

The forces are calculated on the turbine as a whole (rotor and stator), as well as on the runner (the interface between the rotor and stator). This latter is used for comparisons with the BEMT simulations, however it is noted that this also takes into account the forces on the outer ring, which connects the blades together to form the rotor.

5.3.3 BEMT case set-up

This section details all of the inputs used in the BEMT analysis of two designs of OpenHydro TSTs.

5.3.3.1 Flow conditions

The inflow to the ducted BEMT model was selected in order to replicate the flow conditions of the reference CFD study, where uniform profiles of 0.5 - 5.0 ms^{-1} are applied with increments of 0.5 ms^{-1}.

5.3.3.2 Hydrodynamic analysis of blade elements

The OpenHydro blades are made up of rounded edge flat plate foils. Hydrodynamic characteristics of these type profiles are not readily available in the literature and unable to be generated using XFoil due to limitations observed in the panel code method. Therefore it was necessary to determine lift and drag curves using higher complexity CFD simulations. The 2-D RANS analyses performed using *Code_Saturne* within this thesis are used, described in Chater 3, Section 3.

Lift and drag data was generated for two thickness to chord ratios: 0.04 and 0.09. A linear interpolation function has been applied which approximates curves for intermediate t/c ratios. It should be noted that the OCT16 blades have elements of t/c $>$ 0.09 located the roots. As the CFD analyses did not extend to these higher thicknesses, C_L and C_D curves at the maximum $t/c = 0.09$ are used.

Attack angles were analysed at increments of 5°, except $0° \leq \alpha \leq 30°$ where 1° increments are analysed to capture the stall condition.

The Du-Selig and Eggers 3-D stall correction is applied (detailed in Appendix 2 Section 1) which is a function of the chord, (which varies with radial position) as well as TSR (where integers are used to limit the number of datasets).

5.3.3.3 Flat plate hydrofoil coefficients

The full range of CFD generated hydrodynamic coefficients at angles of attack between 0° to 70° are mirrored to extend values to the negative range. As the foil sections are symmetrical, this is achieved by simple translation. These are read into the BEMT model through look-up tables in order to allow the iterative loop to run under all possible inflow angles. It is seen that for the inflow conditions assessed, angles of attack usually converge between -10° to 30°.

The lift and drag coefficient curves are detailed for two Reynolds numbers of 1.0E+06 and 1.0E+07, where Figures 5.11a and 5.11b are for an OCT16 device, and Figures 5.12a and 5.12b displaying curves for a PS2 device.

5.3.3.4 Reynolds number

The chord based Reynolds number is calculated as a function of the resultant velocity, i.e. is a combination of the inflow and rotational velocities. Figure 5.13 shows the radial distributions for the PS2 device, where selected values of inflow velocity and TSR are used to be representative of those typically seen in a 'normal operating mode'.

3 effects can be observed: the 'high' and 'low' inflow velocity limits lead to change of around an order of magnitude in Reynolds number; radial distributions are strongly influenced by the variation in chord along the blade length; the TSR has an effect on both magnitude and radial distribution as the resultant velocity increases with radius.

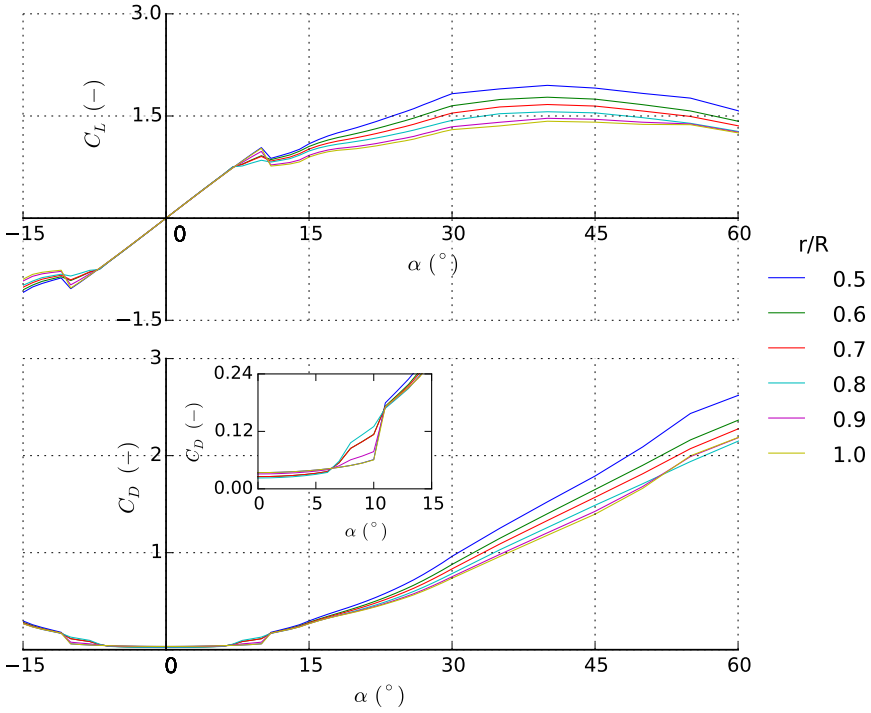

(a) Re_{ch}=1.0E+06,

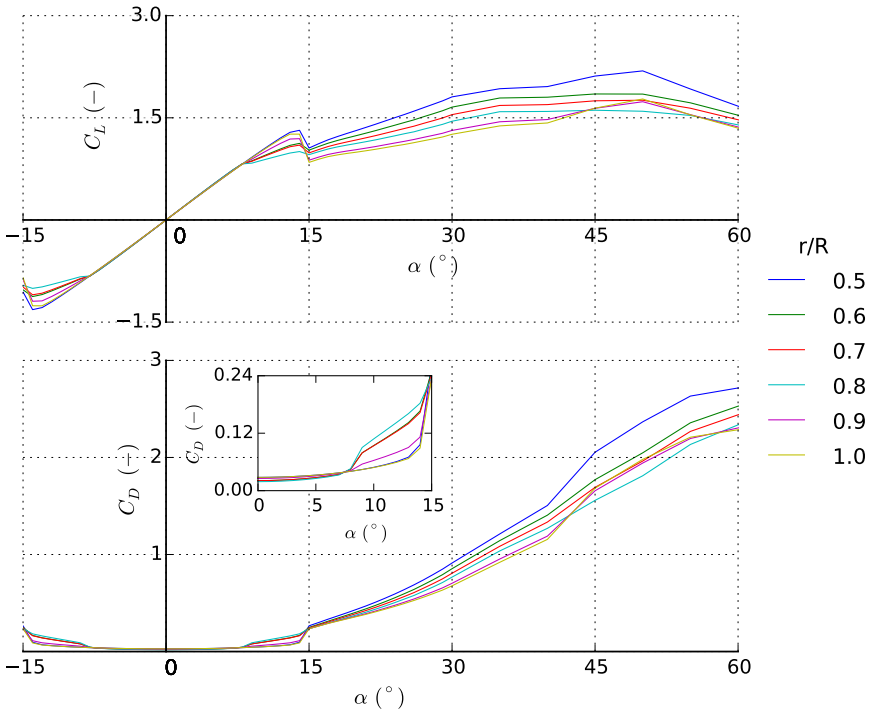

(b) Re_{ch}=1.0E+07,

Figure 5.11: Stall delay corrected coefficients of lift and drag curves at various radial positions of an OpenHydro OCT16 device at TSR = 2

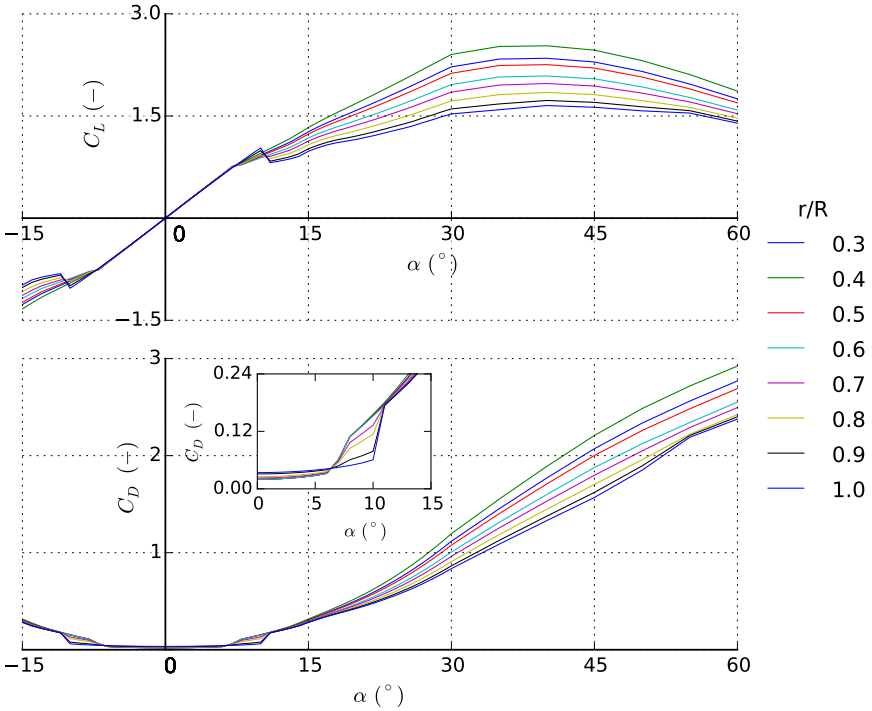

(a) Re_{ch}=1.0E+06,

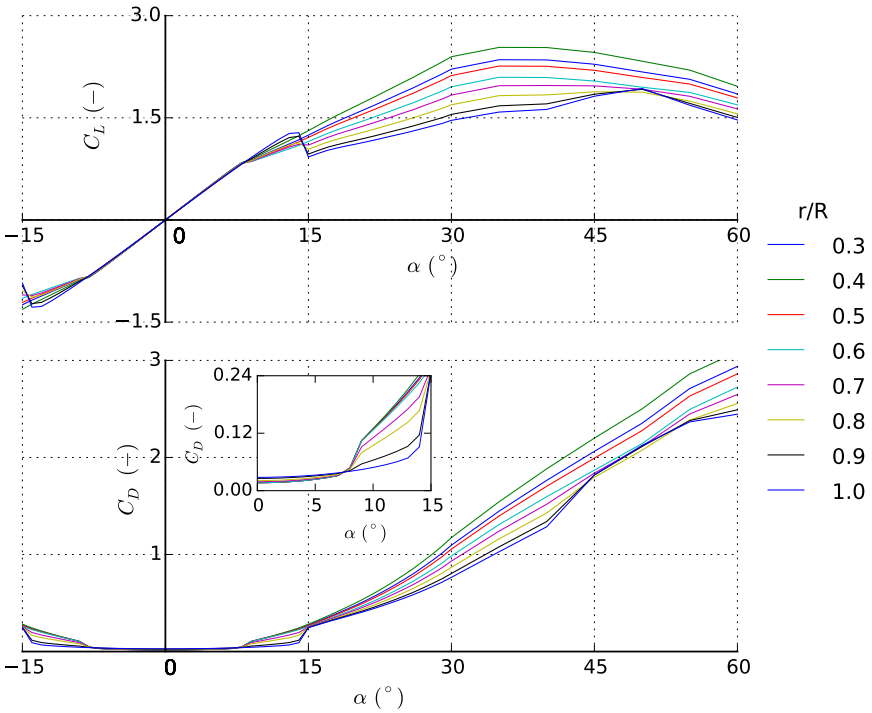

(b) Re_{ch}=1.0E+07,

Figure 5.12: Stall delay corrected coefficients of lift and drag curves at various radial positions of an OpenHydro PS2 device at TSR = 2

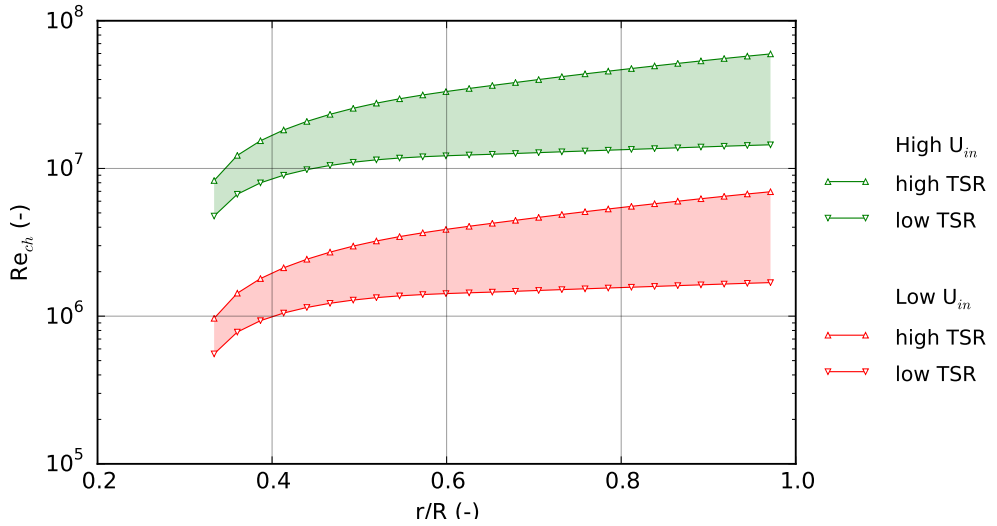

Figure 5.13: Range of Re_{ch} with normalised radius, for arbitrary values of 'low and high' TSR, presented for two arbitrary 'low and high' inflow velocities

5.3.3.5 Linear interpolation functions

For each t/c ratio at a specific Reynolds number, complete C_L and C_D curves for a full range of angles of attack are generated using RANS CFD in 12 hours using 14 cores plus additional preparation time. In order to obtain data for all thickness to chord ratios, at each individual Reynolds numbers seen for this case, a great many additional simulations would be required. To circumvent this, linear interpolation functions have been applied.

The first, as previously mentioned, is used to approximates curves for all t/c ratios (as presented in Chapter 3, Section 3). The second concerns the Reynolds number, which was seen in the previous section to vary significantly as a function of element size, radial location, inflow velocity and TSR. Lift and drag curves are generated for $Re_{ch} = 1.0E + 06$ and $1.0E + 07$. The actual value of Reynolds number is determined in the BEMT loop, where the corresponding coefficients are found through interpolating between the two datasets. This assumes that there will be a linear relationship between C_L and C_D with Re_{ch}, thought to be acceptable for Re_{ch} = 1-10 million, but likely to be influenced more by non-linearities at the more extreme flow conditions.

5.3.3.6 Ducted BEMT model set-up

The ducted BEMT model is based on the equations detailed in Chapter 2, Section 2.2.2. This uses the Lawn (2003) analytical expressions for ducted flow, solved using Shives and Crawford (2011) CFD derived empirical coefficients and specific duct geometry.

The calculation of the Reynolds number is set within the induction factor iterative loop. This allows the incorporation of the axial and tangential induction factors that are calculated at each iteration in order to calculate the velocity at the disc. This is used to get a better value of the resultant velocity seen over the blade, and therefore a better estimation of the Reynolds number using:

$$Re_{ch} = \frac{\sqrt{(U(1-a))^2 + (\omega r(1+a'))^2}c}{\nu} \tag{5.3}$$

Which are then used to attain lift and drag coefficients from the interpolated lookup data.

For both cases, as with the validation case in Section 5.2 the outer ring connects the ends of the blades, thus restricting vortex shedding and their associated reductions in blade hydrodynamic efficiencies. Hence the correction factor in this region is set to unity.

This is also the case at the centre of the OCT16 turbine, where an open centre hub connects the other ends of the blades via an inner ring. This is, as before, a limitation of the BEMT model as the complex nature of the flow in this region is thought to have associated 3-D effects which will impact the hydrodynamic efficiency, as seen in results compared with RANS-BEM, particularly at higher TSR (See Section 5.2.7).

In the case of the PS2, the Prandtl tip loss correction factor is applied. This is to account for flow separation at the blade tips, which are now open to the flow. However, this is based on the principle of the correction factor where it is assumed

that the flow through the centre will be equal to the free stream velocity. This assumption is explored further in the discussion of results.

The Buhl (2005) highly loaded correction is applied, however the induction factors never converge upon a value in the highly loaded regime where this correction takes effect. Therefore calculations are always made with the ducted axial momentum equations.

The CFD domain external boundaries are considered sufficiently far away, so that the simulations are assumed to be open water conditions. A blockage ratio of 2.8% is calculated from the inflow to duct area, which can be assumed negligible and therefore no blockage correction is required.

5.3.4 Results: OCT16 comparison with CFD

Figure 5.14 shows the normalised coefficient of power and thrust curves against TSR. The plot compares results from the ducted BEMT with points from blade resolved CFD studies (Kueny, 2015*b*) at all inflow velocities from 1 - 5 ms^{-1}. Thrust values are rotor only, where the duct structure is not taken into account. Coefficients are normalised against the peak values calculated by the reference CFD. There is a small spread within both the results, caused by the different flow velocities which have different lift and drag coefficients corresponding to the Reynolds number.

It can be seen that there is good agreement between the power predictions, which follow very similar correlations peaking at a TSR between 1.5 and 2.0. There is a slight shift seen in the BEMT curves, such that lower values are seen at lower TSR and higher values at higher TSR. The magnitude of the peak is around 6% lower than the CFD.

The thrust also shows similarities in profile, however the magnitudes predicted by BEMT are significantly lower for all TSR considered, generally by an average

of 40%, up to a maximum of 50%. Additionally, there is much less range within the BEMT lines, suggesting a lower dependency on the different lift and drag coefficients at different flow velocities.

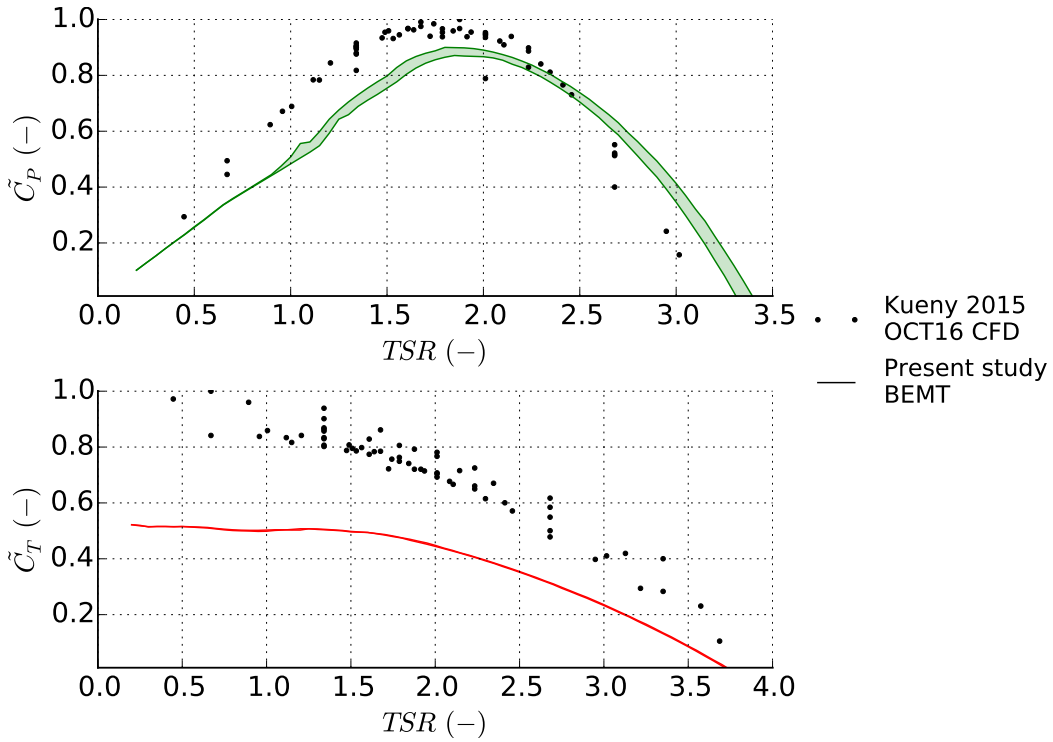

Figure 5.14: Normalised coefficients of power (top) and thrust (bottom) for an OpenHydro OCT16 TST comparing results from ducted BEMT and blade resolved RANS (Kueny, 2015*b*) at all inflow velocities

5.3.5 Results: PS2 comparison with CFD

Figure 5.15 shows the comparison of normalised power and thrust coefficients for the PS2 turbine. The plot shows the blade resolved RANS CFD studies (Kueny, 2015*a*), together with the BEMT results, for all inflow velocities from 1 - 5 ms^{-1}. The thrust refers to the rotor thrust with both the BEMT and CFD results, with the duct structure is excluded. Coefficients are again normalised against the peak values calculated by the reference CFD. There is considerable spread seen in the data points, particularly in power, for the different inflow velocities.

In this case, the power prediction shows a weak correlation, whereby power increases with TSR to a peak condition, before decreasing. There is a spread in the data showing a sensitivity with the inflow velocity, however this is considerably less within the BEMT model. Again, the curve seems to be shifted so less power is predicted at lower TSR, and higher power at high TSR. The average peak powers are similar, however the different ranges make it difficult to make direct comparisons. The optimal TSR also differ, with BEMT predicting a peak occurring between 2.0-2.5, higher than those of the CFD between 1.5-2.0.

The thrust also shows similarities in overall profile, but the magnitudes predicted by BEMT are lower for all TSRs considered, generally by an average of 30%, up to a maximum of 40%. There is little spread between the BEMT lines, suggesting a lower dependency on the different lift and drag coefficients at different flow velocities. The CFD however predicts a wider spread between the inflow velocities.

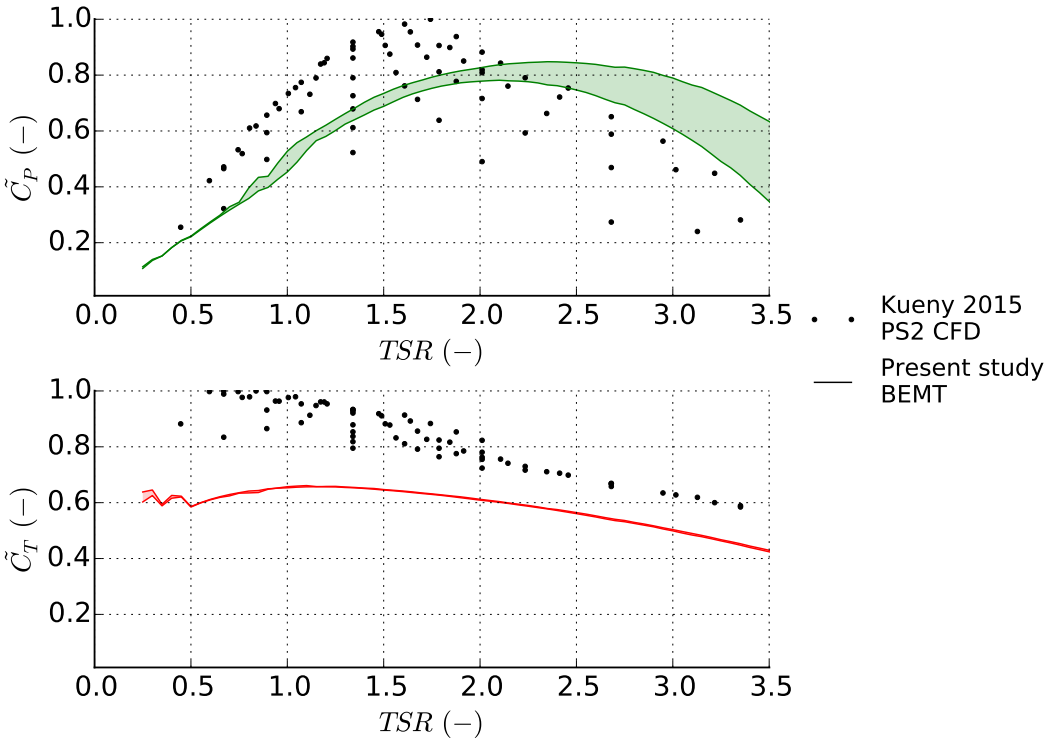

Figure 5.15: Normalised coefficients of power (top) and thrust (bottom) for an OpenHydro PS2 TST comparing results from ducted BEMT and blade resolved RANS (Kueny, 2015*a*) at all inflow velocities

5.3.6 Case discussion

Power predictions from the BEMT models are not unreasonable for the two cases, given the simplicity of the technique compared to the reference CFD simulations. The greatest disagreement is seen in the thrust predictions, which are considerably lower from the ducted BEMT.

5.3.6.1 Wake observations

One objective of the CFD studies was to characterise the wake behind the two devices, which is illustrated in the reports as figures displaying the velocity and pressure fields (Kueny (2015*b*), Kueny (2015*a*)). These can be used to gain insights into some of the flow phenomena occurring behind the turbine, to better understand why there is divergence between the two models.

5.3.6.2 OCT16 open centre hub

One reason that the OCT16 thrust predictions are lower from BEMT is thought to be due to the additional drag from the hub structure, which is not accounted for within the model.

Figure 5.16 shows the streamlines of the wake at two rotational velocities, where there are clearly velocity reductions behind the hub. Additionally, there appears to be some vortex shedding at lower rotational velocities, which causes some convergence oscillations. However, these are different structures in comparison to helical vortices seen at open tips. The thicker foils at the connections to the inner and outer rings are also not fully accounted for, due to a restriction in the data produced for flat plate hydrofoils, meaning a maximum of t/c = 0.09 could be used. From Chapter 3, Section 3, the trend of increasing thickness is likely to increase the drag at low attack angles, but also may increase the angle at which stall occurs.

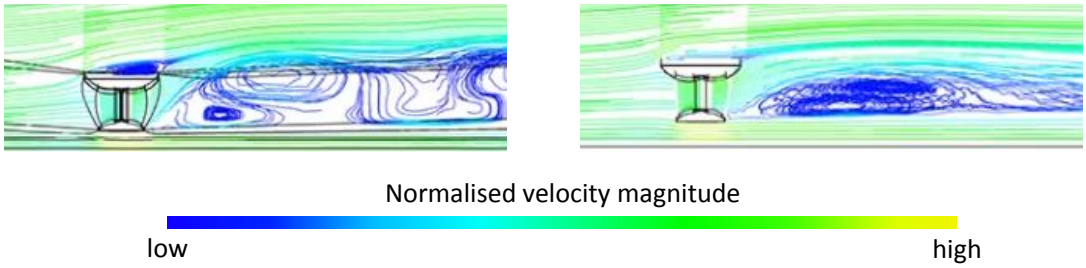

Figure 5.16: Velocity streamlines from blade resolved RANS of flow through an OCT16 turbine Kueny (2015*b*) for low (left) and high (right) rotational velocities

5.3.6.3 Thrust under predictions

BEMT is seen to under predict thrust for the PS2 also, which suggests that the hub and thicker than modelled foils only account for a small proportion of the difference. Clearly there is some other physical behaviour of the flow which is only captured when solving for the flow around the whole blades.

There are a number of possible reasons for this. One explanation stems from the fact that the CFD considers the forces on the 'runner', which refers to the interface between the rotor and stator. Forces are therefore on the blades, as well as the outer ring that connect them together. The additional drag contributions from the outer ring is not considered in BEMT, and so is thought to be a main cause of the disparity.

One other possibility is that the lift and drag curves generated from the 2D foil sections in Chapter 3 are not accurate. As can be seen from the study, the validation against experimental data is limited. There are some seemingly small under predictions in the drag coefficients at low angles of attack, and as the magnitude of the coefficients is so low, a small change could have large impacts on the rotor forces.

5.3.6.4 3-D flow effects

It is beyond the capability of the BEMT method to account for 3-D flow interactions: momentum changes are determined within each annular ring separately, equated to the hydrodynamic forces of each individual blade element. For the case of the PS2, there are thought to be large span wise flow interactions due to the inwards facing blades and open tips at the centre. The amount of radial flow will also be dependent on the rotational velocity of the turbine, and so will change as a function of the TSR. This is a limitation implicit in the BEMT technique, and is considered highly influential, as further explored in the next section.

5.3.7 Detailed analysis

Figure 5.17 shows the radial distributions of: the ratio of disc velocity to inflow; angle of attack; localised thrust coefficient; and base pressure coefficient, at various TSR. Results are presented for a single inflow velocity of 5 ms^{-1}. The OCT16 results are identical for all other inflow velocities, whereas in the PS2 data there is a small change observed with different inflow velocities, which correlates to the larger spread of rotor power and thrust.

Overall trends indicate that increasing TSR results in higher velocity at the disc and lower angles of attack. These lead to smaller coefficients of thrust and higher base pressure coefficients. The different radial distributions between the two devices are representative of the differences in blade design, where the PS2 blades have a much larger change in chord (see Figure 5.8).

5.3.7.1 Blade stall

It can be observed that angles of attack converge well within the ranges that hydrodynamic lift and drag coefficients are generated in the 2-D hydrofoil RANS simulations.

At TSR of 1.5, the angles of attack exceed the angle of stall for the hydrofoils

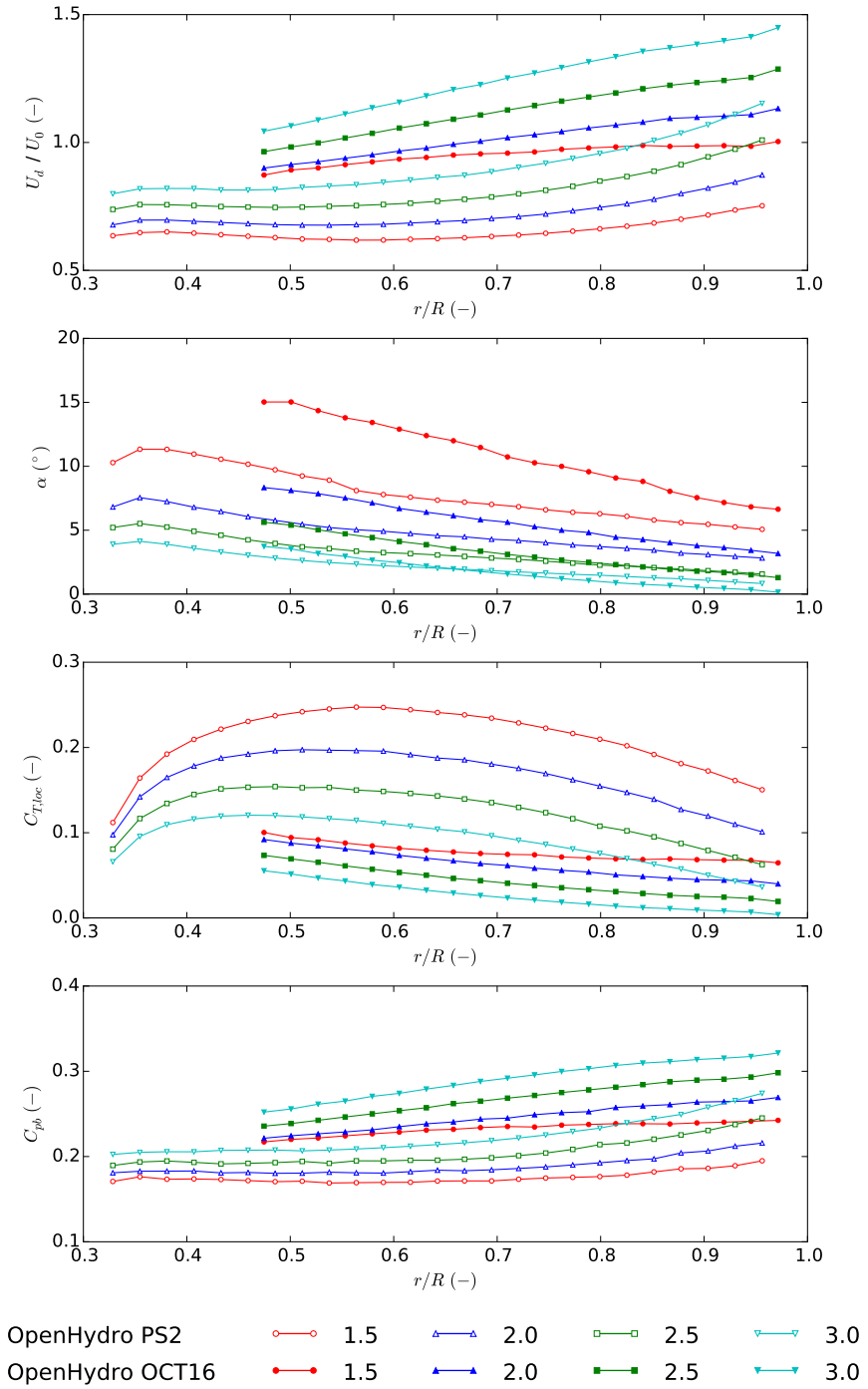

Figure 5.17: Variations of a) normalised flow velocity (top), b) angle of attack, c) local elemental thrust coefficient and d) base pressure coefficient (bottom) with normalised radius, at an inflow velocity of 5 ms^{-1}, for various tip speed ratios, comparing ducted BEMT results for the OpenHydro PS2 (open points) and OCT16 (filled points) TSTs

($\approx 12°$). This occurs at $r/R < 0.7$ for OCT16 and $r/R < 0.4$ for PS2. In the stall regime, highly complex vortex shedding at the hydrofoil edges is observed (in Chapter 3, Section 3). The size of the vortices and frequency of their shedding are dependent on the hydrofoil profiles which vary along the blade length. The BEMT model uses hydrofoil element lift and drag coefficients from the RANS CFD analyses that captures the stall behaviour. However, the complex nature of the boundary layer separation in one blade element will not be captured by the subsequent elements due to the 2-D assumptions.

This is a limitation of the Blade Element method, and therefore a limitation in both BEMT and RANS-BEM. As the blade resolved CFD is able to model the complex 3-D flow interactions and entrainment with fluid within the diffuser, this is thought to be a reason for some of the disparities seen in the power and thrust at low TSRs.

5.3.7.2 Diffuser pressure

It can be seen from the CFD there is a drop of pressure behind the disc and at the outlet to the duct (p_4), as seen from a sample shown in Figure 5.18. Recalling equations of pressure through the duct (Chapter 2, Section 2.2.2.2), this observation is consistent with the analytical function proposed. However, it is difficult to say with any certainty that these are in the same order without higher resolution predictions from the CFD, which are not available for this study.

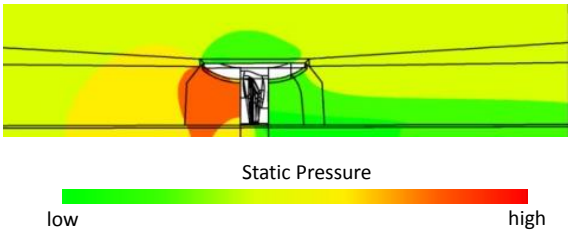

Figure 5.18: Normalised pressure field through a PS2 device (sectional view) generated from RANS blade resolved CFD (Kueny, 2015*a*)

Actual measurements of the pressure though the duct could be used to solve the analytical expressions for ducted flow within the BEMT model. This would improve the application to this specific case, as there would be less reliance on empirical coefficients that are devised from ducts of a different design to OpenHydro.

5.3.7.3 PS2 flow conditions

It is interesting to see the different dependencies on the inflow velocity for the two cases. As the thrust, power and rotational speed are non-dimensionalised with flow velocity, one might expect little variation, as seen in the OCT16 device. The reason for the spread is thought to stem from the calculation of the hydrodynamic forces, as these depend on non-linear variations of lift and drag coefficients, which depend on the Reynolds number. The larger spread in the PS2 device can therefore be explained by the larger variation in blade profile and thus a larger variation in hydrofoil coefficients. The BEMT model somewhat captures this, however the spread is only seen at higher TSR and with a smaller magnitude than the CFD.

Another contribution is thought to stem from the removal of the open centre hub, which leaves the tips open. This can be seen from the velocity streamlines within Figure 5.19, where the CFD predicts strong rotations in the wake. There is a low sensitivity to the rotational velocity on the shape of the wake, where a slightly larger expansion is seen at low TSR. A blade tip vortex is seen to develop at

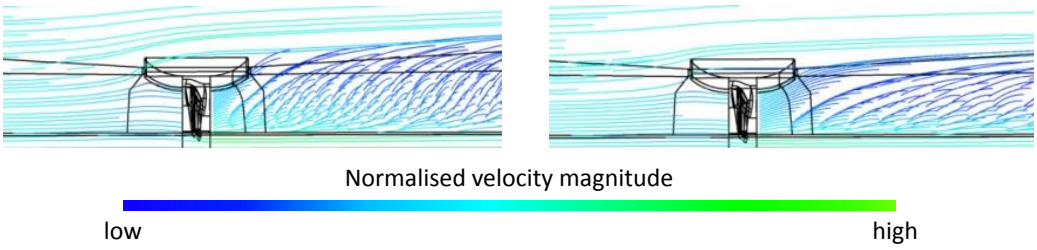

Figure 5.19: Velocity streamlines of flow through a PS2 turbine from blade resolved RANS Kueny (2015*a*) for low (left) and high (right) rotational velocities

TSRs below the optimal value, which is relatively intense at very low rotational velocities. The vortex instabilities correlate to force convergence oscillations seen at these velocities.

5.3.7.4 PS2 tip losses

Within the BEMT model, a tip loss correction factor is applied to the PS2 device, in an attempt to account for the vortex shedding. However, this is based on a concept whereby the helical vortex sheet is approximated to a succession of discs travelling between the wake velocity, and the free stream velocity. Figure 5.20 shows that the velocity through the open centre is significantly higher than the free stream, up to a factor of two times greater under some TSRs. Therefore the basis of this correction factor is not considered accurate for this case.

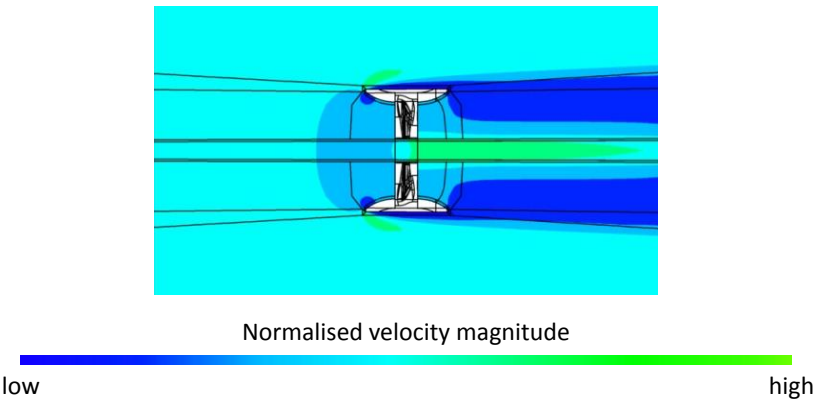

Figure 5.20: Velocity field through a PS2 device, showing acceleration above the free stream through the centre (Kueny, 2015*a*)

5.3.7.5 Limitations in the reference CFD

Resolving the flow around the blade is advantageous, as this solves the complex 3-D flow interactions that are driven from vortex shedding at the tip, vortex shedding from the edges in stall, and radial movement of fluid due to the rotation of the blade. There are also some limitations to the RANS approach used as the reference within this study.

As blade resolved studies have high computational requirements, only one blade is modelled, where a 'stage' type boundary is applied. This calculates the circumferential average exchange of azimuthal pressure and flow velocity between stationary and rotating elements. A more accurate representation would be to model the full turbine, and therefore more accurately solve the flow interactions between each blade. During rotation, particularly at low TSRs where stall is observed and tip vorticies are strongest, there is likely to be strong blade-blade interactions that will affect the axial and tangential forces for the whole rotor. The reference study does not account for this, as only one singular blade is meshed, and is therefore a limitation.

There are also some known limitations to the $k - \varepsilon$ turbulence model in its representation of the boundary layer. *Code_Saturne* documentation (EDF R&D (2015)) recommend designing a mesh to give y^+ values of around 30 at a solid boundary. Within the CFD study of the OCT16 device, at critical zones y^+ values are quoted at <30. This therefore may have implications on the accuracy of the viscous sub-layer, and the corresponding hydrodynamic forces calculated at the blade surface.

Better accuracy of wake dynamics can be achieved using LES or DES methods, however these come at enormous computational costs, and therefore not a practical choice to perform multiple analyses. An even more accurate solution would be to take physical data measured in the field. However these will be greatly influenced by the extremely complex nature of the real flow physics. Examples include turbulence, free surface, and waves effects which are not currently accounted for in this BEMT model.

5.3.8 Sensitivity analysis

A sensitivity study is performed to assess the influence of the tip loss correction, as well as the lift and drag coefficients on the rotor power and thrust predictions. 5 cases are analysed for an inflow velocity of $3ms^{-1}$: i) normal reference; ii) no

tip loss correction applied; iii) C_D + 50%; iv) C_L +20%; v) C_D + 50% and C_L +20%. The impact of these can be seen in Figure 5.21

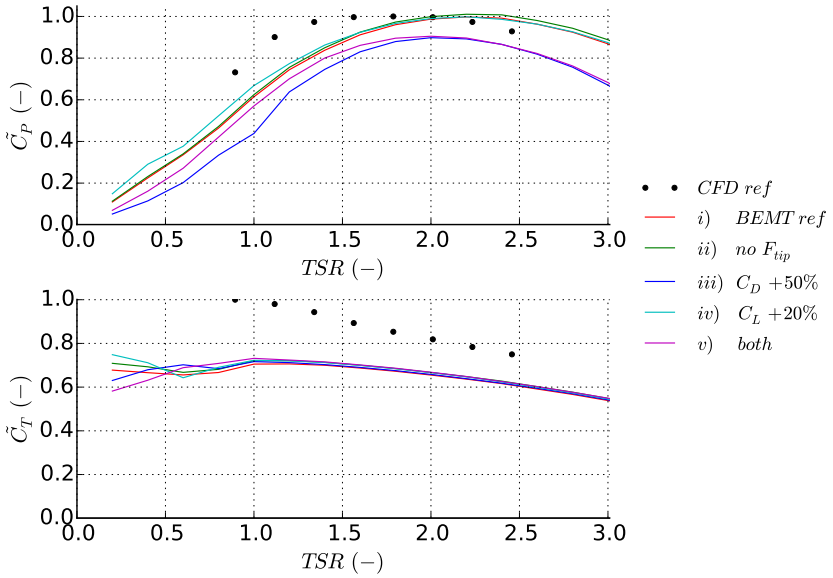

Figure 5.21: Normalised coefficients of power (top) and thrust (bottom) for a PS2 turbine to analyse sensitivities to the tip loss correction factor and hydrofoil coefficients

The overall influences in maximum values of power and thrust are detailed in Table 5.3. It can be seen that increasing the lift coefficients by 20% has the largest influence by increasing the thrust by 6% whilst keeping the peak power and optimal TSR almost constant. The removal of the tip loss correction factor also increases the thrust, but additionally has an influence on the power. Although

Table 5.3: Table of maximum normalised coefficients of power, thrust and optimal TSR showing sensitivity of results to tip loss factor and modified hydrodynamic coefficients

Case	Definition	TSR_{opt}	$\tilde{C}_{Pmax}$	$\tilde{C}_{Tmax}$
i	ref BEMT	2.2	0.998	0.706
ii	no F_{tip}	2.2	1.011 (+1.30%)	0.721 (+2.14%)
iii	C_D + 50%	2.0	0.898 (-9.98%)	0.717 (+1.47%)
iv	C_L + 20%	2.2	0.998 (+0.07%)	0.748 (+5.98%)
v	both	2.0	0.905 (-9.28%)	0.732 (+3.60%)

these are only based on arbitrary numbers, the improvements are not sufficient to reach the same levels of thrust seen by the CFD. Therefore the 3-D flow

assumptions are thought to have the highest impact, which is a limitation implicit in the BEMT technique.

5.4 Engineering application: corrosion

TSTs are exposed to the marine environment and therefore components are at high risk of corroding. This could cause damage which may affect turbine hydrodynamic performance, or lead to catastrophic failure in developed cases.

This short demonstration assessment shows how the developed ducted numerical code can be used in a practical engineering application case. A design change is proposed whereby sacrificial anodes are installed onto the rotor in order to offer corrosion protection to rotating components. The high computational efficiency of the BEMT model can be exploited in order to make fast first stage indications on how these structures would affect the hydrodynamic performance of the turbine.

5.4.1 Corrosion in TSTs

Corrosion is the natural process by which materials degrade due to chemical reactions with the environment. Metals and alloys exposed to saline solutions corrode through an electrochemical process which changes the atomic composition of the materials and in effect their mechanical properties.

A recently installed array of two PS2 devices at the Paimpol-Bréhat site, Brittany (DCNS OpenHydro, 2016) reported a corrosion issue in some of its fasteners (Tidal Energy Today, 2017*a*). This was found to be caused by underspecified materials in parts provided by an external supplier. Whilst the faulty parts were considered minor elements in the overall system, they were used to fix the generator in position, and therefore considered critical. Tests confirmed a long term durability issue, prompting the retrieval of both turbines in 2017 (Tidal Energy Today, 2017*c*) for repair. The fault was also discovered on components of similar turbines as part of the Cape Sharp Tidal Project in Canada. This has resulted in long

delays for deployment into the Bay of Fundy, Nova Scotia (Tidal Energy Today, 2017*b*).

This is an example which demonstrates the importance of adequately protecting against corrosion within TST designs.

5.4.2 Sacrificial anodes

Corrosion can be avoided through careful selection of certain materials with corrosion resistant properties. However this is not always possible, and alternative solutions must therefore be used.

A typical method to reduce the risk is through cathodic protection, whereby sacrificial anodes are installed. This directs the corrosion effects to the sacrificial metal rather than the material to be protected. One issue is that proximity of the anode to the component at risk is essential to their effectiveness.

One design option to protect rotating components is to fix anodes directly onto the outer ring of the rotor, between each blade. A schematic of such a system for the OpenHydro PS2 TST is shown in Figure 5.22. The proposed anodes are

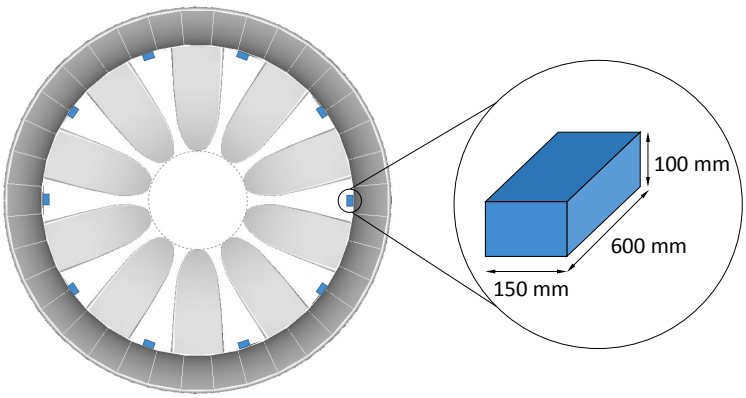

Figure 5.22: Schematic of a PS2 TST with generic sacrificial anodes attached to the rotor

approximated to rectangular section structures of arbitrary dimensions: width = 150 mm, height = 100 mm, and length = 600 mm (parallel to rotor axis).

5.4.3 Incorporating anodes into BEMT model

Installing structures onto the turbine will create additional hydrodynamic drag which results in additional thrust forces. Installing structures onto the rotating components of the turbine will have effects on the flow physics as the turbine rotates, and therefore also likely to impact the hydrodynamic performance.

These effects can be estimated within the BEMT model by taking the anodes as additional elements with specific hydrodynamic coefficients. A drag coefficient of an arbitrary value is assumed $C_D = 1.0$ before the relative impact is tested through imposing a higher value of $C_D = 2.0$. C_L is set to zero.

The effects on the rotor hydrodynamics are then assessed through comparing the resultant power and thrust curves.

5.4.4 Results: impact on power and thrust

Figure 5.23 shows the normalised power and thrust curves, using the unprotected case (no anodes installed) as the reference to assess the relative impact of the anodes. Here, only one midrange inflow velocity is considered. It can be seen that the presence of the anodes has a significant effect on the predicted power, which increase with TSR. The effect on the rotor thrust however is seen to be negligible.

Anodes of $C_D = 1.0$ reduce the peak power coefficient by 2.7%. increasing the drag to $C_D = 2.0$ reduces the peak power further, by 5.0%. The peaks are also seen to shift to a slightly lower TSR.

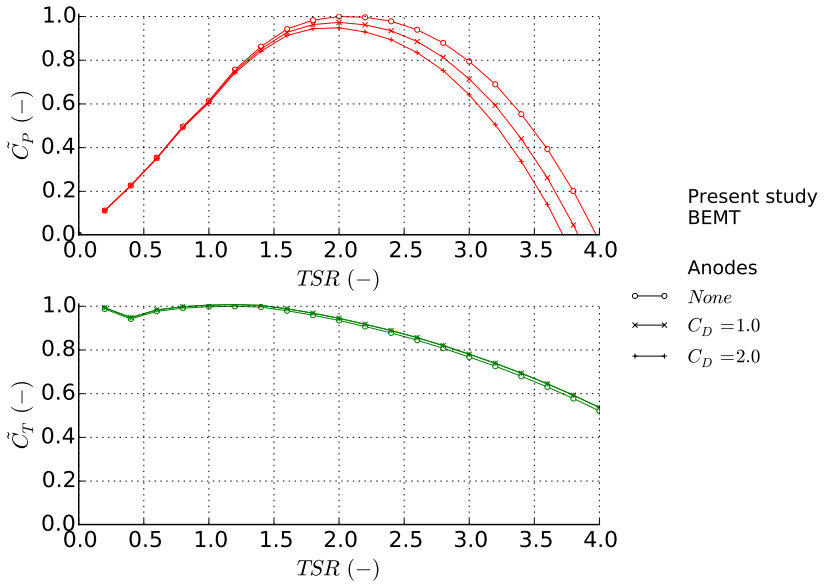

Figure 5.23: Normalised coefficients of power (top) and thrust (bottom) for a PS2 turbine to analyse sensitivities to the additional sacrificial anodes of two different arbitrary drag coefficients

5.4.5 Analysis

It is intuitive to think that the addition of structures which have only associated drag will mainly lead to higher forces in the axial direction, however this result shows the contrary.

If the force vectors located at the anode element is considered (as shown in Figure 5.24) due to there being a zero angle of twist β, the inflow angle ϕ is equal to the angle of attack α. As α is small at the outer radius of the rotor, the forces due to drag will be more line with the rotor plane. As there is no lift, the tangential forces are a function of $\cos(\phi)$ and act in the direction opposing rotation. This reduces the torque by a large amount due to being situated at the outer radius, thus causes large reductions in power. The axial force is a function of $\sin(\phi)$ and is therefore much smaller.

As the rotational velocity of the rotor Ω increases, the relative velocity over the element in the tangential direction U_{tan} becomes larger. This reduces ϕ further,

directing more of the forces in the direction opposing torque. This is the reason behind the larger reductions seen at higher TSRs.

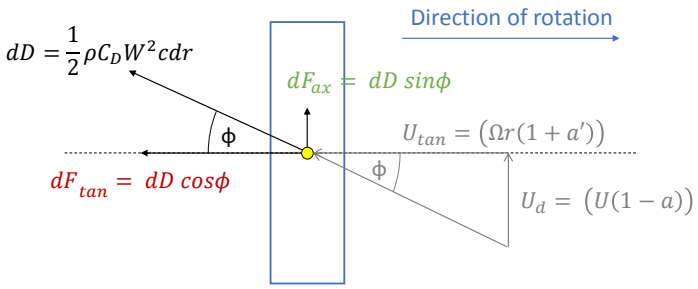

Figure 5.24: Velocity and force diagram for an anode element

This analysis does not aim to accurately represent a physically realisable design of anode. Moreover, simplified inputs have been purposefully selected in order to assess the relative influences one modification has on the overall hydrodynamic performance of the turbine.

This brief assessment has demonstrated the capabilities of the BEMT model to making fast, computationally efficient assessments. These can be used to better understand various aspects of the turbine hydrodynamic behaviour in order to aid early stage engineering decision making.

5.5 Summary

A ducted BEMT model using a modified expression for axial momentum changes through a duct has been developed and tested. The modifications are based on a set of analytical expressions, which are solved using empirical coefficients devised by CFD studies on uni-directional ducts from the literature.

The rotor power and thrust predicted by the ducted BEMT model is very similar to a RANS BEM study (within 2%) for most TSRs tested. This verifies the modified momentum theory that is incorporated into the newly developed code. This is further emphasised by similarities seen in the radial distribution of flow

velocity, angle of attack and local elemental thrust. Some divergence is seen at very high TSRs above the optimal rotational velocity, where BEMT is seen to over predict power by 25% and thrust 10%. This is a result of over predictions in the forces close to the hub, which indicates a limitation in capturing flow around the hub and through the open centre. The ducted BEMT has shown significantly lower computational requirements compared with the coupled RANS BEM method in the order of a few CPU-minutes rather than a few CPU-days.

Two commercial applications have been successfully analysed with the model, using hydrofoil lift and drag curves from 2-D RANS simulations detailed in Chapter 3. Comparison with blade resolved RANS simulations show similar trends and key magnitudes, with reasonable agreement in power but under predictions are seen in thrust by an average of 40% (OCT16) and 30% (PS2). This is thought to be due to the additional thrust contributions from the outer ring connecting the blades, which are not accounted in the BEMT model, and the hub in the case of OCT16 . Additional contributions are thought to stem from the 2-D assumptions inherent in the BEMT technique being unable to capture the complex 3-D flow interactions. These effects are seen to be particularly influential in the case of open tip blades, due to varying amounts of span wise flow and tip vortex shedding, and due to the blade being in stall at TSRs below 1.5.

Accounting for complex 3-D flow requires models of extremely high computational resources, which are less suited to practicable engineering applications. However, these can be used to feed into the development of case specific corrections factors, which can lead to BEMT model improvements. This is currently under investigation through a collaborative study between EDF R&D and the University of Strathclyde. Additional validation has also commenced, using field measurements from OCT16 and PS2 devices deployed at Paimpol-Bréhat to assess the model capabilities of predicting turbine performance that is physically observed in tidal flows.

Chapter 6

Structural Analysis of a Tidal Stream Turbine Blade

TST blades are designed primarily to give an optimal hydrodynamic performance to maximise power production potential. The material properties and the internal structure are selected to ensure a blade can resist the large forces associated with the harsh nature of the marine environment.

The main aim of this chapter is to present a methodology for assessing blade structural integrity by applying forces calculated using the ducted BEMT code developed in this thesis. An example case is detailed, based on an OpenHydro PS2 composite blade but with generic material and structural properties. This is to demonstrate how the benefits of a fast running and computationally efficient hydrodynamic model can be exploited to perform practical engineering assessments and iterations.

A numerical tool is developed to assess the structural integrity of the blades based on: 1) survivability under normal operation; 2) extreme conditions for two tidal sites; 3) fatigue damage from cyclic loading under non-uniform inflow profiles. This work is partially published in Allsop, Peyrard, Bousseau and Thies (2017).

6.1 Introduction

Blades are critical components of a TST, failure of which prevents its principal function of generating power. Due to high operational expenditures (OPEX) related to the offshore environment, TSTs are designed to have minimal maintenance requirements and therefore blade structural integrity is a key consideration. Occurrences of blade failures in the industry have emphasised the necessity of analysing performing structural analysis in order to ensure survivability under specific operating conditions over the required lifetime.

Examples of real life occurrences include: OpenHydro, where a failure case in May 2010 was reported from a deployment in the Bay of Fundy, Nova Scotia (CBC News, 2011). All 12 blades failed, which was reportedly due to extreme flow velocities of 10 knots (5.14 ms^{-1}), 2.5 times greater than those in the design specification. Atlantis also recorded a failure of its experimental composite blades in August 2010 fitted to its twin rotor AK1000 device, installed at the EMEC test facility, Orkney (Atlantis Resources Ltd., 2010). This was reportedly caused by a manufacturing fault, related to a defect in the composite material during the fabrication process (BBC News, 2010).

6.1.1 Approach

Blade structural integrity can be assessed through applying engineering analytical tools to the output of the hydrodynamic analyses detailed in Chapter 5, Section 3.

Hydrodynamic modelling is used to predict the forces exerted on each blade. These can be translated into stresses, which is a quantifiable measure of the structural response to loading, and are a function of the blade geometry and internal structure. If the stresses exceed the limits defined by the material properties, failure will occur. Safety factors are applied to lower the ultimate limits by a specific margin. These are defined by the level of uncertainties in loading conditions and material properties.

Here the integrity of the blades is assessed under two failure modes: survivability under extreme loading; and cumulative fatigue damage under cyclic loading. Operational loads resulting from the hydrodynamic interaction of the blade structure with the fluid are a function of the relative flow velocity. Variations in loads and blade geometry down the blade length result in spatially varying stress levels, which can be determined at a radius and azimuth. Stress hot-spots can be identified as areas with peak stress, indicating areas where the blade is likely to fail.

Fatigue describes the degradation or weakening of a material from repetitive loading. The fatigue life defines the number of times a specific stress level can be applied before failure occurs. The damage defines the accumulation of fatigue degradation over a period of time. This is a function of the number of times a stress level is expected to occur in service, as a proportion of fatigue life. The overall cumulative damage combines the proportion of damage at each stress level to determine if a blade design is adequate for the intended site. Spatial and temporal variations in the flow velocity cause variations in stress, which have an associated impact on the fatigue life of the blades. These are therefore considered in the hydrodynamic load predictions.

6.2 Loading conditions

Blades are subjected to a number of different load types, the majority of which can be categorised into: fixed, operational, environmental, accidental and testing loads. In this section, the focus is on the first three categories, which are related to the blade design, operating parameters and inflow conditions.

6.2.1 Operating environment

OpenHydro have, as of May 2016, deployed two 500kW rated PS2 devices at the Paimpol-Bréhat site, off the coast of Brittany, France. This is part of a pilot

array in collaboration with EDF R&D (DCNS OpenHydro, 2016). Maximum depth averaged velocities simulated using Telemac (Pham and Martin, 2009) are reported as (flood / ebb respectively): spring tide 2.2 / 2.0 ms^{-1}; and neap tide 1.1 / 1.0 ms^{-1}. This study also reports a measurement campaign in 2008 using two ADCPs installed within the race, which measured maximum surface velocities of (flood / ebb) 3.0 / 2.3 ms^{-1}.

A larger array of seven 2 MW rated PS2 devices is currently being developed for deployment in 2018 as part of the Normandie Hydro project (EDF-EN, 2014). The turbines will be installed into a higher energy site in Raz Blanchard (Alderney Race). Recent ADCP measurements of this area (Thiébot et al., 2015) indicate maximum depth average spring tides of: 3.7 / 3.4 ms^{-1} (flood / ebb). Neill et al. (2012) indicate maximum spring tides velocities of 4.0 ms^{-1} from British Geological Surveys, whereas Bahaj and Myers (2004) report a maximum surface velocity of 5.0 ms^{-1} using data from Admiralty charts.

6.2.2 Operational loads

The operational loads are characterised by the axial and tangential forces acting on the blades, that are computed from the BEMT model. These loads vary as a function of the tidal flow velocity, which are a condition of the specific site. Normal operating and extreme tidal velocities for two sites to be considered are shown in Table 6.1. This assumes a 1 ms^{-1} cut-in speed (as per Myers and Bahaj (2005)).

Table 6.1: Operational and extreme tidal velocities (assumed at hub height) for two French case study sites

Site	Location	Normal (ms^{-1})	Extreme (ms^{-1})
1	Paimpol-Bréhat	1.0 - 2.5	3.0
2	Raz Blanchard	1.0 - 4.0	5.0

Blade forces are also a function of the rotational velocity of the turbine, which is

set by the controller to achieve maximum power production. Operational TSRs in the power production zone are between 0.5 - 3.5.

Centrifugal forces also act along the blade axis as a function of the rotational velocity, however have been neglected from this analysis.

6.2.3 Environmental loads

Environmental loads encapsulate a number of different phenomena, including: inflow variations, turbulence, waves, submerged debris, marine growth and temperature. Within this study, only the influences of different quasi-static inflow profiles is assessed, which approximate the effects of viscous friction with the seabed. For operational loading a shear profile with a $1/7^{th}$ power law is assumed, however this is a simplification so as to demonstrate the implications on the blade structure. In reality, the shear profile will be more complex due the interactions with the site bathymetry, which lead to large spatial and temporal variations.

6.2.4 Fixed loads

Fixed loads are non-operating loads, which are taken here as the weight volumetric forces as well as the pressure forces acting on the surface of the blade. The blade is designed to be as neutrally buoyant as possible, in order to balance these forces. However, this cannot be completely achieved as the static pressure changes as the turbine rotates and the blade depth changes, causing the fixed loads to fluctuate.

In order to observe the relative influence of fixed loads on the blade stress, a simplifying assumption is made. A single load is assumed in the form of a weight force, which is set at 20% of the real weight (out of water). This value is selected as a conservative approximate of how much the forces can vary around the neutral buoyancy level. This corresponds to approximately 2 kN, based on a similar TST study (Bir et al., 2011), which is applied as a series of point forces along the blade, in proportion to each individual elemental volume.

6.2.5 Load cases

The blade structural integrity can be assessed based on its ability to withstand different loading conditions. These are defined by a number of load cases, as defined in Bureau Veritas (2015). This study examines the following:

- **Load case 1: normal operation -** defined as a combination of the operational, fixed and environmental loads which are experienced during power generation mode in 'normal' flow and rotational velocities. These are ultimate loads, taking into account appropriate safety factors.
- **Load case 2: extreme operation -** defined by the combination of operational, fixed and environmental loads that occur at the maximum current velocity of the site (assuming power generation mode). These are ultimate loads, taking into account appropriate safety factors.
- **Load case 3: fatigue -** a process of cycle by cycle accumulation of damage, which can cause failure even at stress levels below the maximum allowable limits stipulated by the composite properties. Here, the cyclic stresses driven by the azimuthal variations in load from varying flow velocities as a function of height above the seabed are assessed. Turbulence and wave interactions, as well as vortex induced vibrations are thought to have significant impacts on blade fatigue, and considered for future analysis outside of this current study.

6.3 Blade load distributions

Previously, the BEMT code was used to assess the turbine performance through a measure of the overall rotor thrust and torque. The forces along the blades however are seen to vary considerably along the length, and also show a dependence on azimuth when non-uniform inflow profiles are applied. It is therefore necessary to analyse the elemental forces. These can be output from

BEMT as point forces at the centre of each elemental section, where the method does not explicitly consider the surface pressure distribution.

For illustrative purposes within this section, a single operating condition is presented, with a hub height inflow velocity of $U = 2.0$ ms^{-1} and TSR=2.0.

6.3.1 Coordinate system definitions

Coordinate systems are defined in order to assess the loading and corresponding stresses in reference to specific directions. The global coordinate system of the OpenHydro PS2 turbine can be related to a local coordinate system for a blade, as shown in Figure 6.1.

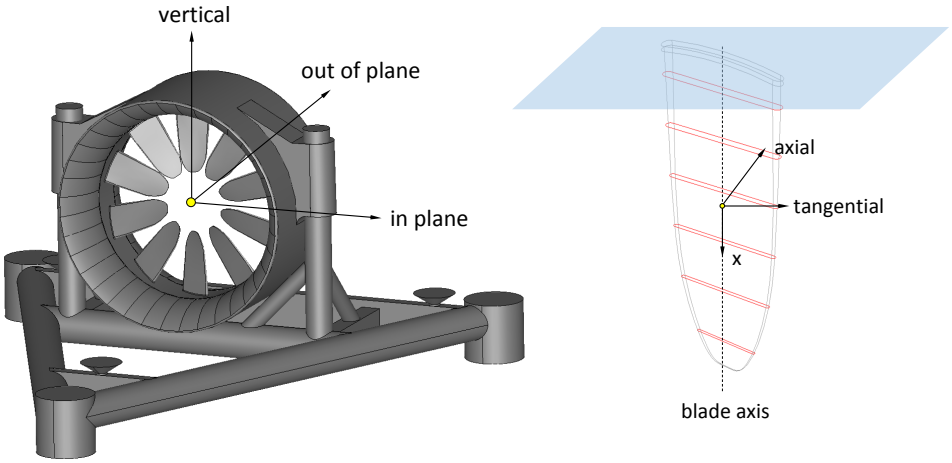

Figure 6.1: CAD model of an OpenHydro PS2 TST indicating global coordinate system (left) and individual blade showing local coordinate system (right)

6.3.2 Blade loads

Operational loads act in the axial, tangential and blade axis directions, thus are always in line with the coordinate system. As the blades rotate, the weight forces remain in the global vertical direction, and therefore act in the blade axis and tangential directions depending on the azimuth (see Figure 6.2). Azimuthal angles are set at 0° in the 9 o'clock position, increasing in a clockwise direction.

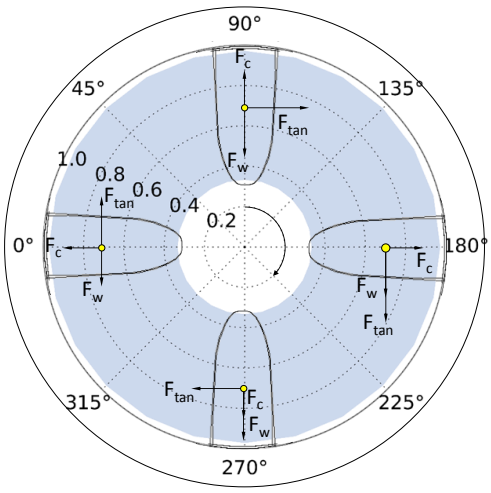

Figure 6.2: Blade forces in the blade local coordinate system relative to the rotor, showing change of weight force direction with azimuth in relation to reference (0° at 9 o'clock position, positive clockwise)

The weight forces can be translated from the global to local coordinate system as a function of the blade azimuth by the following expressions:

$$F_{tan} = F_{tan} + F_w \cos(\Phi + \pi) \tag{6.1}$$

$$F_x = F_w \sin(\Phi + \pi) \tag{6.2}$$

6.3.3 Cyclic loading

When assessing non-uniform inflows, the inflow velocity along the blade varies as a function of height above the seabed. This also causes a variation of operational loads as a function of the azimuth as shown in Figure 6.3. For this single inflow and TSR velocity, under a $1/7^{th}$ power law profile, root shear forces can be seen to fluctuate significantly. A range of 5.1 kN (26%) in axial, and 2.5 kN (31.3%) in tangential forces is seen during one rotation.

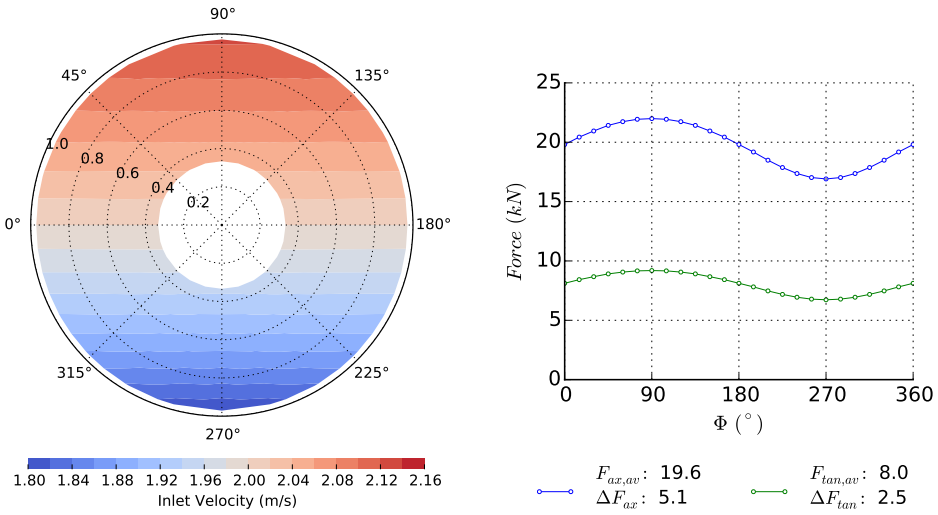

Figure 6.3: Velocity distribution under a $1/7^{th}$ power law with $U_{hub} = 2.0\ ms^{-1}$ (left) and azimuth dependent root shear forces in axial and tangential directions at $TSR = 2.0$ (right)

6.3.4 Beam theory

The blade can be approximated as a cantilever beam, fixed at one end representing the root connection to the outer ring which rotates within the stator, and free at the tip towards the turbine centre. The individual elemental forces in the axial and tangential direction can then be applied as shown in Figure 6.4.

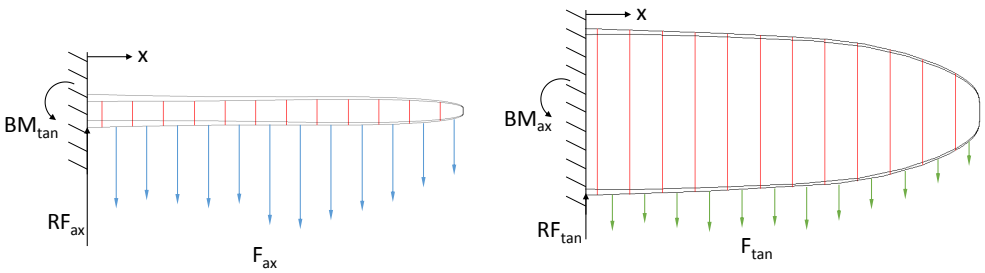

Figure 6.4: Cantilever beam representation of a blade indicating forces and bending moments in the blade local coordinate system

Note that the elemental forces calculated by BEMT are already solved over the element length dr, and are not given per unit length. The resultant force at

the root in each direction can be simply calculated as the sum of the individual elemental forces in each direction:

$$RF_{ax} = \sum_{i=1}^{N} F_{ax_i} \qquad RF_{tan} = \sum_{i=1}^{N} F_{tan_i} \tag{6.3}$$

The root bending moments can also be determined as the sum of the elemental force in each direction multiplied by the distance from the connection point (x):

$$BM_{tan} = \sum_{i=1}^{N} F_{ax_i} x_i \qquad BM_{ax} = \sum_{i=1}^{N} F_{tan_i} x_i \tag{6.4}$$

6.3.5 Shear force and bending moments

The shear force (SF) and bending moment (BM) diagrams for a uniform inflow are shown in Figure 6.5. From this, the resultant force and root bending moment at the connection point ($r/R = 1$) can be determined in the axial and tangential directions. As previously explained, the tangential force is impacted by the blade weight force depending on azimuthal position. As this is a fixed load, the influence on the resultant force at the root will be ± 2 kN, independent of rotational speed.

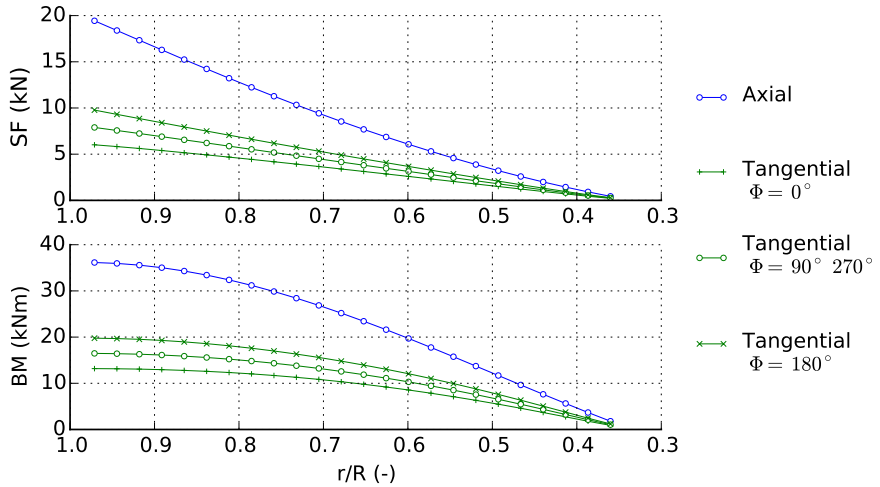

Figure 6.5: Shear force and bending moment diagrams in the blade local coordinate system under a uniform inflow of $U = 2.0\ ms^{-1}$ and $TSR = 2.0$

6.4 Blade properties

In order to demonstrate the application of these loads to assess the structural integrity of TST blades, the loads can be used to determine the stresses. These depend on blade properties including: geometry, materials and structural layout.

6.4.1 Elemental forces

A new coordinate system for the individual blade elements is allocated, as shown in Figure 6.6. Each element is of a rounded edge flat plate hydrofoil with chord (c_i) and thickness (t_i) and an associated length (dr_i), where loads are applied at a single point midway along the length.

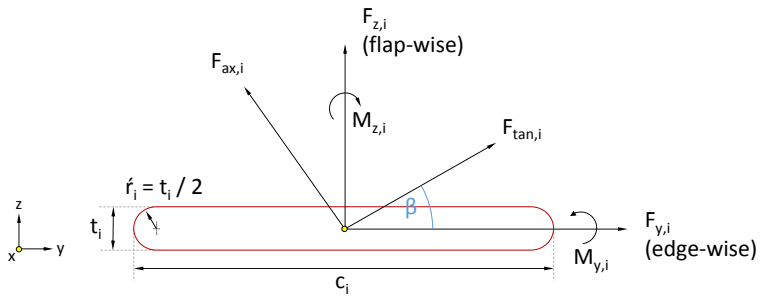

Figure 6.6: Local coordinate system of blade and a singular blade elements

Operational loads are determined from the BEMT model, where axial and tangential forces for each individual element i can be translated to flap-wise (z) and edge-wise (y) forces as a function of the elemental twist angle:

$$F_{z_i} = F_{tan_i} \sin(\beta_i) + F_{ax_i} \cos(\beta_i) \tag{6.5}$$

$$F_{y_i} = F_{tan_i} \cos(\beta_i) - F_{ax_i} \sin(\beta_i) \tag{6.6}$$

Fixed loads are determined by the assumption of blade weight force ($F_w = 2kN$), which is distributed along the blade as a function of the proportion of elemental

volume to overall blade volume:

$$F_{x_i} = F_w \frac{((c_i - t_i)t_i + \pi(t_i/2)^2)\, dr_i}{\sum_{i=1}^{N} ((c_i - t_i)t_i + \pi(t_i/2)^2)\, dr_i} \tag{6.7}$$

6.4.2 Internal structure

TST blades will be of complex structural design, constructed from composite materials with a specific outer layer configuration (with skin and foam ply cores) and incorporating internal structures (such as spars or webbing). Due to a lack of specific information regarding this structure within this study, the rounded edge flat plate hydrofoil sections are considered to be full of uniform, homogeneous material. This is to represent a case where the blade internal volume is filled with a foam or epoxy slurry, which can be used to achieve better neutral buoyancy and hence reduce weight forces (Bir et al., 2011).

This is a simplifying assumption which gives the highest possible moment of area for each t/c ratio, and therefore considered to give the 'best case' stresses.

6.4.3 Material properties and fabrication processes

The main raw materials considered for TST blade applications are: reinforcement fibres which are integrated to carry the mechanical loads; resin systems which are used to link reinforcements together, provide protection from moisture and abrasion as well as to spread forces through the laminates; and core materials used in laminate sandwiches to improve the blade moment of inertia (Bureau Veritas, 2015). Due to a lack of specific information regarding the exact materials and the methods of fabrication, some assumptions are made and defined here.

The composite structure is assumed to consist of laminates of glass fibre. Although carbon fibre is seen to give better structural properties, costs are around 10-20 times higher, and therefore glass fibre is considered a better compromise

between cost and performance for tidal applications (Li et al., 2014). Epoxy resin is selected due to high resistance to water absorption, and high adhesive properties. A sandwich structure is assumed with a foam core, which increases the moments of area of the elemental profiles thus reducing the stress without providing significant additional load bearing capability (Bureau Veritas, 2015).

At present, full scale demonstration turbines have been constructed, where the blade manufacturing process has likely been a batch production. This means that fabrication methods involve techniques optimised for low scale manufacture. Fabrics are assumed to be made up of uni-directional fibres constructed of glass mono-filaments. These are extruded through combining molten silica and alumina which are stretched through a die with holes ranging 5-25 μm (Bureau Veritas, 2015). An injection moulding process is assumed at this early stage, as used in the wind turbine industry (The Crown Estate, 2010) and in other tidal blade analyses such as Evans et al. (2013). With increasing production scale, this may change to a pre-preg process, where benefits include high accuracy resin/fibre ratios, but at the additional cost of curing equipment used to raise the process temperatures.

6.5 Stress analysis

The strength of a structure is determined by its ability to resist loading. Stresses are produced as a result of an imposed force, which causes deformation of the material. Blade stresses can be analysed as a function of the blade element geometries under given loading conditions, using structural mechanics fundamentals (e.g. Hjelmstad (2005)).

6.5.1 Stress tensor definitions

Stress vectors for a single blade element can be defined as shown in Figure 6.7.

These vectors can be combined into a stress tensor matrix, made up of normal

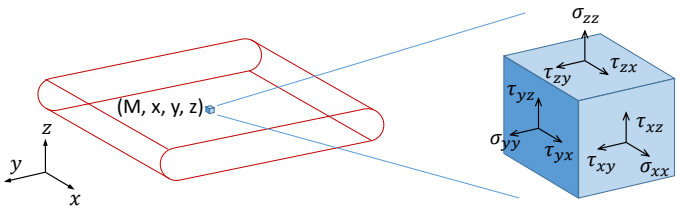

Figure 6.7: Stress tensors for a single blade element

(σ) and shear (τ) stresses expressed as:

$$[\sigma] = \begin{bmatrix} \sigma_{xx} & \tau_{xy} & \tau_{xz} \\ \tau_{yx} & \sigma_{yy} & \tau_{yz} \\ \tau_{zx} & \tau_{zy} & \sigma_{zz} \end{bmatrix} \tag{6.8}$$

6.5.2 Normal stresses

Normal stresses in the blade axis direction can be defined as the combination of direct stress from weight forces, and bending moments around y and z axis:

$$\sigma_{xx_i} = \sigma_{xx,x} + \sigma_{xx,y} - \sigma_{xx,z} \tag{6.9}$$

Where:

$$\sigma_{xx,x} = \frac{F_{x_i}}{A_i}; \qquad \sigma_{xx,y} = \frac{M_{y_i} z_i}{I_{y_i}}; \qquad \sigma_{xx,z} = \frac{M_{z_i} y_i}{I_{z_i}} \tag{6.10}$$

Where A_i is the cross sectional area of the blade element (m^2), M_{y_i} and M_{z_i} are the bending moments (Nm) around each axis; $z_i = t_i/2$ and $y_i = c_i/2$ are the perpendicular distances from the neutral axis to the surface (m), which give the point of highest bending stress. As the foils are symmetrical, and the loads will change direction with the change in direction of the tide, the maximum bending stresses will be the same in compression and tension on the front and back faces.

I_{y_i} and I_{z_i} are second moments of area about the neutral axis (m^4) for each element. These can be calculated as a function of the geometry, assuming a solid

internal material structure. The structure is broken up into sub shapes (subscript j), and then the total second moment of area is determined as:

$$I_i = \sum_{j=1}^{N} I_j + A_i {d_j}^2 \tag{6.11}$$

where d_j is the distance to the centroid of the individual sub shapes. These can be established from the above geometry about each axis as:

$$I_{y_i} = \frac{(c_i - t_i)t_i^3}{12} + \frac{\pi t_i^4}{64} \tag{6.12}$$

$$I_{z_i} = \frac{t_i(c_i - t_i)^3}{12} + \frac{\pi t_i^4}{64} + \frac{t_i^3(c_i - t_i)}{6} + \frac{\pi t_i^2(c_i - t_i)^2}{16} \tag{6.13}$$

6.5.2.1 Direct and bending stress components

The individual components which combine to form the normal stress are: the direct ($\sigma_{xx,x}$) which arise from the blade weight, and bending stresses around the y axis ($\sigma_{xx,y}$) and z axis ($\sigma_{xx,z}$). These can be individually plotted in order to assess the relative size of each. These are shown in Figure 6.8, for a single uniform inflow of $U = 2.0\ ms^{-1}$ and $TSR = 2.0$, as a function of radial location.

The direct stresses due to fixed loads act down the blade axis, and therefore are maximum when blades are in the vertical position (at $\Phi = 90°$ and 270°), and zero in the horizontal position (at $\Phi = 0°$ or 180°). Even at the maximum, the magnitude of the stress is sufficiently small to be described as negligible for this case.

The addition of the weight force does not contribute to bending when $\Phi = 90°$ or 270°. However increases to a maximum when the blades are horizontal $\Phi = 180°$. This is seen to highly impact bending stresses due to moments around the z axis, where values are almost doubled. In the case of bending stresses around the y axis however, the weight has a relatively small impact.

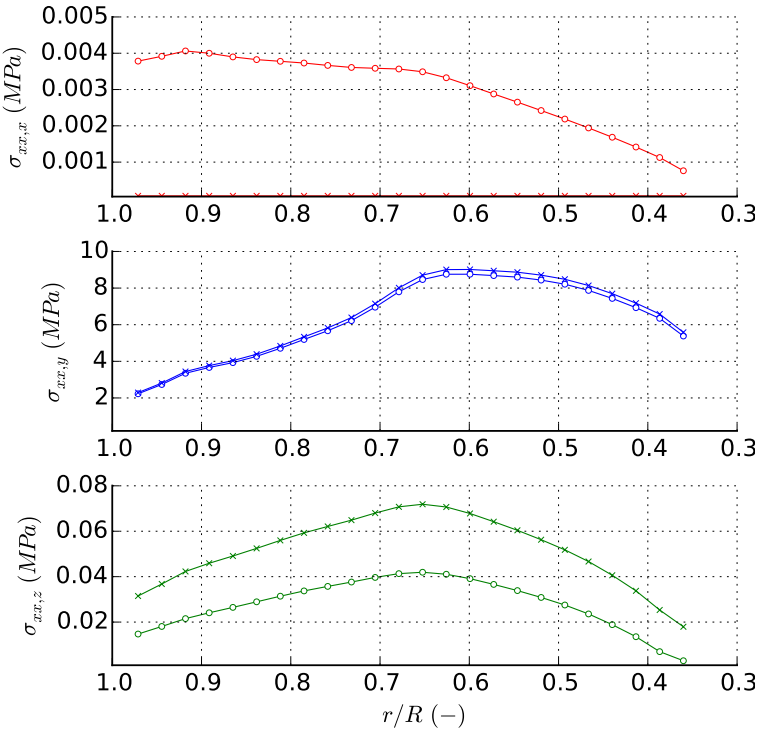

Figure 6.8: Breakdown of the normal stress into direct (top) and bending moments around y-axis (middle) and z-axis (bottom) where circles represent $\Phi = 90°$ and crosses at $\Phi = 180°$

Overall, the bending stresses around the y-axis (from forces in the flap-wise direction) are seen to dominate and are greater by a factor of at least two orders of magnitude.

Here, the normal stress tensors in the other vectors are neglected, so $\sigma_{yy} = \sigma_{zz} = 0$. These are caused by pressure forces around the surface of the blade, which are not directly calculated by this BEMT which outputs elemental forces as single points. This assumption is thought to have minimal impact on the overall result due to the overriding influences of flap-wise bending moments.

6.5.2.2 Tip stress anomaly

An unusually high stress has been located at the blade tip, which is seen at all inflow velocities above 1.0 ms^{-1}. Forces and moments are minima at this

location, however the bending stresses are inversely proportional to the element second moment of area, which is a minimum at the tip. This would naturally lead to larger values.

The issue is that within the analysis, a point loading at the centre of an element length is assumed. This assumption becomes a problem where there are large changes in geometry, as there are larger step changes between elements and forces are not appropriately averaged. For this study, all elements have the same length and therefore the tip does not represent the smooth transition seen in reality. In order to account for this, a better refinement of blade elements is required. Additionally, as detailed in Chapter 5, Section 2.2.11, there are some errors in the treatment of the tip losses within the BEMT model which are thought to cause inaccurate calculations of the hydrodynamic forces in this zone.

This maximum stress occurrence is therefore thought to be an anomaly which does not represent the physical nature of the flow. For this reason the tip element is neglected, so these non-physical effects do not influence the stress distribution on the surrounding blade elements.

6.5.3 Shear stresses

Shear stresses arise from the tendency of a material to slide in a plane parellel to the force component vector. Planes in the x-direction are assessed using the individual element shear forces in each y and z directions. These can be expressed as:

$$\tau_{xy_i} = \frac{F_{y_i} Q_{z_i}}{I_{z_i t_i}} \qquad \tau_{xz_i} = \frac{F_{z_i} Q_{y_i}}{I_{y_i c_i}} \tag{6.14}$$

Where Q is the first moment of area about each axis. Simplifying the geometry to a rectangle, these expressions can be reduced to represent the parabolic distribution through the material in the direction of the force, which peak at

the neutral axis (when $y_i = 0$ and $z_i = 0$) to give:

$$\tau_{xy_i} = C_s \frac{F_{y_i}}{A_i} \qquad \tau_{xz_i} = C_s \frac{F_{z_i}}{A_i} \tag{6.15}$$

Where $C_s = 1.5$ is the coefficient of shear.

Figure 6.9 shows the magnitude of these stresses in two planes, similar to the edge-wise bending stress. Again fixed loads are influential in this condition, almost doubling y-direction shear. However these are still considered of low significance relative to the flap-wise bending stress, which are around 100 times larger.

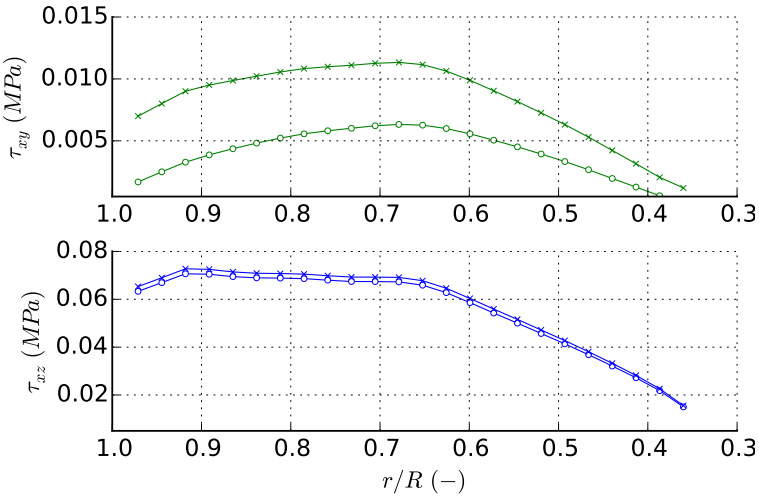

Figure 6.9: Shear stresses in y-vector (top) and z-vector (bottom) where circles represent $\Phi = 90°$ and crosses at $\Phi = 180°$

As the shear stresses from principal loads are relatively small, the shear stresses in all other directions are neglected so: $\tau_{yx} = \tau_{yz} = \tau_{zx} = \tau_{zy} = 0$.

6.5.4 Von Mises stresses

In order to combine the stress tensors into a singular parameter for comparison, the Von Mises stress (Hjelmstad, 2005) can be defined by:

$$\sigma_{vm_i} = \sqrt{\sigma_{xx_i}^2 + 3(\tau_{xy_i}^2 + \tau_{xz_i}^2)} \tag{6.16}$$

6.6 Von Mises stress distribution analysis

The azimuthal and radial variations of Von Mises stress are presented in the following polar plots. These show the effects of introducing: environmental loads through the application of a non-uniform inflow profile; and fixed loads in the form of weight forces. Azimuthal angles are again set at 0° at the 9 o'clock position, increasing in a clockwise direction. A single operating condition is presented with a hub height inflow velocity $U_{hub} = 2.0\ ms^{-1}$ and $TSR = 2.0$.

6.6.1 Normal operational loads: uniform inflow

Figure 6.10 shows that for uniform inflows there is no azimuthal variation, as the velocity is constant everywhere across the disc. It is possible to locate maximum stress concentration zones along the blades to be close to the blade mid-length ($r/R = 0.62$), with a peak value of 8.72 MPa. Although the maximum shear forces, direct forces and bending moments are seen at the blade root, stresses are minimised in this region. This suggests a good level of element thickness, which raises the second moment of area sufficiently to resist these most extreme forces.

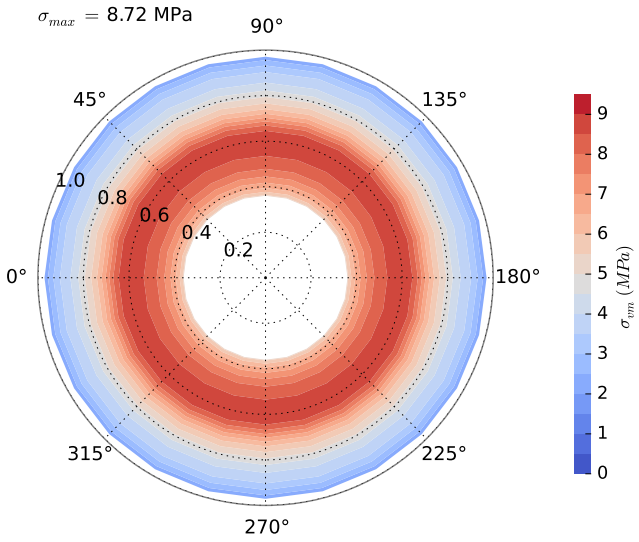

Figure 6.10: Polar plot of Von Mises stress distribution from a uniform inflow velocity profile at $U = 2.0\ ms^{-1}$, $TSR = 2.0$

6.6.2 Environmental loads: non-uniform inflow

A non-uniform inflow profile to approximate the vertical shear from sea bed friction is applied, based on a $1/7^{th}$ power law. The results are shown in Figure 6.11, where it can be seen that this causes a variation with azimuth, as the blade elements pass through different velocities at different locations in the water column. The distribution is symmetrical, as the inflow profile is 2D, with no transverse variations. Peak stress has increased to 9.39 MPa, (7.7 % higher than the uniform case), where a stress hot spot is located again towards the mid-length of the blade, at $\Phi = 90°$.

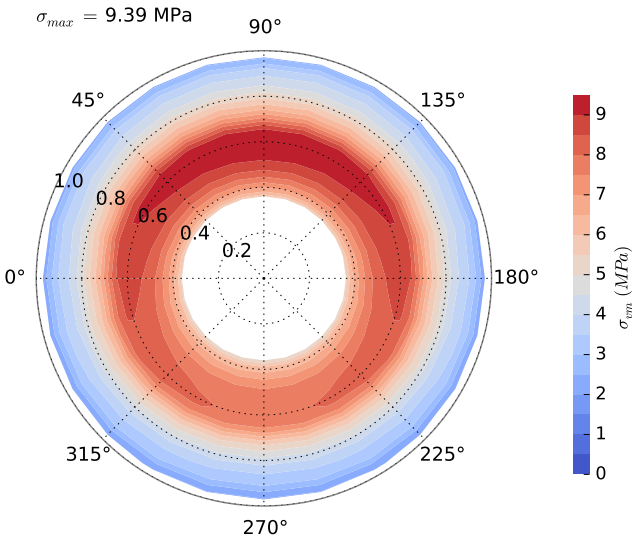

Figure 6.11: Polar plot of Von Mises stress distribution from a non-uniform inflow velocity profile of a $1/7^{th}$ power law at $U_{hub} = 2\ ms^{-1}$ hub height, $TSR = 2.0$

6.6.3 Fixed loads: blade weight

Figure 6.12 shows results of the same case, with the weight force added. This is seen to cause the stress distributions to shift clockwise, as the force combines with the torque in the blade coordinate system tangential direction. Peak stress is again around the blade mid point, calculated at 9.43 MPa (0.4 % greater than

for the neutral buoyancy case), at $\Phi = 105°$. As this is a fixed load, the relative influence will be higher at slower operational velocities.

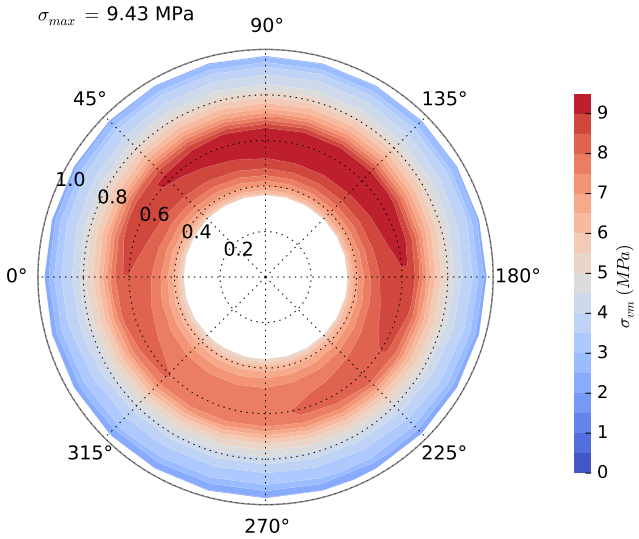

Figure 6.12: Polar plot of Von Mises Stress distribution around the rotor radius, with a 20 % weight force applied, using a non-uniform inflow velocity profile of a $1/7^{th}$ power law at 2 ms^{-1} hub height, for a TSR = 2.0

6.6.4 Cyclic stresses

The cyclic loading from spatial variations in velocity causes cyclic stresses as shown in Figure 6.13, for a single element at $r/R = 0.62$ and for a single TSR = 2.0. This shows the periodic stress, which has one cycle per rotation. The mean and amplitudes are seen to increase as a function of inflow velocity. The proportion of minimum to maximum stress ($R = \sigma_{min}/\sigma_{max}$) is recorded at between 0.78 - 0.86 for all cases.

6.7 Structural analysis

A methodology is here presented to relate Von Mises stresses to blade structural integrity. A demonstration case is described from the assumed blade structure, material properties and fabrication processes. Maximum allowable stresses and

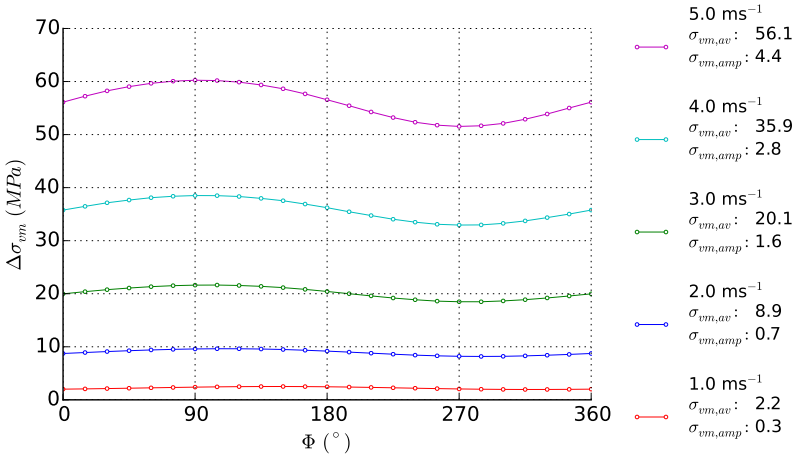

Figure 6.13: Cyclic stresses during one blade rotation of element at $r/R = 0.62$, TSR=2.0 for various hub height velocities, indicating average and amplitude

an S-N curve are calculated using information from an industrial guide on tidal turbines, Bureau Veritas (2015). This defines acceptance criteria, which can be used to assess whether or not the blade will survive under the load cases and site conditions of interest.

Note that the presented case is using surrogate data in order to protect the confidentiality attached to site or project specific information. However, the procedures presented can be subsequently used for more specific structural analysis applications.

6.7.1 Composite data

A lack of specific details on the composite material and structure of commercial TST blades has lead to the assumption of certain properties, which is based on the guidance notes. Classification of blade designs for wind turbines could be used, due to the similarities in overall design compared with TST blades. However there are significant differences in operating conditions which limit their application to ocean environments. In an attempt to account for this, composite materials for use in ship building are considered more suitable, due to the specific nature of the working fluid.

The mechanical characteristics of the laminates can be estimated from the characteristics of the individual raw materials. This information, as well as procedures for estimating theoretical breaking stresses are taken from Bureau Veritas document NR546: Section 4, on "the state of the art materials for composite boat building" (Bureau Veritas, 2015).

The compliance of the characteristics of the raw materials are to be certified by the society in accordance to homologation tests that are reported (Bureau Veritas, 2015). This would require compliance with ISO 527 (or equivalent) for resin systems, and ISO 3268 (or equivalent) for uni-directional fibres.

6.7.2 Composite theoretical breaking stress

Composite mechanical properties can be approximated as a function of the raw material properties, laminate arrangement and fabrication process. Raw material properties of the epoxy resin and glass fibres are detailed in Table 6.2. The molecular arrangement of the glass fibres means they are considered an isotropic material with identical mechanical properties in longitudinal and transverse directions.

Table 6.2: Raw mechanical properties of epoxy resin and glass fibres (taken from (Bureau Veritas, 2017))

Property	Resin		Fibre		Units
Density	ρ_r	1.25	ρ_f	2.57	gcm^{-3}
Poisson's coefficient	ν_r	0.39	ν_f	0.238	-
Tensile Young's Modulus	E_r	3.1	E_f	73.1	GPa
Tensile/compression breaking stress	$\sigma_{br,r}$	75	$\sigma_{br,f}$	1750	MPa
Tensile/compression breaking strain	$\varepsilon_{br,r}$	2.5	$\varepsilon_{br,f}$	2.4	%

Laminates are considered to be made up of unidirectional fibres, arranged so that the axis of each fibre is parallel to the blade axis. This is the direction of the principal stresses (σ_{xx}), and therefore the focus of this structural integrity analysis,

as shear stresses are considered too small to be the main mode of failure at this stage. Note that this is a simplification in order to demonstrate how the structural integrity of the blades can be analysed from BEMT loadings. Considerations on the stresses in the transverse direction and between laminates should be made in the more detailed design phase, with actual information regarding the composite and blade internal structure.

The Young's modulus of a unidirectional laminate can be defined down the longitudinal axis of the fibre (0°) as:

$$E_{0^\circ} = C_{0^\circ} \left(E_f V_f + E_r(1 - V_f)\right) \tag{6.17}$$

Where $C_{0^\circ} = 1.0$ is an experimental coefficient accounting for the specific characteristics of glass fibre type. $V_f = 0.4$ is the volumetric ratio of glass fibre to resin in each laminate, recommended for a hand lay-up laminating process of unidirectional fibres (Bureau Veritas, 2015).

The in-plane theoretical breaking stress in the fibre axis can be defined as:

$$\sigma_{br,0^\circ} = E_{0^\circ} \varepsilon_{0^\circ} C_{res} \tag{6.18}$$

Where $C_{res} = 1.0$ is the coefficient of the epoxy resin system, and the theoretical tensile breaking strain of unidirectional glass fibres is $\varepsilon_{br,0^\circ} = 2.7\%$. Thus, the theoretical breaking stress of a single laminate is: $\sigma_{br,0^\circ}$=839.7 MPa.

6.7.3 Safety factor of composite blades

A minimum rule safety factor (SF) can be defined based on certain aspects of the blade material structure. These are then applied to the main stresses of each laminate. The most conservative maximum stress criteria is taken, which relates

to the breaking of each layer of the laminate.

$$SF \geq \alpha C_V C_F C_R C_I \tag{6.19}$$

Where the individual partial safety factors are defined in Table 6.3. Note that the load predictions include a higher factor of uncertainty of 1.6 rather than 1.1 recommended in the guide, to account for possible under predictions in axial thrust forces (see Chapter 6, Section 2).

Table 6.3: Partial safety factors for TST blade main stress safety factor calculation (calculated from guideline instructions Bureau Veritas (2015))

SF	Value	Description
α_1	1.0	Load Case 1: normal operating conditions
α_2	0.8	Load Case 2: extreme conditions
C_V	1.35	Composite ageing effects: for face skin laminates of a sandwich
C_F	1.4	Fabrication process and reproducibility: for the case of hand lay-up processes
C_I	1.6	Load predictions: computed from a BEMT hydrodynamic model
$C_{R_{0^\circ}}$	2.6	Load type exerted onto reinforcement material: tensile and compressive stress parallel to direction of unidirectional fibre

The two safety factors are calculated to be 7.9 and 6.3 for normal and extreme case conditions respectively.

6.7.4 Maximum allowable stress definition

The maximum allowable stress is defined by the theoretical breaking stress, divided by the safety factor: $\sigma_{maxall} = \sigma_{br,0^\circ}/SF$. These are calculated to be 106.8 MPa and 133.5 MPa for normal and extreme case conditions respectively.

6.7.5 Theoretical S-N curve

The fatigue of a laminate can be assessed through the calculation of the total damage ratio. This is dependent on the types of material, composition, configuration and the process of fabrication.

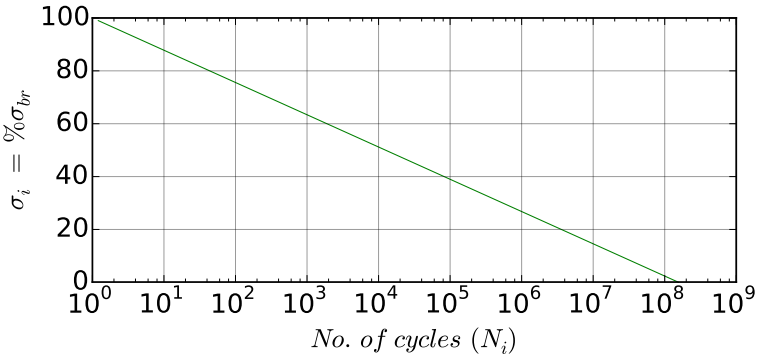

Figure 6.14: SN curve of a glass fibre / epoxy resin composite

The fatigue behaviour can be represented by a S-N curve, which describes the number of cycles that can be achieved at a certain stress level before failure occurs. This is defined by the equation given in the tidal turbine guidance note (Bureau Veritas, 2015) as:

$$N_{Ri} = exp\left(\frac{\sigma_i - 1}{-\alpha_i}\right) \tag{6.20}$$

Where N_{Ri} is the number of cycles to failure at stress level σ_i as a percentage of the maximum allowable stress (σ_{maxall} = 106.8 MPa). This method assumes a single value of minimum to maximum stress ($R = 0.1$) for cycles in tension. This corresponds to a value of $\alpha_i = 0.053$ in the glass fibres within an epoxy resin. Taking as such, a S-N curve is calculated, as presented in Figure 6.14. Only rotational cycles are accounted for here, with unidirectional flow causing tension stresses in the blade, which is more conservative than assessing bi-directional flow. A reversal of flow direction would cause peak stresses to be in compression, which has a different S-N curve and a much greater number of cycles to failure.

The cumulative damage can be defined as the sum of each elementary damage ratio D_i, which is defined by Palgrem-Miners linear damage hypothesis (Marsh et al., 2016) as:

$$D = \sum_{i=1}^{k} D_i = \sum_{i=1}^{k} \frac{n_i}{N_{Ri}} \tag{6.21}$$

Where n_i/N_{Ri} is the ratio of operational to maximum number of cycles at stress level σ_i. This can be attained through rainflow counting the stresses induced from the tidal velocities observed at a specific site, which can be used to determine if the blade will fail within its required lifetime.

6.7.6 Site 1: Paimpol-Bréhat

Load case 1 for normal operating and Load Case 2 for extreme conditions at the Paimpol-Bréhat site (as defined in Table 6.1) are analysed. Figure 6.15 shows the Von Mises stress distributions as a proportion of the maximum allowable stresses ($\sigma_{vm}/\sigma_{maxall}$). The peak Von Mises stresses are less than 20 % of the maximum allowable limit, which would indicate a satisfactory design for these conditions.

6.7.7 Site 2: Raz Blanchard

Load Case 1 for normal operating and Load Case 2 for extreme conditions at the Raz Blanchard site are also analysed, results shown in Figure 6.16. The peak Von Mises stress is 34 % of the allowable limit for Load Case 1, and 45 % for Load Case 2. This indicates that the structural integrity requirements for this site are also met, and further investigations into transverse direction and shear stresses are now recommended.

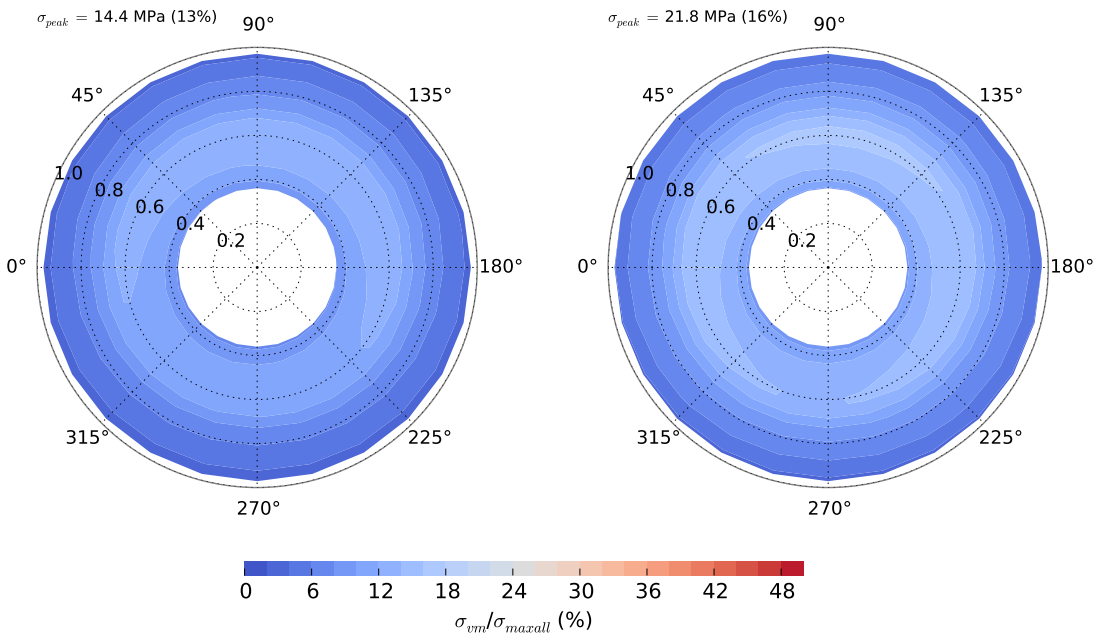

Figure 6.15: Polar plots of Von Mises stress distribution for Site 1, Paimpol-Bréhat: Load Case 1 - normal operation at $U_{hub} = 2.5\ ms^{-1}$, $TSR = 2.2$ (left); and Load Case 2: extreme conditions $U_{hub} = 3.0\ ms^{-1}$, $TSR = 1.4$ (right)

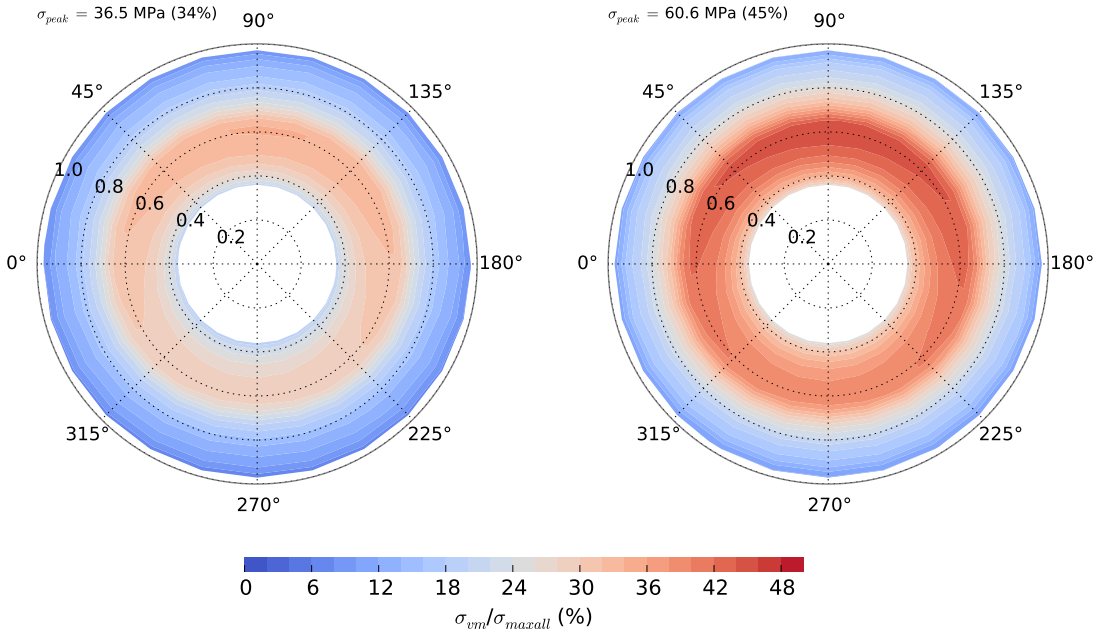

Figure 6.16: Polar plots of Von Mises stress distribution for Site 2, Raz Blanchard: Load Case 1 - normal operation at $U_{hub} = 4.0\ ms^{-1}$, $TSR = 2.3$ (left); and Load Case 2 - extreme conditions $U_{hub} = 5.0\ ms^{-1}$, $TSR = 1.4$ (right)

6.7.8 Fatigue damage

Peak Von Mises stresses for inflow velocities between 1 - 5 ms^{-1}, at TSRs between 1 - 3 are used to calculate the maximum number of cycles to failure, as shown in Figure 6.17. Here it can be seen that the number of cycles to failure is highly dependent on the inflow velocity. A tidal flow of 5 ms^{-1} will have a life 5 orders of magnitude shorter compared to 1 ms^{-1}. The impact from TSR is very low in slow speeds, and are only influential at higher inflow velocities.

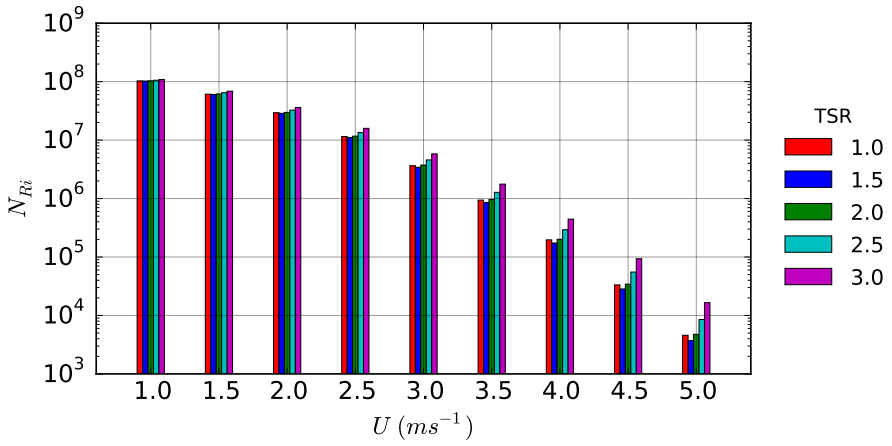

Figure 6.17: Number of cycles to failure (N_{Ri}) of a composite blade under various inflow velocities and TSRs based on a stress ratio $R = 0.1$

The number of rotational cycles at each velocity is required in order to determine if the blade will experience fatigue failure. This requires knowledge of the different velocities at a particular site, which can be obtained from historical data, or calculated using a harmonic analysis. The time evolution data is translated into the frequency domain by using a technique known as rain-flow counting (Marsh et al., 2016). The frequency of occurrence of each velocity within a certain period (the design life) equals the number of cycles. Dividing this by the associated number of cycles to failure for each velocity determines the damage.

In this simple demonstration case, proportions of lifetime (assumed 15 years) are applied under certain velocities seen within the Paimpol-Bréhat site, where the

turbine is assumed to run at a constant $TSR = 2.0$. A skewed bell shaped frequency distribution is assumed, with a peak at 1.5 ms^{-1}. This has been approximated from an ADCP data measured at the site (Pham and Martin, 2009) in order to demonstrate the procedure of performing fatigue life assessments.

The ratio of number of cycles to number of cycles to failure are then summed to assess the cumulative damage, as shown in Table 6.4. Under these assumptions, the overall blade damage is > 1 and therefore passes exceeds the acceptable limit. A result such as this would indicate the blade will experience fatigue failure within it's lifetime in this site, and therefore the recommendation would likely be a design change to reduce the Von Mises stresses, or a fabrication method change to increase the maximum allowable limit. The larger damage contributions from faster flow velocities is partially due to higher stresses reducing number of cycles to failure, but also as a result of the higher number of cycles per minute when running at a constant TSR.

Table 6.4: Number of cycles at a various inflows and their corresponding damage, assuming a constant TST=2.0 and design life of 15 years

U_{hub} (ms^{-1})	Ω (rpm)	% of life	n_i	N_i	D_i
1.0	3	25	5.9E+06	1.0E+08	0.057
1.5	4	50	1.8E+07	6.2E+07	0.286
2.0	6	20	9.4E+06	3.0E+07	0.315
2.5	7	4	2.3E+06	1.2E+07	0.201
3.0	9	1	7.0E+05	3.7E+06	0.188
				total	1.047

6.8 Discussion

The work presented in this chapter demonstrates how the ducted BEMT model can be used to relate blade forces to the structural integrity. The tools developed here can be applied to assess any TST blade given its internal structure and material properties.

6.8.1 Stress analysis

Stresses due to shear and fixed loads are seen to be negligible in the considered cases, particularly at higher inflow velocities. The flap-wise bending stresses are seen to dominate, which could be used to assess blade survivability under normal and extreme operation instead of Von Mises stresses. This would reduce the complexity of the model with little impact on the overall outcome. However, fixed loads have a greater influence at lower velocities, and should not be neglected in assessments of low velocity sites.

The stress distributions along a blade are made using the elemental forces output from the newly developed hydrodynamic model. This highlights the importance of using hydrodynamic coefficients of lift and drag that have been generated for the specific geometry and flow velocity of each individual element. Previously for overall performance and thrust analyses, it was sufficient to take blade averaged values of Reynolds number.

An unrealistic peak in bending stress has been identified at the blade tip, which is removed from the study as it is considered an anomaly. The cause is thought to stem from force averaging over the blade element, where a constant length is taken over the whole blade. A more accurate representation of the rounded geometry towards the tip could be achieved using better refinement of smaller elements in this region.

The treatment of tip loss is also thought to be a source of error contributing to the anomaly. The model calculates the tip losses based on the assumption of free stream velocity through the centre, which is seen to be lower than those predicted in reference CFD studies described in Chapter 5. Smaller losses lead to higher corresponding hydrodynamic forces, and hence larger stresses. In order to better predict these effects, a new tip loss factor should be devised as a function of actual flow through the centre, from wake characterisation models such as coupled RANS BEM. However, there is also thought to be a dependence on the

TSR, which would require more detailed analysis of the flow field from higher complexity blade resolved CFD studies.

6.8.2 Non-uniform steady inflows

A single profile is assessed here as a $1/7^{th}$ power law, which induces an azimuthal variation of stress. This, coupled with the influence of fixed loading on tangential forces, creates stress concentration 'hot-spots' where failure is most likely to occur. These give indications as to where more attention is required in the design stage to either reduce loads or increase structural strength. It also provides valuable information to guide maintenance and inspection activities.

Other environmental loads from temporal variations could be incorporated directly into the current BEMT model through applying a series of quasi steady profiles which vary with time-step. These could be based on recorded site data in order to model a better representation of the actual operational conditions. However, limitations would still exist from the steady flow assumptions.

Unsteady effects are not accounted for within the current model. This flow behaviour is however seen to be highly influential on the hydrodynamic forces on the blades. One study on unsteady planar forcing in a towing tank sees increased out-of-plane bending moments of up to 15% compared to measurements in steady flow Milne et al. (2015). Functions to assess inertial effects and added mass, as well as turbulent inflows and waves are possible to implement into the BEMT model (as explored in Buckland (2013), Moriarty and Hansen (2005), Togneri and Masters (2012)) however are beyond the scope of the current work.

Within Chapter 3, vortex induced vibration is observed around blade elements at certain angles of attack beyond stall. The frequencies of these could have a dramatic influence on the hydro-elastic behaviour of the blade, which would have consequential impacts on the fatigue life. Although pitch systems can be employed to control the angles of attack, this is limited in some operational modes such as

start and stop. If vibrations excite the natural frequency of the blade, this could cause extreme reductions in fatigue life. It is recommended that the whole blade should be analysed using a Finite Element (FE) solver to ensure blades do not resonate.

6.8.3 Assumptions

Following industrial guidelines (Bureau Veritas, 2015), safety factors are determined as a function of partial safety factors stemming from sources of uncertainty or variability within the stress calculations. This was found to be over 7.9 for one case, mainly due to the type of load imposed on the composite, and the method through which the loads are calculated.

One reason for the high factors of safety stem from the sensitive nature of composite materials, where small variations in material can have a large impact on the strength. This highlights the importance of obtaining accurate composite properties through materials testing to ISO standards, as recommended in the text (Bureau Veritas, 2017), and indeed very tight quality control of any engineered composite parts. Changing fabrication methods for larger scale manufacture will reduce some uncertainty and hence safety factor, however the higher related costs are not justifiable at this current technological phase. Improving the accuracy of the BEMT calculations could decrease partial safety factor, and therefore increase the maximum allowable stresses by up to 40%. This would have large implications on the blade survivability predictions.

SN curves are usually derived from material testing using a zero mean cycle stress (Marsh et al., 2016). However, the mean stress in tension or compression is seen to have a large influence on the fatigue life of composites (Westphal and Nijssen, 2012). 'Shifted Goodman diagrams' are developed within the literature, which are used to create CFL (Constant Fatigue Life) diagrams that can be used to assess the number of cycles to failure as a function of mean stress and cycle amplitude (Nijssen, 2006). The fatigue analysis in this study uses an expression for number

of cycles to failure based on industrial standard guidelines, which correct for mean stresses in tension. This accounts for the higher amounts of fatigue damage caused by the mean stress assuming a certain ratio of minimum to maximum stresses (R) equal to 0.1. This study calculates ratios from the non uniform inflow between 0.78-0.86. This corresponds to larger number of cycles to failure, and therefore the applied method is considered more conservative.

The current BEMT model performs 'quasi-steady' analyses, and therefore does not account for dynamic changes in hydrodynamic loads. This is a limitation in the stress analysis, as the dynamic effects could cause large localised loading which may increase stresses beyond the maximum allowable. The unsteady effects will also cause dynamic deformations, which will impact the fatigue behaviour of the blades. This will be considered in future stages at EDF R&D, as an extension of the work presented here.

6.8.4 Computational time

The main benefit of calculating loads through the BEMT model is to exploit its basic form to analysing many operating conditions efficiently. This allows engineering assessments to be carried out with feasible resources and time frames, such as the blade structural analysis presented here. The computational time increases almost linearly with each azimuthal angle added to be analysed, due to the time dependency being mostly related to the iterative loop for convergence in the hydrodynamic model. The present computations were performed using a laptop running an $Intel^{®}\ Core^{TM} - i5$ 2.9 GHz dual core processor with 8 GB RAM. For one flow velocity and TSR with a $\Delta\Phi = 15°$, blade forces are generated in 54 core seconds. To translate these into stresses, the structural analysis tool requires approximately 10 core seconds per case. Therefore to generate a full spectrum of operating conditions in one site, calculations are predicted to take in the region of 24 core hours.

Chapter 7

Overall discussion and conclusions

The work completed in this thesis has developed and tested a hydrodynamic model that can be used to assess ducted, open centre tidal stream turbines. Detailed validation studies have been performed to compare the performance and capabilities of the developed code with experimental measurements, and indirectly validated with higher fidelity CFD models. The high computational efficiency of the model has enabled engineering assessments of the blades, under a range of operational conditions.

The motivation behind this work was to provide robust, efficient and accurate tools in order to reduce the uncertainties in TST technology. This will decrease the risk of performing economic viability assessments and aid EDF in future project decision making.

7.1 Conventional TST modelling

The baseline BEMT code has been built using Python programming language, on well established principles for conventional turbines. Influences from limitations inherent in the method are found to be reduced through the introduction of correction factors, including: 1) a Prandtl tip and hub losses to account for discrete blades; 2) a Buhl variant of the Glauert highly loaded correction to account for the higher thrust levels seen at high axial induction.

Input hydrodynamic characteristic data of standard NACA foils were generated through 'XFoil', a low computationally demanding panel code. Lift and drag coefficient curve predictions, whilst less accurate than a higher complexity RANS study, showed reasonable agreement with wind tunnel tests, achieved at a fraction of the computational effort. A Viterna extrapolation function was successfully employed to extend the data to a larger range of angle of attack, including in the stalled condition. A Du-Selig and Eggars adjustment is used to account for delayed stall effects of a rotating hydrofoil.

A thorough validation of the classical BEMT code has been performed utilising the data of three different experimental scale models of varying size and test set-ups. The model showed excellent convergence, where full power and thrust curves were output within a few minutes running time on a single CPU. Good agreement is seen for two cases, where four test scale inflow velocities and blade pitch angles are examined. A slight over prediction in power and under prediction in thrust is observed at very high TSRs. This is considered to be due to the effects of the high blockage correction applied to the measuremental data. A sensitivity study shows a significant influence of the tip and hub loss factor, accounting for up to a 10% reduction in power. The rotors do not often enter the highly loaded regime under these tests, showing low dependency on the Buhl correction factor.

Comparison with a third experimental case showed some disparities in the results, which were found to be due to: 1) a chord based Reynolds number within

the transition between laminar and turbulent flow regime; 2) large variations of baseline flow velocities observed within the flume section, stemming from Prandtl secondary flows which is a characteristic of low aspect ratio channels.

This section of work concludes that the BEMT method is applicable to tidal stream turbines, and is able to replicate experimental flow conditions to predict the rotor thrust and power with a high level of accuracy. A large sample size of experimental data was used for comparison, examining different model sizes, blade profiles and operating conditions, and as such has raised confidence in the validation. The applied tip loss corrections are shown to improve correlations to better match the measured results and are thus considered highly important in future analysis. There is also a large dependency on the results from the inflow velocity field, highlighting the importance of accurately measuring the inflow conditions.

7.2 Ducted and open centre TST modelling

Classical BEMT is not valid for augmented flow through a duct, and therefore an alternative approach to model the changes in axial momentum was developed. A set of analytical relationships to resolve the pressure gradient within the duct were combined to form a new expression for the axial induction factor, and prescribed to the BEMT iterative procedure. The analytical functions were solved using empirical coefficients derived from CFD studies of uni-directional ducts.

A numerical instability was observed within the BEMT convergence loop, prompting the implementation of an alternative iterative procedure. This was achieved through the use of a least squares minimisation function within $SciPy$, providing higher flexibility on the convergence searching criteria.

The ducted BEMT was indirectly validated through analysis of a generic design turbine, comparing results with a higher complexity coupled RANS-BEM model. Excellent agreement is seen (within 2%), between the overall rotor power and

thrust predictions for the majority of TSRs. The BEMT model exhibits some over predictions by up to of 25% in power and 10% in thrust at the maximum rotational velocity. However this is beyond the optimal power condition. More detailed analysis of the radial forces show this disparity originates close to the hub. This is considered a result of the highly complex flow around the hub geometry, which is not captured within the model.

This thesis was thus able to quantify the ability of the modified axial momentum theory method compared to CFD methods, which was a main objective of the research and is considered to be a key novel contribution to knowledge. The presented study confirms the analytical approach applicability to bi-directional ducts, and shows significant computational time savings, by a few orders of magnitude, compared with a coupled RANS-BEM. The code can now be used to assess commercial cases using ducted open centre turbines with a higher confidence in the model capabilities. In addition, this work has identified limitations seen in capturing the complex flow around the hub at high TSRs, and therefore has highlighted potential implications on the application of the method to turbines that employ over-speed control.

7.3 Commercial application

The ducted BEMT model was used to assess two commercial cases of bi-directional ducted TSTs with high solidity, open centre rotors designed by OpenHydro. The 'OCT16' device incorporates an open centre hub with relatively straight blades. The more recent hubless 'PS2' design however has tapered blades with rounded tips open towards the centre. Where there are connections between the blades, a restriction in the formation of tip vortices is seen, and therefore no tip loss factor was applied.

The blades consist of rounded edge flat plate hydrofoil cross sections, enabling turbine rotation in either direction without the requirement of a pitching system.

A limitation in using panel codes was found for such profiles, and therefore lift and drag coefficient curves were generated using RANS CFD. Numerous studies were made using EDF industrial standard software *Code_Saturne*, results of which showed good agreement with wind tunnel measurements. Interpolation functions were used to extend data tables to a larger range of geometries and Reynolds numbers with minimal additional computational effort. An improved method of applying lift and drag data specific to the geometry of each element at each rotational velocity was incorporated into the BEMT convergence loop.

A comparison of power and thrust results from the BEMT model has been made against high fidelity blade resolved RANS studies. The OCT16 results comparison shows good agreement in the power curves, with the BEMT model predicting a peak within 6% of the RANS model. However, the BEMT model under predicts thrust levels by an average of 40%, up to a maximum of 50%.

The hubless PS2 RANS results exhibited a large spread in power and thrust, which showed a dependency on the different inflow velocity. This observation, not seen in the devices containing a hub, was somewhat captured by the BEMT model, driven by the larger variation in element geometry along the blade length. The power curves show some discrepancy in trend, where BEMT under predicts peak power by up to 18% occurring at a greater TSR than RANS results. Thrust is also under predicted by an average of 30%, and a maximum of 40%.

The Prandtl tip loss factor was only applied to the PS2 device, due to the open tips at the centre. This is used to account for the effects of a discrete number of blades, however shows a low sensitivity due to the rotor being of high solidity. As TSRs are much lower in these cases, the axial induction never enters the highly loaded regime under these tests, showing no dependency on the Buhl correction factor.

The hub and outer ring connecting the blades are neglected within the BEMT model, and thought to be the main source of discrepancy between the thrust

comparisons with RANS results. Wake visualisations from the reference blade resolved CFD studies show highly complex 3-D flow interactions that develop within the duct. These are neglected by the 2-D assumptions inherent to the BEMT technique, and also considered a key cause of the thrust disparities. Improvements could be made through the incorporation of various correction factors, as seen in the classical BEMT model. However, these should be devised specifically to this case configuration, with appropriate justifications from detailed blade resolved CFD analysis.

The work performed in this section has been able to quantify the ability of BEMT to predict TST forces compared to a highly sophisticated CFD code. This is, to the authors knowledge, the first application case study of a BEMT model to analyse a commercial ducted and open centre TST. The analysis concludes that BEMT is able to make reasonable predictions of the turbine power, however is currently not capable of accurately estimating the thrust levels. Further investigation is required into the complex flow interactions that is not captured in the theory.

The developed model has now been incorporated into a higher sophisticated code constructed by EDF R&D which is able to simulate a larger range of flow conditions, to be further examined against field measurements.

7.4 Engineering applications

The impacts on the turbine hydrodynamics from fixing rectangular section sacrificial anodes to the rotor was assessed. This was achieved through modelling the structures as additional elements of a certain drag coefficient within the code. Results indicate significant influences on the power, particularly at higher TSRs, due to the introduction of additional hydrodynamic forces acting in the direction of opposing torque.

A structural analytical tool was further developed to compute the structural

response of TST blades to hydrodynamic loading. This is based on beam theory, applied to an OpenHydro PS2 type device, where elemental forces are generated with the newly developed ducted BEMT model. The blade distributions of Von Mises stresses are determined, enabling identification of hot spots at a higher risk of failure. The peak stresses were discovered at the blade mid-length, driven mainly by the flap wise bending moments. An industrial design guideline from a classification body was used to determine the structural properties of appropriate composite materials for marine applications. Maximum allowable stresses were calculated, which enabled a demonstration into assessments of blade structural integrity under normal operating conditions and extreme loading. The tool was extended to consider cyclic loads exerted onto the blades rotating in non-uniform inflow profiles. A shear profile based on a power law to approximate a viscous boundary layer at the seabed was imposed. An S-N curve is computed to gauge the relative damage and fatigue life from the cyclic stressing. A demonstration case is finally presented to show the tool capability of assessing blade survivability and fatigue life at a particular deployment site.

The structural analysis tool has been built to accept any input data for engineering assessments. Actual data regarding the blade structures and material properties from OpenHydro can now be applied, along with flow data measured at the deployment sites. This will enable EDF to perform third party assessments of the real turbine structure in real tidal flows, to aid decision making for future projects.

7.5 Conclusion

The established numerical models and analyses performed in this thesis fulfil the main aim of this research: to develop tools which perform practical engineering assessments of TSTs. Key contributions of this work include the following:

- A methodology of generating lift and drag coefficients for NACA and flat plate hydrofoils is established, and a database compiled;
- BEMT can be used for conventional, bare devices with high confidence.
- Empirical adjustments can be implemented into this classical model to analyse the hydrodynamic loads of open centre, ducted TST;
- Indirect validation of Ducted BEMT shows good agreement to coupled RANS-BEM. Limitations are identified concerning 3-D interactions, and quantified by comparing with blade resolved RANS;
- Finally an assessment of the structural integrity of OpenHydro blades is demonstrated, finding that the Von Mises stresses are driven by the flap wise bending moment, which peak at the mid-length.

7.6 Recommendations for future work

During the course of this research, several areas of interest were identified as important for further development, and are thus recommended for future work:

Flow within a bi-directional duct

The modifications to axial momentum theory through a duct are based on empirical coefficients from CFD studies of uni-directional ducts. The validation shows a good applicability of these expressions for bi-directional duct geometries, however a relatively small number of data points were available for comparison. Further CFD analysis would increase the confidence in this adjustment, ideally

using studies measuring the pressure gradient specifically through bi-directional ducts.

3-D flow interactions

The 2-D flow assumptions inherent in the BEMT method are thought to be a source of inaccuracy, particularly for open centre configurations. These effects could be alleviated through the incorporation of an appropriate correction factor. Various factors devised for conventional turbines are based on observations of certain flow physics, but this requires detailed input from blade resolved CFD simulations. This forms part of a line of work currently under investigation as a collaborative project between EDF R&D and the University of Strathclyde.

Free surface effects

The presence of a free surface is particular to TSTs, which could have an influence on the wake formation and hence the rotor hydrodynamics. Methods accounting for their effects which can be incorporated into the BEMT model are proposed in the literature, such as Whelan and Graham (2009). Whilst not considered essential in the validation phase, this could be introduced in analyses of full scale deployments, to improve the representation of the real working environment.

Dynamic effects

The current BEMT model is restricted in performing quasi-steady analyses. This neglects dynamic effects which are associated to the unsteady nature of the tides. This could be accounted for through vortex wake methods such as used in lifting line or lifting surface theory. However a balance will be required to limit the additional computational time associated to the increased complexity.

The ducted code incorporating the modified momentum theory has now been introduced into a more sophisticated BEMT model developed by the EDF R&D team. The following extensions to the current work within this code are proposed:

Turbulence

This more advanced code can accept turbulent inflow conditions through the

use of synthetic turbulence models, where stochastic time series velocity data is generated using NREL software TurbSim. This will be employed to provide a better representation of realistic tidal flows. Effects are thought to bring changes to overall rotor performance and thrust predictions, but more importantly on the blade loads, which could have implications for the localised stresses and fatigue life.

Validation with field measurements

An initial validation of the code with field measurements of the OCT16 device at the Paimpol-Bréhat site has commenced, however due to commercial sensitivity could not be presented within this study. Data for the PS2 deployment is now becoming available, and will be used to assess the model capabilities of predicting turbine performance that is physically observed in real tidal flows. Initial indications from this thesis suggest examination of the span-wise flow interactions, particularly at the tips, would be of particular interest.

Vortex induced vibrations

Fluctuations in the lift and drag forces for 2-D hydrofoil sections are seen at high angles of attack, (Zeiner-gundersen, 2015) caused by alternating vortex shedding at the leading and trailing edges. These fluctuations in hydrodynamic forces could cause vortex induced vibrations. This could have enormous implications on the fatigue lift of the blade, particularly if the vibrations reach the blade natural frequency. Finite element analysis could be used to determine the resonant frequency of various structures to ensure this does not occur.

7.7 Publications

Several publications were produced during the course of the research for this EngD, including:

- S. Allsop, C. Peyrard, P. R. Thies, E. Boulougouris, and G. P. Harrison, "Development of a BEMT model for a ducted and hubless, high solidity tidal stream turbine," in 5^{th} Oxford Tidal Energy Workshop, Oxford, UK, 2016.
- S. Allsop, C. Peyrard, P. R. Thies, E. Boulougouris, and G. P. Harrison, "A validated BEM model to analyse hydrodynamic loading on tidal stream turbine blades," in 3^{rd} Asian Wave and Tidal Energy Conference, Singapore, 2016.
- S. Allsop, C. Peyrard, P. R. Thies, E. Boulougouris, and P. Harrison, "Hydrodynamic analysis of a ducted , open centre tidal stream turbine using blade element momentum theory," Ocean Engineering, vol. 141, pp. 531-542, 2017.
- S. Allsop, C. Peyrard, and P. Bousseau, "Adapting conventional tools to analyse ducted and open centre tidal stream turbines," in 12^{th} European Wave and Tidal Energy Conference, Ireland, 2017.

References

Abbott, I. H. and Von Doenhoff, A. E. (1959), *Theory of Wing Sections (Including a Summary of Airfoil Data)*, Dover Publications Inc, New York, Langley.
URL: *http://www.journals.uchicago.edu/doi/10.1086/470266*

Abbott, I. H., VonDoenhoff, A. E. and Stivers, L. S. (1945), Report No 824: Summary of Airfoil Data, Technical Report No. 824: Summary of Airfoil Data., National Advisory Committee for Aeronautics, Langley.
URL: *http://hdl.handle.net/2060/19930092747*

Adamski, S. J. (2013), Numerical Modeling of the Effects of a Free Surface on the Operating Characteristics of Marine Hydrokinetic Turbines, Masters thesis, The University of Washington.

Afgan, I., Apsley, D. and McNaughton, J. (2013), ReDAPT: CFD Simulation of Turbulence at a Tidal Stream Site based on Field Measurements (MD1.5), Technical report, Energy Technologies Institute, Manchester.

Afgan, I., McNaughton, J. and Rolfo, S. (2013), 'Turbulent flow and loading on a tidal stream turbine by LES and RANS', *International Journal of Heat and Fluid Flow* **43**, 96–108.
URL: *http://dx.doi.org/10.1016/j.ijheatfluidflow.2013.03.010*

Allsop, S., Peyrard, C., Bousseau, P. and Thies, P. R. (2017), Adapting Conventional Tools to Analyse Ducted and Open Centre Tidal Stream Turbines, *in* '12th European Wave and Tidal Energy Conference, 27-31 August 2017', Cork.

Allsop, S., Peyrard, C., Thies, P. R., Boulougouris, E. and Harrison, G. P. (2016), A validated BEM model to analyse hydrodynamic loading on tidal stream turbine blades, *in* '3rd Asian Wave and Tidal Energy Conference, 24-28 October 2016', Vol. 2, Singapore.

Allsop, S., Peyrard, C., Thies, P. R., Boulougouris, E. and Harrison, P. (2017), 'Hydrodynamic analysis of a ducted , open centre tidal stream turbine using blade element momentum theory', *Ocean Engineering* **141**(January), 531–542.

Alstom Ocean Energy (2014), ReDAPT: First Year of Operation Report (MC7.2), Technical report, Energy Technologies Institute (ETI).

Archambeau, F., Mechitoua, N. and Sakiz, M. (2004), 'Code_Satunre: A finite volume method for the computation of turbulent incompressible flows - industrial applications', *International Journal on Finite Volumes* **1**, 1–62.

Atlantis Resources Ltd. (2010), 'Atlantis press release: Update on AK1000 blade replacement'.
URL: *https://www.atlantisresourcesltd.com/2010/12/06/december-3rd-2010-update-on-ak1000-blade-replacement/*

Bahaj, A. S., Batten, W. M. J. and McCann, G. (2007), 'Experimental verifications of numerical predictions for the hydrodynamic performance of horizontal axis marine current turbines', *Renewable Energy* **32**(15), 2479–2490.

Bahaj, A. S., Molland, A. F., Chaplin, J. R. and Batten, W. M. J. (2007), 'Power and thrust measurements of marine current turbines under various hydrodynamic flow conditions in a cavitation tunnel and a towing tank', *Renewable Energy* **32**(3), 407–426.

Bahaj, A. S. and Myers, L. (2004), 'Analytical estimates of the energy yield potential from the Alderney Race (Channel Islands) using marine current energy converters', *Renewable Energy* **29**, 1931–1945.

Baker, J. P. (2009), Drag Reduction of a Blunt Trailing-Edge Airfoil, Phd thesis, University of California.

Batten, W. M. J., Bahaj, A. S., Molland, A. F. and Chaplin, J. R. (2006), 'Hydrodynamics of marine current turbines', *Renewable Energy* **31**(2), 249–256.

Batten, W. M. J., Bahaj, A. S., Molland, A. F. and Chaplin, J. R. (2007), 'Experimentally validated numerical method for the hydrodynamic design of horizontal axis tidal turbines', *Ocean Engineering* **34**(7), 1013–1020.

BBC News (2010), 'News article: Blade fault on giant tide turbine AK1000 in Orkney'.
URL: *http://www.bbc.com/news/uk-scotland-highlands-islands-11492829*

Belloni, C. (2013), Hydrodynamics of Ducted and Open-Centre Tidal Turbines (PhD Thesis), PhD thesis, The University of Oxford.

Belloni, C., Willden, R. H. J. and Houlsby, G. (2016), 'An investigation of ducted and open-centre tidal turbines employing CFD-embedded BEM', *Renewable Energy* .

Bir, G. S., Lawson, M. J. and Li, Y. (2011), Structural design of a horizontal-axis tidal current turbine composite blade, *in* 'ASME 30th International Conference on Ocean, Offshore, and Arctic Engineering', number October, National Renewable Energy Laboratory (NREL), Rotterdam, p. 14.

Blackmore, T., Myers, L. E. and Bahaj, A. S. (2016), 'Effects of turblence on tidal turbines: Implicatgions to performance blade loads and condition monitoring', *International Journal of Marine Energy* **14**, 1–26.

Brenton, S.-P., Coton, F. N. and Geir, M. (2007), A Study on Different Stall Delay Models Using a Prescribed Wake Vortex Scheme and NREL Phase VI Experiment, *in* 'EWTEC 2007'.

Buckland, H. (2013), Combined Current , Wave and Turbulent Flows and their effects on Tidal Energy Devices, Phd thesis, Swansea University.

Buckland, H. C., Masters, I., Chapman, J. and Orme, J. (2010), '1 Blade Element Momentum Theory 2 Numerical Implementation', *18th UK Conference on Computational Mechanics (ACME-UK)* (March), 1123–1127.
URL: *www.inore.org/download/77395_acme_4_page.pdf/*

Buhl, M. L. (2005), A New Empirical Relationship between Thrust Coefficient and Induction Factor for the Turbulent Windmill State, Technical report, National Renewable Energy Laboratory.

Bureau Veritas (2015), Current and Tidal Turbines, Guidance Note: NI 603 DT R01 E, Technical Report May 2015.

Bureau Veritas (2017), Hull in Composite Materials and Plywood , Material Approval , Design Principles , Construction and Survey (Rule Note: NR 546 DT R01 E), Technical report.

Burton, T., Jenkins, N., Sharpe, D. and Bossanyi, E. (2011), *Wind Energy Handbook*, 2 edn, John Wiley & Sons Ltd.

Burton, T., Sharpe, D., Jenkins, N. and Bossanyi, E. (2001), *Wind Energy Handbook*, 1 edn, John Wiley & Sons Ltd.

Buvat, C. (2010), ETI PerAWaT Report: WG4 WP1 D3 Calibration tests without turbine (base flow), Technical report, Energy Technologies Institution (ETI), Chatou.

Buvat, C. (2011), ETI PerAWaT Report WG4 WP1 D2: Construction of the scale model of a horizontal axis turbine device and installation of the experimental test platform, Technical report, Energy Technologies Institution, Chatou.

Buvat, C. (2012), ETI PerAWaT Report: WG4 WP1 D4 Performance of tank tests with physical scale model of horizontal axis turbine device installed, Technical report, Energy Technologies Institution (ETI), Chatou.

Buvat, C. and Martin, V. (2010), ETI PerAWaT Report: WG4 WP1 D1 Identification of test requirements and physical model design, Technical report, Energy Technologies Institution (ETI), Chatou.

CBC News (2011), 'Failed tidal turbine explained at symposium'.
URL: *http://www.cbc.ca/news/canada/nova-scotia/failed-tidal-turbine-explained-at-symposium-1.1075510*

Chapman, J. C. (2008), Tidal Energy Device Hydrodynamics in Non-Uniform Transient Flows, PhD thesis, Swansea University.

Chapman, J. C., Masters, I., Togneri, M. and Orme, J. a. C. (2013), 'The Buhl correction factor applied to high induction conditions for tidal stream turbines', *Renewable Energy* **60**, 472–480.
URL: *http://dx.doi.org/10.1016/j.renene.2013.05.018*

Code_Saturne (2014), 'Code_Saturne Users Meeting Schedule, 2014'.
URL: *http://code-saturne.org/cms*

Cresswell, N. W. (2014), The generation potential of diffuser augmented tidal stream turbines, Phd thesis, Durham University.

DCNS OpenHydro (2016), 'OpenHydro Paimpol-Brehat Project Update'.
URL: *http://www.openhydro.com/OpenHydro/media/Documents/News PDFs/30-May-2016.pdf*

DNV GL Garrad Hassan (2012*a*), Bladed User Manual v4.3, Technical report, GL Garrad Hassan.

DNV GL Garrad Hassan (2012*b*), Tidal Bladed Theory Manual, Technical report.

Drela, M. (1989), 'XFOIL: An analysis and design system for low Reynolds number airfoils'.
URL: *http://link.springer.com/chapter/10.1007/978-3-642-84010-4_1*

Drela, M. and Youngren, H. (2001), 'XFOIL Online Documentation'.
URL: *http://web.mit.edu/aeroutil_v1.0/xfoil_doc.txt*

EDF-EN (2014), 'Normaindie Hydro press release'.
URL: *http://www.edf-energies-nouvelles.com/en/press-release/dcns-edf-energies-nouvelles-winners-ademe-call-expression-interest-decisive-step-creation-french-tidal-energy-industry/*

EDF R&D (2015), Code_Saturne 4.0.0 Documentation: Theory Guide, Technical Report April.

El-behery, S. M. and Hamed, M. H. (2009), 'A Comparative Study of Turbulence Models Performance for Turbulent Flow in a Planar Asymmetric Diffuser', *International Journal of Mechanical, Aerospace, Industrial, Mechatronic and Manufacturing Engineering* **3**(5), 580–591.

Evans, R., McAdam, R., Royle, M. and Mcewen, L. (2013), Optimum geometry for axial flow free stream tidal turbine blades, *in* '10th European Wave and Tidal Energy Conference (EWTEC)', Aalborg, Denmark.

Fleming, C. F. and Willden, R. H. J. (2016*a*), 'Analysis of bi-directional ducted tidal turbine performance', *International Journal of Marine Energy* **16**, 162–173.

Fleming, C. F. and Willden, R. H. J. (2016*b*), 'Analysis of bi-directional ducted tidal turbine performance', *International Journal of Marine Energy* **16**, 162–173.

Fleming, C., McIntosh, S. C. and Willden, R. H. J. (2011), PerAWaT Report: WG3 WP1 D2 Model setup for ducted horizontal axis flow turbines, Technical report, Energy Technologies Institute (ETI).

Fuglsang, P., Dahl, K. and Antoniou, I. (1999), Wind tunnel tests of the Risø-A1-18, Risø-A1-21 and Risø-A1-24 airfoils, Technical report, Risø National Laboratory, Roskilde, Denmark.

Garrett, C. and Cummins, P. (2007), 'The efficiency of a turbine in a tidal channel', *Journal of Fluid Mechanics* **588**, 243–251.

Glauert, H. (1926), The analysis of experimental results in the windmill brake and vortex ring states of an airscrew, Reports & Memoranda No. 1026, Technical report, Aeronautical Research Committee.

Glauert, H. (1948), *The Elements of Aerofoil and Airscrew Theory*, second edn, Cambridge Press.

Goett, H. I. and Bullivant, K. W. (1939), NACA report no. 647. Tests of NACA 0009, 0012 and 0018 airfoils in the full-scale tunnel, Technical report.

Gretton, G. I. (2010), 'Development of a computational fluid dynamics model for a horizontal axis tidal current turbine', (WG3 WP5 D1).

Hansen (2004), 'AirfoilPrep excel instructions'.

Hansen, M. O. L. (2008), *Aerodynamics of Wind Turbines*, second edn, Earthscan, London, UK.

Hjelmstad, K. D. (2005), *Fundamentals of Structural Mechanics*, second edn, Springer.

Ingram, D. (2012), ETI PerAWaT Report: WG3 WP2 D5a Tidal array scale numerical modelling . Interactions within a farm (unsteady Flow), Technical report, Energy Technologies Institution (ETI) & The University of Edinburgh.

Jacobs, E. N., Ward, K. E. and Pinkerton, R. M. (1935), The characteristics of 78 related airfoil sections from tests in the veriable density wind tunnel (NACA report no. 460), Technical report, National Advisory Comittee for Aeronautics.

Jamieson, P. (2008), 'Generalized limits for energy extraction in a linear constant velocity flow field', *Wind Energy* **11**(5), 445–457.

Jonkman, B. (2009), TurbSim v1.5 Users Guide (report number NREL/TP-500-46198), Technical Report September, National Renewable Energy Laboratory, US Department of Energy, Colorado.

Jonkman, J., Butterfield, S., Musial, W. and Scott, G. (2009), Definition of a 5-MW reference wind turbine for offshore system development, Technical Report NREL/TP-500-38060, NREL.

Kueny, J. L. (2012), Optimal design of a tidal turbine, *in* 'IOP Conference Series: Earth and Environmental Science', Vol. 15.
URL: *http://www.scopus.com/inward/record.url?eid=2-s2.0-84874043394&partnerID=40&md5=1cd4afc8d42a6e205eb88ef8402db703*

Kueny, J. L. (2015*a*), EDF / Optydro report: Analyse CFD des performances de l'hydrolienne marine "PS2", Technical report.

Kueny, J. L. (2015*b*), EDF / Optydro report: Evaluation CFD des performances de l'Hydrolienne marine "OCT16-01b" et comparaisons avec l'hydrolienne "PS2", Technical report.

Kundu, P. K. and Cohen, I. M. (2002), *Fluid Mechanics*, 2nd edn, Academic Press.

Ladson, C. L., Brooks, C. W., Hill, A. S. and Sproles, D. W. (1996), 'Computer Program to Obtain Ordinates for NACA Airfoils', (December 1996).

Lawn, C. J. (2003), 'Optimization of the power output from ducted turbines', *Proceedings of the Institution of Mechanical Engineers, Part A: Journal of Power and Energy* **217**(August 2002), 107–117.

Leroy, A. (2015), applications par Un nouveau modèle SPH incompressible : vers l ' application à des cas industriels, Phd thesis, Université Paris-Est.

Levy, S. (2013), Aerodynamics of horizontal and vertical axis wind turbines : Implementation of the Blade Element Momentum Theory, Technical Report H-R22-2012-02963-EN, version 1.0, EDF R&D, Clamart, France.

Li, H., Hu, Z., Chandrashekhara, K., Du, X. and Mishra, R. (2014), 'Reliability-based fatigue life investigation for a medium-scale composite hydrokinetic turbine blade', *Ocean Engineering* **89**, 230–242.

MacKay, D. J. (2008), *Renewable Energy - without the hot air*, UIT Cambridge Ltd, Cambridge.
URL: *www.withouthotair.com*

Marsh, G., Wignall, C., Thies, P. R., Barltrop, N., Incecik, A., Venugopal, V. and Johanning, L. (2016), 'Review and application of Rainflow residue processing techniques for accurate fatigue damage estimation', *International Journal of Fatigue* **82**, 757–765.
URL: *http://dx.doi.org/10.1016/j.ijfatigue.2015.10.007*

Masters, I., Chapman, J. C., Orme, J. a. C. and Willis, M. R. (2010), 'Modelling high axial induction flows in tidal stream turbines with a corrected blade element model', *3rd International Conference on Ocean Energy* pp. 1–5.

Masters, I., Chapman, J., Willis, M. and Orme, J. (2011), 'A robust blade element theory model for tidal stream turbines including tip and hub loss corrections', *Journal of Marine Engineering and Technology* **10**(1), 25–35.

Masters, I., Williams, A., Croft, T. N., Togneri, M., Edmunds, M., Zangiabadi, E., Fairley, I. and Karunarathna, H. (2015), 'A comparison of numerical modelling techniques for tidal stream turbine analysis', *Energies* **8**(8), 7833–7853.

McIntosh, S. C., Fleming, C. and Willden, R. H. J. (2010), PerAWaT Report WG3 WP1 D1: Report on model setup for horizontal axis axial flow turbines, Technical report, Energy Technologies Institute (ETI).

McIntosh, S. C., Fleming, C. and Willden, R. H. J. (2012), PerAWaT Report WG3 WP1 D3: Performance and wake structure of a model horizontal axis axial flow turbine, Technical report, Energy Technologies Institute (ETI).

McNaughton, J. (2013), Turbulence modelling in the near-field of an axial flow turbine using Code_Saturne, Phd thesis, The University of Manchester.
URL: *https://www.escholar.manchester.ac.uk/uk-ac-man-scw:200650*

McSherry, R., Grimwade, J., Jones, I., Mathias, S., Wells, A. and Mateus, A. (2011), '3D CFD modelling of tidal turbine performance with validation against laboratory experiments', *Proceedings of the 9th European Wave and Tidal Energy Conference* .

Menter, F. R. (1994), 'Two-Equation Eddy-Viscosity Turbulence Models for Engineering Applications', *AIAA Journal* **32**(8).

Mercier, G. (2014), Modelisation de parcs d'hydroliennes a flux transverse avec une methode d'equivalence, Phd thesis, Universite de Grenoble.

MeyGen (2017), Lessons Learnt from MeyGen Phase 1a Part 1 / 3 : Design Phase, Technical Report May.

Miley, S. (1982), A Catalogue of Low Reynolds Number Airfoil Data, Technical report, Department of Aerospace Engineering, Texas A&M University.

Milne, I. A., Day, A. H., Sharma, R. N. and Flay, R. G. J. (2015), 'Blade loading on tidal turbines for uniform unsteady flow', *Renewable Energy* **77**, 338–350.

Milne, I. a., Day, A. H., Sharma, R. N., Flay, R. G. J. and Bickerton, S. (2011), 'Tidal Turbine Blade Load Experiments for Oscillatory Motion', *9th European Wave and Tidal Energy Conference* .

Moriarty, P. J. and Hansen, a. C. (2005), AeroDyn Theory Manual, Technical report.
URL: *http://www.nrel.gov/docs/fy05osti/36881.pdf*

Munshi, S. R., Modi, V. J. and Yokomizo, T. (1999), 'Fluid dynamics of flat plates and rectangular prisms in the presence of moving surface boundary-layer control', *Journal of Wind Engineering and Industrial Aerodynamics* **79**(1-2), 37–60.

Myers, L. and Bahaj, A. S. (2005), 'Simulated electrical power potential harnessed by marine current turbine arrays in the Alderney Race', *Renewable Energy* **30**, 1713–1731.

Neill, S. P., Jordan, J. R. and Couch, S. J. (2012), 'Impact of tidal energy converter (TEC) arrays on the dynamics of headland sand banks', *Renewable Energy* **37**, 387–397.

Nijssen, L. (2006), Fatigue Life Prediction and Strength Degradation of Wind Turbine Rotor Blade Composites, Phd thesis, Delft University.

Ning, S. A. (2013), AirfoilPrep documentation, Technical Report NREL/TP-5000-58817 (release 0.1.0), Technical Report June, National Renewable Energy Laboratory.

O'Doherty, T., Egarr, D. A., Mason-Jones, A. and O'Doherty, D. M. (2009), An assessment of axial loading on a five-turbine array, *in* 'Institution of Civil Engineers (ICE)', Vol. 162, pp. 57–65.

Offshore Renewable Energy Catapult (2014), Financing solutions for wave and tidal energy, Technical Report November.
URL: *www.Ore.catapult.org.uk*

Olczak, A., Stallard, T., Feng, T. and Stansby, P. K. (2016), 'Comparison of a RANS blade element model for tidal turbine arrays with laboratory scale measurements of wake velocity and rotor thrust', *Journal of Fluids and Structures* **64**, 87–106.

Pham, C.-T. and Martin, V. a. (2009), 'Tidal current turbine demonstration farm in Paimpol-Brehat (Brittany): tidal characterisation and energy yield evaluation with Telemac', *Proceedings of the 8th European Wave and Tidal Energy Conference* pp. 181–188.

ReDAPT (2014), ReDAPT: Initial operation power curve (MC7 . 1), Technical report, The Energy Technologies Institute.

Renewable Energy Policy Network REN21 (2016), Renewables 2016 Global Status Report, Technical report.

ReNews (2016), 'ReNews article: Atlantis to decommission SeaGen'.
URL: *http://renews.biz/101295/atlantis-to-decommission-seagen/*

Rhymes, J. (2015), ReDAPT Reliable Data Acquisition Platform for Tidal ReDAPT Project Dissemination Workshop, *in* 'Ocean Energy Europe', Dublin.

Savidge, G., Ainsworth, D., Bearhop, S. and Christen, N. (2014), Ch 12 Strangford Lough and the SeaGen Tidal Turbine, *in* M. Shields and A. Payne, eds, 'Marine Renewable Energy Technology and Environmental Interactions', chapter Chapter 12, pp. 153–173.

SciPy Community (2016), 'SciPy reference guide'.
URL: *https://docs.scipy.org/doc/scipy-0.18.1/reference/index.html*

Sellar, B. and Sutherland, D. (2015), ReDAPT Tidal energy site characterisation at the Fall of Warness, EMEC, UK (MD3.8), Technical report, Energy Technologies Institute (ETI), Edinburgh.

Shives, M. (2011), Hydrodynamic Modeling, Optimization and Performance Assessment for Ducted and Non-ducted Tidal Turbines, PhD thesis, University of Victoria.
URL: *http://dspace.library.uvic.ca:8080/handle/1828/3801*

Shives, M. and Crawford, C. (2011), 'Developing an empirical model for ducted tidal turbine performance using numerical simulation results', *Proceedings of the Institution of Mechanical Engineers, Part A: Journal of Power and Energy* **226**(1), 112–125.
URL: *http://pia.sagepub.com/content/226/1/112.abstract*

Shives, M. and Crawford, C. (2016), 'Adapted two-equation turbulence closures for actuator disk RANS simulations of wind & tidal turbine wakes', *Renewable Energy* **92**, 273–292.

Stallard, T., Collings, R., Feng, T. and Whelan, J. (2013), 'Interactions between tidal turbine wakes: experimental study of a group of three-bladed rotors.', *Philosophical transactions. Series A, Mathematical, physical, and engineering sciences* **371**(1985), 20120159.
URL: *http://www.ncbi.nlm.nih.gov/pubmed/23319702*

Stallard, T., Feng, T. and Stansby, P. K. (2015), 'Experimental study of the mean wake of a tidal stream rotor in a shallow turbulent flow', *Journal of Fluids and Structures* **54**, 235–246.
URL: *http://dx.doi.org/10.1016/j.jfluidstructs.2014.10.017*

Stallard, T., Stansby, P. and Apsley, D. (2015), ReDAPT: Development of a CFD model of the TGL turbine at the EMEC site (MD1), Technical report, Energy Technologies Institute (ETI), Manchester.

Tangler, J. L. and Selig, M. S. (1997), 'An Evaluation of an Empirical Model for Stall Delay due to Rotation for HAWTS', *Windpower 97* .

Tatum, S. C., Frost, C. H., Allmark, M., Doherty, D. M. O., Prickett, P. W., Grosvenor, R. I., Byrne, C. B. and Doherty, T. O. (2016), 'Wave current interaction effects on tidal stream turbine performance and loading characteristics', *International Journal of Marine Energy* **14**, 161–179.
URL: *http://dx.doi.org/10.1016/j.ijome.2015.09.002*

The Carbon Trust (2011), Marine Renewables Green Growth Paper, Technical report.

The Crown Estate (2010), A Guide to an Offshore Wind Farm, Technical report.

The Crown Estate (2014), Energy and infrastructure outlook 2014-15 Offshore wind, Technical report.
URL: *www.thecrownestate.co.uk/energy-infrastructure*

The Crown Estate (2015), Energy and infrastructure key facts 2015-16 report: UK offshore wind, Technical report.
URL: *https://www.thecrownestate.co.uk/media*

Thiébot, J., Bailly du Bois, P. and Guillou, S. (2015), 'Numerical modeling of the effect of tidal stream turbines on the hydrodynamics and the sediment transport: Application to the Alderney Race (Raz Blanchard), France', *Renewable Energy* **75**, 356–365.

Tidal Energy Today (2017*a*), 'News report: DCNS to retrieve Paimpol-Brehat array for repairs'.
URL: *http://tidalenergytoday.com/2017/01/05/dcns-to-retrieve-paimpol-brehat-array-for-repairs/*

Tidal Energy Today (2017*b*), 'News report: Faulty bit on OpenHydro turbine further delays Fundy project'.
URL: *http://tidalenergytoday.com/2016/08/05/faulty-bit-on-openhydro-turbine-further-delays-fundy-project/*

Tidal Energy Today (2017*c*), 'News report: Naval Energies recovers second Paimpol-Brehat turbine'.
URL: *http://tidalenergytoday.com/2017/07/19/naval-energies-recovers-second-paimpol-brehat-turbine/*

Timmer, W. A. (2008), 'Two-dimensional low-Reynolds number wind tunnel results for airfoil NACA 0018', *Wind Engineering* .

Timmer, W. and Bak, C. (2013), *Aerodynamic characteristics of wind turbine blade airfoils*, Woodhead Publishing Limited.
URL: *http://linkinghub.elsevier.com/retrieve/pii/B9780857094261500040*

Togneri, M. and Masters, I. (2012), 'Parametrising Turbulent Marine Flows for a Blade Element Momentum Model of Tidal Stream Turbines', *Proceedings of the 9th European Wave and Tidal Energy Conference* .
URL: *http://www.see.ed.ac.uk/ shs/EWTEC 2011 full/EWTEC_CD/papers/112.pdf*

Turner, N. (2012), 'The Applicability of Aerodynamic Models to Tidal Turbines'.

Turnock, S. R., Phillips, A. B., Banks, J. and Nicholls-Lee, R. (2011), 'Modelling tidal current turbine wakes using a coupled RANS-BEMT approach as a tool for analysing power capture of arrays of turbines', *Ocean Engineering* **38**(11-12), 1300–1307.
URL: *http://dx.doi.org/10.1016/j.oceaneng.2011.05.018*

UIUC Applied Aerodynamics Group (2015), 'UIUC Airfoil Coordinates Database'.
URL: *http://m-selig.ae.illinois.edu/ads/coord_database.html*

UK Govenment Statistics (2017), Digest of UK Energy Statistics (DUKES) report: electricity, Technical report, Department for Business Energy & Industrial Strategy.

US Energy Information Administration (2016), International Energy Outlook 2016, Technical Report May, Washington DC.
URL: *www.eia.gov/forecasts/ieo%0AThis*

Val, D. V. and Chernin, L. (2011), 'Reliability-Based Design of Rotor Blades in Tidal Stream Turbines', *EWTEC 2011 Proceedings* .
URL: *http://www.see.ed.ac.uk/ shs/EWTEC 2011 full/EWTEC_CD/papers/127.pdf*

van Bussel, G. J. W. (2007), 'The science of making more torque from wind: Diffuser experiments and theory revisited', *Journal of Physics: Conference Series* **75**(012010).

van Rossum, G. (1995), Python Tutorial, Technical report, Centrum voor Wiskunde en Informatica (CWI), Amsterdam.

Viterna, L. a. and Janetzke, D. C. (1982), Theoretical and experimental power from large horizontal-axis wind turbines, Technical report, US Department of Energy, Conservation and Renewable Energy Wind Energy Technology Division.

Westphal, T. and Nijssen, L. (2012), 'Fatigue life prediction of rotor blade composites : Validation of constant amplitude formulations with variable amplitude experiments', *Journal of Physics: Conference* **555**.

Whelan, J. I. and Graham, J. M. (2009), 'A free surface and blockage ratio correction for tidal turbines', *Fluid Mechanics* **624**, 281–291.

Whelan, J. I., Graham J. M. R. and Peiro J. (2009), 'A free-surface and blockage correction for tidal turbines', *Journal of Fluid Mechanics* **624**, 281–291.

Whelan, J. I. and Stallard, T. J. (2011), 'Arguments for modifying the geometry of a scale model rotor', *9th European Wave and Tidal Energy Conference, Southhampton* .

Wilson, R. E. and Lissaman, P. B. S. (1974), Applied aerodynamics of wind power machines, Technical report, Oregon State University, Oregon State University.

Yao, J., Yuan, W., Xie, J. and Zhou, H. (2012), 'Numerical simulation of aerodynamic performance for two dimensional wind turbine airfoils', *Procedia Engineering* **31**, 80–86.
URL: *http://dx.doi.org/10.1016/j.proeng.2012.01.994*

Zeiner-gundersen, D. H. (2015), 'Turbine design and field development concepts for tidal , ocean , and river applications', *Energy Science and Engineering* pp. 27–42.

Zhou, Z., Benbouzid, M., Charpentier, J.-f. and Scuiller, F. (2017), 'Developments in large marine current turbine technologies A review', *Renewable and Sustainable Energy Reviews* **71**(December 2016), 852–858.
URL: *http://dx.doi.org/10.1016/j.rser.2016.12.113*

APPENDICES

Appendix A1

A1.1 Linear momentum theory in channel flow

Channelling effects have been investigated by Garrett and Cummins (2007), who have developed a 1-D analysis of flow in a stream tube between two rigid surfaces. A schematic of the streamtube is shown in Figure A1.1, with notation detailed in Table A1.1

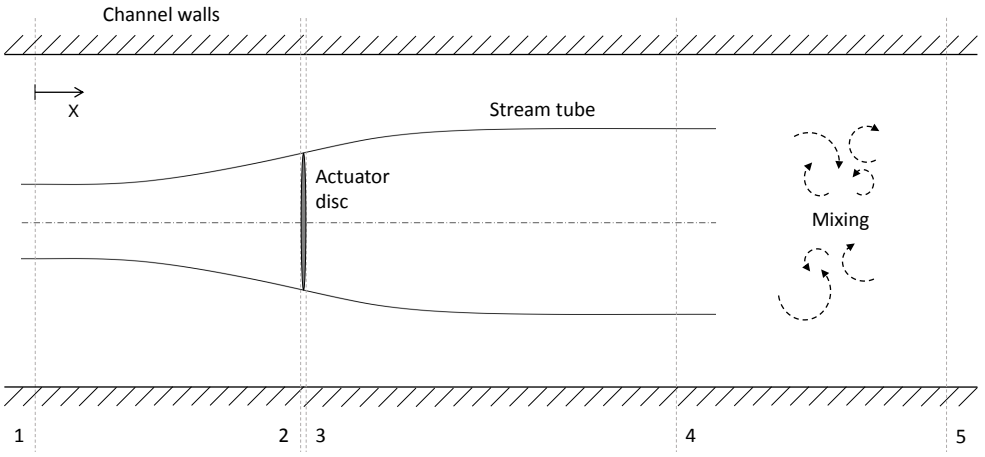

Figure A1.1: Schematic of an actuator disc within a stream tube in channel flow, with numbered cross sectional planes relating to: 1 - upstream; 2 - disc upstream; 3 - disc downstream; 4 - downstream; 5 - far downstream

Table A1.1: Table of notations used in one-dimensional actuator disc theory for channel flow, indicating velocities, areas and pressures at five cross sectional locations within the stream tube (t) and bypass (b)

Location	1	2	3	4	5
Velocity	$U_{t1} = U$	$U_{t2} = U_d$	$U_{t3} = U_d$	U_{t4}	$U_5 = U$
Area	A_{t1}	$A_{t2} = A_d$	$A_{t3} = A_d$	A_{t4}	A_5
Pressure	$p_{t1} = p$	p_{t2}	p_{t3}	$p_{t4} = p_4$	p_5
Velocity	$U_{b1} = U$	U_{b2}	U_{b3}	U_{b4}	
Area	A_{b1}	A_{b2}	A_{b3}	A_{b4}	
Pressure	$p_{b1} = p$	p_{b2}	p_{b3}	$p_{b4} = p_4$	

A1.1.1 Continuity

The area of the channel can be defined in relation to the stream tube (t) and the bypass (b) flow:

$$A_c \ = A_{t1} + A_{b1} \ = A_{t4} + A_{b4}$$

Where the velocities are defined as previously:

$$\begin{aligned} U_{t1} &= U_{b1} = U \\ U_{t2} &= U_{t3} = U_d \\ A_{t2} &= A_{t3} = A_d \end{aligned}$$

Assuming the upstream and downstream regions are sufficiently far from the disc that there is a constant pressure in each plane such that:

$$\begin{aligned} p_{b1} &= p_{t1} = p \\ p_{b4} &= p_{t4} = p_4 \end{aligned}$$

Again, conservation of mass leads to the continuity equations for both the stream

tube and now the bypass:

$$\begin{aligned} \rho A_{t1} U &= \rho A_d U_d &&= \rho A_{t4} U_{t4} \\ \rho A_{b1} U &= \rho A_{b2} U_{b2} &&= \rho A_{b3} U_{b3} = \rho A_{b4} U_{b4} \end{aligned} \tag{A1.1}$$

Combining for the different positions along the stream tube, assuming the flow is incompressible:

$$\begin{aligned} A_{t1} U + A_{b1} U &= A_{t4} U_{t4} + A_{b4} U_{b4} \\ A_c U &= A_{t4} U_{t4} + (A_c - A_{t4}) U_{b4} \\ A_c (U - U_{b4}) &= A_{t4} (U_{t4} - U_{b4}) \end{aligned} \tag{A1.2}$$

A1.1.2 Bernoulli's formulation

Bernoulli's equations in the bypass can be expressed as:

$$\begin{aligned} p_{b1} + \frac{1}{2}\rho U_{b1}^2 = p_{b2} + \frac{1}{2}\rho U_{b2}^2 \quad &\Rightarrow \quad p + \frac{1}{2}\rho U^2 = p_{b2} + \frac{1}{2}\rho U_{b2}^2 \\ p_{b3} + \frac{1}{2}\rho U_{b3}^2 = p_{b4} + \frac{1}{2}\rho U_{b4}^2 \quad &\Rightarrow \quad p_{b2} + \frac{1}{2}\rho U_{b2}^2 = p_4 + \frac{1}{2}\rho U_{b4}^2 \end{aligned}$$

Which combine to:

$$p - p_4 = \frac{1}{2}\rho \left(U_{b4}^2 - U^2 \right) \tag{A1.3}$$

Inside the stream tube, a similar set of expressions can be written:

$$\begin{aligned} p_{t1} + \frac{1}{2}\rho U_{t1}^2 = p_{t2} + \frac{1}{2}\rho U_{t2}^2 \quad &\Rightarrow \quad p + \frac{1}{2}\rho U^2 = p_{t2} + \frac{1}{2}\rho U_{t2}^2 \\ p_{t3} + \frac{1}{2}\rho U_{t3}^2 = p_{t4} + \frac{1}{2}\rho U_{t4}^2 \quad &\Rightarrow \quad p_{t3} + \frac{1}{2}\rho U_{t2}^2 = p_4 + \frac{1}{2}\rho U_{t4}^2 \end{aligned}$$

Combining and substituting Equation A1.3:

$$\begin{aligned} p + \frac{1}{2}\rho U^2 &= p_{t2} + p_4 + \frac{1}{2}\rho U_{t4}^2 - p_{t3} \\ p_{t2} - p_{t3} &= \frac{1}{2}\rho\left(U^2 - U_{t4}^2\right) + (p - p_4) \\ &= \frac{1}{2}\rho\left(U_{b4}^2 - U_{t4}^2\right) \end{aligned} \tag{A1.4}$$

A1.1.3 Momentum change

Considering now the force associated to the momentum change between 1-4, substituting Equations A1.2 and A1.3:

$$\begin{aligned} F_{ax} &= \rho A_c U^2 - \rho A_{t4} U_{t4}^2 - \rho A_{b4} U_{b4}^2 + (p - p_4) A_c \\ &= \frac{1}{2}\rho A_{t4}\left(U_{b4} - U_{t4}\right)\left(U_{b4} + 2U_{t4} - U\right) \end{aligned} \tag{A1.5}$$

The force is equal to the pressure difference across the disc (Δp_d), thus:

$$\begin{aligned} F_{ax} &= (p_{t2} - p_{t3}) A_d \\ &= \frac{1}{2}\rho\left(U_{b4}^2 - U_{t4}^2\right) A_d \end{aligned} \tag{A1.6}$$

A1.1.4 Combining the theories

Equations A1.5 and A1.6 can be equated such that:

$$\begin{aligned} \frac{1}{2}\rho\left(U_{b4}^2 - U_{t4}^2\right) A_d &= \frac{1}{2}\rho A_{t4}\left(U_{b4} - U_{t4}\right)\left(U_{b4} + 2U_{t4} - U\right) \\ U_d &= \frac{U_{t4}\left(U_{b4} + U_{t4}\right)}{U_{b4} + 2U_{t4} - U} \end{aligned} \tag{A1.7}$$

To confirm consistency with the unconstrained case, these equations are applied with an infinite channel area. When $A_c \to \infty$, $U_{b4} \to U$, the velocity at the disc simplifies to: $U_d = U + U_{t4}/2$ which is equivalent to Equation 2.8.

An expression for the downstream bypass velocity can be made by rearranging Equation A1.1 and inserting into Equation A1.2. Firstly it can be stated that:

$$U_{t4}\left(U_{b4}-U\right)=\epsilon U_d\left(U_{b4}-U_{t4}\right) \tag{A1.8}$$

Where $\epsilon = A_d/A_c$ is the blockage ratio. Using Equation A1.7:

$$\begin{aligned} U_{t4}\left(U_{b4}-U\right) &= \frac{\epsilon U_{t4}\left(U_{b4}+U_{t4}\right)\left(U_{b4}-U_{t4}\right)}{U_{b4}+2U_{t4}-U} \\ 0 &= \left(1-\epsilon\right)U_{b4}^2-2\left(U-U_{t4}\right)U_{b4}+\left(U^2-2UU_{t4}+\epsilon U_{t4}^2\right) \end{aligned} \tag{A1.9}$$

Taking the positive root of this quadratic expression then gives:

$$U_{b4}=\frac{U-U_{t4}+\left[U_{t4}^2\left(1-\epsilon+\epsilon^2\right)+\epsilon U^2-2\epsilon UU_{t4}\right]^{\frac{1}{2}}}{\left(1-\epsilon\right)} \tag{A1.10}$$

A1.1.5 Coefficients of power and thrust

The power (neglecting losses) can be written as before, where $P = F_{ax}U_d$. Substituting Equations A1.5 and A1.7, is equal to:

$$P=\frac{1}{2}\rho\left(U_{b4}^2-U_{t4}^2\right)A_d\frac{U_{t4}\left(U_{b4}+U_{t4}\right)}{U_{b4}+2U_{t4}-U} \tag{A1.11}$$

The coefficient of thrust and power are, as before, defined as:

$$C_T=\frac{F_{ax}}{\frac{1}{2}\rho AU^2} = \frac{U_{b4}^2-U_{t4}^2}{U^2} \tag{A1.12}$$

$$C_P=\frac{P}{\frac{1}{2}\rho A_dU^3} = \left(\frac{U_{b4}^2-U_{t4}^2}{U^3}\right)\frac{U_{t4}\left(U_{b4}+U_{t4}\right)}{U_{b4}+2U_{t4}-U} \tag{A1.13}$$

A1.2 Blockage correction for channel flows

Due to the presence of the boundaries of the tunnel, the wake expansion is restricted, leading to higher forces and power output than seen in open water conditions. Blockage correction factors based on actuator disc theory can be applied in order to account for this effect, thus enabling measurements from scale model experiments in channels to be converted into 'equivalent open water' values.

Bahaj, Molland, Chaplin and Batten (2007) detail a method modifying the Glauert expressions for wake expansion based on an actuator disc model as described in above. This method assumes the flow is inviscid and uniform across each plane along the streamtube, where the thrust is a result of the pressure drop across the turbine.

The ratio of the upstream velocity of the blocked case to an unbounded free stream equivalent inflow velocity (U_F) can be defined as:

$$\frac{U}{U_F} = \frac{\frac{U_d}{U}}{\left(\frac{U_d}{U}\right)^2 + \frac{C_T}{4}} \tag{A1.14}$$

Where C_T is the thrust coefficient taken from tank tests.

This can be solved by an iterative process, applying linear momentum theory equations of flow in a channel as defined in Section A1.1. From the continuity equations expressed in Equation A1.8, it can be stated that:

$$\frac{U}{U_{t4}} = \frac{U_{b4}}{U_{t4}} - \epsilon \frac{U_d}{U_{t4}} \left(\frac{U_{b4}}{U_{t4}} - 1 \right) \tag{A1.15}$$

Where the ratio of disc to upstream velocities can be defined by rearranging

Equation A1.10 such that:

$$\frac{U_d}{U_{t4}} = \frac{-1 + \left[1 + \epsilon\left(\left(\frac{U_{b4}}{U_{t4}}\right)^2 - 1\right)\right]^{1/2}}{\epsilon\left(\frac{U_{b4}}{U_{t4}} - 1\right)} \tag{A1.16}$$

Also, through rearranging Equation A1.12:

$$\begin{aligned} C_T &= \left(\frac{U_{t4}}{U}\right)^2 \left(\left(\frac{U_{b4}}{U_{t4}}\right)^2 - 1\right) \\ \frac{U}{U_{t4}} &= \left(\frac{C_T}{\left(\frac{U_{b4}}{U_{t4}}\right)^2 - 1}\right)^{-1/2} \end{aligned} \tag{A1.17}$$

The process is then to:

1. apply values of (U_{b4}/U_{t4}) iteratively into Equations A1.15 and A1.17, until (U/U_{t4}) are equal
2. (U_d/U) can then be determined, through the product of (U_d/U_{t4}) from Equation A1.16, and $(U/U_{t4})^{-1}$ from Equation A1.17
3. The value of (U_d/U) can then be inserted into Equation A1.14 to determine the bounded to unbounded velocity ratio (U/U_F)

This velocity ratio can then be used as a multiplication factor in order to correct measured tip speed ratio, coefficient of thrust and coefficient of power as:

$$TSR_F = TSR\left(\frac{U}{U_F}\right) \tag{A1.18}$$

$$C_{T_F} = C_T\left(\frac{U}{U_F}\right)^2 \tag{A1.19}$$

$$C_{P_F} = C_P\left(\frac{U}{U_F}\right)^3 \tag{A1.20}$$

Which assumes that the turbine rotational velocity (Ω), axial thrust (F_{ax}) and

flow at the disc (U_d) are equal for the open water as in the constrained case. Experimental results from the literature are often presented in their blockage corrected form by the authors, however in situations where this is not the case, the correction factors can be applied in order to make direct comparisons with BEMT.

Appendix 2

A2.1 3D stall delay correction

The 2-D modelling assumptions are limited in application to turbine blades, because they do not take into account the effects of the aerofoil rotation.

The lift and drag data used in BEMT calculations is usually based on 2-D aerofoil analyses from wind tunnel tests or numerical studies using panel codes or CFD. These do not account for the centrifugal and Coriolis effects, which increases the tendency of the boundary layer to remain attached to the foil surface at higher angles of attack. This effectively delays the onset of stall, which can be approximated using a '3-D correction'. The NREL AirfoilPrep routine (Ning, 2013) applies 3D rotational corrections to 2-D wind tunnel data based on the Du-Selig and Eggers adjustments to the lift and drag coefficients respectively (Hansen, 2004).

Stall delay models have the following general form (Brenton et al., 2007):

$$C_{L_{3D}} = C_{L_{2D}} + f_L(C_{L_{inv}} - C_{L_{2D}}) \tag{A2.21}$$

$$C_{D_{3D}} = C_{D_{2D}} + f_D(C_{D_{inv}} - C_{D_{2D}}) \tag{A2.22}$$

Where the inviscid lift and drag coefficients are defined as:

$$C_{L_{inv}} = 2\pi \left(\alpha - \alpha_{(lift=0)}\right) \tag{A2.23}$$

$$C_{D_{inv}} = C_{D_{(\alpha=0)}} \tag{A2.24}$$

The Snel model proposes a simplified form of the 3D boundary layer equations for the lift coefficient (Snel, et al., 1994):

$$f_L = 3\left(\frac{c}{r}\right)^2 \tag{A2.25}$$

The Du-Selig stall delay model is an extension of this, based on the analysis of 3D integral boundary layer equations and in the form (Timmer and Bak, 2013):

$$f_L = \frac{1}{2\pi}\left(\frac{1.6\,(c/r)}{0.1267}\frac{a-(c/r)^{\frac{d}{\Lambda}\frac{R}{r}}}{b+(c/r)^{\frac{d}{\Lambda}\frac{R}{r}}} - 1\right) \tag{A2.26}$$

$$f_D = \frac{1}{2\pi}\left(\frac{1.6\,(c/r)}{0.1267}\frac{a-(c/r)^{\frac{d}{2\Lambda}\frac{R}{r}}}{b+(c/r)^{\frac{d}{2\Lambda}\frac{R}{r}}} - 1\right) \tag{A2.27}$$

Where $\Lambda = \Omega R/\sqrt{U^2 + (\Omega R)^2}$ is the modified tip speed ratio accounting for rotational effects and a, b and d are empirical correction factors set to unity by Du and Selig, which is repeated in other studies (Park, et al., 2006).

Although the Du-Selig method includes a function for drag coefficient adjustment, AirfoilPrep implements the Eggers model (Moriarty and Hansen, 2005):

$$C_{D_{3D}} = C_{D_{2D}} + \Delta C_D \tag{A2.28}$$

Where:

$$\Delta C_D = \Delta C_L \frac{\sin(\alpha) - 0.12\cos(\alpha)}{\cos(\alpha) - 0.12\sin(\alpha)} \tag{A2.29}$$

Using the 3D lift coefficient as defined by Du-Selig above (Ning, 2012):

$$\Delta C_L = C_{L_{3D}} - C_{L_{2D}} \tag{A2.30}$$

A2.2 Extrapolation method

Analyses are usually limited to a small range of angles of attack, which is not sufficient to cover the large range of possible angles that could be seen in blade operation. In order to circumvent these limitations, semi-empirical correction factors can be applied to the 2-D lift and drag data.

As the attack angle increases beyond stall, the adverse pressure gradient on the leading edge surface grows, whilst the separation point on the suction surface moves forwards. At a specific point, the leading edge boundary layer completely detaches, and the foil enters a 'deep-stall condition' Timmer and Bak (2013). This causes highly unsteady flow with periodic vortex shedding, which are time averaged when assessing lift and drag coefficient curves.

Post stall conditions can be characterised by the following empirical expressions as developed by Viterna and Janetzke (1982), derived from three different rotor configurations:

$$C_L = \frac{C_{D_{max}}}{2}\sin(2\alpha) + k_1\frac{\cos^2(\alpha)}{\sin(\alpha)} \tag{A2.31}$$

$$C_D = C_{D_{max}}\sin^2(\alpha) + k_2\cos(\alpha) \tag{A2.32}$$

Where:

$$k_1 = \left(C_{L_s} - C_{D_{max}}\sin(\alpha_s)\cos(\alpha_s)\right)\frac{\sin(\alpha_s)}{\cos^2(\alpha_s)} \tag{A2.33}$$

$$k_2 = \frac{C_{D_s} - C_{D_{max}}\sin^2(\alpha_s)}{\cos(\alpha_s)} \tag{A2.34}$$

In order to ensure continuity with pre stall aero data, k_1 and k_2 are defined at a constant (stall) angle (denoted by s) as the point of highest lift. $C_{D_{max}}$ is the drag at $\alpha = 90°$ and can be defined as function of aspect ratio: $C_{D_{max}} = 1.111 + 0.018AR$ for where the aspect ratio $AR \leq 50$.

This is an approximation defined in fluid dynamics texts to calculate the drag coefficient of flat plates as adopted, where the aspect ratio is defined: $AR = R/c_{75\%}$ (taken at 75% down the blade length). These equations are based on matching the total maximum rotor power, and therefore already account for 3-D effects.

Appendix 3

A3.1 Menter's $k-\omega$ SST turbulence model

The formulation of the two equation model uses the original $k-\omega$ formulation at the near-wall, blended to a transformed $k-\varepsilon$ model in the free stream (Menter, 1994). This gives the combined transport equations for the turbulent kinetic energy k in terms of dissipation frequency ω as:

$$\frac{\partial(\rho k)}{\partial t}+\frac{\partial(\rho u_j k)}{\partial x_j}=P-\beta^*\rho\omega k+\frac{\partial}{\partial x_j}\left[(\mu+\sigma_k\mu_t)\frac{\partial k}{\partial x_j}\right] \tag{A3.35}$$

with the specific dissipation rate given by:

$$\frac{\partial(\rho\omega)}{\partial t}+\frac{\partial(\rho u_j\omega)}{\partial x_j}=\frac{\gamma\rho P}{\mu_t}-\beta\rho\omega^2+\frac{\partial}{\partial x_j}\left[(\mu+\sigma_\omega\mu_t)\frac{\partial\omega}{\partial x_j}\right] + 2(1-F_1)\frac{\rho\sigma_{\omega 2}}{\omega}\frac{\partial k}{\partial x_j}\frac{\partial\omega}{\partial x_j} \tag{A3.36}$$

where:

$$P=\tau_{ij}\frac{\partial u_i}{\partial x_j} \tag{A3.37}$$

If ϕ_1 represents all constants in the $k-\omega SST$ model and ϕ_2 for the constants in the transformed $k-\varepsilon$ model, then:

$$\phi=F_1\phi_1+(1-F_1)\phi_2 \tag{A3.38}$$

Where a blending function is introduced:

$$F_1 = tanh(arg_1^4), \quad arg_1 = min\left[max\left(\frac{\sqrt{k}}{\beta^*\omega y}; \frac{500\mu}{\rho y^2\omega}\right); \frac{4\rho\sigma_{\omega 2}k}{C_{k\omega}y^2}\right] \tag{A3.39}$$

$$C_{k\omega} = max\left(\frac{2\rho\sigma_{\omega 2}}{\omega}\frac{\partial k}{\partial x_j}\frac{\partial \omega}{\partial x_j}; 10^{-20}\right) \tag{A3.40}$$

With all constants are defined in Table A3.2. This is used to describe the turbulent eddy viscosity as:

$$\mu_t = \frac{\rho a_1 k}{max(a_1\omega; \Omega F_2)} \tag{A3.41}$$

Where Ω is the magnitude of vorticity, and:

$$F_2 = tanh(arg_2^2), \qquad arg_2 = max\left(\frac{2\sqrt{k}}{\beta^*\omega y}; \frac{500\mu}{\rho y^2\omega}\right) \tag{A3.42}$$

Table A3.2: Constants used in $k-\omega SST$ models

	σ_k	σ_ω	β	γ	β^*	a_1
ϕ_1	0.85	0.500	0.075	0.553	0.09	0.31
ϕ_2	1.00	0.856	0.0828	0.440	0.09	

A3.2 Turbulence model testing

A test perform was performed to compare the temporal lift and drag predictions from various turbulence models including: kω-SST; $k-\epsilon$ Linear Production (LP), with and without a Scalable Wall Function (SWF); Spalart-Allmaras (SA); and an R_{ij} Elliptical Blending Reynolds Stress Model (EBRSM). Note that the same mesh was used for each case, which was are constructed to give $y^+ \sim 1$. Also a constant timestep of 5.0E-04 s is applied in each case. Each turbulence model has its own set of mesh and viscous sub-layer thickness requirements, and therefore this study only provides a general indication of model performances.

The results of this test are shown in Figure A3.2. The largest influences occur at the start of the simulations, where the $R_{ij} - \epsilon$ appears to exhibit the largest instabilities. All models converge within a similar time of ∼4 s. Most models converge to similar drag coefficient with the exception of the $k - \epsilon$, which can be resolved with the inclusion of a scalable wall function. There is a noticeable difference in the lift predictions, where the kω-SST and Spalart Almaras are around 15% higher that the other models.

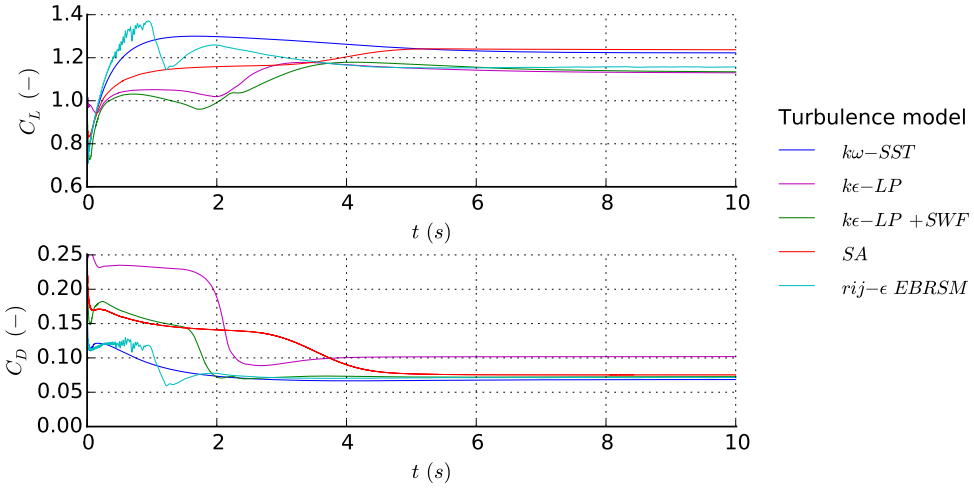

Figure A3.2: NACA0018 aerofoil coefficients of lift (top) and drag (bottom) with time (t) at Re_{ch}= 3.4E+06, comparing different turbulence models at $\alpha = 15°$

Appendix 4

A4.1 Reference CFD parameters for OpenHydro TSTs

Optydro is an engineering consultancy with expertise in numerical simulations of turbines and design optimisation of hydraulic machinery. The company has previously provided consultation on design optimisation of ducted TSTs (Kueny, 2012). CFD studies of the OCT16 (Kueny, 2015*b*) and PS2 (Kueny, 2015*a*) OpenHydro devices were performed by Professor Kueny of Optydro Concept, which are used as references throughout this comparative study. The complete set of simulation parameters are detailed in Table A4.3.

Model domain: The models only consider the turbine rotor and stator, where the foundation and support structures are removed. The overall domain is made up of a cylinder with the turbine at the centre. The turbine rotor and stator assemblies are antisymmetric, and therefore a $1/10^{th}$ domain size has been analysed to reduce the computational time. The rotor is cut to produce a 36° segment of a single blade connected to an outer ring which rotate within the stator. The PS2 stator consists of 36 facets, where 4 are modelled to represent a 40° segment, whereas for the OCT16 a segment of 45° is taken.

Boundary conditions: The domain is split into rotating and stationary sections. Rotating elements are assigned to the volume within the duct. A 'stage' (or

'mixing plane') type model is imposed at the interface between rotating and stationary elements, which calculates the circumferential average exchange of azimuthal pressure and flow velocity.

For the PS2 device, the rotor/stator interface does not include an axis of rotation. Therefore a central cylinder is placed at the blade tips with a third rotor/stator interface. The central cylinder is modelled with periodic boundaries.

The external face of the cylindrical domain is deemed sufficiently far away to limit any interactions with the boundaries. A constant pressure equal to atmospheric pressure is imposed on the cylinder external boundaries, equal to the mean pressure calculated at the exit. The inflow velocity is imposed as a constant at the inlet. The surfaces of the turbine are modelled as solid 'no-slip' walls. The sea bed and the free surface are neglected.

Mesh constuction: The domain surfaces are discretised to increase the mesh density at the surfaces of the blade and rotor. A mesh quality control was imposed to limit: orthogonality (skewness), aspect ratio and expansion ratio. A mesh convergence study for the PS2 geometry determined that the height of the first element required a minimum value of 1 mm. However, a value of 0.5 mm was selected to achieve y^+ values to guarantee good functionality of the turbulent wall boundary conditions.

Turbulence model: Two turbulence models were considered based on a $k-\varepsilon$ and Spalart-Allmaras. Although the final results are comparable in both cases, there are larger temporal fluctuations in the case of the Spalart-Allmaras model, where a longer time is required to achieve convergence. A $k-\varepsilon$ turbulence model with the option of an extended wall function was therefore applied to both device models.

Table A4.3: Table of blade resolved RANS simulation parameters for OCT16 (Kueny, 2015*b*) and PS2 (Kueny, 2015*a*) turbines (n/a = not available)

Parameter	OCT16	PS2
Domain		
Upstream	1.5 D	1.5 D
Downstream	4 D	1.5 D
External cylinder diameter	6 D	6 D
Rotor segment	36°	36°
Stator segment	45°	40°
Mesh discretisation		
External normal faces	40x64	40x64
External cylindrical faces	120x64	120x64
Rotor radial concentric rings	21	21
Total mesh		
No. of blocks	20	48
No. of Nodes	2.13 mill	4.23 mill
1st element height		
Rotating domain	0.02 mm	0.5 mm
Exterior domain	0.5 mm	n/a
Mesh quality		
Orthogonality (skewness)	$> 28.6°$	$> 20.9°$
Aspect ratio	< 4000	< 1020
Expansion ratio	< 12	< 17
Overall y+	< 270	< 100
Critcal zones y+	< 30	< 50